

ENVIRONMENTAL RESEARCH

RESEARCH AND TECHNOLOGY BRANCH

TD
890
C75
MOE

c.2
a aa

Environment
Ontario

Jim Bradley, Minister



Copyright Provisions and Restrictions on Copying:

This Ontario Ministry of the Environment work is protected by Crown copyright (unless otherwise indicated), which is held by the Queen's Printer for Ontario. It may be reproduced for non-commercial purposes if credit is given and Crown copyright is acknowledged.

It may not be reproduced, in all or in part, for any commercial purpose except under a licence from the Queen's Printer for Ontario.

For information on reproducing Government of Ontario works, please contact ServiceOntario Publications at copyright@ontario.ca

CRITICAL EVALUATION OF
ATMOSPHERIC POLLUTANT
PARAMETERIZATION FROM
SATELLITE IMAGERY

R. A. C. PROJECT NO. 349 G

Prepared for Environment Ontario by:

N.T. O'Neill, A. Royer, L. Hubert,
CARTEL, Universite de Sherbrooke,
Sherbrooke, Quebec,
and
J.R. Miller, J. Freemantle,
CRESS, York University,
Downsview, Ontario
and
G. Austin, A. Davis,
Dept. of Physics
McGill University,
Montreal, Quebec

JANUARY 1990



Copyright: Queen's Printer for Ontario, 1990
This publication may be reproduced for
non-commercial purposes with appropriate
attribution.

TD
890 ABHB
C75
MOE

DISCLAIMER

This report has been reviewed by the Research Advisory Committee of Environment Ontario and approved for publication. Approval does not necessarily signify that the contents reflect the views and policies of the Ministry of the Environment, nor does mention of trade names or commercial products constitute endorsement or recommendation for use.

CRITICAL EVALUATION OF ATMOSPHERIC POLLUTION PARAMETERIZATION FROM SATELLITE IMAGERY

TABLE OF CONTENTS

	Page
EXECUTIVE SUMMARY	V
LIST OF TABLES	VII
1. INTRODUCTION	1
1.1 Background	1
1.2 General Approach	2
2. AEROSOL MODEL DEFINITIONS AND OPTICAL PARAMETER COMPUTATIONS	4
2.1 Aggregate Aerosol Models	4
2.1.1 Component Aerosols Defined	4
2.1.2 Particle Size Dependence on Ambient Relative Humidity	5
2.1.3 Definition of Models Employed	7
2.1.4 Surface Number Density Considerations	11
(a) Extreme Sulfate Variations	11
(b) Surface Number Density Variations	13
2.2 Optical Parameter Variations	13
2.2.1 Optical Parameter Computations	13
2.2.2 Influence of Relative Humidity	15
2.2.3 Correlation of scattering and absorption coefficients with component concentrations	17
(a) Point volume coefficients	17
(b) Vertically integrated coefficients	24

	Page
2.2.4 Effects of Changes in Aggregate Aerosol Models and Equivalent Surface Number Concentration	25
(a) External Aggregate Aerosol Model	25
(b) Internal Aggregate Aerosol Model	25
 3. RADIATIVE TRANSFER SIMULATIONS	 27
3.1 The 5S Model and Required Input/Output parameters	27
3.2 Model Dependency	30
3.3 Effect of Vertical Inhomogeneities	30
3.4 Selected Results	31
3.4.1 Variation of aggregate aerosol model	31
3.4.2 Ground albedo variations	34
3.4.3 Relative humidity effects	34
3.4.4 Absorption Effects	38
3.4.5 Dependence on satellite bands	38
3.4.6 Illumination Geometry	44
(a) Viewing geometry	44
(b) Solar geometry	46
 4. INVERSION ANALYSIS	 48
4.1 Slope Calculations ($dSO_4 = / dX$)	49
4.2 Error contributions (ΔX)	54
4.2.1 Effects of surface reflectance	54

	Page
4.2.2 Sulfate Mass Scattering Efficiency	56
(a) Variations in relative humidity	58
(b) variations in dry sulfate log normal parameters	58
(c) Contributions due to other fine particle constituents	59
4.2.3 Influence of Optical Absorption by Soot	59
4.2.4 Noise and Radiometric resolution	61
4.2.5 Aggregate aerosol model (discrimination of component aerosol contributions)	63
4.2.6 Radiative transfer model	65
(a) analytical approximations	65
(b) vertical inhomogeneity	66
4.2.7 Other Sources of Error	66
4.3 Cumulative sulfate Errors (ΔSO_4)	66
4.4 Operational Considerations	69
4.4.1 Geometrical Effects	69
4.4.2 Wavelength Passband	70
5. GENERAL CONCLUSIONS AND RECOMMENDATIONS	71
ERRATUM	73
REFERENCES	75

APPENDICES

A. Optical Modelling Background	
A.1 Symbols and Definitions	1
A.2 Relative Humidity Modelling	9
A.3 Some Useful Approximations	16
B. Comparison of Radiative Transfer Models Used to Determine Atmospheric Optical Parameters from Space	26
C. Particle Growth Model Considerations	47

ACKNOWLEDGEMENTS

This project was financed by the Ontario Ministry of the Environment (Project No. 349G). We would also like to acknowledge the support of NSERC, Canada (Grants Numbers A8643 and A1765).

EXECUTIVE SUMMARY

Remote sensing techniques applied to atmospheric monitoring problems offer a spatial and temporal database coverage which cannot be duplicated by conventional ground based measuring programs. However, in spite of these obvious advantages, the methods of interpretation and inversion of remotely sensed optical data are often more qualitative than quantitative. The sensitivity of existing techniques for the inversion of satellite imagery data is not well understood in terms of discriminating constituent types and threshold levels of detection. This lack of technical support has retarded the definition of a comprehensive strategy for satellite sensor development geared towards the remote sensing of tropospheric aerosols.

The objective of the present study was to simulate the atmospherically scattered signal received by a satellite sensor and hence to evaluate the sensitivity of this signal to atmospheric aerosols in general and to atmospheric pollutants in particular. The emphasis of the investigations was on broadband scattering and continuum absorption effects (i.e. the level of information which can be extracted from typical remote sensing satellites) rather than the high spectral resolution properties characteristic of structured molecular absorption phenomena. In the long term this type of research is geared towards the development of an operational satellite monitoring system within the context of the long range transport of atmospheric pollutants (LRTAP) programs.

The simulations were performed as a function of environmental, geometrical and operational parameter constraints. The environmental modelling included the effects of urban and rural type aerosols where the absolute and relative concentration of water soluble (sulfate) particles was allowed to vary and where particle growth and refractive index effects of relative humidity were incorporated. Combined aerosol modes which included fine particle (sulfate based), coarse particle (quartz based), and absorptive aerosols (carbon based) were incorporated as external (independent) aerosol mixtures. Some tests were performed in terms of internal (colayered) aerosol mixtures in order to evaluate the effect of the mixture assumption on the results of the sensitivity study.

The variability of the simulated signals indicate that information on the vertically integrated contribution of submicron scattering and absorbing aerosols can be usefully extracted. Inasmuch as the dominant optical variations occur in the lower troposphere this extracted information can be correlated with ground level concentrations. Furthermore, investigations into the dependence of the satellite signal on vertical inhomogeneity (altitude dependent mixing ratios) indicated a degree of insensitivity which significantly simplifies the radiative transfer calculations and the inversion methodology.

The optical effects of ground level sulfates (predominantly in the form of ammonium salts) are strongly influenced by the ambient relative humidity. Such induced variations in sulfate optical activity result in a ground level mass scattering efficiencies which may vary by a factor of 4 or 5 across the naturally occurring range of relative humidity. Furthermore the scattering contribution by non sulfate fine particle constituents yields scattering efficiencies (per unit mass of sulfates) which, although remarkably consistent, may vary significantly from one region to the next. Because large angle aerosol scattering effects are dominated in the visible spectral region by fine particle aerosols and because fine particle scattering is predominantly a volume or mass effect the variation of the mass scattering efficiencies due to size changes in the dry dimensions of the fine particles is minimal.

The implications of the former variations in terms of satellite remote sensing is that one must, within the context of achieving a sulfate measuring precision of $\pm 5 \mu\text{g}/\text{m}^3$, either directly measure the ground level mass scattering efficiencies or develop a methodology which permits their computation from ground based meteorological measurements combined with parameters extracted from the satellite data.

Fine particle mode (submicron) particles can be distinguished from coarse particle (supermicron) particles by means of two or more bands placed in the spectral region between 0.4 and 1.5 μm . The specificity of sulfates within the fine particle mode is more a function of the dominance of fine particle (water soluble) aerosols in terms of optical effects and in turn the predominance of the sulfate fraction in the water soluble component. At ground level the

optical contribution due to sulfates is typically the largest particularly in conditions of high relative humidity and total extinction. Accordingly, even in the absence of information relating to the contribution of other components (but with information on relative humidity) one can extract an estimate of dry sulfate mass to within a factor of 2 or better.

The study also showed that inversion algorithms should be restricted to reflectances well below and above the Kaufman critical surface reflectance. The critical surface reflectance condition, which is characterized by a counterbalance between atmospheric backscatter and attenuation of surface reflected signals, induces inversion singularities since the satellite signal is effectively transparent to the mass loading of scattering particles. It was also found that the satellite signal was fairly insensitive to the presence of carbonaceous soot over small surface reflectances (scattering atmosphere) but conversely was strongly dependent over high surface reflectances. This suggests that an inversion methodology would be best served by formulating the sulfate inversion around low reflectance pixels in the image and the soot inversion around high reflectance pixels. In the former case one would consider water pixels and vegetation pixels (in the chlorophyll absorption band near $0.65 \mu\text{m}$) while in the latter case one could employ for example snow or bare soil surfaces.

The extraction of mass loading parameters from the total signal received by the satellite sensor implies some apriori knowledge of the ground surface reflectance in the satellite image. To a certain degree this requirement can be circumvented by restricting measurements to spectral regions and scene surfaces whose reflectance is small. However to fully exploit the potential of the satellite data requires a calibration program involving the establishment of reflectance calibration sites and the multi-temporal analysis of repetitive satellite images.

The operational parameter constraints were keyed to the specifications of selected remote sensing satellites which are either operational or will be by at least 1995. These included the NOAA and GOES meteorological satellite series, the Landsat and SPOT resource monitoring satellites and the oceanographic satellite SEAWIFS. The meteorological satellites offer a relatively high rate of image repetition over the same area but are constrained to one or two coarse spectral bands and a large spatial resolution. The 10 bit NOAA sensors, although less than adequate with respect to the number and resolution of spectral bands, offer the best dynamic range and radiometric resolution characteristics of existing spaceborne sensors. The current SPOT and Landsat satellites acquire high spatial resolution images (order of tens of meters) at comparatively high spectral resolution but with a coarse repetition cycle (order of weeks) and a radiometric resolution which is marginal for detecting differences induced by significant changes in sulfate concentration.

The Landsat SEAWIFS sensor, due to be launched in 1991, offers a spectral resolution, repetition rate (2 days), an image overlap capability and a radiometric resolution which more closely approximate the requirements for passive atmospheric remote sensing. Within the near future the HIRIS and MODIS sensors possibly coupled with vertical structure data from the laser sounder (LASA) represent the realization of a sensor package for which one of the major design constraints was the remote sensing of atmospheric constituents. The latter sensors will be part of the EOS space station package to be launched in 1995.

A comparison of radiative transfer models indicated that the analytical 5S model developed by D. Tanré and co-workers represented the most optimal compromise of speed and accuracy in terms of applying a pixel by pixel inversion algorithm to large satellite images. Comparison with a multiple scattering, multiple layer model demonstrated however that, for non nadir conditions, modifications to the model were required in order to achieve an accuracy commensurate with more rigorous solutions. These modifications are relatively easy to implement, and add little to the computation time.

The simulation analysis was sufficiently promising to warrant a program of simultaneous ground based, airborne and satellite measurements as a subsequent phase to the present work. This program should include as well the acquisition and analysis of high spectral resolution airborne data to address the specificity problem.

LIST OF TABLES

Table 2.1.1.1	Log Normal Parameters
Table 2.1.3.1	Aggregate Aerosol Models
Table 2.1.4.1	Ground Based Measurements of Sulfate Concentrations and Aerosol Scattering Coefficients
Table 2.1.4.2	Maximum Surface Number Densities of Aggregate Aerosol Models
Table 2.1.4.3	Number Density Values (N) Used in the Radiative Transfer Calculations
Table 2.2.1.1	Computed Optical Parameters (Particle Size Distribution (PSD) independent of altitude)
Table 2.2.1.2	Refractive Indices of water and dry component aerosols which were employed in all optical calculations
Table 2.2.2.1	Sample refractive index calculations as a function of relative humidity (wavelength of 0.55 μm)
Table 3.1	Radiative Transfer input/output parameters
Table 3.2	Radiative Transfer Calculations (input parameter variations)
Table 3.4.5.1	Apparent reflectance variation corresponding to an $\text{SO}_4^{=}$ variation from 0 to 50 $\mu\text{g}\cdot\text{m}^{-3}$ normalized to the total satellite sensor noise error tabulated in Table 4.2.4.1
Table 3.4.6.1	Observer's zenith angle and scattering angle in the solar plane for a solar zenith angle of 45 degrees
Table 4.2.1.1	Table of measured ground reflectances and their uncertainties for a number of surface types derived from Landsat data (from Royer et al. 1988)
Table 4.2.3.1	Single scattering albedo as a function of wavelength, relative humidity and aerosol model
Table 4.2.3.2	Error rate $(\delta\rho^*/\delta\omega_0)_{f,\rho}$ for nadir geometry, 45 degrees solar zenith angle and 0.633 μm wavelength (units of percentage change per .01 increment in ω_0)
Table 4.2.4.1	Noise Equivalent Reflectances (NER) and Quantization Error Reflectances (QER)
Table 4.3.1	Input parameter precision required to achieve a sulfate concentration precision of 1.6 $\mu\text{g}/\text{m}^3$ per parameter
Table 6.1	Corrected Number Densities

1. INTRODUCTION

The principal objective of this study was the simulation of the atmospherically reflected signal received by a satellite imaging sensor and an evaluation of the sensitivity of this signal to atmospheric aerosols. Within this context we sought to evaluate the sensitivity of the signal to pollutant aerosols with an emphasis on fine particle sulfates. The motivation for an analysis of this nature is to evaluate the potential for employing satellite imagery as a means towards monitoring spatial and temporal variations of anthropogenic aerosols. Such an evaluation is essential towards understanding how remote sensing technology can be applied to enhance or complement operational measuring techniques employed in long range pollutant (LRTAP) problems.

The sensitivity study was then employed to define an error budget for an inversion procedure which sought to extract altitude integrated concentrations of sulfates given realistic values and uncertainties in both operational and environmental parameters. The operational parameters included radiometric specifications of a variety of existing and planned satellite sensors while the environmental parameters encompassed the solar, atmospheric and surface characteristics likely to have a significant effect on the total measured satellite signal. The incentive for this sensitivity analysis was to permit a more judicious selection of operational parameters and an understanding of tradeoff considerations given different levels of uncertainty in the environmental parameters.

1.1 Background

The exploitation of ground based optical measurements for the quantification of atmospheric turbidity and (at least implicitly) aerosol concentration variations has been carried out by astronomers since the early 1900s (Roosen et al., 1973). In more recent times, meteorologists have recognized the utility of optical measurements as a means of quantifying the aerosol presence in the atmosphere (Middleton, 1952).

One of the most apparent optical effects of aerosols is the attenuation of visible light reflected from structures at distances of kilometers from an observer. This phenomenon which is predominantly due to the scattering of light out of the line of sight of the observer is to a great extent influenced by the fine particle (accumulation) mode in the radius size range between .1 and 1 μm . Numerous studies have shown that ground level scattering coefficients and measures of visibility are strongly correlated with the sulfate component over urban and rural sites (see for example the references detailed in Table 2.1.4.1.). Other researchers have observed that scattering by carbonaceous products and ammonium nitrate can be important at least in urban areas (Sloane, 1983) while absorption by carbonaceous soot may significantly effect the light scattering budget in rural areas (Japar et al., 1986; Ackerman and Toon, 1981) and in particular over urban sites (Rosen et al., 1978; Ackerman and Toon, 1981; Sloane, 1983; Richards and Bergstrom, 1986).

These types of optical correlations have inspired a few researchers in the remote sensing field to investigate the applicability of satellite optical imaging as a means of monitoring at least the most optically important atmospheric pollutants. In fact the use of remote sensing for the detection of both anthropogenic and natural aerosols from space has, in the past ten years, begun to be recognized as a viable monitoring option (Lyons, 1980; Quenzel, 1982; Chung, 1986). This approach represents a natural evolution of ideas since the remote sensing community has for some time been concerned with the estimation of aerosol optical effects as a means of predicting and eliminating the atmospheric contribution to surface reflected signals (Turner and Spencer, 1972; Ahern et al., 1977; O'Neill et al. 1978; Gordon, 1978).

The principal application of satellite detection methodologies to date has involved the detection of massive aerosol dust clouds where the optical effects are actually dominated by supermicron particles (Kaestner et al., 1982; Legrand et al., 1985; Takayama and Takashima, 1986; Deuze et al., 1988; Egan, 1986; 1988; Legrand et al., 1988; Tanré et al., 1988). Since no satellite sensor, designed specifically for downward looking aerosol detection exists, the analysis

of remote sensing techniques has been performed in terms of meteorological and earth resources satellites. These investigations include work with NOAA data (Kindman et al., 1985; Freemantle et al., 1986; Takayama and Takashima, 1986; Carson and Needling, 1977; Ahmad et al., 1988; Rao et al., 1988), GOES data (Griggs, 1979; Fraser et al., 1986; Tsonis and Leaitch, 1986; and Tsonis, 1987), METEOSAT (Kaestner et al., 1982; Deuze et al., 1988; Legrand et al. 1985, 1988), and the Landsat earth resources satellite (Meckler et al., 1977; Fraser, 1986; Otterman et al., 1982; Royer et al., 1988; Tanré et al., 1988). In the Soviet Union results have been reported for the Meteor satellite (Ivanchik et al., 1985).

In terms of the fine particle mode a number of researchers have attempted to extract indicators related to sulfate loading from satellite images (Lyons, 1980; Fraser and Kaufman, 1984; Tsonis and Leaitch, 1986; Tsonis, 1987). These investigations were primarily empirical in nature and sought to compare satellite derived estimates of sulfate content with a comparatively few ground based measurements. The simulation approach employed in this study permits a more flexible and fundamental understanding of the important variables in the error budget for extracting sulfate content. Provided the models employed are physically realistic and are based on realistic input data this technique will assist in the interpretation of empirical results while enabling a comprehensive evaluation of input parameter optimization. Even in those cases where the modeling is inexact in an absolute sense the relative sulfate sensitivity as a function of operational and environmental input parameters will provide information useful for the development of an inversion methodology.

1.2 General Approach

The simulation approach adopted in this work entails the development of models which are sufficiently realistic to be applicable on a general scale without being overly encumbered in unnecessary detail. Whether a particulate model attribute can be considered a detail depends ultimately on its contribution to the satellite measured signal relative to the noise level of that signal.

Initially the modelling efforts included the definition of aerosol size distributions for aerosol constituents known to be optically active in the tropospheric boundary layer. In this regard we were aided by existing climatological models derived from extensive optical and in situ measurements. As well airborne particle size distribution measurements made during different seasons over rural and urban regions in southeastern Canada were employed in an effort to obtain regionally representative particle characteristics.

Aggregate aerosol models consisting of three externally mixed (independent) particle size modes (carbonaceous soot, water soluble and dust like) were used as standard inputs throughout the simulations. The hygroscopic component of these aggregate aerosol models was assumed to be primarily due to the narrow fine particle water soluble mode which itself was assumed to consist primarily of sulfate particles. The effects of relative humidity were then incorporated by applying a particle growth model to the sulfate component of the fine particle mode and computing the modified size distribution.

Standard values of refractive index were employed in order to define the optical characteristics of each particle size mode. In the case of the sulfate component the refractive index was computed as a volume weighted mean of the dry sulfate refractive index and that of pure water. Assuming spherical particles, a Mie scattering code was utilized to compute the scattering and absorbing coefficients characterizing a single aggregate aerosol particle (or the additive effects of a number of such identical particles) and the relative angular scattering distribution (phase function) as a function of relative humidity.

These *point volume optical parameters* were then effectively integrated or averaged over altitude with the assumption that the aggregate aerosol particle size distribution was itself independent of altitude. The columnar optical parameters so obtained were then entered into a radiative transfer equation (5S) which had been preselected on the basis of speed and accuracy considerations. The 5S model was utilized to simulate the signal received by a satellite sensor over a variety of operational and environmental parameters including columnar sulfate concentration, sensor passband, surface reflectance, aggregate aerosol model, carbonaceous soot absorption and relative humidity.

Given the results of the radiative transfer simulations, the partial derivatives (*error rates*) relating changes in sulfate concentration to changes in the operational and environmental parameters were computed. The uncertainties in these latter parameters were then evaluated in order to obtain an error budget for sulfate concentrations computed from satellite optical data. This error budget was analyzed in order to characterize those operational and environmental parameter ranges which were optimal for the development of satellite based inversion methodology for the extraction of sulfate concentration.

CHAPTER 2

AEROSOL MODEL DEFINITIONS AND OPTICAL PARAMETER COMPUTATIONS

2.1 Aggregate Aerosol Models

In this section we characterize the component particle size modes and the manner in which they are combined in order to define the two basic aggregate aerosol models (standard and urban). The aggregate aerosol model specifically refers to an average aerosol particle defined by the fractional number density contribution of each component (see also Appendix A.1).

2.1.1 Component Aerosols Defined

Table 2.1.1.1 is a compilation of aerosol component model parameters which characterize the gross size distribution mode features of dry urban and continental aerosols. All the models employ the log normal size distribution as a convenient and standardized means of specifying distinct modal contributions (c.f. Appendix A.1). Nearly all the models include three distinct modes (i) a water soluble mode whose optical properties are, at least within the scope of this study, indistinguishable from sulfate properties, (ii) a soot mode characteristic of carbon based particles which are predominantly responsible for aerosol absorption effects (Rosen et al., 1978)) and (iii) a large particle mode "dust like" component which depending on its origin may or may not be hygroscopic (see Section 2.1.2 below).

The entries labelled SRA represent standard models defined for the World Meteorological Organization by working groups concerned with aerosol modelling for climatic impact studies (WCP-55). The tabulations labelled SRA++ were an attempt by the working group to improve the somewhat unrealistic characterization of the water soluble and dust like components defined in the initial (SRA+ in Table 2.1.1.1) tabulations. The Leaitch model parameters (Leaitch and Issac, 1988) represent the results of a series of aircraft particle size measurements made at two different altitudes during different seasons over sites in Ontario, Québec, New York state, Nova Scotia and the Northwest territories. Finally the Shettle and Fenn parameters were extracted from a report which dealt extensively with the optical effects of relative humidity (Shettle and Fenn, 1979).

For the simulations presented in this report we settled on a hybrid model which combined the water soluble and soot results of Leaitch and Issac (1988) with the dust like SRA definitions. The Leaitch and Issac models were employed principally because they represented size distribution data acquired over an area relevant to Canadian LRTAP interests (southeastern Canada). The universality of Leaitch's data and the differences between his model parameters and those of the SRA model are points worth considering. However for our purposes we merely note that a remarkable consistency was obtained in the fine particle mode of Leaitch's data over a diversity of sites. Similar results in terms of the value of τ_N were obtained by Kim et al. (1988) over a part of central USA but for less monodispersive aerosols (σ in the order of 1.8).

The fine particle accumulation mode, which in our three component model described above includes the water soluble mode and the soot mode, is (at least in the visible spectral region) the primary aerosol component responsible for the large angle scattering and attenuation effects which influence the satellite signal. Sloane (1983, 1984, 1986) has noted that the fine particle mode consists primarily of sulfates and nitrates in the form of ammonium salts ($(\text{NH}_4)_2\text{SO}_4$ and NH_4NO_3), carbonaceous soot, organic carbon and residue which includes soil derived particles.

Within the context of optical scattering properties, one can justifiably argue that the fine particle mode is composed primarily of sulfates. Although this concept is not essential to the development of a remote sensing inversion methodology it certainly simplifies matters when and if it applies.

The ammonium salts are hygroscopic and can be regarded as the principal components of the water soluble mode. Of the remaining non hygroscopic components, only carbonaceous soot is distinctly different in optical properties from the ammonium salts. However, above the deliquescence point of the salts (see Appendix A.2) hygroscopic particle growth effects increase their optical mass scattering efficiency relative to the non hygroscopic particles. Within the water soluble mode itself numerous authors have argued that the sulfate salts are more efficient scatterers per unit mass than the nitrate salts (Tang et al., 1981; Sloane, 1982).

The implication of these assertions is that the optical scattering effects of sulfates are dominant whenever the mass of sulfates is comparable to the other fine particle mode components. In regards to mass distributions, Fraser and Kaufman (1984) have observed that, for the eastern United States, the ratio of sulfate mass (SO_4^{2-}) to the other fine particle mode constituents falls within the range 0.4 - 1.5. Furthermore, numerous optical scattering studies over a variety of meteorological conditions have demonstrated a predominant correlation between generic aerosol scattering and sulfate mass (Husar and Patterson, 1980; Pierson et al., 1980; Macias et al., 1980; Leaderer and Stolwijk, 1980; Fraser and Kaufman, 1984; Vossler and Macias, 1986).

Accordingly within the scope of the work presented below the fine particle mode and thus the water soluble mode are identified with sulfates. This argument, it should be noted, applies to information extracted from scattering measurements in the visible spectral region and to externally mixed aerosol (see Section 2.1.3 below).

2.1.2 Particle Size Dependence on Ambient Relative Humidity

An important influence on the optical activity of aerosol particles is the ambient water vapour concentration or relative humidity which acts to cause deliquescence of hygroscopic aerosols. This deliquescence produces changes in intrinsic optical properties associated with a change in physical dimensions of the hygroscopic nuclei. The changes in intrinsic optical properties include a water volume induced decrease in refractive index along with an increase in scattering power due to relative humidity induced particle growth.

In Appendix A.2 we describe a simple model, based on the standard log normal size distribution, which accounts for the optical effects of ambient relative humidity. Figure (2.1.2.1) shows some results for the particle growth model in the form of size distribution plots for the Leaitch water soluble model at different relative humidities. Since the total number of particles remains constant the area of the curve $dN / d\log r$ is fixed while the volume curve $dV / d\log r$ grows in magnitude with increasing relative humidity.

The effects of relative humidity on the other aerosol components were neglected. This is a reasonable approach given that the soot particles as well as the soil derived component of supermicron particles are non hygroscopic (Sloane, 1983). Hygroscopic supermicron particles such as NaCl marine salts (Hindman et al., 1985) were assumed to contribute negligibly to the optical effects in a continental or urban atmosphere.

Table 2.1.1.1.

Log normal parameters @

SRA model +		Standard deviation	
Model	$r_N (\mu m)$	$r_V (\mu m)$	σ
Water soluble	.005	.183	2.99
Dust like	.50	18.3	2.99
Soot	.0118	.05	2.00

SRA model ++		Standard deviation	
Model	$r_N (\mu m)$	$r_V (\mu m)$	σ
Water soluble	.0285	.2	2.239
Dust like	.471	6.00	2.512
Soot	.0118	.05	2.00

Leaith et al. (1988) *			
Water soluble	.12	.138	1.24
Soot \$.12	.138	1.24
Water soluble / soot (internally mixed)	.12	.138	1.24

Shettle and Fenn (1979) **			
Rural water soluble	.027	.19	2.24
Rural dust like	.43	5.5	2.51
Urban water soluble	.025	.16	2.24
Urban dust like	.40	5.1	2.51

+ standard model WCP-55, (Table 2.2 in their Appendix A)

++ WCP-55; (p. 31 of their Table 4.5 which replaces their Table 2.2 of Section 2)

* Average of his 5 sites ($.85 \leq r \leq 1.2 \mu m$), 0% r.h.

** 0% r.h.

\$ Personal communication (Leaith, 1988); soot like water soluble centered around $.3 \mu m$ diameter

@ See Appendix A.1 for discussion of log normal parameters

Note: 1. $\ln r_V = \ln r_N + 3 \ln^2 \sigma$ for log normal distribution 2. $\log \sigma = \text{stand. dev. of } \log(r/r_N) \text{ (or } \log(r/r_V) \text{)}$

2.1.3 Definition of Models Employed

In order to understand the optical effects of sulfate concentration variations over a realistic and representational range of atmospheric aerosol models one must make a judicious choice of standard models. These "aggregate aerosol models" should, according to our viewpoint, permit investigations into (a) the effects of relative humidity on the combined contributions of hygroscopic and non hygroscopic aerosols (b) the optical effects of *internal* and *external mixing* and (c) the effects of varying degrees of correlation between the sulfate component and the other aerosol components.

Two fundamental aggregate aerosol models were defined to represent (A) typical urban and (B) continental conditions (Table 2.1.3.1). The volume fraction parameters for the dry version of these models (0% relative humidity) were extracted directly from the modified SRA standard models described in the appendix of the WCP-55 report (see Table 2.1.3.1 and the WCP reference below). The log normal parameters employed for each of the three components of the aggregate models (Table 2.1.1.1) were actually a combination of the SRA parameters (for the dust like component) and data based on the findings of Leaitch et al. (1988) for the water soluble and soot components.

For each fundamental aggregate aerosol model the effects of relative humidity variations were considered in terms of 6 nominal values (0, 50, 70, 80, 90, and 95 %). Computations performed for the 0% case were intended to play the role of standard calculations, independent of the relative humidity particle growth model, which could be more directly linked with other work based on the dry particle parameters. The other relative humidity values represent a realistic range of values in the continental and urban regions of eastern North America.

Questions relating to the manner in which the component aerosols physically coexist is the basis for considering the externally and internally mixed models listed in Table 2.1.3.1 (labelled I and II respectively). For both the continental and urban aggregate models we investigated their optical variations in terms of component aerosols which could be treated as (I) independent constituents (externally mixed) or (II) as components which could coexist as the same particle (internally mixed). In the latter case (which is treated in Appendix C) the aggregate aerosol was imagined to consist of a soot core surrounded by a water soluble mantle (and further surrounded by a water mantle in the case of non zero relative humidity) and a distinct dust like component. However with the exception of Appendix C we employed the externally mixed interpretation for all optical and radiative transfer calculations performed in this work.

The parameters of Table 2.1.3.1 are fractional coefficients which fix the values of unitless optical parameters (refractive index, phase function, single scattering albedo etc.). Cumulative effects which depend on particle number density (number of particles per cm³ as described in Appendix A.1) ultimately affect the radiative transfer calculations and hence the magnitude of the signal computed at satellite altitudes. If one maintains the number density or volume fractions defined in Table 2.1.3.1 then variations in the number of each type of particle are significantly constrained in that component number density concentrations are perfectly correlated. Perturbations from this rather rigid model were considered by permitting the water soluble component to vary independently of the other components. These departures from the standard urban and continental models defined of Table 2.1.3.1 (termed *urban variant* and *continental variant*) thus allowed a much more comprehensive analysis of optical effects due to variations in the water soluble component. The details of the urban and continental variant models are given below in Section 2.1.4.

NUMBER DISTRIBUTION AT DIFFERENT RELATIVE HUMIDITY

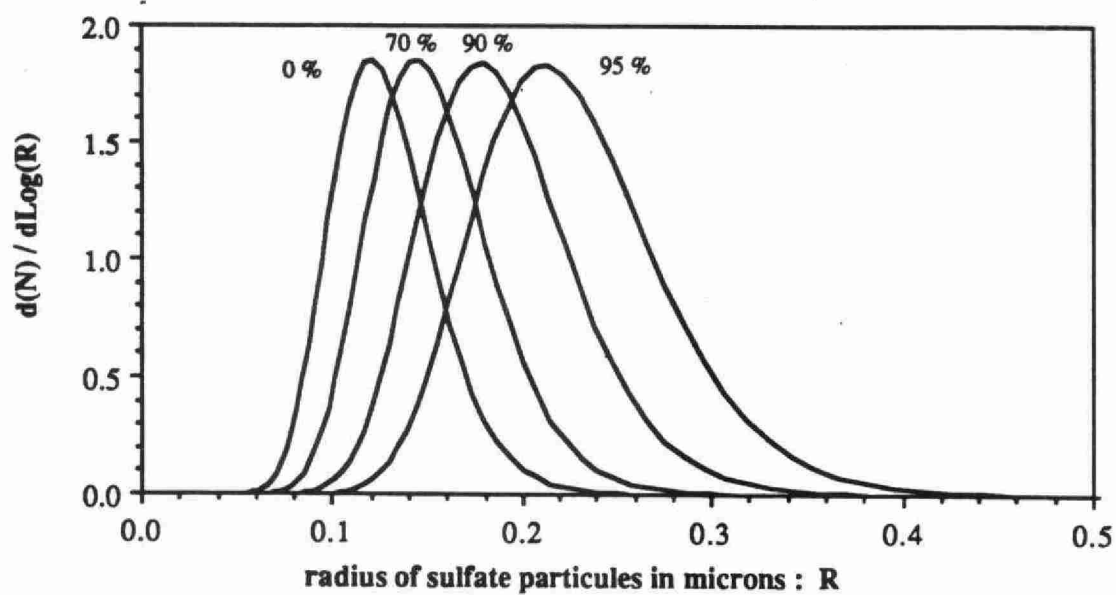


Fig. 2.1.2.1 a)

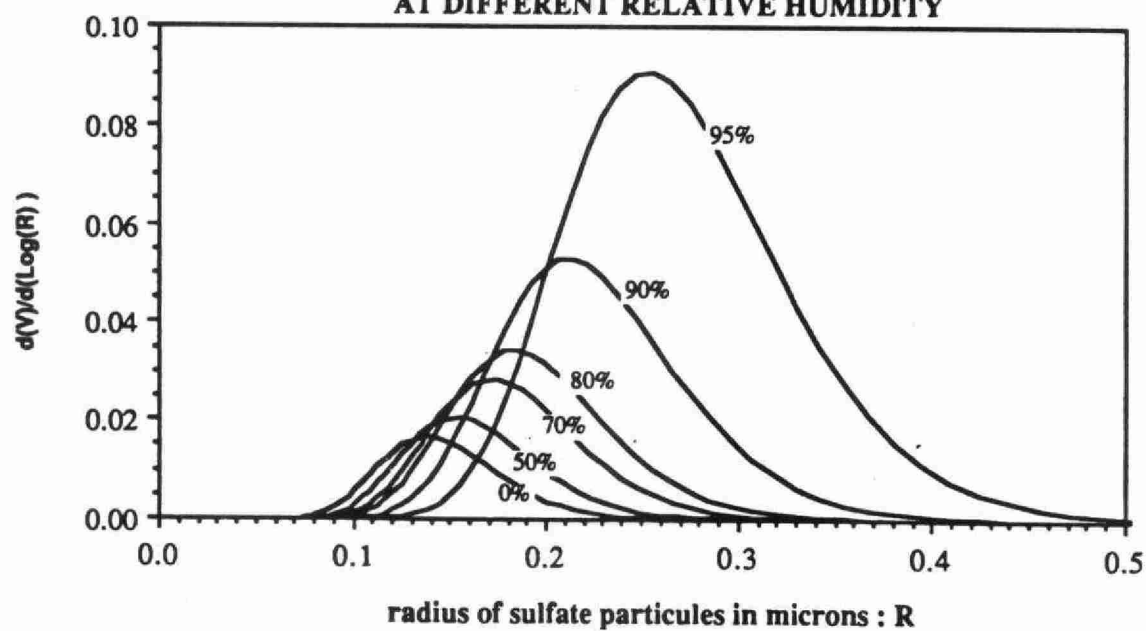
VOLUME DISTRIBUTION OF SULFATE PARTICLES
AT DIFFERENT RELATIVE HUMIDITY

Fig. 2.1.2.1 b)

Table 2.1.3.1. Aggregate Aerosol Models**I: Externally Mixed Case**

A)		Continental Model					
Component / r.h.	γ_i	c_i					
		0%	50%	70%	80%	90%	95%
Water soluble model	.96566E00	.29	.3072	.3533	.4495	.5715	.6466
Dust like (dry)	.10433E-2	.70	.6830	.6376	.5427	.4225	.3484
Soot	.33299E-1	.01	.0098	.0091	.0078	.0060	.0050

B)		Urban/industrial Model					
Component / r.h.	γ_i	c_i					
		0%	50%	70%	80%	90%	95%
Water soluble model	.73487E00	.61	.6861	.7760	.8155	.8821	.9320
Dust like	.91668E-4	.17	.1368	.0976	.0804	.0514	.0296
Soot	.26504E00	.22	.1771	.1264	.1041	.0665	.0384

II: Internally Mixed Case

A)		Continental Model					
Component / r.h.		c_i					
		0%	50%	70%	80%	90%	95%
Water soluble / soot	.29/.01*	.3072/.0098	.3533/.0091	.4495/.0078	.5715/.0060	.6466/.0050	
Dust like (dry)	.70	.6830	.6376	.5427	.4225	.3484	

B)		Urban/industrial Model					
Component / r.h.		c_i					
		0%	50%	70%	80%	90%	95%
Water soluble / soot	.61/.22	.6861/.1771	.7760/.1264	.8155/.1041	.8821/.0665	.9320/.0384	
Dust like (dry)	.17	.1368	.0976	.0807	.0514	.0296	

- Note:
1. Water soluble component is that of Leitch and Issac (Table 2.1.1.1)
 2. * "Insoluble fraction" for e.g. = .01/.3 (volume fractions same as for externally mixed model)
 3. The volume fraction coefficients (c_i) are computed from a knowledge of the number density fractions (γ_i) (c.f. Appendix A.1) and the log normal parameters derived from the particle growth models defined in Appendix A.2.
 4. Dust like refers to SRA++ model parameters (Table 2.1.1.1)

TABLE 2.1.4.1 GROUND BASED MEASUREMENTS OF SULPHATE CONCENTRATIONS AND AEROSOL SCATTERING COEFFICIENTS

Dry Sulfate mass concentration (SO ₄ =) [μg/m ³]			Aerosol volume Scattering coefficient [10 ⁻⁴ m ⁻¹]			Aerosol scattering coefficient per unit dry mass SO ₄ = [m ² /g]			Relative humidity [%]		Measurement time period	Area	Reference	Optical fraction due to sulphates \$ [%]	Comments	
MIN	MEAN	MAX	MIN	MEAN	MAX	MIN	MEAN	MAX	λ	MIN	MEAN	MAX				
2		20											yearly	East,N.E. USA	1	
5		50	1		10								2 months	St-Louis	1	
	14		.1	2	6.5		13.9±1.2*				70##		2 weeks	Alleghany Mtns	2	pollution episode sulphates in form (NH ₄) _x HySO ₄ (x + y = 2)
	24.7			3.7			15.0#		525	46			summer	St-Louis	4	73** type A (author's definition)
	18.9			3.0			15.9#		525	53			summer	St-Louis	4	63** type B
	4.7			0.8			17.0#		525	41			summer	St-Louis	4	31** type C
							13.0*		525	41	53		summer	St-Louis	4	summer mean
.25		20												central Ontario	5	
						4.4*		8.5*						urban centres	6	40-70 ***
	2.0			.25**			12.5#		525				daily	S.W. USA	7	56** ≤ 1 000 km flights
	8.9			.95**			10.7#		525				daily	S.W. USA	7	43** ≤ 1 000 km flights (smelter upwind)
	2.9			.27**			9.3#		525				daily	S.W. USA	7	11** ≤ 1 000 km flights (smelter upwind)
	3.0@		.1	1.63	6		>53#		500	56			daily	Denver	8	12** 65 8hr. measurements
				2.5					500	70	100		daily	Denver	8	ref. 8 characterized
				2.3					500	60	100		daily	Denver	8	by high carbon
				.8					500	0	60		daily	Denver	8	(high absorption)
				.6					500	0	40		daily	Denver	8	
5		50											summer	East USA	9	
5		35											daily	N.Y. City	9	pollution episode
						2.0*		30.0*						rural/urban	3	
						4.0*		21.0*							10	

REFERENCES

- Husar & Patterson (1980)
- Pierson et al (1980)
- Cited in ref. 2 (table 8, 10 references)
- Vossler & Macias (1986)
- Tsonis & Leaitch (1986)
- cited in ref. 4 (table II, 6 references)
- Macias et al. (1980)
- Sloane (1984)
- Lyons (1980)
- Leaderer & Stolwijk (1980; Table 3, derived from visibility data)

LEGEND

- # simple ratio of mean aerosol scattering coefficient to mean SO₄= (dry) density
- * regression slope
- ** calculated from Mie computations given measured size distributions and component refractive indices
- \$ sulphate volume scattering coefficient / total aerosol volume scattering coefficient
- @ overestimate: SO₄ extracted from (NH₄)₂ SO₄ assuming 0 r.h.
- *** normalized to total scattering coefficient
- ## authors estimate based on temperature of air stream exiting heated nephelometer

Note: Typically the aerosol scattering coefficient per unit mass SO₄= measurements are made with a heated nephelometer (relative humidity effects largely removed). Therefore the table values (except for those of ref. 4) represent a dry scattering measurement normalized to a dry sulfate mass. Ref. 4 values represent ambient r.h. aerosol volume scattering coefficients compared with dry SO₄= concentrations.

2.1.4 Surface Number Density Considerations

(a) Extreme sulfate Variations

Table 2.1.4.1 is a compilation of sulfate concentration and optical scattering coefficient measurements made at or near ground level over a variety of temporal and spatial parameters. The table lists (when available) extreme conditions along with averages over sampling periods which vary from days to months and over urban and rural geographical regions. Some of the listings include, as well, readings of relative humidity made in conjunction with the ground based measurements.

The extrema for the data compiled vary from 1 to 50 μgm^{-3} of (dry) SO_4 or from (1 to 50) $\times [132/96.1]$ dry $(\text{NH}_4)_2\text{SO}_4$. This ammonium salt form of sulfate is, according to many researchers (Sloane, 1983, 1984, 1986 for example), the dominant sulfate compound. Employing the notation of Appendix A.1 we have for dry $(\text{NH}_4)_2\text{SO}_4$:

$$\mu N \leq 69 \times 10^{-12} \quad (2-1)$$

where μ is the average mass of an ammonium sulfate particle and N is the number density (cm^{-3}). Accordingly:

$$N \leq 69 \times 10^{-12} / [D (4/3) \pi r_3^3] \quad \text{particles per cm}^3 \quad (2-2)$$

where D is the density of ammonium sulfate particles (approximately 1.8 gm/cm^3 ; Vossier and Macias, 1986), and $(4/3) \pi r_3^3$ is the average volume of a log-normal distribution particle (c.f. Appendix A.1)

For the log normal (Leitch, water soluble) parameters defined in Table 2.1.1.1 we obtain $r_3 = .129 \mu\text{m}$ and hence:

$$N_{\text{max}} = 4300 \text{ cm}^{-3} \quad (2-3)$$

Equating the sulfate component to the water soluble component we proportion the particle size distribution according to the γ_i values of Table 2.1.3.1 and hence obtain the following maximum number densities at ground level (externally mixed model):

Table 2.1.4.2 Maximum Surface Number Densities of Aggregate Aerosol Models

	Continental	Urban / industrial
	# density [cm^{-3}]	# density [cm^{-3}]
Water soluble	4300	4300
Dust like	4.6457	0.53638
Soot	148.28	1550.85
Total	4452.93	5851.38

Table 2.1.4.3
Number density values (N) used in the radiative transfer calculations

				Corresponding volume scattering coefficients* [10 ⁻⁴ m ⁻¹]					
surface # density (N)				delta N * sigma at indicated relative humidities (%)					
[cm ⁻³]	[cm ⁻³]	N(initial)*	sigma	0	50	70	80	90	95
delta N	N(initial)								
(A)									
CONTINENTAL VARIANT									
water sol.	430	0	0	0,215732	0,257445	0,346665	0,418242	0,658605	1,184306
dust like	0	2,3229	0,145383	0	0	0	0	0	0
soot	0	74,14	0,038732	0	0	0	0	0	0
total	430	76,46	0,184116	0,215732	0,257445	0,346665	0,418242	0,658605	1,184306
scat effec [m ⁻² /g]				4,257477	5,080683	6,841437	8,254007	12,99757	23,37228
URBAN VARIANT									
water sol.	430	0	0	0,215732	0,257445	0,346665	0,418242	0,658605	1,184306
dust like	0	0,26819	0,016785	0	0	0	0	0	0
soot	0	775,42	0,405097	0	0	0	0	0	0
total	430	775,688	0,421882	0,215732	0,257445	0,346665	0,418242	0,658605	1,184306
scat effec [m ⁻² /g]				4,257477	5,080683	6,841437	8,254007	12,99757	23,37228
(B)									
CONTINENTAL STANDARD									
water sol.	430	0	0	0,215732	0,257445	0,346665	0,418242	0,658605	1,184306
dust like	0,46457	0	0	0,029076	0,029076	0,029076	0,029076	0,029076	0,029076
soot	14,828	0	0	0,007746	0,007746	0,007746	0,007746	0,007746	0,007746
total	445,2926	0	0	0,252554	0,294267	0,383487	0,455064	0,695427	1,221129
scat effec [m ⁻² /g]				4,984170	5,807377	7,568130	8,980701	13,72427	24,09897
URBAN STANDARD									
water sol.	430	0	0	0,215732	0,257445	0,346665	0,418242	0,658605	1,184306
dust like	0,053638	0	0	0,003357	0,003357	0,003357	0,003357	0,003357	0,003357
soot	155,085	0	0	0,081019	0,081019	0,081019	0,081019	0,081019	0,081019
total	585,1386	0	0	0,300109	0,341822	0,431042	0,502619	0,742982	1,268683
scat effec [m ⁻² /g]				5,922657	6,745863	8,506617	9,919188	14,66275	25,03746

Notes:

scat effec = change in the total volume scat coef per unit change in the mass of dry sulfate
cross sections obtained by multiplying Mie efficiencies (Q) by πr^2 where r is the effective
mean surface radius of a log normal distribution

* Sample cross sections (sigma) [units of 10⁻¹⁰ cm²]
(wavelength of 0.555 micrometers)

Model	Dust like	Soot	Water soluble (sulfate)					
			0%	50%	70%	80%	90%	95%
sigma (scat)	625,871	5,22423	5,01703	5,9871	8,06198	9,72656	15,3164	27,542
sigma (abs)	233,511	6,7545	0,18244	0,15912	0,12833	0,113436	0,085325	0,060371

b) Surface Number Density Variations

In an effort to characterize the extremes of surface number density variation for sulfate like particles as well as the other constituents of the aggregate aerosol models we defined two different cases of surface number density variation for the continental and urban aggregate aerosol models discussed in Section 2.1.3 (Table 2.1.3.1). The detailed surface number density descriptions of these 4 different cases (*Standard continental*, *urban continental*, *continental variant* and *urban variant*) along with sample optical parameter computations are given in Table 2.1.4.3.

In the first (variant) case we considered departures from the standard aggregate aerosol models by permitting the water soluble (sulfate like) constituent to vary independently. Accordingly the sulfate like number density was varied between 0 and 4300 cm^{-3} (10 equal increments) while maintaining the other constituents at half of the extreme values tabulated above. As a consequence the standard number density fractions defined in Table 2.1.3.1 were reobtained at a sulfate number density of $4300/2 = 2150 \text{ cm}^{-3}$. This approach thus affords a distinctly different viewpoint wherein the optical effects of aerosols are dominated by sulfate variations which are totally uncorrelated with the other constituents.

In the second (standard) case the number densities of the continental and urban industrial aggregate aerosol models were varied uniformly while maintaining the number density proportions γ_i defined in Table 2.1.3.1. This approach thus assumes correlated changes between the number densities of all constituents at all relative humidities. In application the number densities were allowed to vary from 0 to the maximum values defined above in increments of one tenth of the maximum value.

2.2 Optical Parameter Variations

2.2.1 Optical Parameter Computations

Having defined the aggregate aerosol models one is in a position to compute the point optical (Mie) parameters at a given radius and wavelength and subsequently to integrate these parameters over the size distributions defined in Section 2.1 (Royer et al. 1985). Table 2.2.1.1 lists the required input parameters to the optical scattering computations along with the derived output parameters. The upper half of the table deals with point optical parameters which in principle represent a 3 dimensional volume function in the atmosphere but which in practice are permitted to vary only in the vertical direction or as assumed in this work, are independent of position. The second half of the table lists columnar parameters which represent vertically integrated analogs to the point optical parameters.

For a given radius and wavelength the Mie algorithms are employed to compute the scattering and attenuation cross sections and the phase function (c.f. Appendix A.1) for each aerosol component characterized by refractive index m_i . The integration of the phase function over solid angle weighted by the cosine of the scattering angle yields the *asymmetry factor* (g). This coefficient which is indicative of the anisotropy of the phase function is a required input to the 5S radiative model (c.f. Section 3.1 below). Given the size distribution functions discussed in Section 2.1 the particle size distribution averaged optical parameters are computed by performing a numerical quadrature across the optically active radius region for each aerosol component. The aggregate aerosol models are then optically combined in terms of a fractional number density weighted average to obtain total average point optical parameters.

Knowledge of the number density distribution and the radius dependent particle sized distributions as a function of altitude enables one to calculate the cumulative properties of each optical parameter for a complete atmospheric column. A significant simplification is obtained if it is assumed that the particle size distributions are independent of altitude and that the altitude profile ($h_i(z)$ in Table 2.2.1.1) is the same for all aggregate aerosol model components. The first assumption permits a direct link between cumulative parameters such as optical depth and point optical parameters (or equivalently between columnar number densities and ground concentrations) while the latter assumption guarantees a constant optical mixing ratio or hence a scattering phase function which is independent of altitude. Neither assumption is particularly valid in an atmosphere grossly divided into highly forward scattering tropospheric aerosols and nearly isotropic molecular scattering above the troposphere. Fortunately however the

cumulative implications of these simplifications at the atmospheric boundary layers are not strong. In Section 3.3 we discuss in more detail the level of errors encountered when altitude dependent atmospheric parameters are replaced by representative means.

Table 2.2.1.1 Computed Optical Parameters (Particle Size Distribution (PSD) independent of altitude)

Type	Parameter	Symbol	Derived optical parameters	Symbol
Point	refractive index	$m_i = m_{i1} - m_{i2} j$	attenuation cross section	$\sigma(m_i, \alpha)$
	wavelength	λ	scattering cross section	$\sigma^{sca}(m_i, \alpha)$
			conservative phase function	$poi(m_i, \alpha, \cos \chi)$
		\wedge		
	unit particle size distribution	$n_i(r)$	PSD averaged unit attenuation cross section	$\sigma_i(\lambda)$
			PSD averaged unit scattering cross section	$\sigma_i^{sca}(\lambda)$
			PSD averaged conservative phase function	$poi(\cos \chi)$
	number density fraction	γ_i	aggregate aerosol model parameters	$\sigma(\lambda)$
	fraction by volume	c_i		$\sigma^{sca}(\lambda)$
				$po(\cos \chi)$
				g^*
Columnar	altitude profile	$h_i(z) = N_i(z) / N_i(0)$	altitude optical profile	$\kappa_i(z, \lambda) / \kappa_i(0, \lambda)$
				$\kappa_i^{sca}(z, \lambda) / \kappa_i^{sca}(0, \lambda)$
	equivalent column length	H_i	optical depths	$\tau_i = N_i(0) H_i \sigma_i(\lambda)$
	surface # density	$N_i(0)$		$\tau_i^{sca} = N_i(0) H_i \sigma_i^{sca}(\lambda)$

$$\tau = N(0) \sum_i \gamma_i(0) \sigma_i(\lambda)$$

$$\tau^{sca} = N(0) \sum_i \gamma_i(0) \sigma_i^{sca}(\lambda) H_i$$

* asymmetry factor

Table 2.2.1.2 is a compilation of standard refractive indices which we employed throughout this work to characterize the intrinsic dry optical properties of the water soluble, soot, and dust like components. The effect of particle growth as a function of relative humidity on the refractive index (water soluble case) was accommodated by computing the volume weighted mean of dry particle and pure water indices as detailed in Appendix A.2.

Table 2.2.1.2 Refractive indices of water and dry component aerosols which were employed in all optical calculations

wavelength (microns)	water	Water-Soluble	Dust-Like	Soot
0.400	1.339 -i1.86E-9	1.530 -i0.005	1.530 -i0.008	1.750 -i0.460
0.488	1.335 -i9.69E-10	1.530 -i0.005	1.530 -i0.008	1.750 -i0.450
0.515	1.334 -i1.18E-9	1.530 -i0.005	1.530 -i0.008	1.750 -i0.450
0.550	1.333 -i1.96E-9	1.530 -i0.006	1.530 -i0.008	1.750 -i0.440
0.633	1.332 -i1.46E-8	1.530 -i0.006	1.530 -i0.008	1.750 -i0.430
0.695	1.331 -i3.05E-9	1.530 -i0.007	1.530 -i0.008	1.750 -i0.430
0.860	1.329 -i3.29E-7	1.520 -i0.012	1.520 -i0.008	1.750 -i0.430
1.536	1.318 -i9.97E-5	1.510 -i0.023	1.400 -i0.008	1.770 -i0.460
2.250	1.292 -i3.90E-4	1.420 -i0.010	1.220 -i0.009	1.810 -i0.500
3.750	1.369 -i3.50E-3	1.452 -i0.004	1.270 -i0.011	1.900 -i0.570

Source: Colwell (1983)

2.2.2 Influence of Relative Humidity

Figure 2.2.2.1 illustrates some typical variations of the real (scattering) and imaginary (absorption) parts of the refractive index as a function of the relative humidity for the Leaitch water soluble distribution. These examples calculated for the wavelengths ranging from 0.4 μm to 3.75 μm show the typical decrease in the real part of the refractive index from the dry particle value (Table 2.2.1.2) to the pure water value of less than 1.4. The somewhat intricate variation of the complex part of the refractive index results from the non monotonic spectral behavior of the dry particle at 0% relative humidity and the subsequent transition with increasing relative humidity to the strongly monotonic (but comparatively small magnitude) water index. Table 2.2.2.1 shows explicitly some calculations of refractive index carried out for a wavelength of 0.55 μm .

Table 2.2.2.1 Sample refractive index calculations as a function of relative humidity (wavelength of 0.55 μm)

(Leaitch model, water soluble, Dry density = 1.8 g/cm³ (NH₄)₂SO₄) used in growth model)

Relative humidity	Refractive index	
	real part	complex part
0%	1.530	-i .006
50%	1.515	-i .0055
70%	1.481	-i .0045
80%	1.433	-i .0030
90%	1.395	-i .0019
95%	1.378	-i .0014

Figure 2.2.2.2 shows the effect as a function of particle size parameter ($\alpha = 2\pi r / \lambda$) of a change in relative humidity on the components of the scattering coefficient for the Leaitch water soluble model (wavelength of 0.55 μm). The three graphs illustrate well that the increase in volume scattering coefficient with relative humidity is more due to the physical increase in the size of the particles than to a change of intrinsic optical properties. This follows from the expression for the differential contribution of a given particle size to the total scattering coefficient (c.f. Appendix A.1) viz:

$$d\kappa^{\text{scat}} / d\alpha = Q(\alpha) dS / d\alpha \quad (2-4)$$

where $Q(\alpha)$, the scattering efficiency is plotted in Figure 2.2.2.2(a). $dS / d\alpha$ the differential surface contribution due to particles of size parameter α is plotted in Figure 2.2.2(b) and the product is plotted in Figure 2.2.2.2(c). Although some of the increase in moving from 0% to 95% relative humidity is due to a movement up the principal (first) peak of the scattering efficiency curve it is clear that the large disparity in Figure 2.2.2.2(c) is more attributable to the surface magnitude disparity evident in Figure 2.2.2.2(b).

In terms of the maximum number densities defined in Table 2.1.4.2 the volume scattering coefficient for dry sulfate particles at 50% relative humidity is given by:

$$\begin{aligned} \kappa^{\text{scat}} &= Q \pi r_2^2 N(0) \\ &= 2.6 \times 10^{-4} \text{ m}^{-1} \end{aligned} \quad (2-5)$$

where $r_2 = .126 \mu\text{m}$ is the mean log normal surface radius (Appendix A.1) calculated using the Leaitch parameters of Table 2.1.1.1 and the scattering efficiency $Q (\approx 1)$ was calculated by integrating the differential in equation (2-4) (Figure 2.2.2.2c) over size parameter. For a typical aerosol scale height of 1 km this value of $\kappa^{\text{scat}}(0)$ then yields a maximum dry sulfate scattering optical depth of .22.

If on the other hand we consider the wet sulfate at 95% relative humidity the integrated volume scattering coefficient is enhanced considerably. Assuming the same maximum number density we obtain:

$$\kappa^{\text{scat}} = 11.8 \times 10^{-4}$$

where r_2 has now increased to .207 μm and the scattering efficiency is approximately 1.8. For a scale height of 1 km the wet sulfate volume scattering coefficient corresponds to a maximum wet sulfate optical depth of .98. This value is consistent with the optical depth magnitude reported in Tsonis & Leaitch (1986). The volume scattering coefficient maximums can be compared with the entries of Table 2.1.4.1 (after multiplying the latter by 10).

In Figure 2.2.2.3 we have plotted the variation of the scattering phase function ($p_0(\cos\chi)$) defined in Appendix A.1) computed for the Leaitch water soluble model as a function of scattering angle and relative humidity and at two different wavelengths. The fairly large increase of the forward (0°) scattering peak with increasing relative humidity and the corresponding decrease of backscatter at angles larger than about 40 degrees is generally symptomatic of both an increase in average particle size and a decrease in refractive index associated with the increasing water content of the scattering particles. It should be noted that the implications of the phase function induced decrease in backscatter on the signal scattered toward the satellite sensor are generally outweighed by the corresponding increase in the volume scattering coefficient. An increase in wavelength (0.55 μm to 1.536 μm in Figure 2.2.2.3) effectively defines particles which are optically smaller and more isotropic in their scattering properties.

Figure 2.2.2.4 is a plot of single scattering albedo computed for the Leaitch water soluble model as a function of relative humidity for wavelengths ranging from 0.4 μm to 3.750 μm . The consistently smaller values of single scattering albedo at the larger wavelengths result because the scattering particles in this wavelength regime are optically small (average size parameter $\alpha = 2\pi r / \lambda < 1$). For optically small particles Rayleigh (or dipole)

absorption and scattering phenomena dominate. Since Rayleigh absorption varies as α while Rayleigh scattering varies as α^4 (Wickramasinghe, 1973; Kattawar and Plass, 1967) it is clear that an increase in wavelength will, depending on the actual value of the refractive index, induce an increasing dominance of absorption effects over scattering or hence a decreasing value of the single scattering albedo. At increasing values of relative humidity the single scattering albedo is larger because the imaginary part of the refractive index is decreasing (Figure 2.2.2.1) and/or because the α^4 variation becomes increasingly more important with increasing particle size.

Figure 2.2.2.5 indicates the variation of the asymmetry factor (g ; defined in Section 2.2.1) for the sulfate type particles as a function of relative humidity and at different relative humidities. This parameter is effectively an indicator of directional anisotropy in the scattering phase function (a value of zero indicates an isotropic phase function while a large positive value is induced by a strong forward scattering peak). It illustrates well the tendency towards a more isotropic phase function as (a) the wavelength increases and (b) the relative humidity decreases. Both effects which result at least in part from an increase in optical particle size can be inferred qualitatively from the behavior of the phase function in Figure 2.2.2.3.

Figure 2.2.2.6 shows the variation of the *spherical albedo* as a function of relative humidity and at incremental values of sulfate concentration (0.55 μm wavelength). This parameter which is strictly not an intrinsic optical parameter indicates the effective (angularly integrated) reflectance of the atmosphere for an observer looking up. It is included because it demonstrates well the near linearity of atmospheric scattering with the mass loading of sulfates and because the classical non linear enhancement of scattering effects with increasing relative humidity is clearly evident.

2.2.3 Correlation of scattering and absorption coefficients with component concentrations

(a) Point volume coefficients

An important parameter in the analysis of the optical behavior of sulfates is the dry sulfate *mass scattering efficiency* given by:

$$\varepsilon(\lambda) = \Delta\kappa^{\text{scat}}(\lambda) / \Delta\text{SO}_4 = [\text{m}^2 / \text{g}] \quad (2-6)$$

where $\kappa^{\text{scat}}(\lambda)$ is the total aerosol volume scattering coefficient [m^{-1}] and SO_4 is the mass density of dry sulfate particles [g/m^3]. In terms of number density (N) the dry sulfate mass density is given by:

$$\text{SO}_4 = \eta D (4/3)\pi r_3^3 N \quad (2-7)$$

where η is the ratio of gram molecular weights of SO_4 and ammonium sulfate ($(\text{NH}_4)_2\text{SO}_4$) and represents the conversion factor to SO_4 given that the sulfate particles are assumed to be in the form of ammonium sulfate. The factor D is the density of a single ammonium sulfate particle (taken as $1.8 \text{ g}/\text{cm}^3$) while the spherical volume term $(4/3)\pi r_3^3 N$ is the total volume occupied by all the sulfate particles, assumed to be described by a log normal particle size distribution with an average volume radius r_3 (c.f. Appendix A.1).

REFRACTIVE INDEX VERSUS RELATIVE HUMIDITY

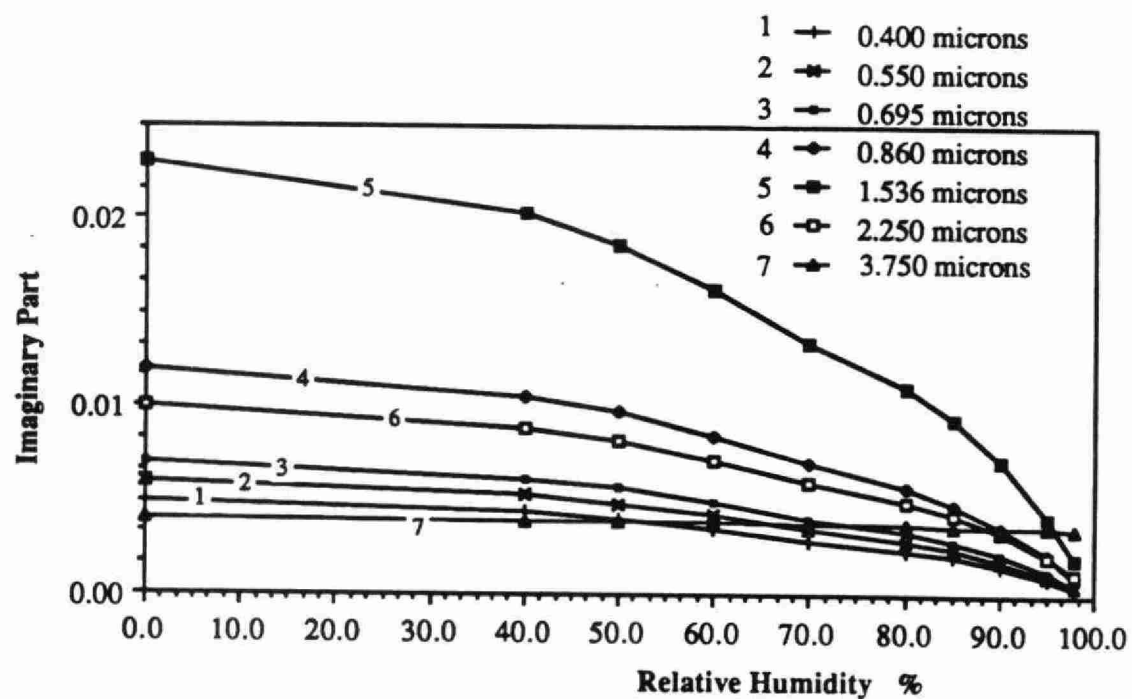
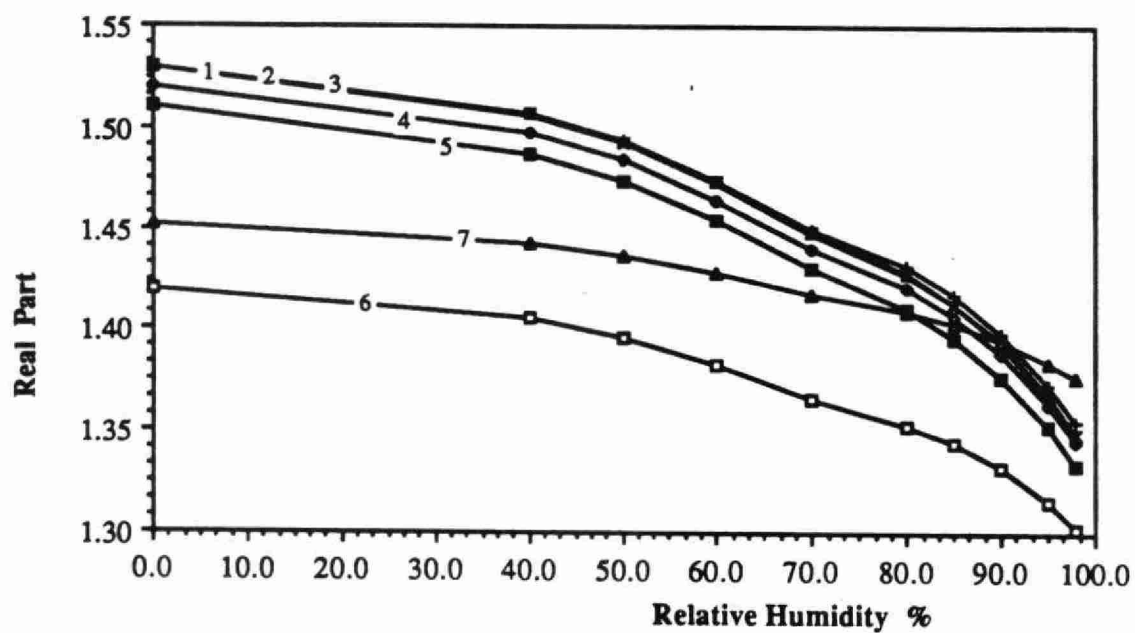


Fig. 2.2.2.1

**SURFACE DISTRIBUTION
AT 0% AND 95% RELATIVE HUMIDITY**

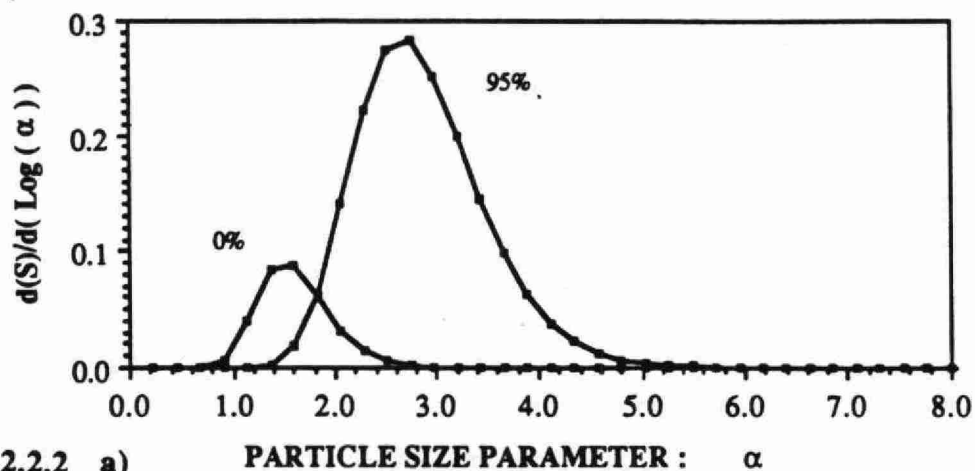


Fig. 2.2.2.2 a)

**SCATTERING EFFICIENCY (Q) VERSUS PARTICLE
SIZE PARAMETER AT 0% AND 95% RELATIVE HUMIDITY**

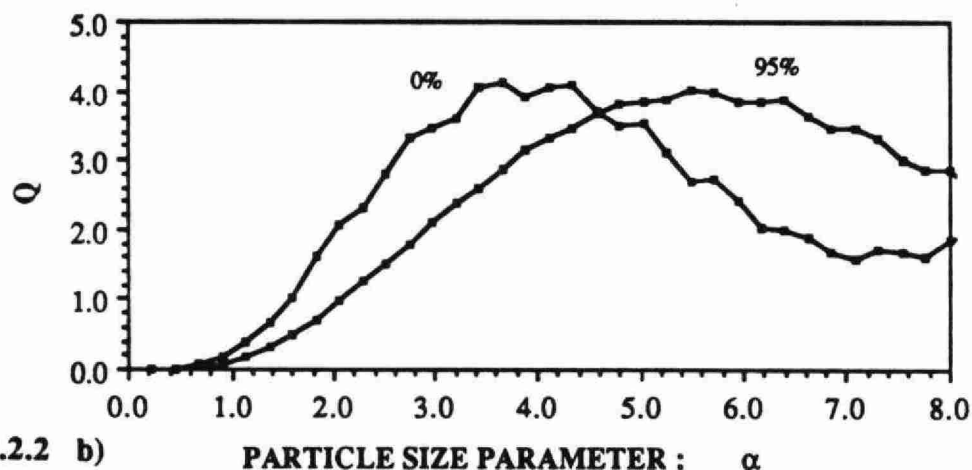


Fig. 2.2.2.2 b)

**CONTRIBUTION OF A GIVEN PARTICLE SIZE
PARAMETER TO THE TOTAL SCATTERING EFFICIENCY
AT 0% AND 95% RELATIVE HUMIDITY**

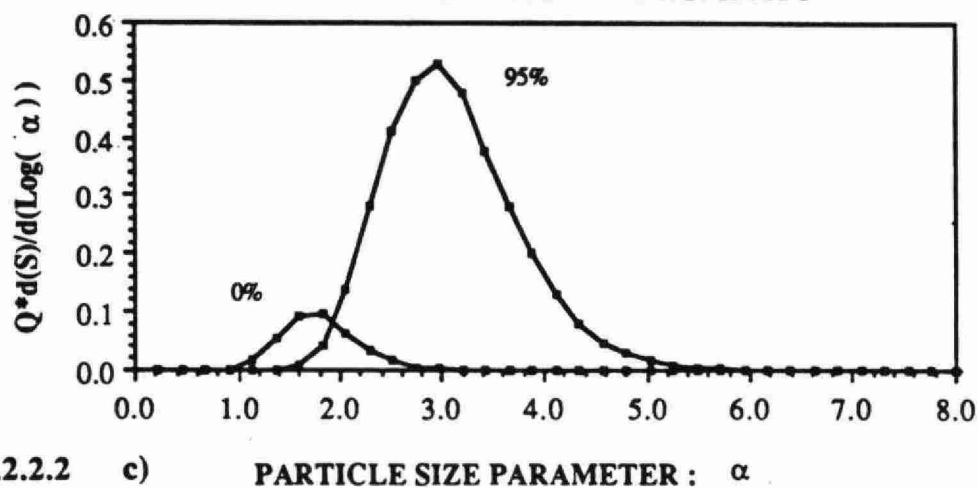
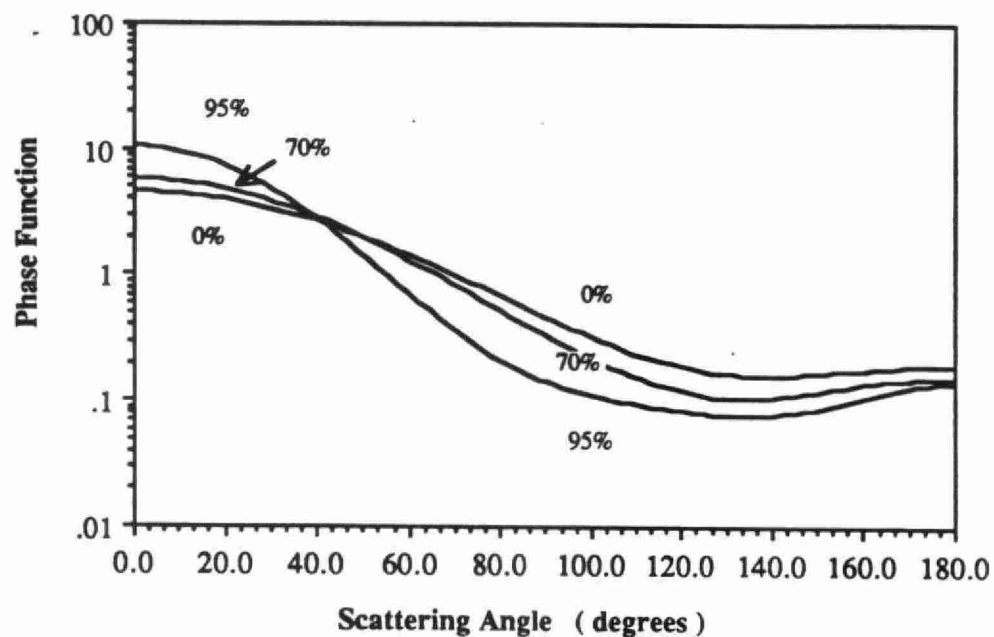


Fig. 2.2.2.2 c)

PHASE FUNCTION OF SULFATE TYPE PARTICLES
FOR DIFFERENT RELATIVE HUMIDITY AT 0.550 MICRONS



PHASE FUNCTION OF SULFATE PARTICLES
FOR DIFFERENT RELATIVE HUMIDITY AT 1.536 MICRONS

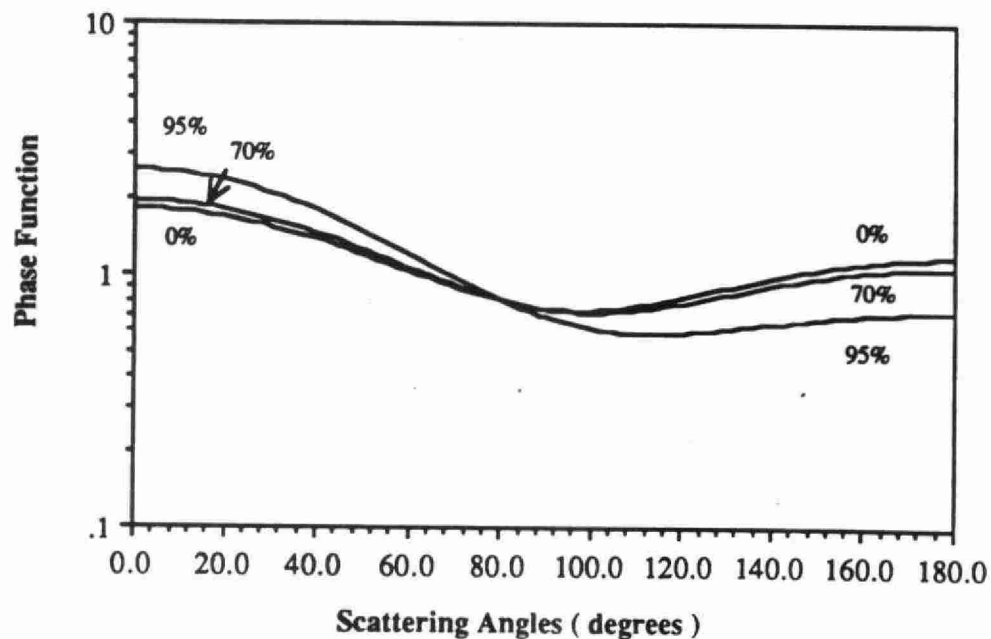


Fig. 2.2.2.3

WATER SOLUBLE SINGLE SCATTERING ALBEDO VERSUS RELATIVE HUMIDITY

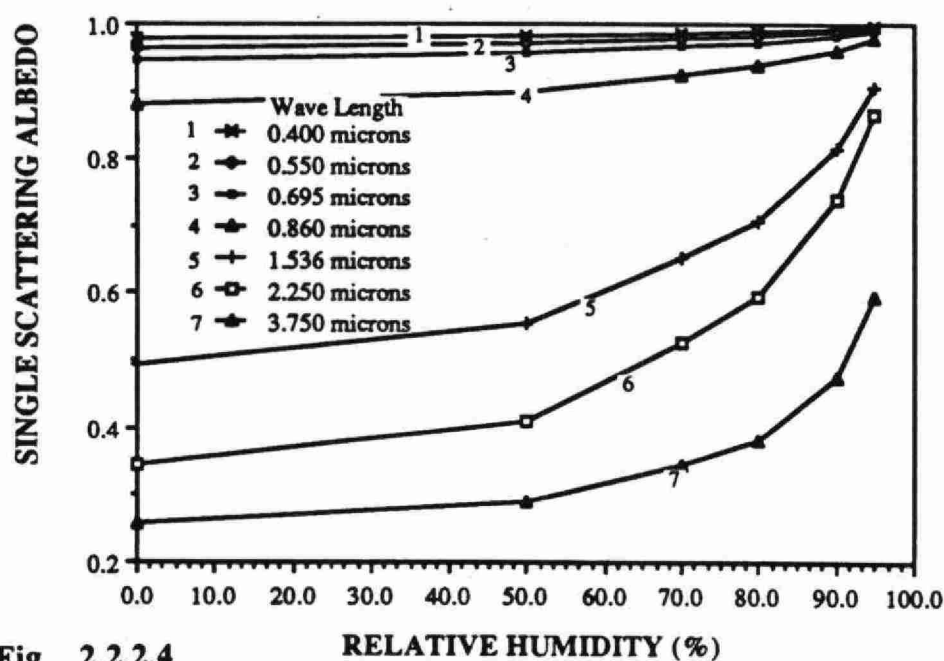


Fig. 2.2.2.4

WATER SOLUBLE ASSYMETRY FACTOR VERSUS RELATIVE HUMIDITY

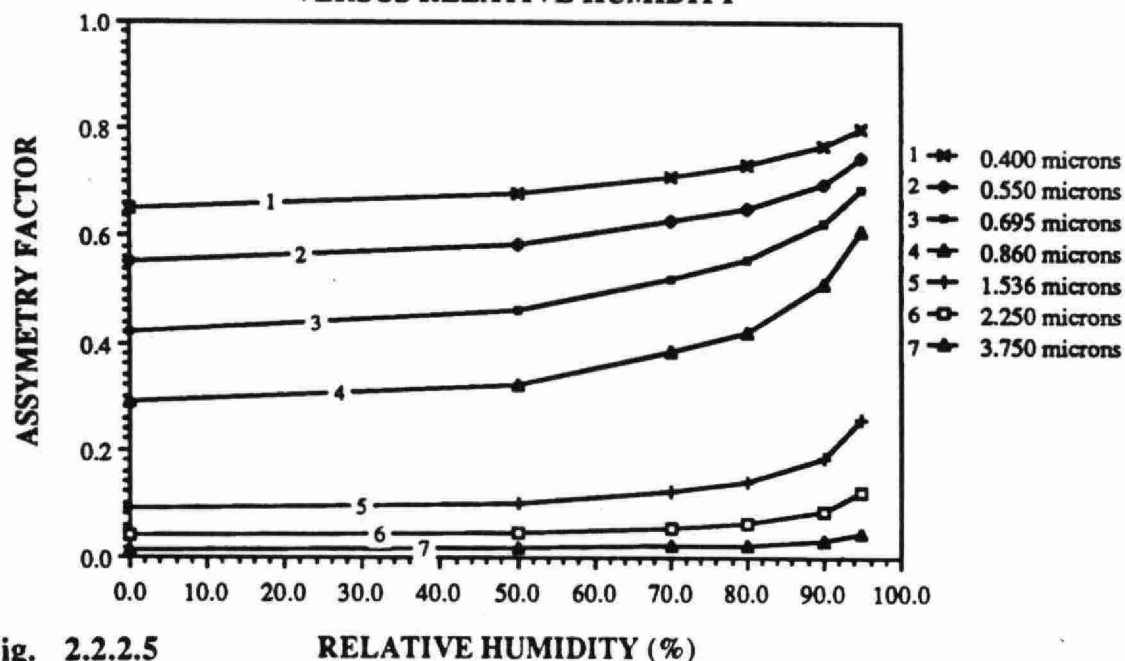


Fig. 2.2.2.5

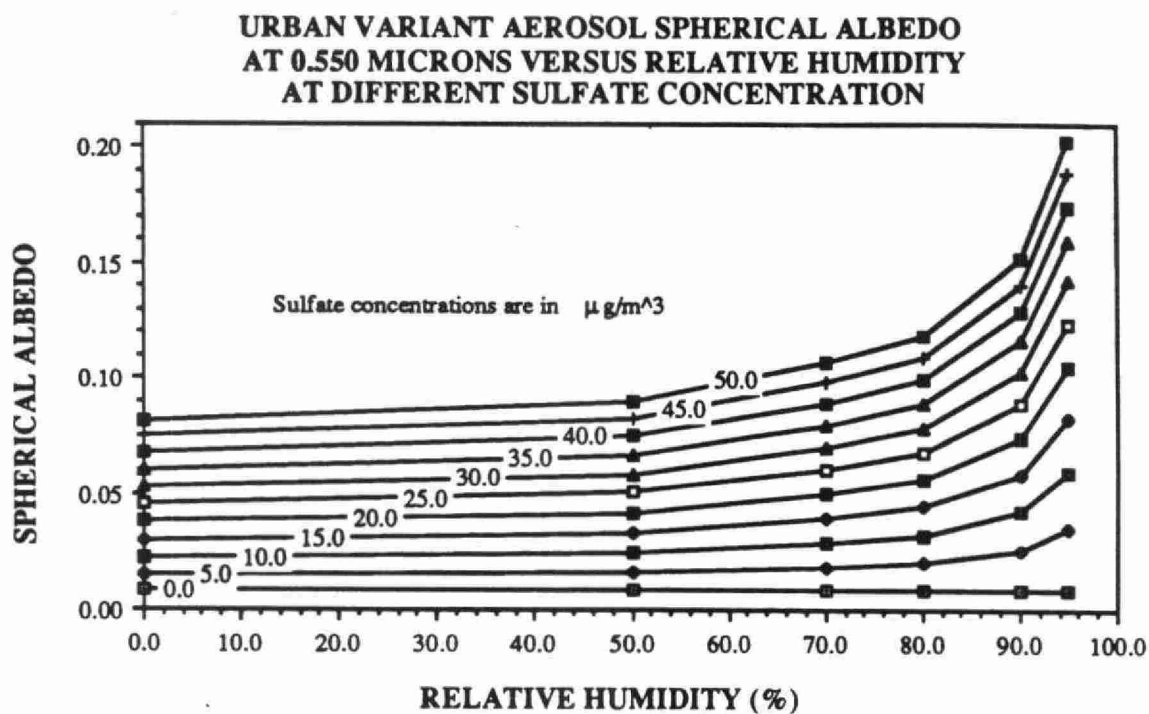


Fig. 2.2.2.6

The entries of Table 2.1.4.3 are Mie computations of the component and total aerosol volume scattering coefficients as well as the sulfate mass scattering efficiency for different aggregate aerosol models (standard and variant surface number density cases) as a function of relative humidity. Employing the above expressions with a value of $r_3 = .129 \mu\text{m}$ (derived from the log normal parameters of the Leitch model in Table 2.1.1.1) yields:

$$\begin{aligned}\epsilon(\lambda) &= \Delta\kappa^{\text{scat}}(\lambda) / ((96.1/132) \times 1.6186\text{E-}14 [\text{g}] \Delta N [\text{cm}^{-3}] \times 10^6 [\text{m}^{-3}/\text{cm}^{-3}]) \\ &= 8.486\text{E}7 \Delta\kappa^{\text{scat}}(\lambda) / \Delta N [\text{m}^2/\text{g}]\end{aligned}\quad (2-8)$$

where ΔN is taken as 430 cm^{-3} in Table 2.1.4.3. This relation yields the scattering efficiencies of Table 2.1.4.3.

The range of sulfate mass scattering efficiencies listed in Table 2.1.4.3 are commensurate with ground based measurements such as those detailed in Table 2.1.4.1. At a dry relative humidity of 50% the expression above produces values of $\epsilon(\lambda)$ ranging from 5.1 to $6.7 \text{ m}^2/\text{g}$. In comparison the *in situ* measurements of Table 2.1.4.1 range from 2.0 to a high of 30.0 with an apparent higher frequency in the neighbourhood of 10 - $15 \text{ m}^2/\text{g}$.

It should be noted that the values in Table 2.1.4.1 are open to interpretation in terms of the effects of relative humidity on the measured volume scattering coefficient. As Kaufman and Fraser (1983) point out the measuring device (nephelometer) heats the scattering aerosols so that the ambient humidity is reduced with an accompanying decrease in the total aerosol scattering coefficient. They go on to say that the nephelometer based measurement can only be reliably used for relative humidities less than 70%. In only one of the cases for which we have documentation did the authors take pains to eliminate the heating effect and obtain scattering coefficients at the ambient relative humidity (Vossier & Macias, 1986). Except for these data then, one should generally regard the entries of Table 2.1.4.1 as estimates of the sulfate mass scattering efficiency at relative humidity values somewhere below 70%.

The occurrence of higher values of mass scattering efficiencies $\epsilon(\lambda)$ in the *in situ* measurements is in our viewpoint not due to the existence of larger fine particle modes such as those reported for some urban atmospheres (Vossier & Macias; Hering & Friedlander, 1982) or less monodisperse fine particle modes such as those observed by Tang et al. (1981). These deviations from the assumed aggregate aerosol models, can add a significant contribution to the optical scattering signal but do not add significantly to the sulfate mass scattering efficiency (c.f. Appendix A.3). This reasoning along with the fact that these types of particle modes were not measured in Leitch's (1988) airborne program led us to exclude their incorporation in the aggregate aerosol models discussed in Section 2.1.

The more likely reason why the *in situ* measurements appear to produce larger scattering efficiencies relates to the fact that our fine particle mode is assumed to consist entirely of sulfate plus a comparatively small amount of soot. In reality other fine particle aerosol components may contribute in the order of 30 to 90 % of the volume scattering coefficient (Table 2.1.4.1). The implication of a significant non sulfate contribution is clearly that the scattering coefficients calculated for a pure sulfate fine particle mode will be proportionately smaller than the nephelometer measured coefficients. This disparity between Mie calculations based on the sulfate component only and regression slopes derived from nephelometer measurements was pointed out as well by Vossier & Macias (1986; p. 1239). The excellent correlation coefficients which are typically obtained between the aerosol scattering coefficient and sulfate mass are in part due to non sulfate particles which covary with the sulfates.

Given a representative value for $\epsilon(\lambda)$ and a measurement of the aerosol scattering volume coefficient $\kappa^{\text{scat}}(\lambda)$ one can in principle calculate the sulfate mass density $[\mu\text{g}/\text{m}^3]$ from:

$$\text{SO}_4 = 10^6 \times (\epsilon(\lambda))^{-1} \kappa^{\text{scat}}(\lambda) \quad (2-9)$$

For the urban variant model of Table 2.1.4.3 a relative humidity of 0% yields $.17 \text{ g}/\text{m}^2$ for $(\epsilon(0.55 \mu\text{m}))^{-1}$. In comparison Fraser and Kaufman (1984) present a regression based expression which at 0% relative humidity and $0.55 \mu\text{m}$ yields $0.10 \text{ g}/\text{m}^2$ for ϵ^{-1} . As discussed above, the difference between the two values is probably due to the

covariance of other fine particle constituents with sulfate (in addition to a non covarying quantity which they modelled as a covarying contribution with associated errors).

(b) Vertically integrated coefficients

If both sides of the point volume expression above are integrated over altitude one obtains:

$$\Sigma SO_4 = 10^6 \times (\epsilon(\lambda))^{-1} \tau^{scat}(\lambda) \quad (2-10)$$

where ΣSO_4 represents a mass density per unit cross sectional area of an atmospheric column [$\mu g/m^2$] while $\tau^{scat}(\lambda)$ is the total measured aerosol scattering optical depth. If the integrated sulfate expression is divided by 1000 one obtains an *equivalent sulfate surface concentration* [$\mu g/m^3$] in terms of a forced aerosol scale height of 1000 meters (the scale height is defined in Appendix A.1). The equivalent surface concentration represents the surface concentration required to yield the actual columnar concentration ΣSO_4 if the scale height of the aerosol mixing layer is fixed at 1 km.

The relevance of this parameter in terms of the actual surface concentration is clearly related to the natural variation of the scale height and indeed whether aerosols can be realistically modelled in terms of a mixing layer characterized by a exponentially decreasing number density. Elterman (1970) developed a vertical scale height model referenced to the horizontal visual range, which implied a very strong correlation between columnar quantities (optical depth) and surface quantities (visual range and volume scattering coefficient) and which served as common departure point for a decade of radiative transfer work. His investigations, performed for horizontal visual ranges from 2 to 13 km, showed that scale heights ranging from .84 to 1.23 km could adequately represent the variation of aerosol volume attenuation coefficients between ground level and an effective upper boundary to the mixing layer at about 5 km. This spread of visual ranges, meant to encompass the so called haze regime between a clear atmosphere and fog, is clearly of particular interest in sulfate surveillance problems.

The work of Isaac et al. (1988), however, indicated some rather significant variations in the altitude profile of the mixing layer with important implications on the computed scale height. Kaufman and Fraser (1983) presented results for visual ranges from 5 to 16 km (roughly corresponding to Elterman's haze regime) which also implied that integrated and surface measurements were often not well correlated. They point out that variations in scale height of the order of a kilometer produce large errors in vertically integrated aerosol mass estimates given that one has ground level measurements of visibility but no information on the scale height. The analogue to this observation in terms of satellite based estimates of columnar mass loading is that large errors in the estimate of ground based concentrations can be expected if no information about the scale height is available. Given a large uncertainty in the mixing layer scale height, the relevant parameter extracted from satellite observations is thus the total integrated sulfate concentration (ΣSO_4). However we will continue to use the concept of equivalent sulfate surface concentration in order to better relate our results to standard ground based pollution measurements.

2.2.4 Effects of Changes in Aggregate Aerosol Models and Equivalent Surface Number Concentration

(a) External Aggregate Aerosol Model

Figure 2.2.4.1 is a graph of total aerosol scattering optical depth as a function of equivalent sulfate surface concentration for all the aggregate aerosol models and surface number density cases listed in Table 2.1.4.3 (wavelength of $0.55 \mu\text{m}$). The computations, which were performed using the volume scattering coefficients listed in Table 2.1.4.3 and an effective scale height of 1 km, explicitly show the uncertainty in the total aerosol scattering optical depth (or alternatively the equivalent sulfate surface concentration) associated with the manner in which constituent number densities are combined to yield total number densities. By way of illustration the graph shows an uncertainty of approximately 10, 8 and $2 \mu\text{g}/\text{m}^3$ sulfate for relative humidities of 0% 80% and 95% respectively if one has no information on which of the four models in Table 2.2.4.3 was employed to derive the volume scattering coefficients. This error is in effect associated with an uncertainty in $\epsilon(\lambda)$ (see also the discussion in Section 4.2.2 (c))

In general the standard models yield larger aerosol scattering optical depths than the variant cases simply because all aerosol constituents are permitted to vary (as opposed to only sulfates) and hence the total number densities are larger at every sulfate increment. The urban aerosol models yield larger aerosol optical depths than the continental models principally because of a larger soot component which contributes a small but significant portion to the total scattering. The dust like or large particle contribution is not a significant factor in determining the gross visible wavelength scattering attributes of a particular model.

(b) Internal Aggregate Aerosol Model

The results presented in Appendix C indicate less of a dependence on external versus internal aerosol model than on the manner in which particle growth effects were modelled. Indeed the differences at the larger relative humidities were traced to the functional dependence of the wet to dry particle radii and in turn to the ratio of water mass to dry particle mass in terms of water activity. The mass ratio model which was employed for the calculations throughout this text (c.f. Appendix A.2) were found to give lower results than those of Appendix C as well as those obtained by Tang et al. (1981). Presumably this difference relates to the fact that our model was based on an average aerosol while those of Tang et al. and Appendix C were strictly derived for pure sulfates. In light of the rather disparate results presented by Tang et al. (1981) the lack of difference between the external and internal model calculations bears further investigation.

**TOTAL AEROSOL OPTICAL DEPTH VERSUS SULFATE
CONCENTRATION AT DIFFERENT RELATIVE HUMIDITY**

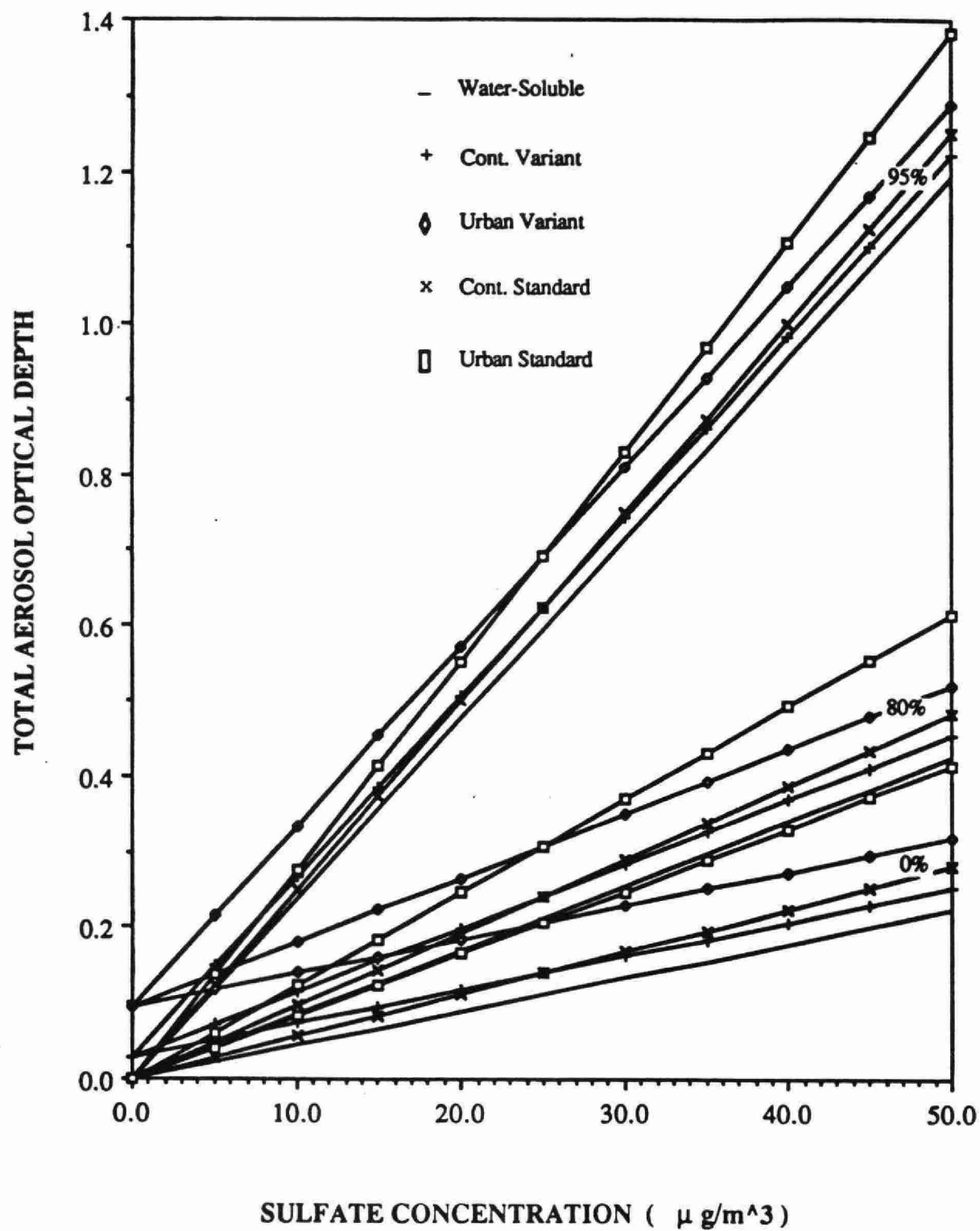


Fig. 2.2.4.1

CHAPTER 3

RADIATIVE TRANSFER SIMULATIONS

Given the optical parameter variations typified by the results presented in Chapter 2 one is in a position to apply these numbers as input parameters to a radiative transfer model which effectively integrates the contribution from each point in the atmosphere to obtain the signal measured by the satellite. This problem is non trivial since solar photons incident on aerosols in the lower atmosphere may undergo several scattering events before being directed into the field of view of the satellite sensor. In addition the integrated effect of multiply scattered photons redirected into the sensor field of view is complicated by the distinctly different optical properties of the upper atmosphere in comparison to the lower boundary layer whose properties we wish to investigate. One is then confronted with a classical radiative transfer dilemma of having to compromise between arbitrarily accurate but time consuming solutions and approximate solutions which rationalize the intrinsic optical parameters and hence reduce execution time. This question of computation time is further aggravated by considerations of the large size of remote sensing image databases and the specific requirement that an inversion must be performed on each point in the image.

The principal objective of Section 3 is to demonstrate how the output parameter of the radiative transfer model (exoatmospheric reflectance) is influenced by the input environmental and operational parameters. Once this is understood we can proceed to the inverse problem of evaluating sulfate sensitivity in terms of the satellite signal and how uncertainties in the other input parameters will affect inversions which are performed.

We briefly describe the input and output parameters required for the radiative transfer calculations as well as the choice of radiative transfer model employed. The relevance of the optical parameters described in Section 2.2 is made apparent by indicating how these same parameters act as critical inputs to the radiative transfer computations.

3.1 The 5S Model and Required Input/Output parameters

The model employed for the radiative transfer calculations was the 5S model (Appendix B). This model is a multiple scattering analytical solution to the radiative transfer problem posed in a plane parallel vertically homogeneous atmosphere. It's principal feature is an impressively rapid execution time suited to the data intensive requirements of remote sensing. The limitations of the model which stem from the simplifying assumptions employed in its derivation are discussed in Section 3.2.

Table 3.1 indicates the operational and optical (environmental) parameters required as input to the 5S model. (detailed descriptions of the optical input parameters are given in Appendix A.1). For each input vector of parameters one outputs an apparent reflectance:

$$\rho^* = t_{mol}(\theta) \{ \langle \rho \rangle T(\theta, \tau, g, \omega_0) T(\theta_s, \tau, g, \omega_0) / [1 - \langle \rho \rangle s(\tau, g, \omega_0)] + \rho_a(\phi, \theta, \theta_s, \tau, \omega_0 \rho_0(\cos \chi)) \} \quad (3-1)$$

which is simply the upwelling radiance at the top of the atmosphere normalized to the incident solar radiation on a plane parallel to the earth's surface (see Appendix B for example). The first term accounts for the attenuation of radiation reflected of the terrestrial surface while the second term is due to atmospheric backscattering only. The multiplicative transmission term ($t_{mol}(\theta)$) models the effects of the most important molecular absorbers. All non geometrical parameters are in general a function of wavelength.

One can perform computations of ρ^* at a single wavelength or over a satellite passband by interpolating between 10 reference wavelengths (Table 3.2) for which fairly precise radiative transfer calculations were carried out by the authors of 5S. The geometrical parameters include the observers zenith angle (θ) measured relative to nadir and the observers azimuth angle measured relative to the solar azimuth (ϕ). An illustrative diagram showing these angles as well as the solar zenith angle for a typical satellite geometry is included in Appendix B (Figure 2.1).

The effective target reflectance $\langle \rho \rangle$ is an area weighted average of the target reflectance (ρ_t) and the average background reflectance (ρ_b). The parameter F in Table 3.1 is the weighting function which defines the relative influence of the target and the average background reflectance on the photons which have been reflected and subsequently scattered. R defines the average size of the homogeneous target surrounding the pixel being viewed.

The point optical volume attenuation parameters in generally enter into the radiative transfer equation as explicit variables. However in the case of 5S where one effectively assumes an constant optical mixing ratio (c.f. Section 3.3) these parameters enter indirectly in terms of their integrated analogue of optical depth. The scattering phase function ($p_0(\cos \chi)$) which is a weighted mean of the molecular and aerosol phase functions is computed directly in the molecular case and entered in tabular form at fixed scattering angles for each of the aerosol component modes. The asymmetry coefficient g is computed from the phase function (c.f. Appendix A.1 and Section 2.2.1).

The single scattering albedo (ω_0) represents the fraction of scattering to total energy in an elemental volume ($\kappa^{\text{scat}} / \kappa$). If one assumes constant number density mixing ratios with altitude its value is simply given by the ratio of scattering to total optical depths. The total optical depth τ represents the sum of the aerosol scattering, molecular scattering, aerosol absorption and molecular absorption contributions. The molecular contributions (ozone, water vapour etc.) are computed for standard atmospheric models while the aerosol contributions vary with the type of aggregate aerosol model, the relative humidity and the surface number density of each aerosol component. It should be noted as well that absorption by molecular water vapour was tied to the relative humidity variations at a fixed average temperature.

The spherical albedo (s) and total transmission term (T) represent cumulative atmospheric radiative transfer effects and are derivable in approximate analytical form from the radiative transfer equation.

Table 3.1 Radiative Transfer input/output parameters

Type	Parameter	Symbol
Spectral	wavelength	λ
Geometrical	observer zenith angle	θ_v
	observers azimuth relative sun	ϕ
Atmospheric boundary	solar zenith angle	θ_s
	background reflectance	ρ_b
	target reflectance	ρ_t
	relative spatial albedo function	$F(R)$
	effective target reflectance	$\langle \rho \rangle$
Point optical	aggregate optical parameters	$\kappa(\lambda)$ $\kappa^{\text{sca}}(\lambda)$ $p_0(\cos \chi)$
Columnar parameters		τ
Molecular (absorptive) transmission		t_{mol}
Output	apparent reflectance	ρ^*

Table 3.2. Radiative Transfer Calculations (input parameter variations)

Parameter	Variations	number	Comment
Bands*	SEAWIFS	6	
	SPOT-1	3	
	TM	6	
	MSS Landsat	4	
	METEOSAT	1	
	GOES	1	
	AVHRR (NOAA 9)	2	
	(NOAA 10)	2	
ϕ	0, (30), 180	7	
θ_v	0 (10) 70	8	
θ_s	30, 45, 60, 70, 75	5	
ρ_b	Vegetation, water, sand	3	standard 5S reflectance model
	(0, .2, .5)	3	(low, medium and high ref.)
$\rho_t = \rho_b = \rho$			
F(R)	5S mean	1	
$\sigma(\lambda), \sigma_{sca}(\lambda)$	Continental standard	6 aggregate aerosol models@	
$\rho_o(\cos \chi), \omega_o(\lambda)$	Continental Variant	6 x 11 aggregate aerosol models	
	Urban / industrial standard	6 aggregate aerosol models@	
	Urban / industrial Variant	6 x 11 aggregate aerosol models	
τ, τ_{sca}	Standard models	11 increments of water soluble (sulfate) number density (c.f. Table 2.1.4.3)	
	Variant models	11 increments of total aerosol number density (c.f. Table 2.1.4.3)	
$\tau_{mol^{sca}}, \tau_{mol^{abs}}$		5S standard values	

@ One model per relative humidity (0%, 50%, 70%, 80%, 90%, 95%)

* The 5S computations are interpolated between the 10 reference wavelengths for which optical (Mie) parameters are required as input in order to obtain an effective continuum in wavelength. A quadrature sum is then performed over the satellite passband of interest. The 10 reference wavelengths are .400, .488, .515, .550, .633, .695, .860, 1.536, 2.250, and 3.750 μm .

Table 3.2 is a tabulation of the sets of input parameters employed in this study to investigate the variation of the exoatmospheric signal (apparent reflectance) as calculated by the 5S model. Apparent reflectances in different satellite bands are obtained by convoluting the 5S monochromatic (apparent) reflectances with spectral response functions stored in the 5S program. The geometrical angular parameters were chosen to obtain a representative range of values at a resolution which previous experience had shown was sufficiently dense to ensure reasonably linear segments between calculation points. For simplicity the target reflectance was chosen to be the same as the background reflectance. The background reflectances selected for investigation were fixed values between 0 and .5 in addition to standard tabulations for low turbidity water, vegetation and sand. A host of aggregate aerosol models (defined in Section 2.1.4) were in addition employed to represent the range of aggregate aerosol models which might be encountered in the lower atmosphere.

3.2 Model Dependency

In a study complementary to this work the effects on the computed satellite signal due to differences in the radiative transfer models employed was evaluated (Royer et al., 1988; Appendix B). Investigations into the optimal model which best combined the requirements of speed and accuracy indicated that the 5S model with certain qualifications was the best compromise for purposes of satellite data inversion. The limitations of this model are fairly well understood and it is sufficiently fast that a simple iterative inversion procedure can be used to extract atmospheric optical depths and subsequently sulfate densities.

In brief the investigations showed that the simplifying assumptions incorporated in 5S induce a variety of small errors in the calculated apparent reflectance which become progressively larger with increasing solar or observers zenith angle, with decreasing wavelength and as a function of the proximity of the actual ground reflectance to the critical ground reflectance (Section 3.4.3). These errors were thought to be primarily due to the manner in which aerosol and molecular scattering are decoupled in the model and as such were linked with the related factors of interparticle scatter between molecules and aerosols and the vertical inhomogeneity of the atmosphere. In later work we noted that the separation of these two phenomena was not obvious. It was observed that these errors could be considerably reduced by effectively transforming the 5S model into a two layer rather than a single layer representation of aerosol and molecular scattering. However in the interests of simplicity this correction was not incorporated in the present analysis.

3.3 Effect of Vertical Inhomogeneities

The kernel of the radiative transfer equation is the scattering phase function whose form changes with altitude depending on the relative contributions of the different aerosol and molecular phase functions (see Appendix A.1 for a description of the scattering phase function and Appendix B for a general discussion of radiative transfer concepts). These relative contributions which are determined by optical mixing ratios of volume scattering coefficients to total volume extinction are dominated by aerosols in the troposphere and by molecules above the troposphere. Because aerosol scattering is so strongly anisotropic in comparison to molecular scattering, the scattering phase function undergoes significant changes in form as a function of altitude.

Since such vertical inhomogeneities have important implications in terms of the degree of complexity and computation time of a radiative transfer code it is imperative that one understands their influence on the radiative transfer mechanisms in the atmosphere. In particular, is it reasonable to hypothesize that the radiation leaving the boundary layers of the atmosphere can be effectively evaluated using an equivalent radiative transfer model whose kernel phase function is a vertically averaged mean. Such an approach which clearly can only apply to lines of sight which view the entire atmosphere considerably simplifies the radiative transfer computations and hence the inversion methodology.

The results of the study described in Appendix B corroborate the concept of equivalent mean atmospheres. Except for very large solar zenith angles or observer's zenith angle a single layer radiative transfer model computes apparent

reflectances to values better than .005 in moderately loaded atmospheres (aerosol optical depths less than 0.5). In cases where this may be insufficient (see the noise discussion in Section 4.2.4) simple bias relations referenced to the single layer model can be developed. This latter approach is currently being investigated.

With respect to accuracy the 5S model performs less well than an arbitrarily accurate single layer model. This degraded performance is a non trivial result of the manner in which the single layer characteristics of this model are coupled with the analytical approximations employed in its derivation.

3.4 Selected Results

3.4.1 Variation of aggregate aerosol model

Figures 3.4.1.1 and 3.4.1.2 are plots of apparent reflectance versus equivalent sulfate surface concentration for the four number density models (urban standard and variant and continental standard and variant as discussed in Section 2.1.3), surface reflectances of 0.0 and 0.5 and for two different relative humidities. These apparent reflectance variations illustrate the different effects of changing the number density model in the context of a predominantly scattering atmosphere (zero surface reflectance) and a predominantly attenuating atmosphere (surface reflectance of 0.5).

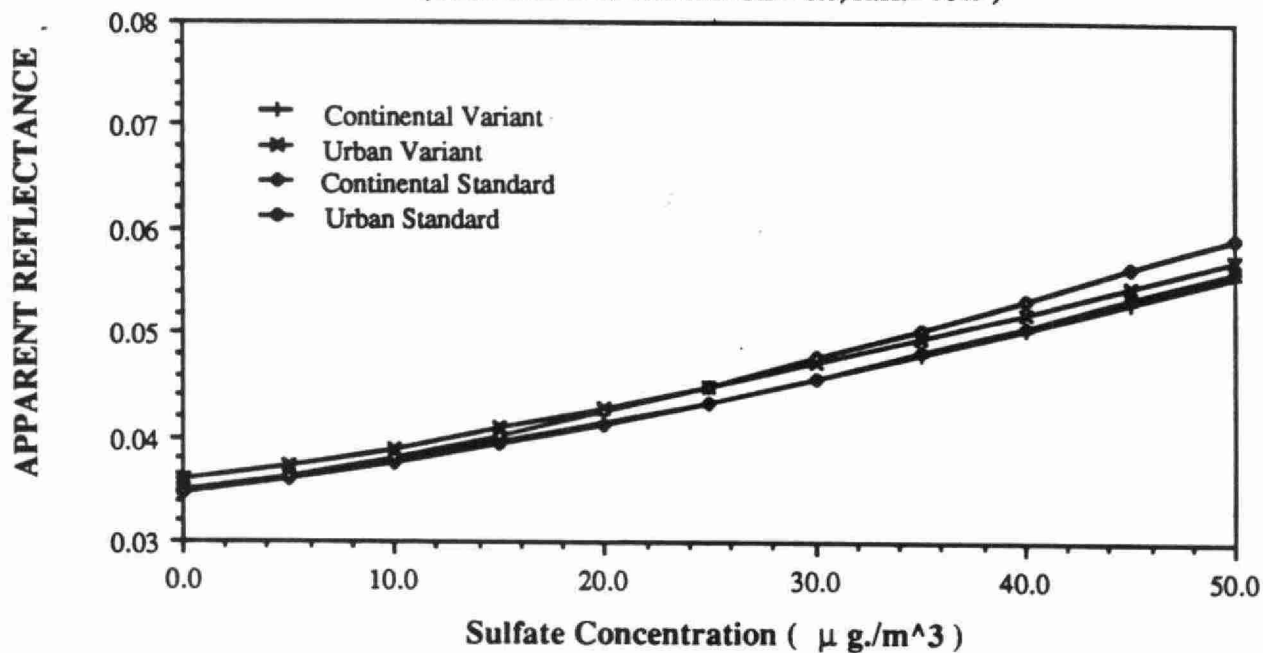
In the case of zero surface reflectance a maximum apparent reflectance difference of .006 occurs between the continental variant and urban standard models, at a relative humidity of 90% and at the maximum equivalent sulfate concentration of $50 \mu\text{g}/\text{m}^3$. At smaller relative humidities and surface concentrations this value decreases considerably (see also the discussion in Section 4.3 below). The lack of strong relative variation between number density models is not surprising given the similar type of behavior observed in the aerosol scattering optical depth plots of Figure 2.2.4.1.

However a second more subtle reason derives from the fact that the main difference between the models is the variation in the optical effects due to the soot component. The addition of soot particles (as occurs for example in changing from the continental standard to the urban standard atmosphere) causes a roughly equivalent increase in both the scattering and absorption volume coefficients of this component. The enhanced atmospheric backscattering effects of the increase in scattering coefficient is accordingly offset by the increase in absorptive attenuation. The consequence of this is that the change in aggregate aerosol model is nearly transparent to a satellite measurement of apparent reflectance.

Such is not the case for a large surface reflectance where the attenuating properties of the atmosphere dominate the apparent reflectance measurement. Here the absorptive and scattering increases due to the soot particles are actually combined since scattering in this context plays an attenuating role (outscattering between the ground and the observer in addition to outscattering of surface reflected sunlight which has been scattered one or more times into the receiver field of view). Counter balancing this attenuation effect, but of lesser importance, is the scattering contribution such as that observed in the zero albedo case plus the scattering of surface reflected radiation. The net effect is a decrease in apparent reflectance which is however less severe than the purely attenuating decrease given by $\Delta\rho^* / \rho^* \sim \Delta\tau$ (where $\Delta\tau$ is the change in optical depth due to the change in aggregate aerosol model).

One can observe also that the standard aggregate aerosol curves are considerably more linear than the variant model curves. This behavior would appear to stem from the fact that the variant model goes through a relative increase in scattering properties (ω_0 increases) with increasing sulfate concentration. Note that since the same is true for the zero reflectance surface the effect must be more prevelant in the surface reflected/scattered radiation.

**APPARENT REFLECTANCE AT 0.550 MICRONS
FOR DIFFERENT AGGREGATE AEROSOL MODELS
(GROUND REFLECTANCE = 0.0, R.H.= 70%)**



**APPARENT REFLECTANCE AT 0.550 MICRONS
FOR DIFFERENT AGGREGATE AEROSOL MODELS
(GROUND REFLECTANCE = 0.5, R.H.= 70%)**

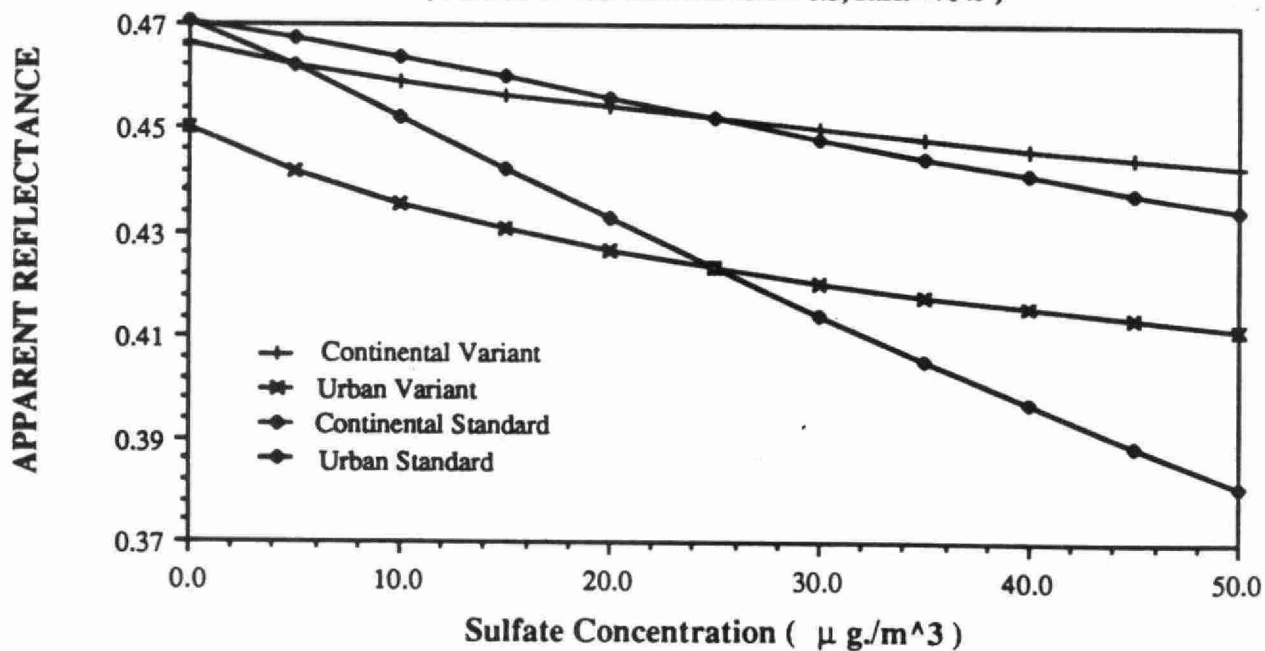
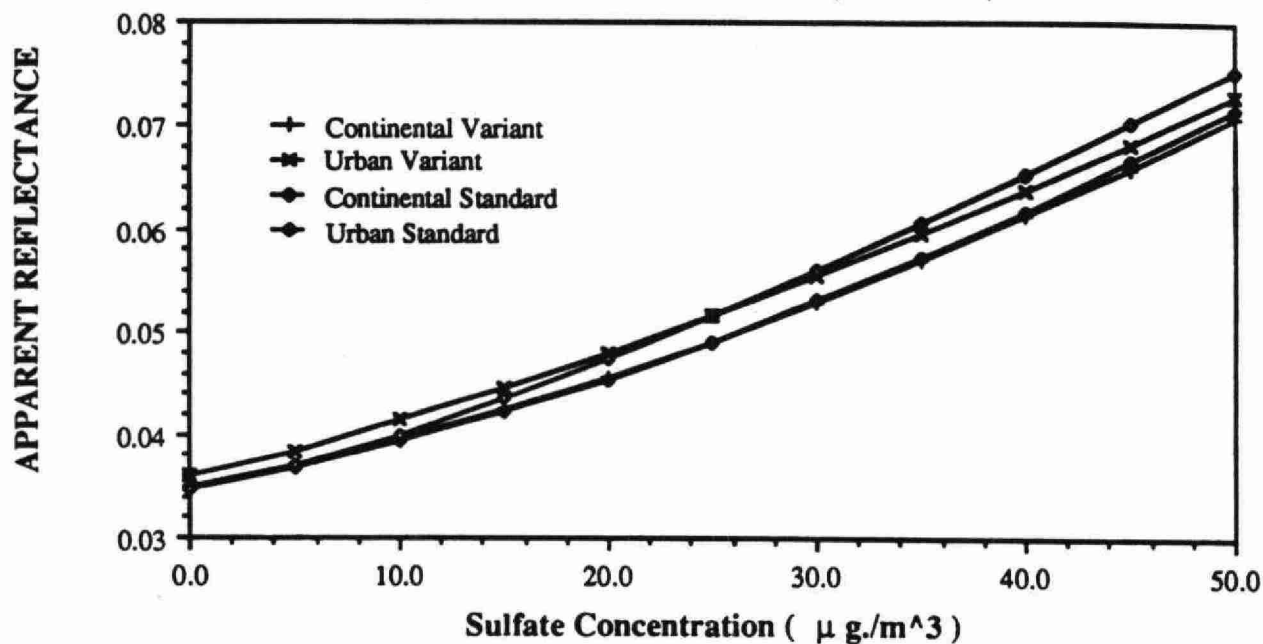


Fig. 3.4.1.1

**APPARENT REFLECTANCE AT 0.550 MICRONS
FOR DIFFERENT AGGREGATE AEROSOL MODELS
(GROUND REFLECTANCE = 0.0, R.H.= 90%)**



**APPARENT REFLECTANCE AT 0.550 MICRONS
FOR DIFFERENT AGGREGATE AEROSOL MODELS
(GROUND REFLECTANCE = 0.5, R.H.= 90%)**

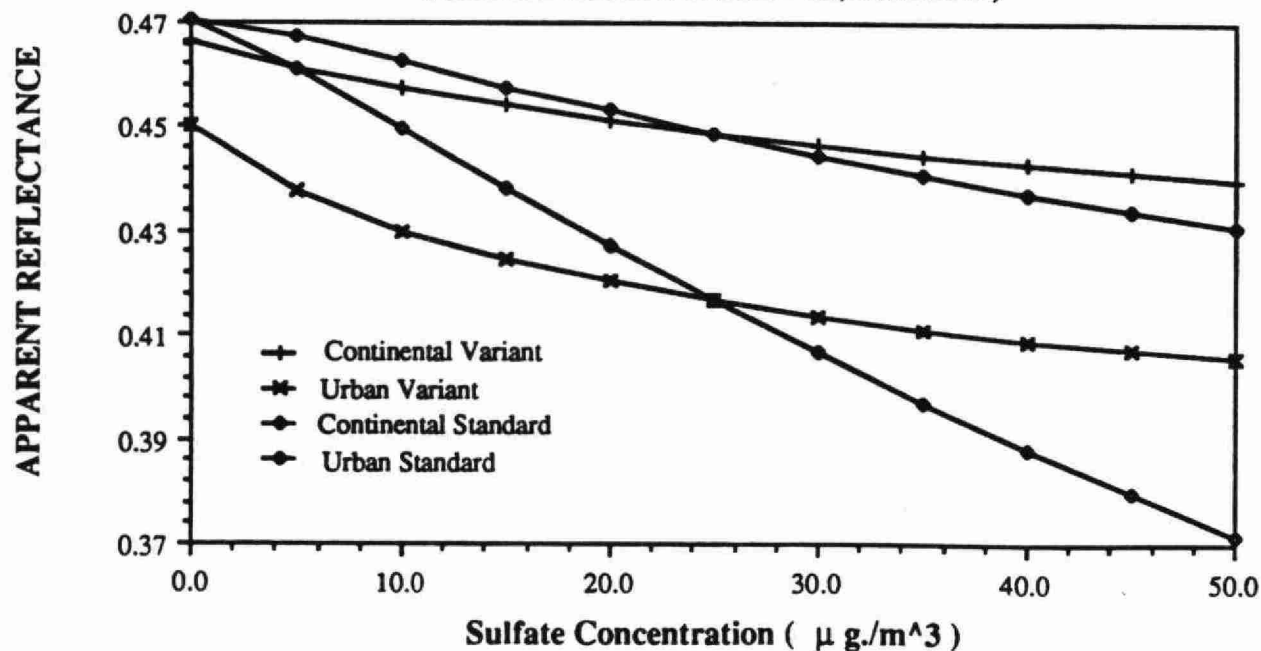


Fig. 3.4.1.2

3.4.2 Ground albedo variations

The contribution to the total satellite signal of photons reflected at the ground and directly transmitted or rescattered into the sensor field of view is one of the single most important influences on the behavior of the apparent reflectance as a function of aerosol or sulfate concentration. Figure 3.4.2.1 illustrates this behavior for a variety of surface reflectance values and relative humidities, a nadir viewing geometry and a wavelength of $0.55 \mu\text{m}$.

The most notable effect of variations in surface reflectance is clearly the change in slope from positive to negative as the surface reflectance is increased. This phenomenon which has serious implications in terms of inversion algorithms for sulfate concentration is due to the competing influences of atmospheric attenuation and absorption (c.f. Appendix B). The reflectance for which the slope is actually zero (Kaufman, 1982) is indeed a singularity at which the two influences are perfectly balanced independent of atmospheric optical thickness. For surface reflectances below this *critical surface reflectance* the satellite signal is dominated by scattering effects and accordingly increases with an increase in the number of scattering particles (sulfate particles). If the actual surface reflectance is greater than the critical surface reflectance then attenuation effects of surface reflected photons dominate and the satellite signal actually decreases with an increase in the number of scattering particles.

The critical reflectance singularity is best illustrated by a Kaufman type plot of apparent reflectance (less surface reflectance) as a function of surface reflectance. In Figure 3.4.2.2 the effectively linear segments which correspond each to a particular value of optical depth clearly intersect at a well defined critical reflectance. Since the position of the intersection point is a strong function of the average atmospheric single scattering albedo the singular behavior of the apparent reflectance in the neighbourhood of the point can be turned to advantage by utilizing it to quantify atmospheric absorption (see Section 4.2.3 below).

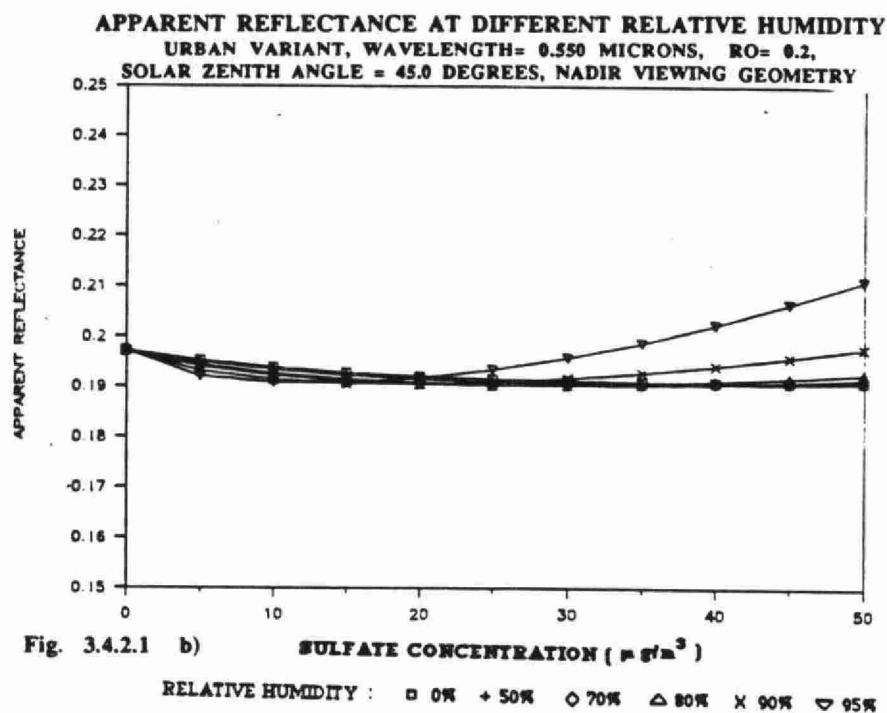
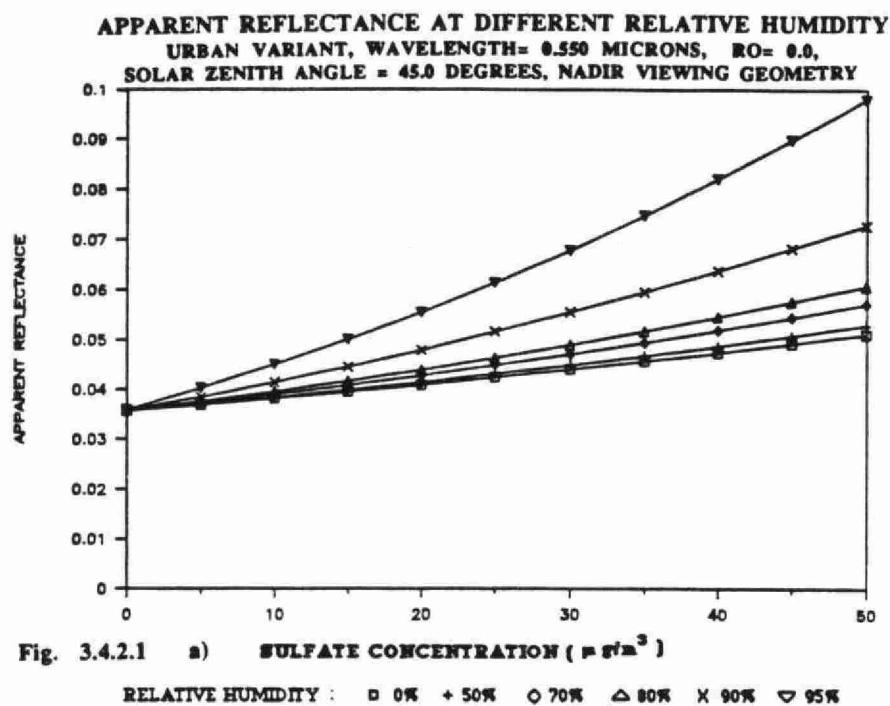
However the key point to note is that the satellite signal is only weakly sensitive to atmospheric aerosol composition over those areas for which the surface reflectance is close to the critical reflectance. This point is further developed in terms of inversion errors for sulfate concentration in Section 4 below.

3.4.3 Relative humidity effects

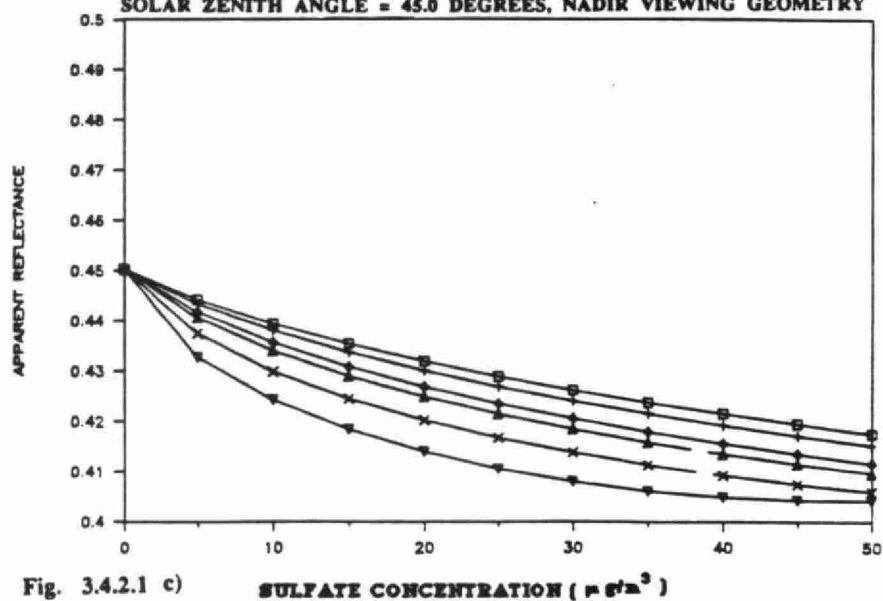
Referring again to Figure 3.4.2.1 one can observe the significant effects of relative humidity on the computed value of apparent reflectance over a range of relative humidities. The three ground reflectances (0, .2 and .5 in (a), (b), and (c) respectively) correspond to values well below, at and well above the critical ground reflectance and as such the variations in slope of the three curves with different ground reflectances illustrate well the tradeoff effects of atmospheric attenuation and scattering discussed in Section 3.4.2 above.

At a surface reflectance of zero (Figure 3.4.2.1(a)) the increase in apparent reflectance with increasing sulfate is most significant when the relative humidity is high and the scattering cross sections of a given concentration of sulfate particles are maximum. At large reflectances above the critical reflectance (Figure 3.4.2.1 (c)) the effects of attenuation dominate and the larger cross sections associated with higher relative humidities effect a decrease in apparent reflectance as the relative humidity increases.

At values of reflectance near the critical reflectance one expects a flat or nearly flat response curve for apparent reflectance versus sulfate concentration. Figure 3.4.2.1(b) does show this lack of sensitivity along with a weak minima for the larger relative humidities (note that the apparent reflectance scale is strongly magnified). The weak minima results from the fact that the Kaufman singularity is not well defined at the higher relative humidities. Figure 3.4.3.2 (relative humidity of 95%) illustrates this point and in comparison to Figure 3.4.2.2 clearly demonstrates how a value of reflectance chosen in the neighbourhood of the cluster of intersection points induces a non linear relationship between apparent reflectance and optical depth (sulfate concentration).

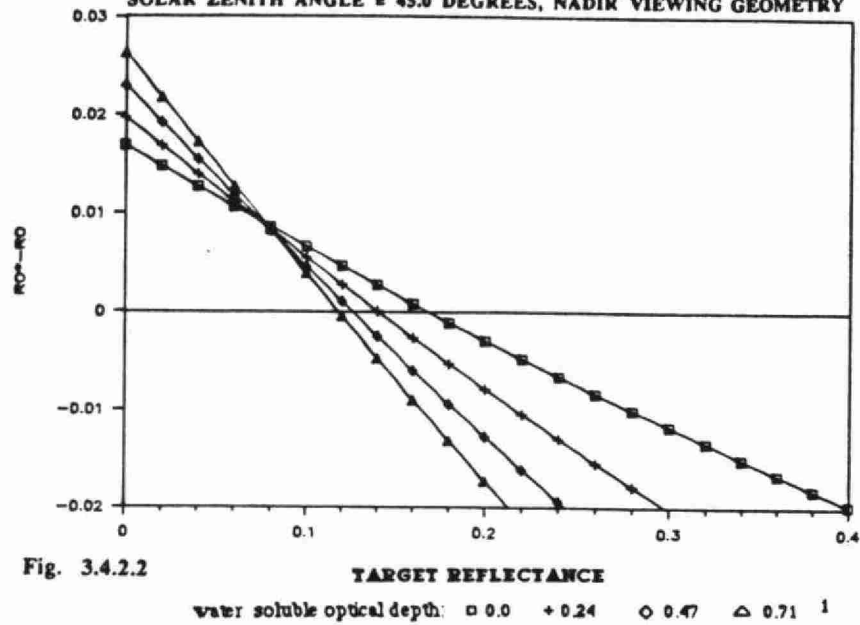


APPARENT REFLECTANCE AT DIFFERENT RELATIVE HUMIDITY
URBAN VARIANT, WAVELENGTH= 0.550 MICRONS, RO= 0.5,
SOLAR ZENITH ANGLE = 45.0 DEGREES, NADIR VIEWING GEOMETRY

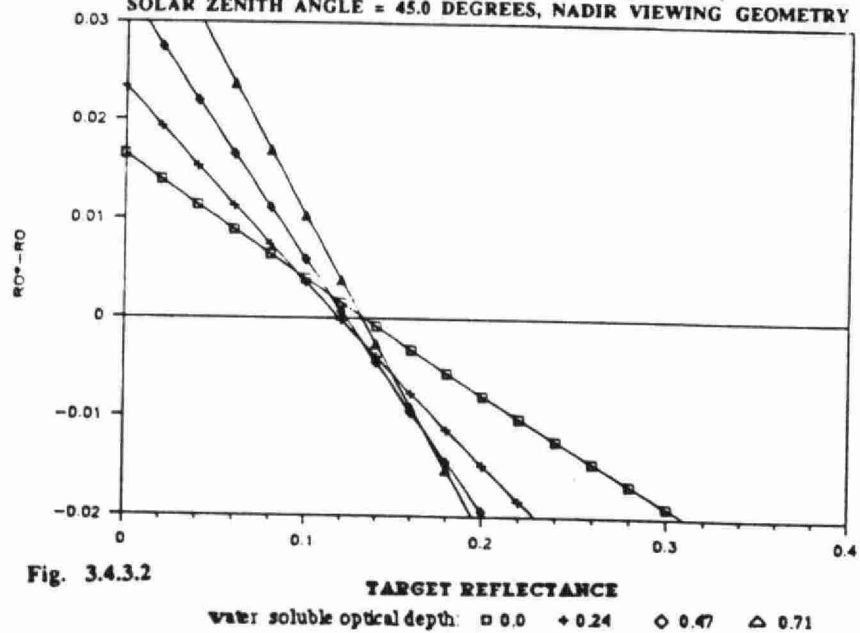


RELATIVE HUMIDITY : \square 0% $+$ 50% \diamond 70% \triangle 80% \times 90% ∇ 95%

APPARENT- TARGET REFLECTANCE AS A FUNCTION OF
TARGET REFLECTANCE FOR DIFFERENT SULFATE OPTICAL DEPTH
MSS BAND 2, URBAN STANDARD, RH= 0%,
SOLAR ZENITH ANGLE = 45.0 DEGREES, NADIR VIEWING GEOMETRY



APPARENT- TARGET REFLECTANCE AS A FUNCTION OF
TARGET REFLECTANCE FOR DIFFERENT SULFATE OPTICAL DEPTH
MSS BAND 2, URBAN STANDARD, RH= 95%,
SOLAR ZENITH ANGLE = 45.0 DEGREES, NADIR VIEWING GEOMETRY



3.4.4 Absorption Effects

Figure 3.4.4.1 shows the variation of apparent reflectance as a function of equivalent soot concentration. The insensitivity of the apparent reflectance to increasing soot absorption for zero surface reflectance is the same scattering/absorption offsetting effect previously discussed in Section 3.4.1. Similarly the comparatively large slope observed for high surface reflectance is indicative of the dominance of attenuation effects (Section 3.4.1). The sulfate and soot inversion implications of these variations is discussed in Sections 4.2.3, 4.2.5 and 4.3. Conversion of the soot concentrations to single scattering albedo values is discussed in Appendix A.3 (Figure A.3.3).

Note that the soot concentration variation is arranged so that the urban standard and continental standard fractional number densities are obtained at $13.8 \mu\text{g}\cdot\text{m}^{-3}$ of soot. The soot concentrations reduce by a factor of .436 if the remarks of Chapter 6 are taken into account.

3.4.5 Dependence on satellite bands

Figure 3.4.5.1 illustrates the variation of the apparent reflectance (nadir geometry) as a function of equivalent sulfate concentration for a low reflectance target (5S lake standard) over a range of satellite bands located in the visible and near infrared spectral region. The magnitude differences between the various curves is primarily due to the λ^{-n} type of falloff expected in the aerosol scattering optical depth (see Section 4.2.5b for example). Figure 3.4.5.2 and 3.4.5.3 are plots of the same parameters but for vegetation and sand targets. The vegetation results pass from a typical scattering atmosphere response for visible bands to an attenuating atmosphere response in the near IR. The insensitivity of the sand target results because the sand reflectance is near the critical reflectance of the atmosphere. The reader is referred back to Section 3.4.2 for a more complete discussion of reflectance effects.

A more relevant characterization of the low reflectance lake data (Figure 3.4.5.) is presented in Table 3.4.5.1 where the extreme variations of apparent reflectance, due to a change of equivalent sulfate concentration from 0 to $50 \mu\text{g}/\text{m}^3$, are normalized to the noise equivalent reflectance and radiometric resolution reflectance (extracted from Table 4.2.4.1) for each of the satellite sensors. A discussion of the implications of these signal to noise ratios is left to chapter 4. It suffices here to note that, for small surface reflectance, only those sensors with 10 bit resolution (or for which the dynamic range straddles the low reflectance range characteristic of atmospheric phenomena) can yield sufficient on the signal variations due to sulfates.

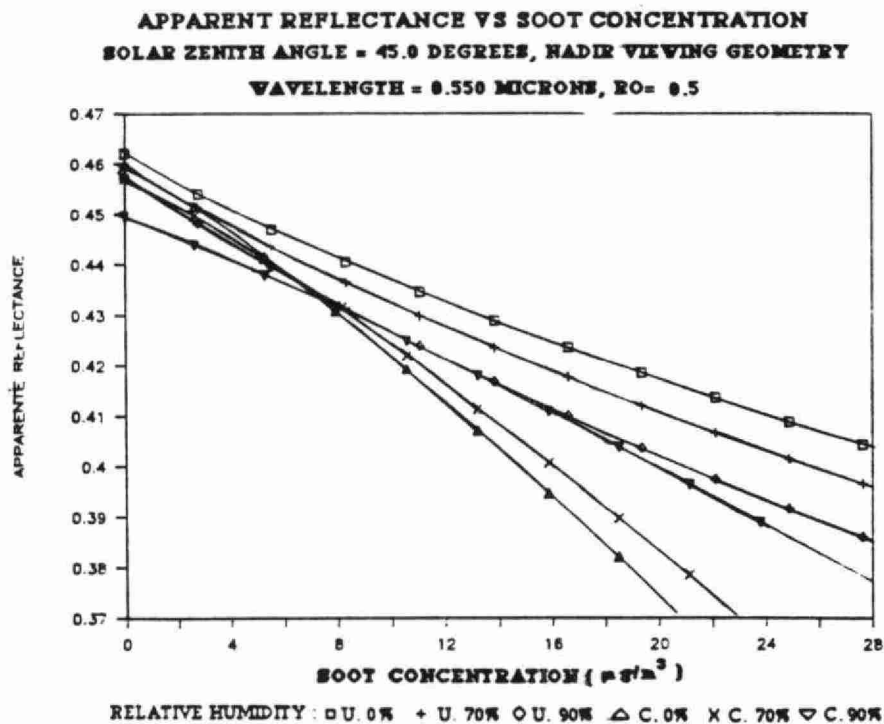
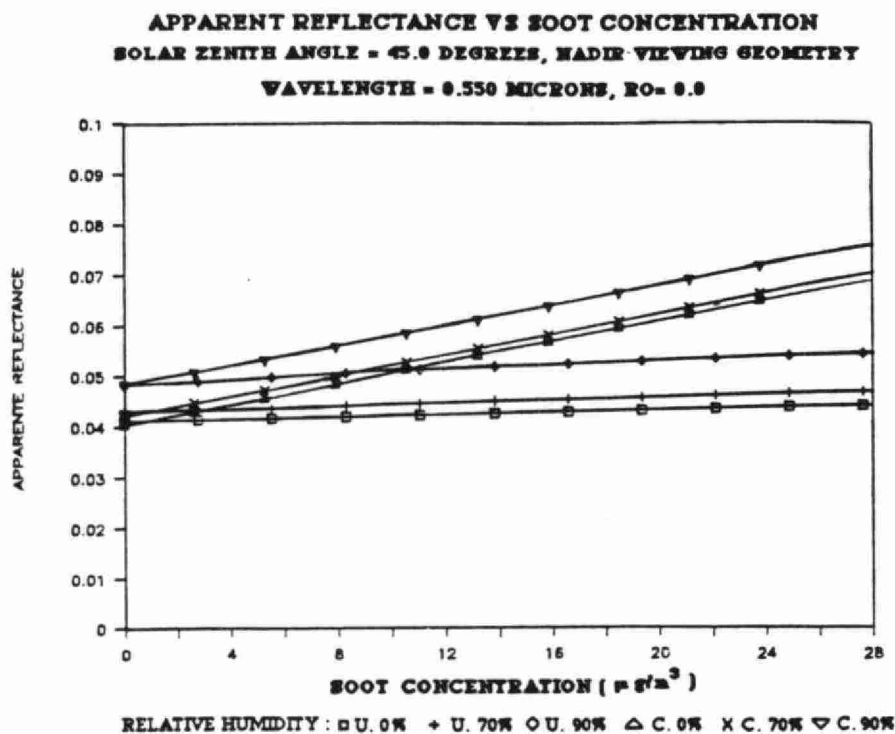


Fig. 3.4.4.1

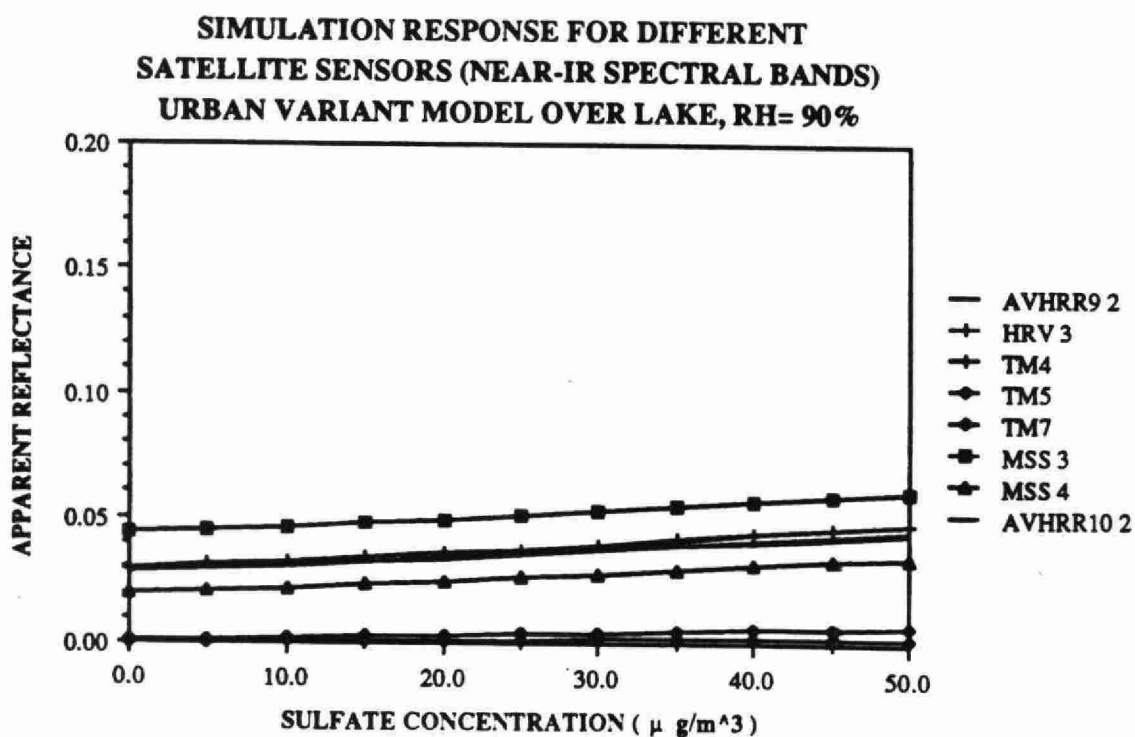
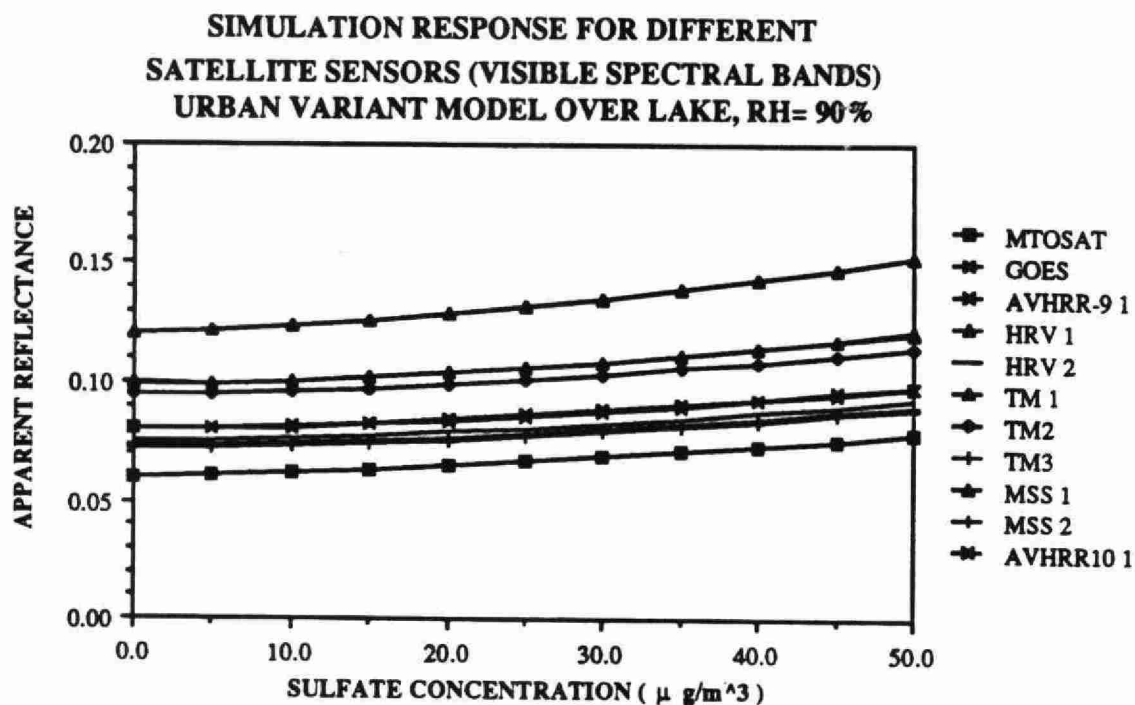
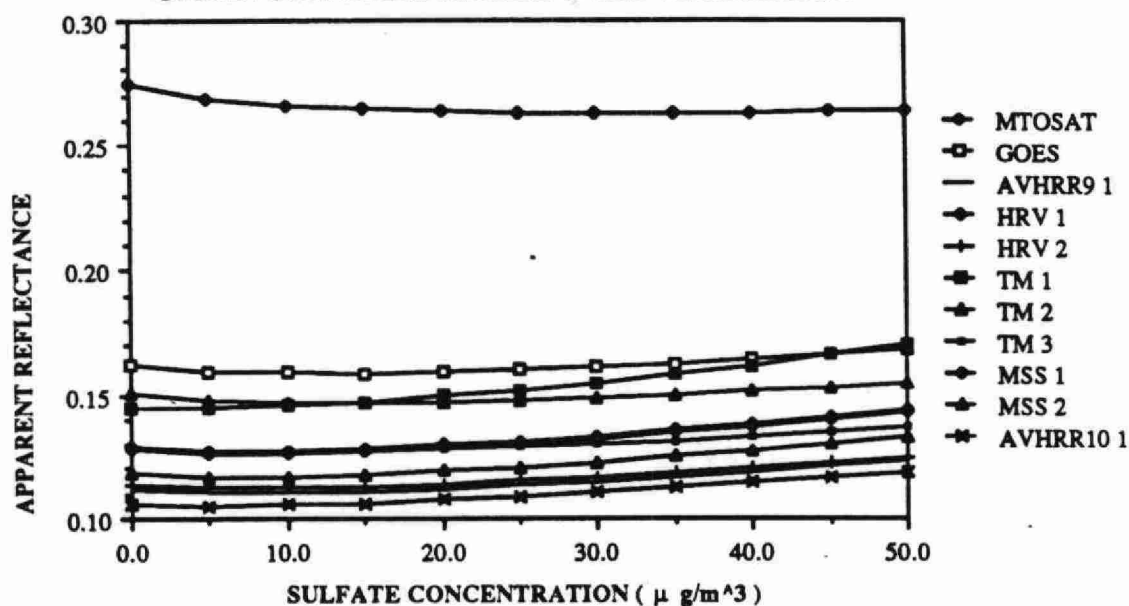


Fig. 3.4.5.1

**SIMULATION RESPONSE FOR DIFFERENT
SATELLITE SENSORS (VISIBLE SPECTRAL BANDS)
URBAN STANDARD MODEL OVER VEGETATION**



**SIMULATION RESPONSE FOR DIFFERENT
SATELLITE SENSORS (NEAR-IR SPECTRAL BANDS)
URBAN VARIANT MODEL OVER VEGETATION, RH= 90%**

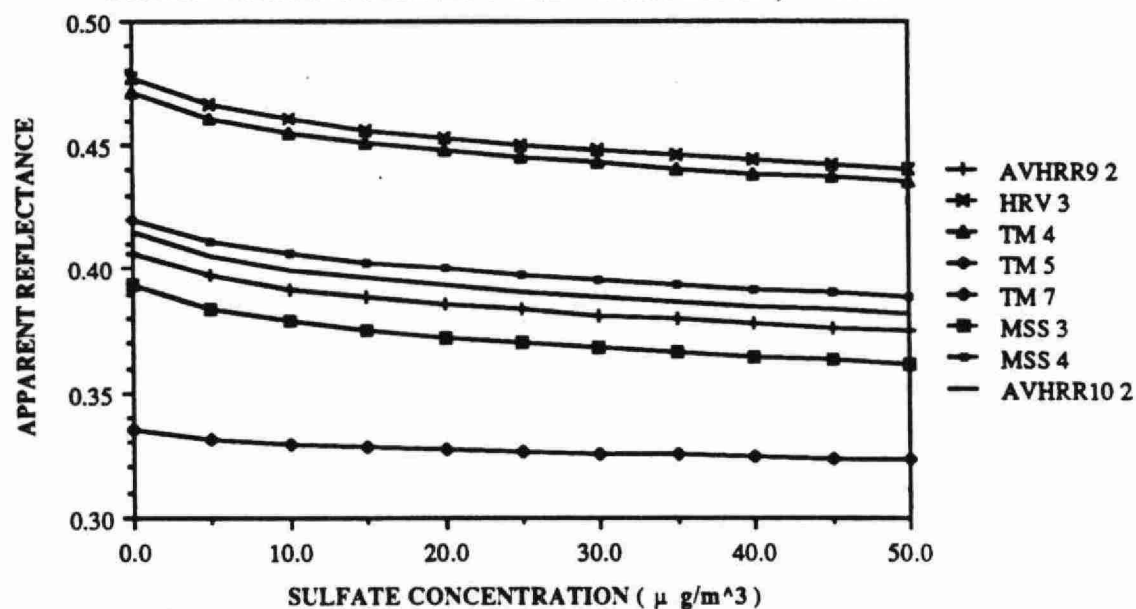


Fig. 3.4.5.2

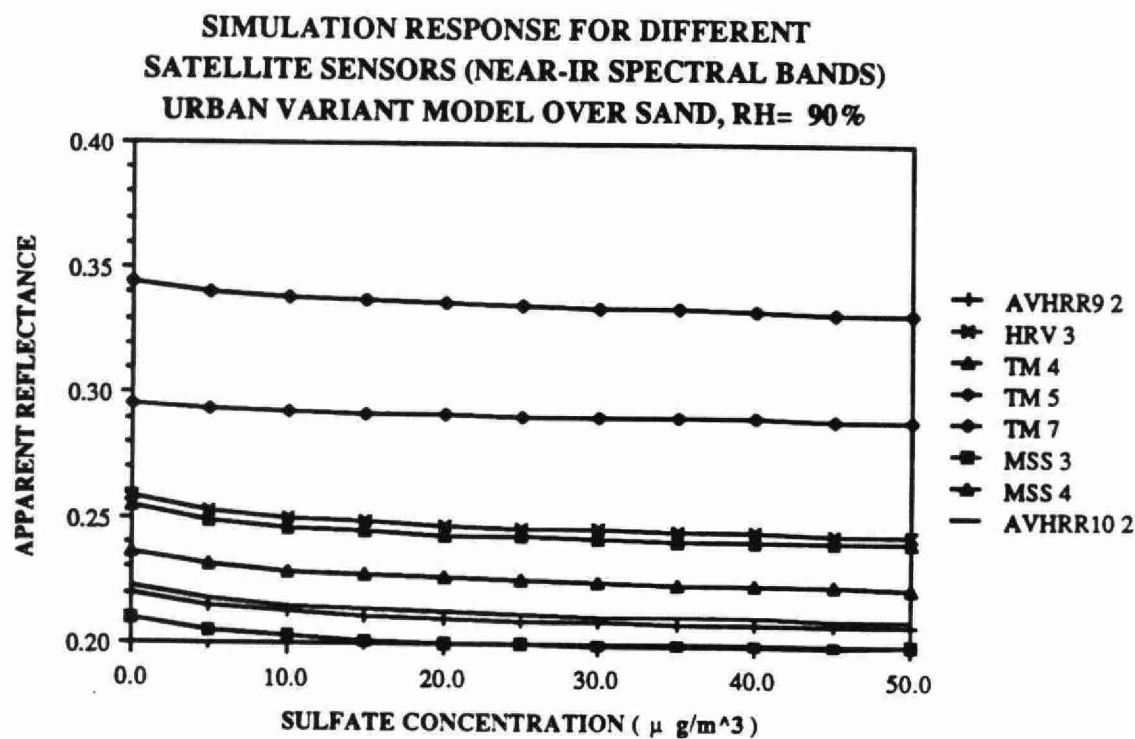
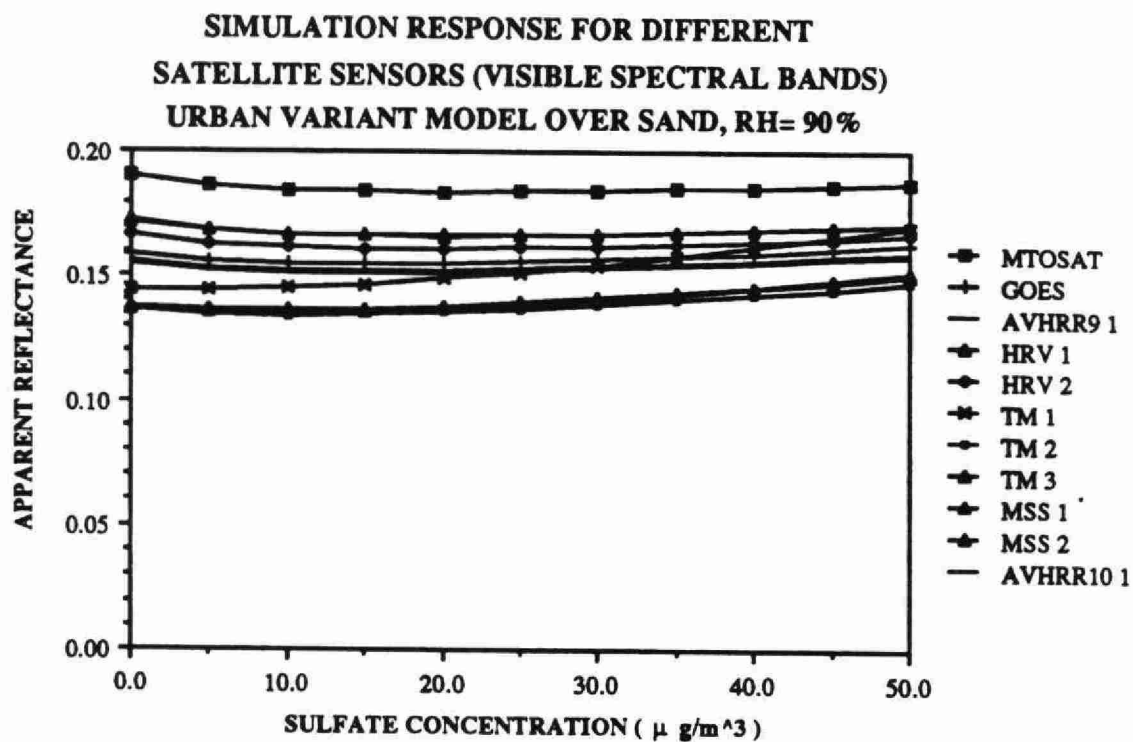


Fig. 3.4.5.3

TABLE 3.4.5.1 Apparent reflectance variation corresponding to an SO_4^{2-} variation from 0 to 50 $\mu\text{g}\cdot\text{m}^{-3}$ (normalized to the total satellite sensor noise error tabulated in table 4.2.4.1)

Satellite	Sensor	Band	Band width [micrometers]	Bits/ pixel	Signal/Noise
Landsat -5	TM	1	.45 - .52	8	4.8
		2	.52 - .60	8	3.2
		3	.63 - .69	8	3.0
		4	.76 - .90	8	4.2
		5	1.55 - 1.75	8	0.4
		7	2.08 - 2.35	8	0.1
	MSS	1	.5 - .6	7	3.1
		2	.6 - .7	7	2.7
		3	.7 - .8	7	2.2
		4	.8 - 1.1	7	1.9
SPOT	HRV	XS1	.50 - .59	8	5.0
		XS2	.61 - .69	8	
		XS3	.79 - .90	8	3.9
NOAA	AVHRR (9,10,11)	1	.58 - .68	10	10.3
		2	.715 - .982	10	6.4
METEOSAT			.4 - 1.1	6	6.7
GOES	VAS/VISSER		.54 - .75	6	10.3
Landsat-6	SEAWIFS	1	.443 - .453	10	58.8
		2	.490 - .510	10	50.3
		3	.555 - .575	10	56.0
		4	.655 - .675	10	69.2
		5	.745 - .785	10	41.7
		6	.843 - .887	10	107.0

3.4.6 Illumination Geometry

(a) viewing geometry

Figure 3.4.6.1 shows the variation of the apparent reflectance as a function of sulfate concentration for different values of observers zenith angle. The calculations were made for a relative humidity of 95%, a surface reflectance of zero and the standard 45° value for the solar zenith angle. The left hand side of each graph corresponds to look directions on the anti solar side (observers back to the sun) while the right hand side of each graph represents the solar side. The distinction is best explained in terms of Table 3.4.6.1 below:

Table 3.4.6.1 Observers zenith angle and scattering angle in the solar plane for a solar zenith angle of 45 degrees

	<u>solar side</u>						<u>anti solar side</u>					
observers zenith angle	50	40	30	20	10	0	10	20	30	40	50	
scattering angle	95	105	115	125	135	145	155	165	175	185	195	

Note: the scattering angle is measured from the direction of the sun's rays to the direction of the ray scattered into the sensor field of view. In the solar plane the calculation of the scattering angle can be performed by geometrical means. Off the solar plane the calculation is best performed using spherical geometry (see for e.g. Turner & Spencer(1972)).

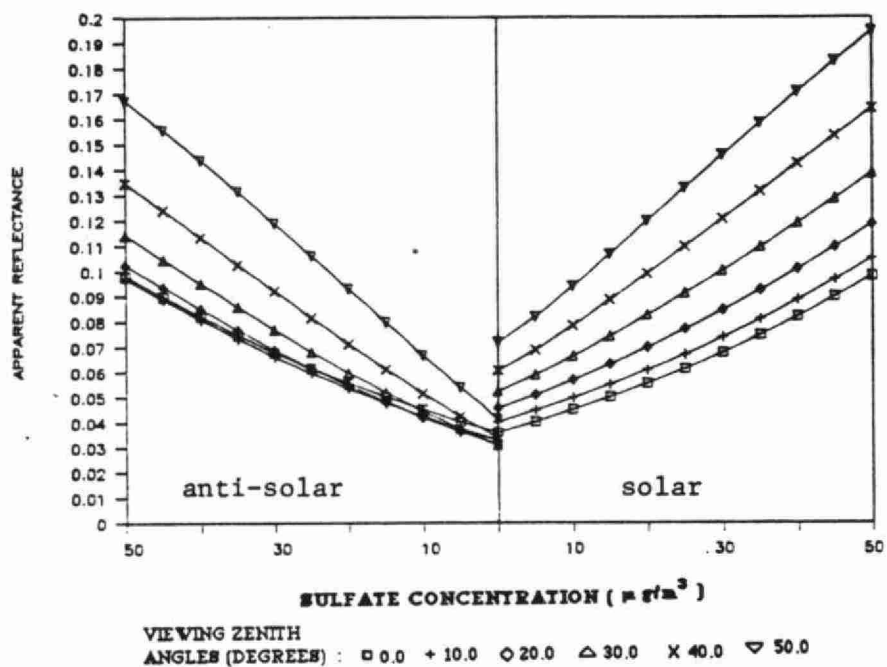
For zero surface albedo the apparent reflectance dependence on viewer geometry is predominantly a function of zenith angle and can be taken as being $\sim 1/\cos\theta$ where θ is the observers zenith angle (Deschamps et al. 1983). Second order departures from this first order variation are induced by the angular form of the scattering phase function. The scattering phase function, which for low order scattering considerations varies as the scattering angle from the sun, induces variations as a function of the observers zenith angle and the observer's azimuth angle.

With respect to the shorter wavelength ($0.55\mu\text{m}$) variation in Figure 3.4.6.1 we note that the extreme end of the solar side of the soot phase function dominates (by about a factor of three) the extreme end of the anti solar side and that the phase function decreases monotonically between the two extremes. Since, for the urban variant aggregate aerosol model, the soot particles are optically dominant at zero sulfate concentration (see for example Table 2.1.4.3) the variation with $1/\cos\theta$ on the solar side is much stronger than on the anti solar side where the decreasing phase function actually competes with increasing $1/\cos\theta$. These differences are less apparent at large sulfate concentration since the sulfate scattering phase function is much more symmetric about an observer's zenith angle of 0 degrees. At larger wavelengths (Figure 3.4.6.1 (b)) the aggregate aerosol scattering phase function is much more Rayleigh like (more isotropic) and the disparity between solar and anti solar directions is less obvious.

At large surface reflectance the apparent reflectance response curves are somewhat complicated by the competing effects of scattering and attenuation. At zero sulfate concentration the $1/\cos\theta$ and phase function variation mentioned above exceed attenuation effects on the solar side while the opposite is true on the anti solar side. The $1/\cos\theta$ effects of scattering and/or the changes in single scattering albedo with increasing sulfate concentration contribute to exaggerated non linearities of the apparent reflectance curves at the larger observer's zenith angles.

Figure 3.4.6.2 shows in the case of large surface reflectance a more promising variation to consider is the derivative of the apparent reflectance with respect to the cosine of the observer's zenith angle. Using this approach we can observe a comparatively well behaved monotonic increase as a function of sulfate concentration. It should be noted however that the apparent reflectance variation is not large and accordingly implies a fine signal sensitivity.

APPARENT REFLECTANCE AT DIFFERENT VIEWING ZENITH ANGLES
 URBAN VARIANT, SOLAR ZENITH ANGLE = 45.0,
 WAVELENGTH = 0.550 MICRONS, RH = 95%, RO = 0.0



APPARENT REFLECTANCE AT DIFFERENT VIEWING ZENITH ANGLES
 URBAN VARIANT, SOLAR ZENITH ANGLE = 45.0,
 WAVELENGTH = 0.550 MICRONS, RH = 95%, RO = 0.5

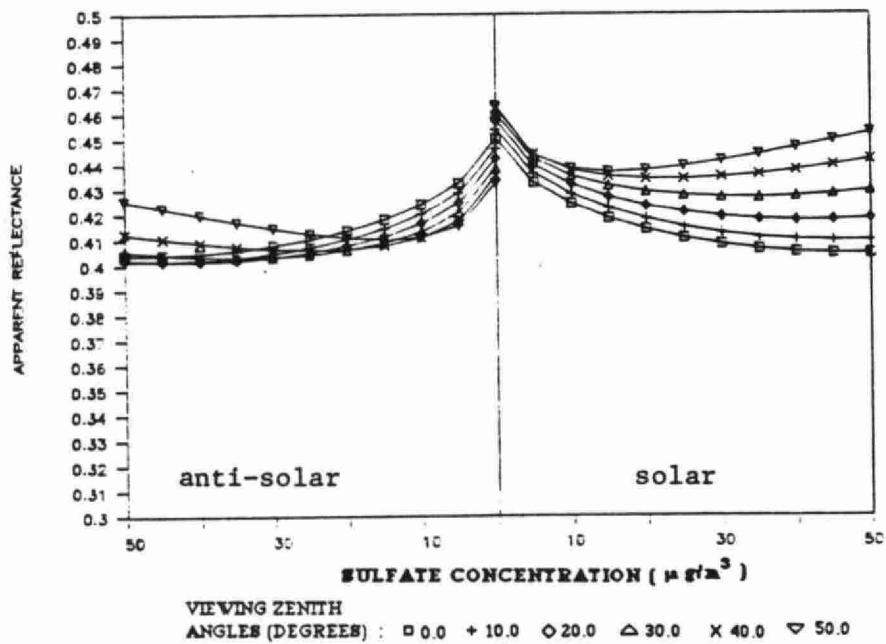


Fig. 3.4.6.1

DIFFERENCE IN APPARENT REFLECTANCE PER -0.1 INCREMENT IN
COSINUS VIEWING ZENITH ANGLE VS SULFATE CONCENTRATION

URBAN VARIANT, SOLAR ZENITH ANGLE = 45.0,
WAVELENGTH = 0.550 MICRONS, RH = 95%, RO = 0.5

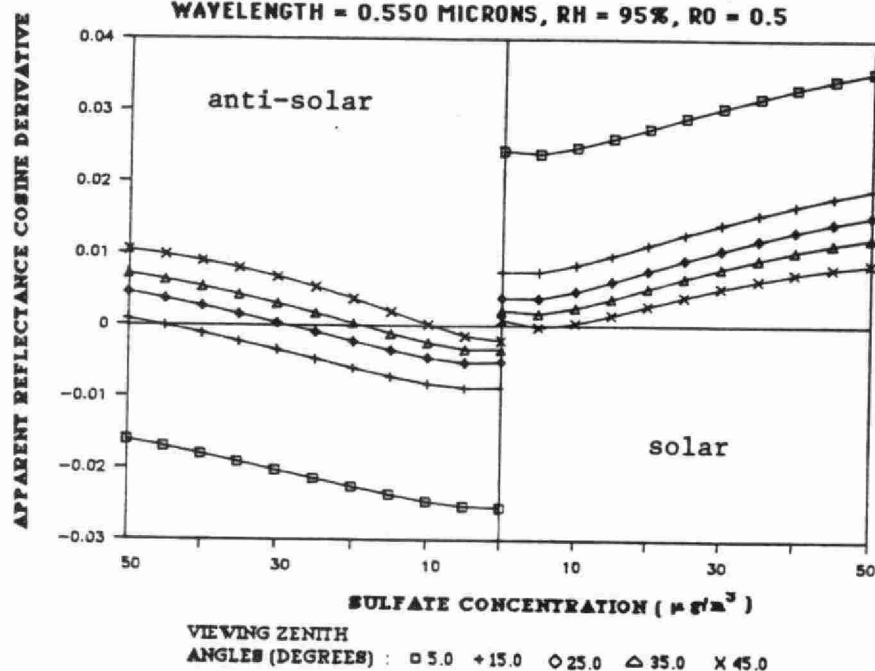
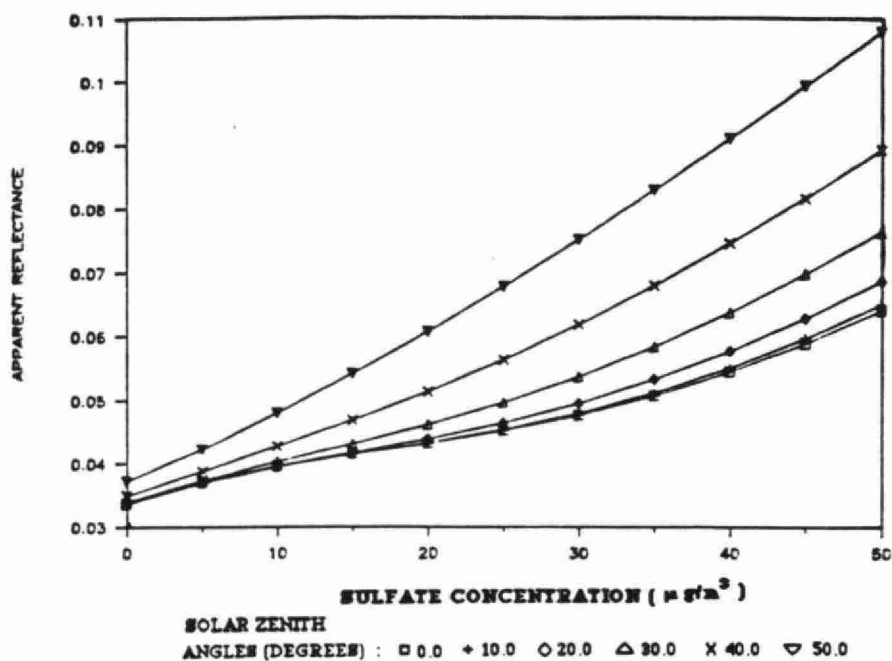


Fig. 3.4.6.2

(b) solar geometry

Given that the apparent reflectance for zero surface reflectance varies approximately as $1/\cos\theta$ at fixed solar zenith angle (θ_s) one can appeal to the principle of reciprocity (Chandrasekhar, 1960) to argue that the apparent reflectance varies approximately as $\mu_s = 1/\cos\theta_s$ at fixed observer's zenith angle. This type of behavior is readily apparent for the zero reflectance case of Figure 3.4.6.3. The same argument of reciprocity can be applied to relate the solar zenith angle dependency to the observer's zenith angle dependency in the case of large surface reflectance (surface albedo = 0.5 in Figure 3.4.6.3).

APPARENT REFLECTANCE AT DIFFERENT SOLAR ZENITH ANGLES
 URBAN VARIANT, VIEWING ZENITH ANGLE = 0.0,
 WAVELENGTH = 0.550 MICRONS, RH = 95%, RO = 0.0



APPARENT REFLECTANCE AT DIFFERENT SOLAR ZENITH ANGLES
 URBAN VARIANT, VIEWING ZENITH ANGLE = 0.0,
 WAVELENGTH = 0.550 MICRONS, RH = 95%, RO = 0.5

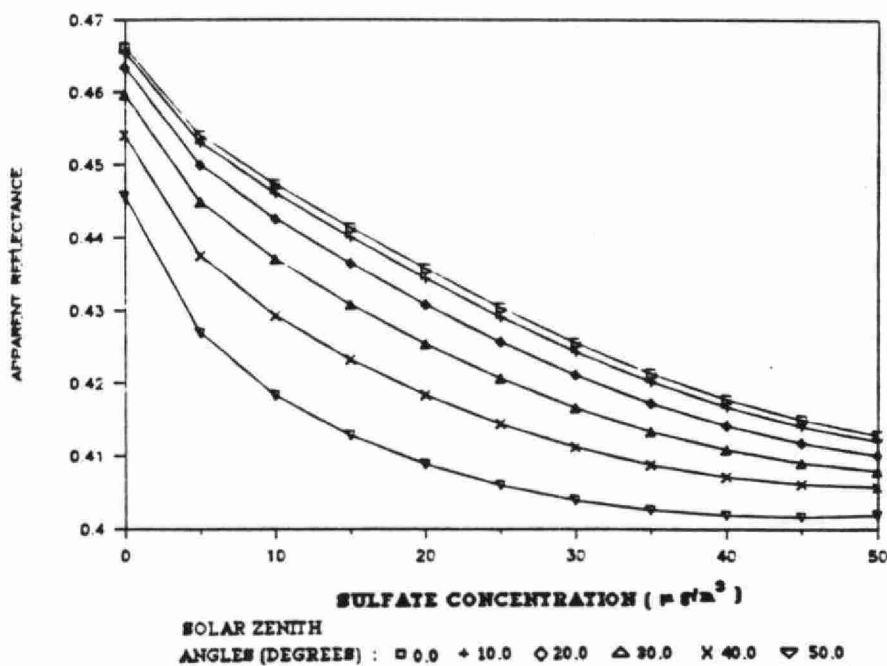


Fig. 3.4.6.3

CHAPTER 4

INVERSION ANALYSIS

The inversion methodology for extracting optical parameters and eventually sulfate concentrations requires that the satellite measured total radiance be converted to an apparent reflectance. This apparent reflectance along with all the operational and auxiliary environmental parameters is then entered into an iterative algorithm whose kernel is the 5S model. In reference to equation (2-10) and (3-1) we can describe the iterative operation as:

$$\tau = f(\rho^*(\tau), \phi, \theta, \theta_0, \lambda, \langle \rho \rangle, \omega_0 \rho_0(\cos \chi)) \quad (4-1a)$$

$$\tau_{aer}^{scat} = \tau(\lambda, \gamma, N(0), H_{aer}, f, \omega_0) - \tau_{aer}^{abs} - \tau_{mol}(\lambda) \quad (4-1b)$$

$$\begin{aligned} SO_4^= &= \Sigma SO_4^= / H_{aer} \\ &= 10^6 \times (\epsilon(\lambda, \gamma, f, \omega_0))^{-1} \tau_{aer}^{scat} / H_{aer} \end{aligned} \quad (4-1c)$$

where $SO_4^=$ is the equivalent sulfate surface density, τ_{aer}^{abs} is the aerosol absorption optical depth and τ_{mol} is the absorption and scattering optical depth for molecules. In equation (4-1b) the total optical depth (τ) is shown explicitly to be a function of a vector of fractional number densities (γ), the total surface number density ($N(0)$), the aerosol scale height H_{aer} , the relative humidity (f) and the single scattering albedo (ω_0). The dependency of the aerosol absorption optical depth (which is the same as the scattering optical depth) has been suppressed. In order to investigate the sensitivity of sulfate extraction from the inversion procedure the differential $dSO_4^=$ will be investigated in terms of those parameters whose uncertainty can cause significant errors in the sulfate concentration calculation. Symbolically one can write:

$$\begin{aligned} dSO_4^= &= \left(\frac{\delta SO_4^=}{\delta \rho^*} \right)_{\rho, \epsilon} \Delta \rho^* + \left(\frac{\delta SO_4^=}{\delta \rho} \right)_{\rho^*, \epsilon} \Delta \rho + \left(\frac{\delta SO_4^=}{\delta \epsilon} \right)_{\rho, \rho^*} \Delta \epsilon \\ \Delta \rho^* &= \left(\frac{\delta \rho^*}{\delta \omega_0} \right)_{\epsilon, \rho} \Delta \omega_0 + \dots \end{aligned} \quad (4-2)$$

where the key parameters of surface albedo, apparent reflectance and sulfate mass scattering efficiency are shown explicitly while those variables considered as noise or of secondary importance are expressed in terms of the contribution to the uncertainty in apparent reflectance (ρ^*). As is the custom, the subscripts of each partial derivative (hereafter termed *error rates*) indicate which parameters are held constant. This list of parameters is, for the sake of simplicity shortened to include only the three key parameters mentioned above. Whether one expresses the error directly in terms of a given parameter of interest or as part of a contribution to $\Delta \rho^*$ is clearly subjective since the latter cases can be equivalently expressed as:

$$\left(\frac{\delta SO_4^=}{\delta \rho^*} \right)_{\rho, \epsilon} \Delta \rho(\Delta \omega_0) = \left(\frac{\delta SO_4^=}{\delta \rho^*} \right)_{\rho, \epsilon} \left(\frac{\delta \rho^*}{\delta \omega_0} \right)_{\rho, \epsilon} \Delta \omega_0 = \left(\frac{\delta SO_4^=}{\delta \omega_0} \right)_{\rho, \epsilon} \Delta \omega_0 \quad (4-3)$$

The three key error rates are evaluated in Section 4.1 below while the separate error contributions ($\Delta\rho^*$, $\Delta\rho$ and $\Delta\epsilon$) are analyzed in Section 4.2.

4.1 Error Rate Calculations ($\delta SO_4 = / \delta X$)

Figure 4.1.1 is a typical calculation of sulfate equivalent surface concentration uncertainty per unit percent uncertainty in the apparent reflectance ($\delta SO_4 / \delta \rho^*$). These set of curves were computed for the urban variant model from the plots of apparent reflectance versus equivalent sulfate concentration shown in Figure 3.4.2.1. The variation in Figure 4.1.1(a) shows clearly why the sulfate error is expected to be smaller at large equivalent sulfate concentrations and small ground surface reflectances (scattering atmosphere). Alternatively Figure 4.1.1(c) illustrates that the error per unit uncertainty in apparent reflectance decreases with decreasing surface concentration when the surface reflectance is large (attenuating atmosphere). This behavior clearly implies one technique for inversion error minimization which involves the choosing of bright targets for low sulfate loading and dark targets for high sulfate loading.

In the case of surface reflectances near the critical reflectance (Figure 4.1.1(b)), one not unexpectedly, finds a large error potential about the sulfate values which display a minima in Figure 3.4.2.1(b). The error rate curves rapidly deteriorate to large negative positive values below and above the asymptote defined by the minimum in Figure 3.4.2.1(b).

Figures 4.1.2 (a), (b) and (c) which were computed from the database used to create Figure 3.4.2.1 show the sulfate equivalent surface concentration deviation per unit increment in sulfate mass scattering efficiency ($\delta SO_4 = / \delta \epsilon$) ρ^* modified by the factor $-\epsilon$, when the uncertainty in mass scattering efficiency is due to an uncertainty in relative humidity. These error rate values were effectively extracted by measuring the distance (ΔSO_4) between relative humidity curves at constant apparent reflectance and dividing by the corresponding change in mass scattering efficiency. Their sign (in the absence of the multiplicative factor $(-\epsilon)$) is always negative since an increase in relative humidity (which perforce implies an increase in scattering) must necessarily be accompanied by a decrease in sulfate concentration if the apparent reflectance is to remain constant.

The employment of the multiplicative factor $(-\epsilon)$ for the error rate was inspired by the results presented in Appendix A.3 where it was shown that the mass scattering efficiency error rate is to the first order given by $-(SO_4 = / \epsilon)$. In the absence of other influences one expects the modified error rate to be equivalent to the sulfate concentration. For small surface reflectances (scattering dominated atmosphere) the actual error rates lies below the $y = x$ line due to second order effects induced by variations in the scattering phase function. If ϵ increases by virtue of an increase in relative humidity the scattering phase function decreases (in the neighbourhood of large scattering angles typical of satellite remote sensing problems) because of the attendant decrease in refractive index and the increase in particle size (see Figure 2.2.2.3 for example). Because of this decrease the required negative offset in sulfate concentration required to maintain ρ^* constant is reduced. This phenomenon becomes less apparent with increasing optical depth since larger order multiple scattering effects tend to obscure the phase function influence.

If the surface reflectance is large (attenuating atmosphere) the phase function effects are less important at small sulfate concentration and the curves all lie extremely close to the $y = x$ line. At larger sulfate concentrations the scattering effects induce a greater scatter in the curves along with a decrease in the absolute magnitude of the slope. At surface reflectances close to the critical reflectance the transition between scattering and attenuating atmospheres cause rapid slope changes.

**SO₄ CONCENTRATION VARIATION FOR 0.01 APPARENT REFLECTANCE
INCREASING AT DIFFERENT RELATIVE HUMIDITY
URBAN VARIANT, WAVELENGTH= 0.550 MICRONS, RO= 0.0,
SOLAR ZENITH ANGLE = 45.0 DEGREES, NADIR VIEWING GEOMETRY**

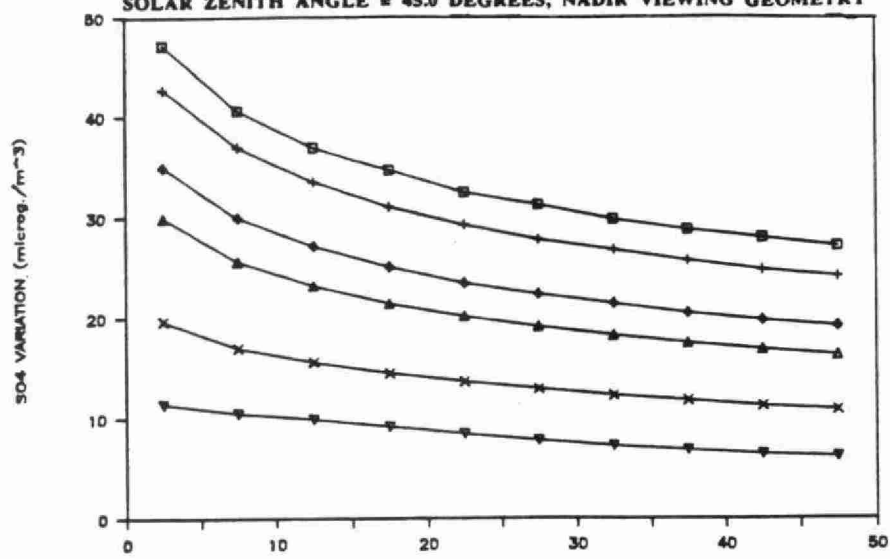


Fig. 4.1.1 a) **SULFATE CONCENTRATION (µg/m³)**
RELATIVE HUMIDITY : □ 0% + 50% ◇ 70% △ 80% × 90% ▽ 95%

**SO₄ CONCENTRATION VARIATION FOR 0.01 APPARENT REFLECTANCE
INCREASING AT DIFFERENT RELATIVE HUMIDITY
URBAN VARIANT, WAVELENGTH= 0.550 MICRONS, RO= 0.2,
SOLAR ZENITH ANGLE = 45.0 DEGREES, NADIR VIEWING GEOMETRY**

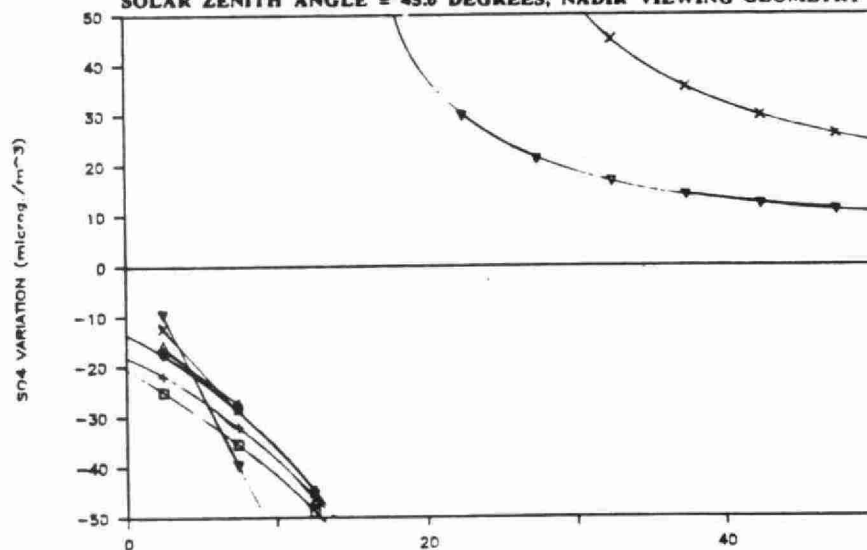
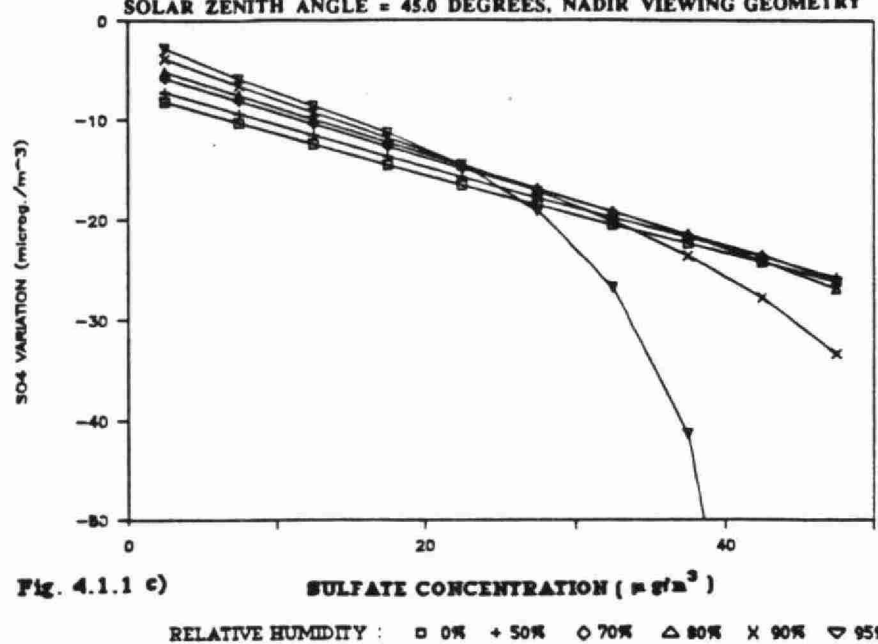
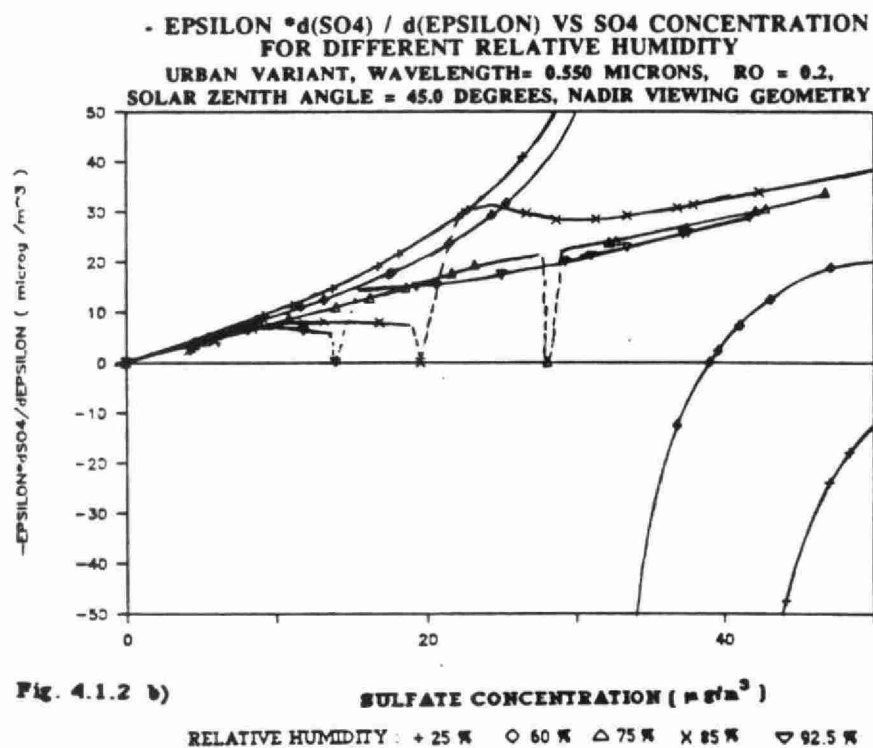
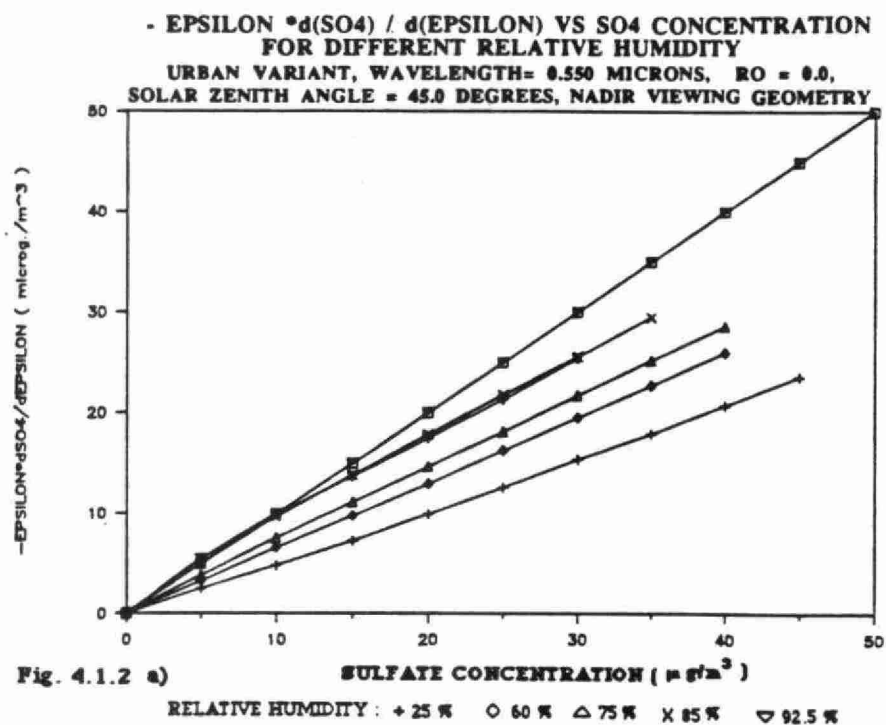


Fig. 4.1.1 b) **SULFATE CONCENTRATION (µg/m³)**
RELATIVE HUMIDITY : □ 0% + 50% ◇ 70% △ 80% × 90% ▽ 95%

**SO₄ CONCENTRATION VARIATION FOR 0.01 APPARENT REFLECTANCE
INCREASING AT DIFFERENT RELATIVE HUMIDITY
URBAN VARIANT, WAVELENGTH= 0.550 MICRONS, RO= 0.5,
SOLAR ZENITH ANGLE = 45.0 DEGREES, NADIR VIEWING GEOMETRY**





• EPSILON $\cdot d(\text{SO}_4) / d(\text{EPSILON})$ VS SO_4 CONCENTRATION
 FOR DIFFERENT RELATIVE HUMIDITY
 URBAN VARIANT, WAVELENGTH = 0.550 MICRONS, $R_0 = 0.5$,
 SOLAR ZENITH ANGLE = 45.0 DEGREES, NADIR VIEWING GEOMETRY

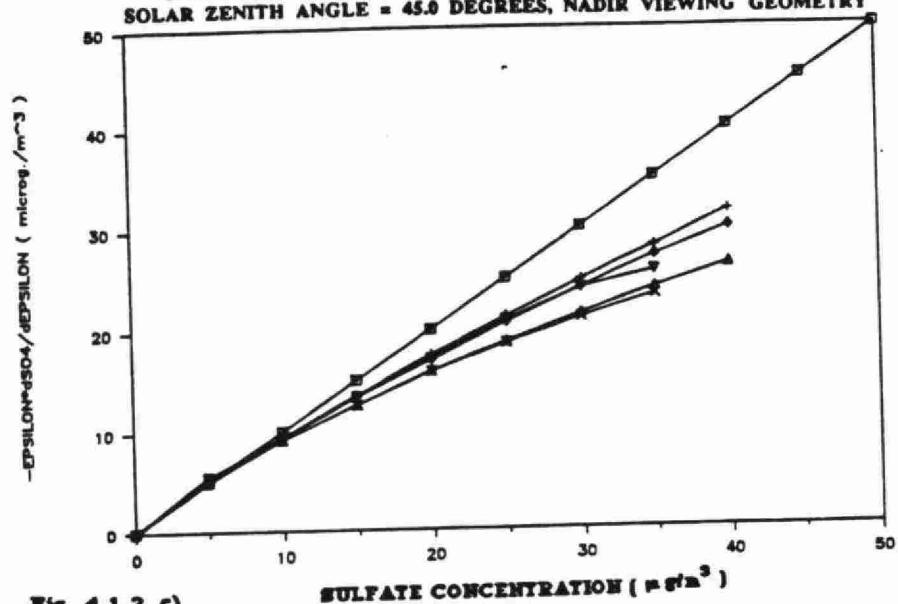


Fig. 4.1.2 c)

RELATIVE HUMIDITY : + 25 % \circ 60 % \triangle 75 % \times 85 % ∇ 92.5 %

The variation between the $y = x$ standard and the other error rate curves may be considered as a range of error rate values whose relevance depends on the inversion methodology and type of uncertainty influencing e . For example if the optical input parameters to the radiative transfer equation are known then in principle the inversion for aerosol optical depth (equation 4-1b) produces negligible error and the uncertainty in the sulfate concentration can be associated with the $y = x$ line. Departures from this somewhat idealistic case include the relative humidity influence discussed above.

The error rates $(\delta SO_4 / \delta \rho)_{p^*, e}$ computed for the same reflectance parameters as Figure 3.4.2.1 are illustrated in Figure 4.1.3 for two different relative humidities. These values which represent the uncertainty in SO_4 per unit percent increment in surface albedo were computed by calculating the SO_4 increment (ΔSO_4) between iso surface reflectance curves for constant values of apparent reflectance.

When the atmosphere is dominated by scattering effects (well below the critical reflectance) an increase in ground reflectance necessitates an offsetting decrease in sulfate concentration (offsetting decrease in atmospheric scattering) if the apparent reflectance is to remain constant. The error rate in this case is accordingly less than zero and as well decreases in absolute magnitude with increasing sulfate concentration as the atmosphere better masks the effects of the surface reflectance increase.

Alternatively if the atmosphere is dominated by attenuation effects (well above the critical reflectance) an increase in surface reflectance necessarily requires an increase in sulfate concentration in order to offset (attenuate) the surface reflectance increase. In this case, then, the error rate is positive and increases with increasing sulfate concentration. The latter effect results because an increase in sulfate represents a gradual change from an attenuation dominated atmosphere to a scattering dominated atmosphere (influence of surface reflectance become increasingly less evident). Accordingly, if one is at a point where attenuation still dominates but where scattering is significant (i.e. large sulfate concentration) the amount of sulfate which must be added to offset a reflectance increase is comparatively larger than that required at low sulfate concentration. Here again a minimization of potential error can in principle be effected by an appropriate selection of dark surfaces for large sulfate loading and bright surfaces for low sulfate loading.

The passage from attenuation to scattering dominated atmosphere is marked by a rapid increase in positive error rate with increasing sulfate concentration if attenuation is dominate and a progressively more negative error rate with decreasing sulfate if scattering is dominate. The two regions can in fact lie on either side of an asymptotic sulfate value depending on the actual surface reflectance and the relative humidity (as is evident in some of the curves of Figure 4.1.3).

4.2 Error contributions (ΔX)

4.2.1 Effects of surface reflectance

A critical requirement for any inversion scheme which attempts to extract an atmospheric parameter from the total measured satellite signal is some apriori knowledge of the contribution due to ground reflectance. In the past this criteria has been surmounted by restricting atmospheric inversion algorithms (or their complement, atmospheric corrections) to clear water regions in the image where the known low reflectance of water contributes relatively little to the total satellite signal (Ahern et al., 1977, Royer et al., 1988b). This oftentimes severe constraint has led researchers to investigate the use of other terrestrial surfaces for which the surface reflectance is small in certain wavelength regions (Kaufman and Sendra, 1988) or for which ground calibrations and/or satellite temporal studies can be used to extract a value of ground reflectance. Another alternative is to view the same pixel in two overlapping images acquired in two different passes. This approach assumes that the aerosol mass loading has not changed substantially between the acquisition time of the two images. The NOAA satellite sensors and in the future SEAWIF's are ideally suited to this purpose since the frequency of consecutive image acquisition is only of the order of an hour.

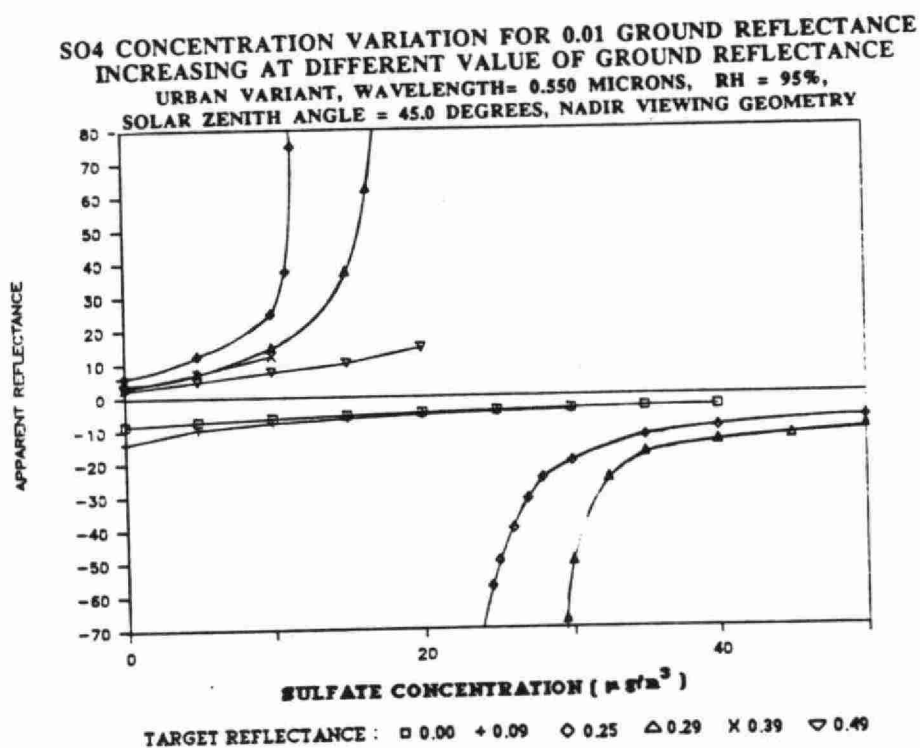
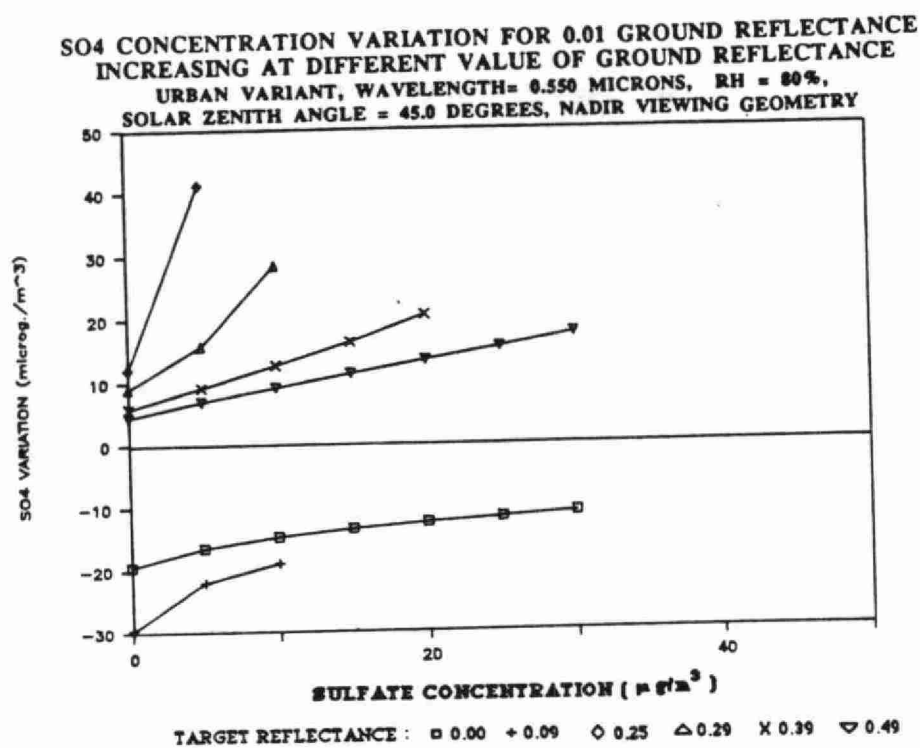


Fig. 4.1.3

With no apriori information on the water quality parameters which characterize the optical turbidity of water one can assume a nominal value of reflectance associated with an uncertainty characteristic of the natural variation of chlorophyll. Employing simulations such as those of O'Neill and Miller (1988) the magnitude of water leaving reflectance (ignoring the Fresnel reflection of skylight and assuming a scene target well removed from the specular sun glitter direction) is of the order of $.008 \pm .005$ in the blue (400 nm), $.009 \pm .003$ in the neighbourhood of 500 nm and $.002 \pm .001$ near 675 nm. These ranges assume that the water can be categorized as being low in inorganic content (case 1 of Morel & Prieur, 1977).

Table 4.2.1.1 indicates the typical means and standard deviations which can be obtained over a variety of surfaces and over an extended time period if one employs atmospherically and radiometrically corrected satellite data to compute surface reflectances. The procedure for extracting such data is distinct from the inversion procedure for obtaining optical depth and sulfate concentrations even though, in principle the same data could be used to do both. The entries of Table 4.2.1.1 thus represent apriori information used to specify the values of the surface reflectance parameter to the radiative transfer calculations employed in the sulfate inversion procedure. The magnitude of the standard deviations reflect to some degree the effects of radiometric uncertainty but are probably more indicative of the reflectance precision which one can hope to achieve given the temporal and spatial variability of natural surfaces across a satellite scene.

In terms of atmospheric remote sensing the lower reflectances of Table 4.2.1.1 such as those of water and forest vegetation in the absorbing spectral region of chlorophyll (MSS band2) are typically optimal for minimizing sulfate inversion errors. In regions where the surface reflectance is large (such as the reflectance peak of vegetation found in MSS bands 3 and 4) the standard deviation is correspondingly large. The inversion error effects of large uncertainties in the surface reflectance depend on the actual surface reflectance of the pixel being evaluated and the average reflectance of surrounding pixels which act as a secondary source of reflected sunlight for atmospheric scattering.

4.2.2 Sulfate Mass Scattering Efficiency

The sulfate mass scattering efficiency is influenced by a number of factors including relative humidity (f), effective particle radius at zero relative humidity ($r_{eff}(0)$) and the relative contribution of sulfates to total aerosol scattering. Symbolically we may write the total error as:

$$d\epsilon = \left(\frac{\partial \epsilon}{\partial f} \right)_{r_{eff}(0), \gamma} \Delta f + \left(\frac{\partial \epsilon}{\partial r_{eff}(0)} \right)_{f, \gamma} \Delta r_{eff}(0) + \left(\frac{\partial \epsilon}{\partial \gamma} \right)_{f, r_{eff}(0)} \Delta \gamma \quad (4-4)$$

where γ represents the fractional number density due to sulfates. The use of this latter parameter is somewhat of a simplification since the variation of ϵ due to variations in the contributions of constituent aerosols is clearly a non trivial phenomenon.

Depending on the apriori information available the above equation can represent a complex variety of sulfate inversion schemes. If one computes the scattering efficiency from first principles as was done in our simulations then the uncertainties in each component represent measurement uncertainties. On the other hand if ground based measurements of $\epsilon(f, r_{eff}(0), \gamma)$ were available in a given scene then the uncertainties are associated with the natural variation of each parameter across the satellite image on which the sulfate inversion is being performed.

Table 4.2.1.1 **Table of measured ground reflectances and their uncertainties (in parenthesis) for a number of surface types derived from Landsat MSS data (from Royer et al. 1988)**

LAND COVER TYPES	MSS 1	MSS2	MSS3	MSS4 MSS ALBEDO	MEAN
Agriculture	0.067 (0.016)	0.065 (0.021)	0.231 (0.036)	0.289 (0.071)	0.175 (0.030)
Forest	0.042 (0.010)	0.031 (0.007)	0.197 (0.027)	0.306 (0.054)	0.163 (0.017)
Urban (high density)	0.092 (0.021)	0.092 (0.019)	0.112 (0.018)	0.117 (0.019)	0.105 (0.018)
Gravel Pits	0.127 (0.026)	0.124 (0.022)	0.136 (0.020)	0.137 (0.001)	0.130 (0.018)
Water	0.010 (0.003)	0.005 (0.002)	0.002 (0.001)	0.001 (0.001)	0.005 (0.001)

(a) Variations in Relative Humidity

The results of both chapters 2 and 3 indicate an evident requirement for apriori information on relative humidity if the inversion methodology depends on a relative humidity model for the calculation of the sulfate mass scattering efficiency. Ideally this information should be extracted from strategically located spectral bands on the same sensor or sensor platform which attempts to measure the sulfate induced signal.

The most promising satellite based method developed to date has been the *split window* technique which employs a differencing algorithm between two or more infrared bands to extract an integrated water content measure (Deschamps et al., 1980). Dalu (1986) reported retrieval accuracies of ± 3 and ± 5 kg/m² for the IRIS (Nimbus 7) spectrometer and AVHRR respectively (.3 and .5 cm equivalent water column).

The form of the water vapour profile with altitude is sufficiently stable that a strong correlation exists between integrated water vapour content and relative humidity at the surface (Hay, 1971). One can accordingly transform satellite derived water content measures into surface relative humidity which in turn can be directly related to the explicitly required parameters employed in the inversion algorithm. For the great lakes region Hay's relation becomes:

$$w = .15 + .0013 f e_s \quad (4-5)$$

where w is the integrated water vapour content in equivalent cm, f is the relative humidity in percent and e_s is the saturation vapour pressure. For a surface temperature of 15°C the error in the computed value of the surface relative humidity (Δf) corresponding to the satellite retrieval error (Δw) is simply:

$$\Delta f = 100\Delta w / 2.39 \quad (4-6)$$

or the order of 10% and 25% for the IRIS and AVHRR sensors respectively.

(b) variations in dry sulfate log normal parameters

In Appendix A.3 it is demonstrated that the aerosol scattering efficiency per unit mass of dry sulfate does not vary greatly over a substantial range of the dry log normal geometric mean radius and the log normal geometric standard deviation ($r_N(0)$ and σ defined in Appendix A.2 and Table 2.1.1.1).

This phenomenon which results because aerosol scattering is predominantly volume or mass dependent in the fine particle (sulfate) range implies that the error analysis arguments developed above for fixed $r_N(0)$ and σ and referenced to dry sulfate mass are applicable to log normal parameter values larger than the nominal values given in Table 2.1.1.1 (.12 and 1.24 for $r_N(0)$ and σ respectively). Accordingly (for identical ambient conditions) a unit volume of large sulfate particles produces approximately equivalent optical/radiative transfer effects as a unit volume of small but more numerous sulfates if their mass is identical. This assumes that changes in directional scattering properties (phase function) are second order with respect to their effect on the exoatmospheric reflectance (refer to the discussion in Appendix A.3). The range of particle size over which the approximate constancy of $\epsilon(\lambda)$ holds is a function of relative humidity and wavelength. However in coarse terms one may vary σ between 1.2 and 1.8 for $r_N(0) = .12$ and between 1.2 and 1.4 for $r_N(0) = .24$ without affecting a change of greater than 20 % between any of the computed values (relative humidity $\leq 90\%$, wavelength = 0.55 μm).

Outside of this region or for more precise calculations one may employ all the error rate versus sulfate concentration curves reported above by utilizing an approximate normalizing factor. The method of computing this normalizing factor is demonstrated in Appendix A.3. Generally a decrease in mass scattering efficiency implies a proportionate increase in the magnitude of the computed error rate.

(c) Contributions due to other fine particle mode constituents

The discussion presented in Section 2.2.3 indicated that the most likely reason for the rather large discrepancy of ϵ values derived from ground truth measurements was due to the covariance of other fine particle constituents with sulfate. Comparisons of measurements made by different authors show a strong discrepancy which would appear to be due to the local nature of the fine particle aerosol mode. For the most part however the measurements made by any given author almost invariably indicate a strong aerosol scattering coefficient to sulfate mass correlation and hence a correspondingly small uncertainty associated with the value of ϵ (typically $\sim 1 \text{ m}^2/\text{g}$).

4.2.3 Influence of Optical Absorption (Single Scattering Albedo)

Kaufman (1987) developed a method for measuring the average aerosol atmospheric single scattering albedo (ω_0) based on a multi image determination of the critical surface reflectance (c.f. Sections 3.4.2 and 3.4.3). His technique exploits the presence of optical depth singularities such as those of Figure 3.4.2.2 by employing the corresponding critical reflectance as an indicator of the single scattering albedo. Since the critical surface reflectance is independent of optical depth its variation is strongly correlated with atmospheric absorption and accordingly facilitates the development of an inversion methodology for the extracting of ω_0 . The weakness of the technique resides in its dependence on invariant values of ω_0 and surface albedo over two or more images acquired at different dates. Given two images for which ω_0 is approximately constant Kaufman reports a computed error of less than 10% for reasonably typical environmental and operational parameters (solar zenith angle = 45 degrees, refractive index = 1.43 - .0035i, log linear size distribution, wavelength = 610 nm) and associated errors.

By the same token localized ground measurements of carbonaceous soot absorption on the filter of a high volume sampler (such as those used by the Ontario Ministry of the Environment for their pollution index) may be employed to compute a ground level value of absorption coefficient (Rosen and Novakov, 1983) from which a value of ω_0 may be extracted if scattering or extinction coefficient measurement are available. Alternatively, if estimates of the relative humidity and the number density (or mass) ratio of soot particles to sulfates are available a value of the aerosol single scattering albedo can be extracted (c.f. Appendix A.3 (b)). The tacit assumption of this approach, that externally mixed (independent) carbonaceous soot particles play a dominant role in atmospheric absorption, is strongly supported in the literature (Bergstrom, 1973; Rosen et al., 1978; Japar et al., 1986).

The accuracy of the absorbing and scattering coefficient measurements which one can infer from the literature to be of the order of 10-20 % (Japar et al., 1986; Ruby and Waggoner, 1981) implies a similar uncertainty in ω_0 . A vertical profile of ω_0 must then be assumed or measured in order to establish an average atmospheric value (the simplest approach is to assume that the mixing ratio of aerosol scattering to absorbing particles is effectively independent of altitude).

If only measures of soot absorption are available one can still infer an average atmospheric value of ω_0 given some estimate of the scale height of the soot particles along with a ground based measure of total optical depth. In the absence of any absorption information whatsoever one can set coarse limits of $.8 \pm .2$ in an urban atmosphere and $.9 \pm .1$ in a rural atmosphere for visible wavelengths of radiation (Ackerman and Toon, 1981, Table 4.2.3.1).

The computations of Kaufman (1987) indicate apparent reflectance uncertainties which range from .002-.005 per .01 in single scattering albedo increment at large values of surface reflectance (.4) down to values less than .001 per .01 increment in ω_0 at zero surface reflectance. These calculations were performed at the solar zenith angle, refractive index and wavelength parameters given above over a aerosol scattering optical depth variation between 0 and .6. This variation in aerosol scattering optical depth roughly corresponds to our standard 0 - 50 $\mu\text{g}/\text{m}^3$ equivalent sulfate surface concentration variation at 90 % relative humidity at an aerosol scale height of 1 km. In comparison the difference between the continental standard and urban standard results for which the single scattering albedo goes through a significant change in ω_0 (approximately .164 at 90% relative humidity and 0.633 μm wavelength) indicated uncertainty magnitudes of less than .0005 and .004 respectively for 0 and .4 surface reflectance across an ω_0 increment of .01.

Table 4.2.3.1
Single scattering albedo as a function of wavelength, relative humidity and aerosol model

	Relative humidity					
	0 %	50 %	70 %	80 %	90 %	95 %
0.55 micrometers						
<u>Component aerosols</u>						
soot	0,436	0,436	0,436	0,436	0,436	0,436
dust like	0,728	0,728	0,728	0,728	0,728	0,728
water sol.	0,965	0,974	0,984	0,988	0,994	0,998
<u>Optical averages</u>						
urban/industrial standard	0,725	0,752	0,794	0,819	0,871	0,921
continental standard	0,898	0,914	0,936	0,946	0,966	0,981
3.75 micrometers						
<u>Component aerosols</u>						
soot	0,015	0,015	0,015	0,015	0,015	0,015
dust like	0,880	0,880	0,880	0,880	0,880	0,880
water sol.	0,258	0,289	0,346	0,383	0,475	0,594
<u>Optical averages</u>						
urban/industrial standard	0,193	0,194	0,199	0,204	0,224	0,263
continental standard	0,834	0,833	0,829	0,826	0,819	0,809

scat effec = change in the total volume scat coef per unit change in the mass of dry sulfate

cross sections obtained by multiplying Mie efficiencies (Q) by πr^2 where r is the effective mean surface radius of a log normal distribution (see below)

Optical average computed as the weighted mean of scattering cross sections normalized to the weighted mean of total cross sections (Appendix B). The weights are computed as fractional number densities (Table 4)

Model	Dust like	Soot	Water soluble (sulfate)					
			0 %	50 %	70 %	80 %	90 %	95 %
r2 (microm.)	1,098704	0,125683	0,125683	0,134909	0,150531	0,160488	0,185800	0,222392

Cross sections (sigma) [units of 10^{-10} cm^2]

0.55 micrometers

sigma (scat)	625,871	5,22423	5,01703	5,9871	8,06198	9,72656	15,3164	27,542
sigma (abs)	233,511	6,7545	0,18244	0,15912	0,12833	0,113436	0,085325	0,060371

3.75 micrometers

sigma (scat)	622,9660	0,014128	0,003305	0,004752	0,008482	0,012009	0,027173	0,076048
sigma (abs)	85,34780	0,944820	0,009523	0,011668	0,016047	0,019380	0,030049	0,052040

Table 4.2.3.2 below summarizes calculations of the error rate $(\delta\rho^* / \delta\omega_o)_{r.h.,\rho}$ performed for nadir geometry and a wavelength of .55 μm . The calculations were performed using the data points plotted in Figure 3.4.1.3 (along with a second set for 90% relative humidity). The significantly greater values of the error rate at the larger value of surface reflectance (0.4) illustrate well the inherent difference between the effects of soot particles at small and large surface reflectances (c.f. Sections 3.4.1 and 3.4.4).

Table 4.2.3.2 Error rate $(\delta\rho^* / \delta\omega_o)_{r.h.,\rho}$ for nadir geometry, 45 degrees solar zenith angle and 0.55 μm wavelength (units of percentage change in ρ^* per .01 increment in ω_o)

Surf. ref.	0		0.5	
Rel. hum.	70	90	70	90
Sulfate concentration [$\mu\text{g}/\text{m}^3$]				
0	0.0	0.0	0.0	0.0
25	-.011	-.028	0.20	0.34
50	-.024	-.039	0.38	0.63

4.2.4 Noise and Radiometric resolution

Table 4.2.4.1 is a compilation of radiometric reflectance errors as a function of wavelength band for the principal satellite sensors being investigated. The noise equivalent reflectances (NER) represent actual noise specifications for the given sensor which are either evaluated in pre launch calibrations or during the operational lifetime through the utilization of standard sources and/or homogeneous ground targets. The quantization error reflectance (QER) is simply the quantization resolution of the sensors translated into an apparent reflectance error.

Since the satellite sensor specifications are typically given in terms of radiance or digital levels one employs the apparent reflectance relation:

$$\rho^* = \pi L / \mu_s E_s \quad (4-7)$$

to write:

$$\Delta\rho^* = \pi \Delta L / \mu_s E_s \quad (4-8)$$

where ΔL is an error specification in terms of radiance, μ_s is the cosine of the solar zenith angle, and E_s is the exoatmospheric solar irradiance. The parameter μ_s was wherever possible taken to be the nominal value of 0.5 (solar zenith angle of 60 degrees) in order to yield a maximum noise over a realistic range of solar zenith angles. The solar irradiance was either extracted from the specifications for the sensor of interest or when this was not available computed from standard tables (Wolfe & Zissis, 1978) assuming a square spectral response function.

Often the noise figure for a particular sensor is given in terms of signal to noise ratio (SNR) at a particular reflectance (ρ^*). In this case the NER can be obtained by ratioing the above two equations:

Table 4.2.4.1 Noise Equivalent Reflectances (NER) and Quantization Error Reflectances (QER)

Satellite	Sensor	Band	Band width [micrometers]	NER	Bits/ pixel	QER	Ref.	Total error	Notes
Landsat-5	TM	1	.45 - .52	0,0065	8	0,0011	1,8	0,0066 €	
		2	.52 - .60	0,0057	8	0,0023		0,0062	
		3	.63 - .69	0,0057	8	0,0019		0,0058	
		4	.76 - .90	0,0033	8	0,0028		0,0043	
		5	1.55 - 1.75	0,0168	8	0,0018		0,0169	
		7	2.08 - 2.35	0,02	8	0,0028		0,0202	
	MSS	1	.5 - .6	0,0057	7	0,0036	1,8	0,0068	
		2	.6 - .7	0,0057	7	0,0029		0,0064	
		3	.7 - .8	0,0065	7	0,0033		0,0073	
		4	.8 - 1.1	0,007	7	0,0041		0,0081	
	SPOT	HRV	XS1	.50 - .59	0,0038	8	2,9	0,0044 *,**	
			XS2	.61 - .69	0,0056	8		0,0061	
			XS3	.79 - .90	0,0031	8		0,0047	
NOAA	AVHRR (9,10,11)	1	.58 - .68	0,0017	10	0,00058	3	0,0018 *,\$	
		2	.715 - .982	0,0017	10	0,00058		0,0018	
METEOSAT			.4 - 1.1	0,0013	6	0,0023	4,7	0,0027 *	
GOES	VAS/VISSER		.54 - .75	NA	6	0,0025	4,6	0,0018 €,**	
Landsat-6	SEAWIFS	1	.443 - .453	0,00049	10	0,00023	5	0,00054 **,*,+	
		2	.490 - .510	0,00035	10	0,00017		0,00039	
		3	.555 - .575	0,00031	10	0,00016		0,00035	
		4	.655 - .675	0,00023	10	0,000092		0,00025	
		5	.745 - .785	0,00019	10	0,000081		0,00039	
		6	.843 - .887	0,00016	10	0,000069		0,00017	

References

1. Slater (1980)

2. Colloque SPOT (1988)

3. Lauritson et al. (1979)

4. Melila & Anderson (1986)

5. Baker et al. (1987)

6. Frouin & Gauthier (1987)

7. Dedieu (1983)

8. Royer et al. (1987)

9. Royer et al (1988)

Notes

€ calculated for a maximum digital level of 64 (radiance or reflectance varies as the square of the digital level)

* NER = quadrature sum of 60 deg. sol. zen. angle along column and cross diode noise in ref. 2

** NER = reflectance / SNR (reflectance either quoted or computed from nominal radiance and E(0) where E(0) = the exoatmospheric solar irradiance

\$ nominal values, slight differences exist between each NOAA sensor

QER = reflectance error given an error of one quantization level = $\pi \cdot [\text{radiance p digital level}] / [\cos(\text{SZA}) \cdot E(0) \cdot \text{SQRT}(3)]$

€ Total error = $\text{SQRT}(\text{NER}^2 + \text{QER}^2)$

** solar zenith angle = 60 degrees

+ Launch scheduled for 1990, values shown are expected specifications

$$\Delta\rho^* = \rho^* / \text{SNR} \quad (4-9)$$

The radiometric resolution uncertainty (QER) represents a band of values encompassed by ± 1 about any digital level. Accordingly, if the sensor is characterized by "n" bits per pixel, and radiances L_{\min} and L_{\max} corresponding to zero and the maximum number of digital levels respectively, the quantization error radiance is given by:

$$\Delta L^2 = [(L_{\max} - L_{\min}) (1/2^n)]^2 / 3 \quad (4-10)$$

where the divisor 3 results from a computation of the root mean square value of a pillbox probability encompassed by the digital level limits of -1 and 1. After conversion to reflectance the two contributions to the degradation of radiometric resolution are combined according to:

$$\Delta\rho^* = [\Delta\rho^*(\text{NER})^2 + \Delta\rho^*(\text{QER})^2]^{1/2} \quad (4-11)$$

where one assumes that the two sources of noise are independent.

The NER and QER values of Table 4.2.4.1 computed for SEAWIFS were deduced from the nominal values detailed in Table A-2 of Baker et al. (1987). L_{\max} in this case was assumed to be the saturation radiances while L_{\min} was taken to be approximately zero. It is worth noting that the SEAWIFS target radiometric parameters are at least a factor of two better than any of the other reflectance error values given in Table 4.2.4.1. In general the current generation of 7 and 8 bit sensors are characterized by a NER of the order of half a percent while the 10 bit NOAA sensors are down in the .2 % range. In all cases the QER values are commensurate with NER tabulations.

4.2.5 Aggregate aerosol model (discrimination of component aerosol contributions)

One of the most critical elements in the development of an inversion methodology specific to sulfates is clearly how to distinguish the radiative transfer effects of sulfate from those of other aerosol contributors. In principle this can be achieved given a sufficient number of spectral bands and a distinct difference between the spectral behavior of the major optical contributors.

The most easily accomplished discrimination is effected between the dust like and sulfate components. Figure 4.2.5 shows some calculations of apparent reflectance as a function of wavelength for two different values of total aerosol content (defined in terms of the total aerosol optical depth at 0.55 μm), a relative humidity of 80% and at zero surface reflectance. In order to better isolate the relative influence of dust and sulfate particles the separate curves have been calculated for pure samples of each type of particle (in the nomenclature of Table 2.1.3.1 two externally mixed aggregate aerosol models were defined with (i) $\gamma_1(\text{SO}_4) = 1$, $\gamma_2(\text{dust}) = 0$ and (ii) $\gamma_1 = 1$, $\gamma_2 = 0$). As well the pure Rayleigh contribution (zero aerosol optical depth) has been subtracted in order to enhance the contrast between the two curves.

As the wavelength increases from the visible spectral region to the near IR (.4 - 3.75 μm) one can characterize a transition of sulfate particles from optically small ($1 < 2\pi r_{\text{eff}} / \lambda < 10$) to optically very small ($2\pi r_{\text{eff}} / \lambda < 1$) and dust like particles from optically large ($2\pi r_{\text{eff}} / \lambda > 10$) to optically small. The optical effects associated with these transitions are such that the sulfate volume scattering coefficient become increasingly less important with increasing wavelength while that of the dust like particles remains relatively unaffected. In the range 0.4 to 0.86 μm the sulfate extinction which is approximately the same as the scattering optical depth decays roughly as $\lambda^{-2.4}$ while at longer wavelengths the extinction decay is even more rapid with Rayleigh absorption playing a progressively more important role (see Section 2.2.2 for a discussion of Rayleigh absorption).

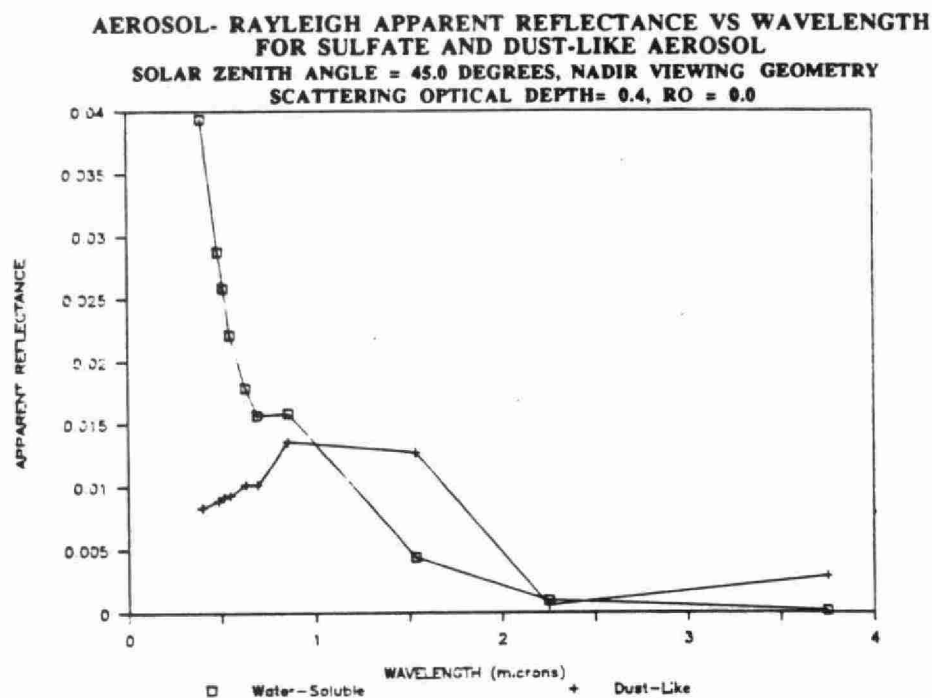
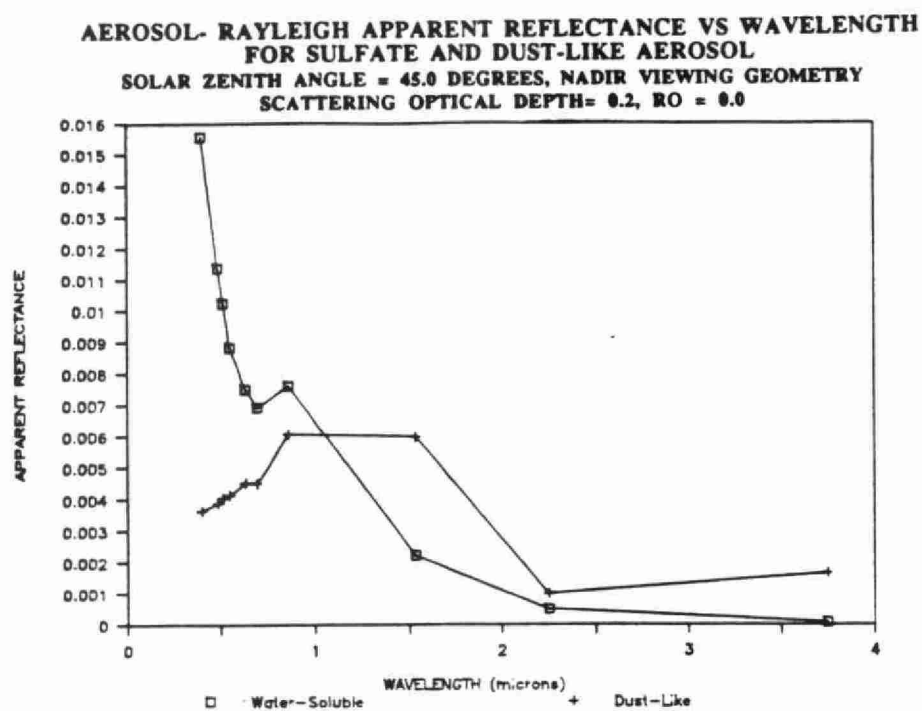


Fig. 4.2.5

The net effect of these spectrally different optical properties is to produce a dominance of sulfate scattering in the visible and a dominance of dust scattering in the near IR. The crossover point does not occur at $0.55\ \mu\text{m}$ (i.e. where optical depths are equal) but rather at a larger wavelength due to the fact that the optically large dust like particles suffer from weak backscattering properties (comparatively small phase function values outside of the anisotropic cones at 0 and 180 degrees scattering angle). A sudden drop in the dust like backscatter phase function for the $2.25\ \mu\text{m}$ and $3.75\ \mu\text{m}$ wavelengths produces the comparatively low reflectance values seen in Figure 4.2.5. The phase function decrease results from a substantial decrease in the real part of the refractive index (see Table 2.2.1.2 for example).

Spectral data can accordingly be employed to distinguish dust like (or even cloud) particles from sulfate particles without any apriori information on the content of the aerosol cloud in the field of view. To avoid cumbersome multiparameter inversion schemes the problem of properly interpreting spectral data should be approached from a semi-empirical correlation search between the spectral curve slopes observed in Figure 4.2.5 and the contribution of the major aerosol optical components. If this procedure is found to be reasonably independent of optical depth (aerosol mass loading) one can develop an inversion methodology for extracting particle size information and sulfate concentration extraction in two independent steps.

The concentration of carbonaceous soot relative to the concentration of sulfates can be estimated if an independent measure of the aerosol single scattering albedo can be computed from the satellite data (c.f. Appendix A.3). This could be computed using Kaufman's technique although the requirements of this approach appear to be rather stringent (c.f. Section 4.2.3). An alternative approach would be to exploit the comparatively high sensitivity of the apparent reflectance to soot concentration over high reflectance surfaces (c.f. Section 3.4.1). In this way highly reflecting pixels in a given scene would be the main source of soot concentration information while low reflectance pixels would be used as the primary source of information for sulfate concentration. The employment of highly reflecting surfaces necessarily implies a calibration program to deduce the intrinsic reflectance of the targeted surface or the utilization of multi look angles afforded by overlapping images.

It is difficult to imagine a satellite based inversion algorithm, even a multispectral inversion algorithm capable of detecting realistic concentrations of secondary scattering particles (such as ammonium nitrate) based on broadband responses to atmospheric scattering. This lack of sensitivity results because of the lack of difference between the intrinsic optical properties of the secondary scatterers and because scattering is largely a volumetric effect independent of the chemical nature of the scattering particle (see Appendix A.3). It is, on the other hand, entirely feasible to envisage a high spectral resolution imaging system (such as the EOS MODIS and HIRIS sensors) which detects anthropogenically generated gases by differential absorption techniques. In this case the strategic placement of high resolution spectral bands about one or more absorption features unique to a given molecular species provides a highly discriminating means of trace gas detection. Ground based instruments of this nature have been developed for the detection of ozone, nitrogen dioxide and sulfur dioxide (Kerr et al., 1980; Syed & Harrison, 1980; Kerr & Evans, 1980).

4.2.6 Radiative transfer model

(a) analytical approximations

The results presented in Appendix B (see also Section 3.2) indicate that at near nadir directions the error expected in employing the 5S analytical approximate is of the order of .005 in apparent reflectance for solar zenith angles less than 60 degrees, wavelengths between $0.4\ \mu\text{m}$ and $1.6\ \mu\text{m}$, surface albedos between 0 and 0.4 and an aerosol optical depth in the neighbourhood of 0.5. Assuming a reasonably linear correlation between apparent reflectance and optical depth this corresponds to a maximum error of the order of .01 at an aerosol optical depth of unity or hence in conditions roughly equivalent to a wet atmosphere of 95% relative humidity with an equivalent sulfate surface density of $50\ \mu\text{g}/\text{m}^3$ (c.f. Table 2.1.4.3).

In off nadir directions the apparent reflectance error derived in Appendix B increases rapidly with the cosine of the observers zenith angle to values as large as .05 at 60 degrees (solar zenith angle less than 45 degrees, wavelength of

.55 μm) or hence roughly .1 for the extreme case discussed immediately above. This error is more a function of the analytical approximations employed in the 5S model than of the problems associated with vertical inhomogeneity in the atmosphere (c.f. Section 3.2 above and (b) below).

(b) vertical inhomogeneity

Comparisons of the satellite level signal computed for a multilayer inhomogeneous atmosphere and a single layer model (c.f. Section 3.3 and Appendix B) indicated that the apparent reflectance error associated with replacing the vertically detailed atmosphere by an equivalent average atmosphere were small. At near nadir directions the error was of the same order as 5S while for off nadir directions the error was significantly smaller than that of 5S (less than .005 for solar zenith angles up to 60 degrees and a wavelength of 0.55 μm).

4.2.7 Other Sources of Error

Sections 4.2.1 to 4.2.6 deal with what we consider to be the major sources of error in a sulfate inversion methodology for which different levels of apriori information can be exploited. Other sources of error which are typically second order in magnitude exist and can contribute to the error budget. These include polarization contributions from the atmosphere and the sensor optics, uncertainty in Rayleigh (molecular) scattering parameterization and variations associated with changes in surface temperature and pressure (Penndorf, 1957; Young, 1981), variations in ozone optical depth (O'Neill, 1982), uncertainties associated with the parameterization of water vapour absorption in the visible continuum (Tomasi, 1979) and nitrogen dioxide in the blue spectral region (O'Neill, 1982) and non Lambertian surface reflectance effects.

4.3 Cumulative sulfate Errors (ΔSO_4)

Table 4.3.1 lists typical input parameter error values required in order to achieve a precision of $\pm 1.6 \mu\text{g}/\text{m}^3$ per input parameter in the extraction of sulfate concentration. The choice of $1.6 \mu\text{g}/\text{m}^3$ is simply a figure of merit which is indicative of the average precision which should be attained if a total precision of $\pm 5 \mu\text{g}/\text{m}^3$ is targeted in the presence of 10 independent and equal errors ($[10 \times 1.6^2]^{(1/2)} \sim 5 \mu\text{g}/\text{m}^3$).

The three sets of entries defined under the heading scattering efficiencies refer to the precision required in the relative humidity, the effective radius and the sulfate fractional number density (as per Section 4.2.2) for a sulfate precision per component of $1.6 \mu\text{g}/\text{m}^3$. The manner in which one interprets this required precision is again a function of the apriori information available for determining the mass scattering efficiency. As stated in Section 4.2.2 two pertinent examples include (a) the scenario where the mass scattering efficiency is calculated from first principles and the dependent parameter uncertainties (in f , $r_{\text{eff}}(0)$ and γ) are measurement errors or (b) measurements of $\epsilon(\lambda)$ are available in the image and the dependent parameter uncertainties represent natural variations between the ground points. In any case, as shown in Appendix A.3, the mass scattering efficiency error rate from which the precision values were determined is always of the order of $-\text{SO}_4 = \epsilon(\lambda)$.

At larger relative humidities (e.g. 90 % in Table 4.3.1) the required precision in relative humidity ($\sim 1\%$) is unattainable by current methods applied to existing satellite sensors (see Section 4.2.2 above). One must either relax the precision requirements on this variable or appeal to other measuring techniques. Ground based measurements certainly achieve this order of accuracy and could be employed either to calibrate existing satellite estimates of water content or directly from a surface mapping tied to the measured values. The accuracy performance, in particular as related to the spatial surface gradient of relative humidity was not investigated.

In the near future the space station sensor MODIS (Esaia, 1986) will incorporate spectral bands specifically for measurements of water content by means of differential absorption. In addition the instrument package will include an active laser system (LASA) whose capabilities include the measurement of water vapour profiles by means of differential absorption.

Table 4.3.1 Input parameter precision required to achieve a sulfate concentration precision of $1.6 \mu\text{g}/\text{m}^3$ per parameter

Atmospheric /geometric input perms.	Urban variant model							
solar zen. ang. (deg.)	45	45	45	45	45	45	45	45
obser. zen. ang. (deg.)	0	0	0	0	0	0	0	0
obser. azi. ang. (deg.)	0	0	0	0	0	0	0	0
surface ref.	0	0	0	0	.5	.5	.5	.5
rel. humidity	70	90	70	90	70	90	70	90
wavelength (um)	.55	.55	.55	.55	.55	.55	.55	.55
sulfate conc ($\mu\text{g}/\text{m}^3$)	25	25	50	50	25	25	50	50
scale height (km)	1	1	1	1	1	1	1	1
required input parameter precision								
scattering efficiency								
(a) rel. humidity	3.6	0.5	1.9	.22	4.6	.40	1.8	.17
(b) effective rad. (um)	.06	.04	.03	.02	.05	.05	.03	.03
(c) SO ₄ frac. * density	0.2	0.2	.08	0.1	0.1	0.3	.08	0.2
surface ref.	.001	.002	.001	.003	.001	.001	.001	.0005
sing. scat. albedo	.06	.05	.04	.04	.005	.003	.002	.0007
noise reflectance	.0007	.001	.0008	.002	.001	.001	.0006	.0004
SO ₄ frac. * density	.07	.06	.06	.05	n/a	n/a	n/a	n/a
scale height (km)	.06	.06	.03	.03	.06	.06	.03	.03

Notes on parameter
precision

scattering efficiency

(a) rel. humidity	computed from Figure 4.1.2 * $d(\epsilon)/df$ computed from
(b) effective rad.	computed from Figure 4.1.2 and Figure A.3.1
(c) SO ₄ frac. * density	computed from Figure 4.1.2 * $d(\epsilon)/d(\gamma)$ computed from Table 2.1.4.3 (urban standard minus cont. standard) and ϵ values (needed to denormalize Figure 4.1.2) from Figure 4.1.3
surface ref.	computed from Figure 4.1.3
sing. scat. albedo	computed from Figures 3.4.1.1, 3.4.1.2, 4.1.1, and Table 4.1.1
noise reflectance	computed from Figure 4.1.1
sulfate frac. * density	computed using Figure 4.2.5 (difference between pure sulfate dust like converted to an approximate value for $d(\text{app. ref.})/d(\text{sulfate frac.})$ and Figure 4.1.1)
scale height (km)	using equation (4-1c)

The precision values listed for the dry effective radius were obtained by computing a value of $\delta\epsilon/\delta r_{\text{eff}}(0)$ from the weak slopes observable in Figure A.3.1 (approximately 1.1 and 2.2 per $.1 \mu\text{m}$ increment in effective radius for 70 and 90 % relative humidity respectively). The computed values are within the naturally occurring variation about the mean reported by Young et al. (1988) and Leaitch and Isaac (1988) (note that one must convert their geometric mean radii to values of effective radii using the relation given in Appendix A.3).

The third source of error in the mass scattering efficiency relates to the contribution of other fine particle constituents to the total aerosol scattering. The values shown in the table were computed from the differences in the urban and continental aggregate aerosol models (Table 2.1.4.3). As pointed out in Section 4.2.2 (c), this source of error alone induces variations in the mass scattering efficiency which are significant. The implication of these findings is that a working value of this parameter must be measured or inferred on a regional scale.

For the conditions defined in Table 4.3.1 ground surface reflectances need to be known to an accuracy of about .001. The surface reflectance uncertainties tabulated in Table 4.2.1.1 indicate that this level of accuracy is only achievable over water surfaces in the visible wavelength region. The use of other surfaces is not excluded but would require a dedicated calibration program to reduce the typical error levels associated with remotely sensed surface reflectance. The most promising surface other than water is vegetation in the chlorophyll absorption wavelength band centered at about $.65 \mu\text{m}$. Table 4.3.1 excludes any calculations of errors near the critical surface reflectance since the results of Section 4.1 demonstrate clearly that the associated inversion errors would be prohibitive.

For small surface reflectances the addition of soot particles to a relatively pure sulfate mixture has minimal effect on the computed apparent reflectance (c.f. Sections 3.4.1 and 4.2.3). Accordingly the required single scattering albedo accuracy in Table 4.3.1 is achievable by a few well placed ground measurements (for example). For large surface reflectances, however, the apparent reflectance is strongly dependent on changes in soot concentration and the required accuracy is prohibitive (better than .01). This dependency can however be turned to advantage by developing reflectance inversion techniques for extracting soot indicators over highly reflecting surfaces while emphasizing sulfate inversion over low reflecting surfaces.

In the absence of a single scattering albedo estimate an inversion applied as per equation 4-1 yields a scattering optical depth which is overestimated but which, at least for large surface reflectances, will be an approximation to the total optical depth. Accordingly the nominal sulfate mass computed using equation 4-1c is actually a value related to the combined concentration of soot and sulfates.

The noise and radiometric resolution requirements of Table 4.3.1 are only achieved by the 10 bit NOAA and SEAWIF's sensors and the 6 bit METEOSAT and GOES sensors in terms of the specifications presented in Table 4.2.4.1. The rather coarse radiometric resolution of the GOES and METEOSAT sensors is in fact well suited to sulfate detection levels since the range of these sensors is adapted to the low light signals associated with atmospheric phenomena. These sensors are however constrained by the low saturation levels which necessarily result from their small dynamic range.

The accuracy required in the sulfate fractional number density is derived from Figure 4.2.5 and indicates the uncertainty permitted in the sulfate fractional number density (γ_i defined in Appendix A.1) to achieve the $1.6 \mu\text{g}/\text{m}^3$ figure of merit. The procedure for obtaining these entries involved a coarse approximation of converting the optical depths in Figure 4.2.5 (2 and 4) to equivalent sulfate concentrations at 70 % and 90 % relative humidity (using Table 2.1.4.3), and then, assuming linearity of apparent reflectance and sulfate concentration, extrapolating the $\Delta\rho^*$ obtained from Figure 4.2.5 (at $0.55\mu\text{m}$) to 25 and $50 \mu\text{g}/\text{m}^3$. The figure quoted in Table 4.3.1 is accordingly the allowable error in the sulfate fractional number density between an aerosol atmospheric state of pure sulfates ($\gamma_s = 1$) and an aerosol atmosphere characterized by an equivalent optical load of pure dust particles ($\gamma_s = 0$). The computed values for $(\delta\gamma_s / \delta\rho^*)_{\epsilon,p}$ are shown in Table 4.3.2 below:

Table 4.3.2 $(\delta\gamma_s / \delta\rho^*)_{\epsilon, \rho}$ values (per percent in ρ^*)

	rel. hum	70%	90%
sulfate conc. [$\mu\text{g}/\text{m}^3$]			
25		1.4	.59
50		.63	.29

An estimate of γ_s for (at least for the fine particle fraction for which sulfates are the dominant component) is possible in the light of the discussion presented in Section 4.2.5(b) above. The implementation of such an approach requires two or more satellite bands which span the range between .4 and 1.6 μm and a noise/radiometric resolution superior to the figures presented in Table 4.2.4.1.

The figure of merit for sulfate mass scattering efficiency is simply derived from equation 4-1c where one assumes an accurate scattering optical depth has been extracted and hence where the ratio $\Delta\epsilon/\epsilon$ (expressed as a percent) is simply equivalent to the relative uncertainty in equivalent sulfate concentration. The major contributor to $\Delta\epsilon$ is the uncertainty associated with the relative contribution of sulfates to scattering by the fine particle mode. Natural variations of ϵ (c.f. Table 2.1.4.1 and Section 2.2.3) considerably exceed the required precision of Table 4.3.1. The most pragmatic method of reducing this uncertainty is to correlate satellite derived values of aerosol scattering optical depth with ground based measurements of dry sulfate concentration over measuring sites where the other input optical parameters have been evaluated. The verification of this approach would best be accomplished by simultaneous nephelometer measurements. Alternatively a season of nephelometer measurements at rural and urban sites could be employed to establish empirical values of the mass scattering efficiency as a function of a minimal set of meteorological parameters.

The scale height entry indicates the level of accuracy required in this parameter if one attempts to extract a real value of sulfate surface concentration. As above this error was derived from equation 4-1c assuming no error in the other dependent parameters.

4.4 Operational Considerations

4.4.1 Geometrical Effects

(a) Observation Geometry

As stated in Section 3.4.6 the principal effect of non nadir geometry in a zero reflectance atmosphere is to induce apparent reflectances which vary roughly as $1/\mu$ (where $\mu = \cos\theta$ is the cosine of the observers zenith angle) for small surface albedo. In keeping with the ideas presented in Appendix A.3 one may consider the apparent reflectance as being roughly proportional to the extended mass scattering efficiency $\epsilon(\lambda, \mu) = \epsilon(\lambda, 1)/\mu$. One then expects the error rates to scale by a factor of the order of μ for otherwise equivalent conditions (at least for small to intermediate values of the observer's zenith angle where non linear multiple scattering effects and non spherical geometry conditions are less important). It is advantageous then to favour larger zenith angle measurements provided the errors themselves do not covary with zenith angle. In principle this is not the case unless the input parameters to the inversion procedure are themselves determined from non nadir inversions of the satellite data.

At large surface reflectances the non linearities induced by the competing effects of scattering and attenuation suggest that alternative methods for sulfate inversion should be investigated. The use of apparent reflectances differentials over increments of viewing angle bears investigation (c.f. Figure 3.4.6.3). This approach which relates zenith angle dependent apparent reflectance differentials with sulfate concentration is well suited to NOAA and SEAWIF's data whose overlapping images at large viewing angles (inter image frequency of about 100 minutes) are particularly amenable to studies of angular variation. In addition, because equivalent pixels can be selected as targets, the problems of surface reflectance calibration are considerably reduced. The excellent signal to noise characteristics of the SEAWIF's sensor enhance this multi-image capability.

(b) Solar Geometry

As discussed in Section 3.4.6 the effects of variations in solar zenith angle are analogous to variations in the observer's zenith angle. Accordingly the same statement concerning larger zenith angles applies in the case of solar geometry as well. For sun synchronous orbits such as those associated with the NOAA, Landsat and SPOT satellite sensors the solar zenith angle for a characteristic 1500 GMT midlatitude crossing varies between a minimum of 30 degrees in summer to 70 degrees in winter. The meteorological satellites (GOES and Meteosat) which acquire images at half hour intervals are subject to solar zenith angle variations from 90 degrees to a minimum depending on the latitude and solar declination (time of year).

4.4.2 Wavelength Passband

In terms of first order models such as the one presented in Appendix A.3 the sulfate error rates vary as $1/\epsilon$ in atmospheric states well removed from the transition point between scattering and attenuation dominated atmospheres. As such the error rates increase with wavelength roughly as $(\lambda/\lambda_{\text{ref}})^\alpha$ where α is the commonly employed Angstrom coefficient (see Shaw et al., 1972 for example) and λ_{ref} is a reference wavelength (0.55 μm in our case). The value of the Angstrom coefficient is typically of the order of 1.3 (in comparison the Leaitch pure sulfate log normal model of Table 2.1.1.1 yields a value near 2.2 for wavelengths between .4 and .860 μm).

This spectral tendency which reflects a decreasing sensitivity with increasing wavelength was observed for error rate calculations at different wavelengths (not presented in the text) and is qualitatively evident in apparent reflectance computations such as the satellite passband dependent curves presented in Figure 3.4.5.1. Clearly however the increasing sulfate error rates cannot be the only optimization criteria since decreasing reflectance noise values and decreasing uncertainty in the surface reflectance can effectively offset the error rate degradation. This offsetting effect in terms of a decrease in reflectance noise is indeed the case for the visible bands of the TM sensor and for SEAWIFS (Table 2.4.5.1). In terms of surface reflectance considerations the decreasing reflectance of water pixels with increasing wavelength effectively induces a decreasing uncertainty (c.f. Table 4.2.1.1) which can be effectively taken advantage of in the near IR spectral region. Of the bands presented in Table 4.2.4.1 the SEAWIF's band 4 is clearly one of the most relevant in regards to exploiting the above considerations.

CHAPTER 5

GENERAL CONCLUSIONS AND RECOMMENDATIONS

We list here the general conclusions and recommendations extracted from the radiative transfer simulations and the computations of error rates. The reader is referred to the main body of the text for details. The principal reference source in the text is given in parenthesis.

- o Inversion algorithms must be referenced to low or high surface reflectances well removed from the Kaufman critical reflectance (Section 4.2.7)
- o The measured satellite signal is reasonably independent of the carbonaceous soot component over low reflecting surfaces and strongly dependent over high reflecting surfaces. This infers an inversion scheme would be best optimized by concentrating or weighting the sulfate inversion over low reflectance surfaces and the soot inversion over highly reflecting surfaces (Section 4.2.5).
- o Heavy mass loadings of dust can be discriminated from sulfates if two or more wavelengths in the visible and near IR (.4 to 1.5 μm) are available and provided the sensor noise specifications are adequate (Section 4.2.5).
- o In principle 10 bit radiometric resolution is the minimum requirement for sensors not optimized to the low intensity levels characteristic of atmospheric scattering phenomena. Of the sensors investigated only the NOAA series and the SEAWIF's sensors meet these specifications. Coarser resolution sensors which are optimized METEOSAT and GOES are restricted by saturation over highly reflecting targets.
- o For a nadir look direction, a wavelength of 0.55 μm and a range of sulfate concentrations between 0 and 50 $\mu\text{g}/\text{m}^3$ a cumulative precision in the order of 5 $\mu\text{g}/\text{m}^3$ is obtained given the following constraints (Section 4.3):
 - fractional sulfate scattering efficiency known $\sim (2.8 \mu\text{g}\cdot\text{m}^{-3} / \text{SO}_4^-)$ (quadrature sum of 3 independent errors). This is equivalent to the conditions (1.6 $\mu\text{g}/\text{m}^3$ error per component):
 - (a) relative humidity known to $\sim 3\%$ @ 70% r.h. and $\sim .3\%$ @ 90% r.h.
 - (b) dry effective radius smaller than .02 μm
 - (c) sulfate fractional number density $\sim .05$
 - surface reflectance known to $\sim .002$. Presently this is only possible for water surfaces. The most promising candidate surface other than water is vegetation in the chlorophyll absorption band centered near .65 μm .
 - single scattering albedo known to better than $\sim .05$ for a low reflectance surface. The accuracy requirement for a highly reflecting surface is prohibitive
 - fractional number density of sulfates known to $\sim .05$ in the context of a pure sulfate/dust atmosphere
- o At non nadir observing angles the atmospheric scattering is more responsive to sulfate presence. The sulfate error rates are correspondingly decreased as are the computed errors, if the input parameter uncertainties do not themselves covary with the observation geometry (Section 4.4.1). The NOAA and particularly SEAWIF's sensors are well suited to non nadir investigations because of their large swath width and because the overlap obtained permits multi-angle investigations of the same pixel.

- o At large surface reflectances and non nadir angles the satellite signal is non linear with sulfate concentration. In this case, methods of apparent reflectance differentials over zenith angle bear investigation (Section 4.4.1(a)).
- o The preferred operating wavelength (or the key wavelength in a multispectral inversion scheme) is constrained primarily by error rates which vary roughly as λ^α and the spectral form of the surface reflectance. For water this implies an optimum wavelength in the red/near IR region of the spectrum (Section 4.4.2). A band centered in the chlorophyll absorption minima at .65 μm could be employed in an inversion procedure over vegetation surfaces (Section 4.2.1).
- o If the relative humidity effects on the mass scattering efficiency can be specified sufficiently accurately then a high relative humidity atmosphere is the preferred state for measurements of sulfate concentration (Section 4.3).
- o The 5S model is sufficiently accurate for nadir computations but must be improved for large off nadir angles (Section 4.2.6)
- o High spectral resolution imaging systems such as the EOS sensors HIRIS and MODIS can be exploited to detect molecular absorbers by differential absorption techniques. The high spectral resolution capability is less effective for scattering based phenomena where the spectral information content is coarse (Section 4.2.5).
- o The achievement of the inversion precision targeted above requires at the very least a coordinated summer and winter campaign of ground based measurements tied to a multi-temporal set of NOAA or preferably SEAWIF's overflights. The components of the ground campaign would include:
 - sulfate mass concentration measurements
 - nephelometer measurements
 - selection and reflectance calibration of standard homogeneous test sites (ground based and airborne reflectance measurements)
 - carbonaceous soot measurements
 - multi-spectral sunphotometer measurements
 - fine particle size distribution measurements
 - measurements of relative humidity and other meteorological parameters (pressure, temperature, wind magnitude and direction)

Since the lion's share of these measurements are already performed in existing networks (CAPMON network, AES sunphotometer network etc.) a considerable part of the work would involve coordinating and collating network measurements with supplementary measurements and with the satellite data.

ERRATUM

During the editing of the above report it was realized that a small but persistent error was imbedded in the calculations. This error does not influence any of the conclusions but would be understandably annoying for anyone trying to duplicate our calculations. The source of the error stems from the manner in which the aerosol optical depth was entered into the 5S model. The value actually entered was the aerosol scattering optical depth while the input required by 5S is in fact the total aerosol optical depth. These two values generally differ only slightly at least in the visible portion of the wavelength spectrum. In any case, as explained below, the error is effectively set to zero by reinterpreting the number densities or concentrations used as inputs to the optical and radiative transfer calculations.

The aerosol scattering optical depth (c.f. Appendix A.1) is expressed as:

$$\tau_a^{sca} = \sigma_s^{sca} N_s + \sigma_c^{sca} N_c + \sigma_d^{sca} N_d$$

where a, s, c, and d refer respectively to aerosol, sulfate, carbonaceous soot, and dust like, and where N refers to the particle number density in units of cm^{-3} . If τ_a^{sca} is assumed to be a total aerosol optical depth then one can adjust the number density definitions such that it in fact does represent a total aerosol optical depth viz:

$$\begin{aligned} \tau_a &= \tau_a^{sca} = \sigma_s (\sigma_s^{sca}/\sigma_s) N_s + \sigma_c (\sigma_c^{sca}/\sigma_c) N_c + \sigma_d (\sigma_d^{sca}/\sigma_d) N_d \\ &= \sigma_s (\sigma_s^{sca}/\sigma_s) N_s + \sigma_c (\sigma_c^{sca}/\sigma_c) N_c + \sigma_d (\sigma_d^{sca}/\sigma_d) N_d \\ &= \sigma_s (\omega_{o,s} N_s) + \sigma_c (\omega_{o,c} N_c) + \sigma_d (\omega_{o,d} N_d) \end{aligned}$$

where the $\omega_{o,i}$'s are the pure single scattering albedo's for each component. This last expression indicates that the nominal aerosol scattering optical depths entered can be viewed as total aerosol optical depths if the number densities are modified by a factor equal to the pure single scattering albedo for the component of interest. Table 6.1 lists the precise values of these modifications. In general the sulfate concentration changes by less than 3% while the soot concentration decreases by a factor of the order of two. This latter decrease is the only significant change as far as the simulation studies are concerned. In those few cases (chapter 3 to 5) where references are made specifically to the soot concentration, an appropriate modification based on the above argument is included in the text and referenced to this section. Otherwise no attempt was made to perform a general correction according to the above relation. If more precise calculations are required the reader need only apply the corrected values in Table 6.1.

Table 6.1 Corrected number densities: NI (cm⁻³)

a) Values used initially as per Table 2.1.4.3

	dust-like	soot	sulfate
C.V.	2.3229	74.1400	0
U.V.	0.2682	775.4200	430
U.S.	0.4646	14.8280	860
C.S	0.0536	155.0850	1290
			1720
			2150
			2580
			3010
			3440
			3870
			4300

b) Effective values if the scattering aerosol optical depth entered is treated as total aerosol optical depth

	dust-like	soot	sulfate					
			0.0%	50.0%	70.0%	80.0%	90.0%	95.0%
C.V.	1.69172	32.3263	0.00	0.00	0.00	0.00	0.00	0.00
U.V.	0.19532	338.0963	414.9	417.22	420.40	421.98	424.83	427.07
C.S.	0.33834	6.4653	829.82	834.45	840.80	843.95	849.66	854.14
U.S.	0.03906	67.6197	1244.74	1251.67	1261.20	1265.93	1274.48	1281.21
			1659.65	1668.89	1681.60	1687.90	1699.31	1708.28
			2074.56	2086.12	2102.00	2109.88	2124.14	2135.35
			2489.47	2503.34	2522.40	2531.85	2548.97	2562.41
			2904.38	2920.56	2942.80	2953.83	2973.80	2989.48
			3319.30	3337.79	3363.20	3375.81	3398.62	3416.55
			3734.21	3755.01	3783.60	3797.78	3823.45	3843.62
			4149.12	4172.23	4204.00	4219.76	4248.28	4270.69

REFERENCES

- Ackerman, T. P., O. B. Toon, (1981), Absorption of Visible Radiation in Atmosphere Containing Mixtures of Absorbing and Nonabsorbing Particles, *Applied Optics*, **20**, pp. 3661-3668.
- Ahern, F. J., Goodenough, D. G., Jain, S. C., Rao, V. R., G. Rochon, (1977), Landsat Atmospheric Correction at CCRS, 4th Can. Symp. on Rem. Sens., Québec City, May (1977).
- Ahmad, Z., Sutton J., Stowe, L., C. R. N. Rao, (1988), A Regression Method for Estimating Atmospheric Aerosol Properties from Current and Modified Versions of the NOAA/AVHRR Instrument, *Int. Radiation Symp.*, Lille, France, 18-26, August 1988.
- Baker, J. (chairman), (1987), System Concept for Wide-Field-of-View Observations of Ocean Phenomena from Space, Report of the Joint EOSAT/NASA SeaWiFS Working Group, NASA, Washington D.C., EOSAT, Lanham Md.
- Bergstrom, R. W., (1973), Comments of the Estimation of Aerosol Absorption Coefficients in the Atmosphere, *Contributions to Atmospheric Physics* (translation of *Beitrag zur Physik der Atmosphäre*), **46**, pp. 198-202.
- Begni, G., Henry, P., Levoy, M., et M. Dinguirard (1987), La qualité des images SPOT, *Compte rendu du Colloque SPOT-1, Utilisation des images, Bilan et résultats*, Paris, France, novembre 1987, pp. 1505-1515.
- Carlson, T. N., Wendling, P., (1977), Reflected Radiance Measured by NOAA3 VHR as a Function of Optical Depth for Saharan Dust, *J. App. Meteor.*, **16**, pp. 1368-1371.
- Chandrasekhar, S., (1960), *Radiative Transfer*, Dover Pub. Inc., New York.
- Colwell, R. N., (1983), *Manual of Remote Sensing*, American Society of Photogrammetry, Sheridan Press, Falls Church, Virginia.
- Dalu, G., (1986), Satellite Remote Sensing of Atmospheric Water Vapour, *Int. J. Rem. Sens.*, **7**, pp. 1089-1097.
- Dedieu, G., Deschamps, P. Y., and Y. H. Kerr, (1983), Solar Irradiance at the Surface from Meteosat Visible Data, *Machine Data of Remotely Sensed data Symposium*, pp. 1-4.
- Deirmendjian, D. (1969), *Electromagnetic Scattering on Spherical Polydispersions*, American Elsevier, New York.
- Deschamps, P. Y., t. Phulpin, (1980), Atmospheric Correction of Infrared Measurements of Sea Surface Temperature Using Channels at 3.7, 11, and 12 μ m, *Boundary-Layer Meteorology*, **18**, pp. 131-143.
- Deschamps, P. Y., Herman, M., D. Tanré, (1983), Modeling of the Atmospheric Effects and its Applications to the Remote Sensing of Ocean Colour, *Applied Optics*, **22**, p. 3751-3758.
- Deuze, J. L., Devaux, C., Herman, M., Santer, R., D. Tanré, (1988), Saharan Aerosols over the South of France: Characterization Derived from Satellite Data and Ground Based Measurements, *J. of Applied Meteor.*, **27**, p. 680-686.
- Egan, W. G., (1986), Satellite Remote Sensing of the Optical Properties of the Sahara and the Climatological Significance, 20th Inter. Symp. on Rem. Sens. of Envir., Nairobi, Kenya, pp. 95-114.

- Elterman, L., (1970), Vertical-Attenuation Model with Eight Surface Meteorological Ranges 2 to 13 kilometers, Air Force Cambridge Research Laboratories, Bedford, Mass.
- Fraser, R. S., (1986), Satellite Measurements of Mass of Sahara Dust in the Atmosphere, *App. Optics*, **15**, pp. 2471-2479
- Fraser R. S., Kaufman, Y. J., (1984), Satellite Measurements of Aerosol Mass and Transport, *Atmospheric Environment*, **18**, pp. 2577-2584.
- Freemantle, J., Miller, J. R., K. S. Jammu, (1984), Atmospheric Aerosol Variability over the Great Lakes from NOAA-7 AVHRR Imagery, *Proc. of the 9th Can. Symp. on Rem. Sens.*, St. John's, NFLD, 13-17 Aug. 1984, pp. 263-270.
- Frouin, R., Gauthier, C., Calibration of NOAA-AVHRR, GOES-5 and GOES-6 VISSR/VAS solar channels, *Rem. Sens. of Envir.*, **22**, pp. 73-101.
- Griggs, M., (1987), Satellite Measurements of Tropospheric Aerosols, NASA CR-3459, NASA-15898, 58p.
- Gordon, H. R., (1978), Removal of Atmospheric Effects from Satellite Imagery of the Oceans, *Applied Optics*, **17**, pp. 1631-1635.
- Hanel, G., (1976), The Properties of Atmospheric Aerosol Particles as Functions of The Relative Humidity at Thermodynamic Equilibrium with the Surrounding Moist Air, *Advances in Geophysics*, Academic Press, pp. 73-188.
- Hay, J. E., (1971), Precipitable Water Over Canada, *Atmosphere*, **9**, pp. 128-143
- Hindman, E. E., Durkee, P. A., W. Kuenning, (1985), Properties of Aerosol Particles Detected by Satellites in Coastal regions, *J. Rech. Atmos.*, **19**, pp. 315-322.
- Husar, R. B., D. E. Patterson, (1980), Regional Scale Air Pollution: Sources and Effects, *Annals New York Academy of Sciences*, pp. 399-417.
- Isaac, G. A., Leaitch, W. R., J. W. Strapp, (1988), The Vertical Distribution of Aerosols and Acid Related Compounds in Air and Cloudwater, submitted to *Atmospheric Environment*.
- Ivanchik, M. V., Klyvslinikov, S. I., Krovotyntsev, V. A., Serebrennikov, A. N., (1985), Remote Sensing of Dust Formations in the Atmosphere, *Sov. J. Remote Sensing*, **4**, pp. 375-380.
- Japar, S. M., Brachaczek, W. W., Gorse R. A., Jr., Norbeck, J. M., W. R. Pierson, (1986), The Contribution of Elemental Carbon to the Optical Properties of Rural Atmospheric Aerosols, *Atmospheric Environment*, **20**, pp. 1281-1289.
- Jennings, J.G. J.B. Gillespie (1978), Mie Theory Sensitivity Studies - The Effects of Aerosols Complex Refractive Index and Size Distribution Variations on Extinction and Absorption Coefficients part II: Analysis of the Computational Results, ASL report, VS Army Electronics Research and Development Command.
- Kaestner, M., Koepke, P., H. Quenzel, (1982), Monitoring of Saharan Dust over the Atlantic Using Meteosat-VIS Data, XXIV COSPAR, Ottawa, Canada
- Kattawar, G. W., G. N. Plass, (1967), Electromagnetic Scattering from Absorbing Spheres, *Applied Optics*, **6**, pp. 1377-1382.

- Kaufman, Y. J., J. H. Joachim, (1982), Determination of Surface Albedos and Aerosol Extinction Characteristics from Satellite Imagery, *J. Geoph. Res.*, **87**, pp. 1287-1299.
- Kaufman, Y. J., R. S. Fraser, (1983), Light Extinction by Aerosols during Summer Air Pollution, *Journal of Climate and Applied Meteorology*, **22**, pp. 1694-1706.
- Kaufman, Y. J., (1987), Satellite Sensing of Aerosol Absorption, *Jour. Geophys. Res.*, **20**, pp. 4307-4317.
- Kaufman, Y. J., C. Sendra, (1988), Algorithm for automatic atmospheric corrections to visible and near-IR satellite imagery, *Int. J. Remote Sensing*, **9**, pp. 1357-1381.
- Kerr, J. B., McElroy, C. T., Olafson, R. A., (1980), Measurements of Ozone with the Brewer Ozone Spectrophotometer, *Proc. Inter. Ozone Symposium*, Boulder, Col., pp. 74-79.
- Kerr, J. B., W. F. J. Evans, (1980), Monitoring of Sulphur Dioxide at Downsview with the Brewer Ozone Spectrophotometer, Internal Report APRB 111X35, Atmospheric Environmental Research, Environment Canada.
- Kim, Y. J., Sievering, H., J. F. Boatman, (1988), Airborne Measurement of Atmospheric Particles in the Lower Troposphere Over the Central United States, *Jour. Geophys. Res.*, **93**, pp. 12631-12644.
- Lauritson, L., Nelson, G. J., F. W. Porto, (1979), Data Extraction and Calibration of Tiros-N/NOAA Radiometers, NOAA Technical Memorandum NESS-107, NOAA, US Dept. of Commerce.
- Legrand, M., Bertrand J. J., M. Desbois, (1985), Dust Clouds over West Africa: A Characterization by Satellite Data, *Ann. Geophys.*, **3**, pp. 377-786.
- Legrand, M., Desbois, M., VORN?, K., (1988), Satellite Detection of Saharan Dust: Optimum Imaging During Nighttime, *J. Climate*, submitted for publication.
- Leitch, W.R., G.A. Isaac (1988), Tropospheric Aerosol Size Distribution in Eastern and Northern North America Between 1 000 and 500 Mb: Signatures for Condensation and Stratospheric Intrusions, Atmospheric Environment Service internal report.
- Leaderer, B. P., J. A. Stolwijk, (1980), Optical Properties of the Urban Aerosol and Their Relation to Chemical Composition, *Annals New York Academy of Sciences*, pp. 70-85.
- Lyons, W. A., (1980), Evidence of Transport of Hazy Air Masses From Satellite Imagery, *Annals of New York Academy of Sciences*, pp. 418-433.
- Macias, E.S., Blumenthal, D.L., Anderson, J.A., B.K. Cantrell (1980), Size and Composition of Visibility-Reducing Aerosols in Southwestern Plumes, *Annals of New York Academy of Sciences*, pp. 233-257.
- Malila, W. A., D. M. Anderson, (1986), Satellite Data Availability and Calibration documentation for Land Surface Climatology Studies, International Satellite Land-Surface Climatology Project (ISLSCP), North American ISLSCP Retrospective Analysis Program (IRAP), ISLSCP Report No. 5, University Corporation for Atmospheric Research, Boulder Colorado.
- Meckler, Y., Quenzel, H., Ohring, L., I. Maurus, (1977), Relative Atmospheric Aerosol Content from ERTS Observations, *J. Geophys. Res.*, **82**, pp. 967-970.
- Middleton, W. E. K., (1952), *Vision Through the Atmosphere*, University of Toronto Press, Toronto.
- Morel, A., L. Prieur, (1977), Analysis of Variations in Ocean Color, *Limnology and Oceanography*, **22**, pp. 709-722.

O'Neill, N. T., Miller, J. R., F. J. Ahern, (1978), Radiative Transfer Calculations for Remote Sensing Applications, 5th Can. Symp. on Rem. Sens., Victoria, August (1978).

O'Neill, N. T., (1982), A Radiative Transfer in an Urban Atmosphere, Ph. D. thesis, York University, Toronto, Ont.

O'Neill, N. T., J. R. Miller, (1988), On Calibration of Passive Optical Bathymetry through Depth Soundings: Analysis and Treatment of Errors Resulting from the Spatial Variation of Environmental Parameters, accepted for publication in the Int. Jour. of Rem. Sens.

Otterman, J., Fraser, R. S., O. P. Bahethi, (1982), Characterization of Tropospheric Desert Aerosols at Solar Wavelengths by Multispectral Radiometry from Landsat, J. of Geophys. Res., **87**, pp. 1270-1278.

Penndorf, R., (1957), Tables of the Refractive Index for Standard Air and the Rayleigh Scattering Coefficient for the Spectral Region Between 0.2 and 20.0 microns and their Application to Atmospheric Optics, J. Optical Soc. of America, **47**, pp. 176-182.

Pierson, W.R., Brachaczek, W.W., Truer, T.J., Butler, J.W., T.J. Korniski (1980), Ambient sulfate Measurements on Allegheny Mountain and the Question of Atmospheric sulfate in the Northeastern United States, Annals New York Academy of Sciences, pp. 145-173.

Richards, L. W., R. W. Bergstrom Jr., (1986), The Optical Effects of Fine-Particle Carbon on Urban Atmospheres, Atmosphere Environment, **20**, pp. 387-396.

Roosen, R. G., R. J. Angione, C. H. Klemcke, (1973), Worldwide Variations in Atmospheric Transmission: 1. Baseline Results from Smithsonian Observations, Bulletin American Meteorological Society, **54**, pp. 307-315.

Rosen, H., A. D. Hansen, L. Gundel, T. Novakov, (1978), Identification of the Optically Absorbing Component in Urban Aerosols, Applied Optics, **17**, 3859-3861.

Rosen, H., T. Novakov, (1983), Optical Transmission Through Aerosol deposits on Diffusely Reflective Filters: a Method for Measuring the Absorbing Component of Aerosol Particles, Applied Optics, **22**, pp. 1265-1267.

Royer, A., Bernier, R., Adler, U., E. Pilon, (1985), Calcul de diffusion de la lumière par les aérosols: Descriptions des programmes "MIELOR" et résultats obtenus.

Royer, A., Charbonneau, L., Brochu, R., Murphy, M. M., P. M. Teillet, (1987), Radiometric Comparison of the Landsat-5 TM and MSS sensors, Int. J. Remote Sensing, **8**, pp. 579-591.

Royer, A., Charbonneau, L., (1988a), Interannual Landsat-MSS Reflectance Variation in an Urbanized Temperate Zone, Remote Sensing of Environment, **24**, pp. 423-446.

Royer, A., Davis, A., N. T. O'Neill, (1988b), Analyse des effets atmosphériques dans les images HRV de SPOT, Canadian Journal of Remote Sensing, **14**, pp. 80-91.

Ruby, M. G., A. P. Waggoner, (1981), Intercomparison of Integrating Nephelometer Measurements, Environmental Science and Technology, **15**, pp. 109-113.

Shaw, G. E., J. A. Reagan, B. M. Herman, (1972), Investigation of Atmospheric Extinction Using Direct Solar Radiation Measurements with a Multiple Wavelength Radiometer, Journal of Applied Meteorology, **12**, pp. 374-380.

Slater, P. N., (1980), Remote Sensing: Optics and Optical Systems, Addison-Wesley, Reading Mass.

- Sloane, C.S. (1983), Optical Properties of Aerosols - Comparison of Measurements with Model calculations, *Atmospheric Environment*, **17**, pp. 409-416.
- Sloane, C.S. (1984), Optical Properties of Aerosols of Mixed Composition, **18**, pp. 871-878.
- Sloane, C.S. (1986), Effect of Composition on Aerosol Light Scattering Efficiencies, *Atmospheric Environment*, **20**, pp. 1025-1037.
- Shettle, E.P., R.W. Fenn (1979), Models for the Aerosols of the Lower Atmosphere and the Effects of Humidity Variations on their Optical Properties, AFGL-TR-79-0214, Air Force Geophysics Laboratory, Hanscom AFB, Massachusetts.
- Syed, M. Q., A. W. Harrison, (1980), Ground Based Observations of Stratospheric Nitrogen Dioxide, *Can. J. Phys.*, **58**, pp. 788-802.
- Takayama, Y., T. Takashime, (1986), Aerosol Optical Thickness of Yellow Sand over the Yellow Sea Derived from NOAA Satellite Data, *Atmos. Envir.*, **20**, pp. 631-638.
- Tang, I. N., Wong, W. T., H. R. Munkelwitz, (1981), The Relative Importance of Atmospheric Sulfates and Nitrates in Visibility Reduction, *Atmospheric Environment*, **15**, pp. 2463-2471.
- Tanré, D., Deschamps P. Y., Devaux C., M. Herman, (1988), Satellite Measurements of the Saharan Aerosol Optical Thickness over Land Surface, *IRS88*.
- Tomasi, C., (1979), Weak Absorption by Atmospheric Water Vapour in the Visible and Near-Infra-Red Spectral Region, *Il Nuovo Cimento*, **2C**, pp. 511-526
- Toon, O.B., Pollack, J.B., B.N. Khare (1976), The Optical Constants of Several Atmospheric Aerosol Species: Ammonium Sulfate, Aluminium Oxide, and Sodium Chloride, *Journal of Geophysical Research*, **81**, No 33, pp. 5733-5748.
- Tsonis, A., (1987), A Method for Inferring Aerosol Properties From Satellite Data over Forested Terrain, *Atmospheric Environment*, **21**, pp. 2467-2471.
- Tsonis, A., W.R. Leaitch (1986), Minimum Detectable Pollution Levels from Satellite Imagery, *Geophys. Res. Lett.*, **13**, pp. 56-59.
- Turner, R. E., M. M. Spencer, (1972), Atmospheric Model for the Correction of Spacecraft Data, *Proc. of the 8th Int. Symp. on Rem. Sens. of Environ.*, Ann Arbor, pp. 895-934.
- Vossier, T.L., E.S. Macias (1986), Contribution of Fine Particle sulfates to Light Scattering in St. Louis Summer Aerosol, *Environmental Science and Technology*, **20**, pp. 1235-1243.
- Young, A. T., (1981), On the Rayleigh-Scattering Optical Depth of the Atmosphere, *J. App. Met.*, **20**, pp. 328-330.
- WCP-55, 1983, World Climate Research Program Report of the Experts Meeting on Aerosols and Their Climatic Effects, WMO, Williamsburg, 28-30 March 1983, 107 p.
- Wickramasinghe, N. C., (1973), Light Scattering Functions for Small Particles and Applications in Astronomy, Wiley, New York.
- Wolfe, L. W., G. J. Zissis, (1978), The Infrared Handbook, Prepared by the Environmental Research Institute of Michigan for the Office of Naval Research, Department of the Navy, Washington DC.

APPENDIX A

A.1 Symbols and Definitions

A.2 Relative Humidity Modelling

A.3 Some Useful Approximations

APPENDIX A.1: SYMBOLS AND NOMENCLATURE

Optical Parameters for a Given Aerosol Component

The size distribution of a heterogeneous collection of aerosol particles is commonly referred to in terms of the number density per cm^{-3} per unit radius interval viz:

$$n_i(r) = N_i \hat{n}_i(r)$$

$$\text{where } \int_0^{\infty} n_i(r) dr = N_i$$

is the total number per cm^{-3} and hence where the normalized size distribution has the property:

$$\int_0^{\infty} \hat{n}_i(r) dr = 1$$

The total extinction cross section, assuming independent scattering, is the sum of all Mie cross sections for all particles in the distribution:

$$\sigma_i(\lambda) = \int_0^{\infty} \sigma(m_i, \alpha) \hat{n}_i(r) dr$$

where m_i is the refractive index and $\alpha = 2\pi r / \lambda$ is the size parameter.

The contributors to the extinction cross section are pure absorption and outscattering from the incident beam:

$$\sigma_i(\lambda) = \sigma_i^{\text{sca}}(\lambda) + \sigma_i^{\text{ext}}(\lambda)$$

where

$$\sigma_i^{\text{sca}}(\lambda) = \int_0^{\infty} \sigma^{\text{sca}}(m_i, \alpha) \hat{n}_i(r) dr$$

$$\sigma_i^{\text{abs}}(\lambda) = \int_0^{\infty} \sigma^{\text{abs}}(m_i, \alpha) \hat{n}_i(r) dr$$

are the particle size distribution averaged absorption and scattering cross sections respectively. Multiplying by the total number of particles per unit volume yields the volume extinction, scattering and absorption coefficients:

$$\kappa_i(\lambda) = N_i \sigma_i(\lambda)$$

$$\kappa_i^{\text{sca}}(\lambda) = N_i \sigma_i^{\text{sca}}(\lambda)$$

$$\kappa_i^{\text{abs}}(\lambda) = N_i \sigma_i^{\text{abs}}(\lambda)$$

In terms of the Mie scattering nomenclature the conservative scattering phase function is given by:

$$p_o(m_i, \alpha, \cos \chi) = \frac{i_1(m_i, \alpha, \cos \chi) + i_2(m_i, \alpha, \cos \chi)}{2} \frac{1}{\alpha^2 Q_{sca}}$$

$$\text{where } Q_{sca} = \frac{\sigma^{sca}(m_i, \alpha)}{\sigma(m_i, \alpha)}$$

is the scattering efficiency and i_1 and i_2 (or i_L and $i_{||}$ respectively) are the standard Mie intensity functions (Born and Wolf, 1965, Wickramasinghe, 1973). The conservative scattering phase function is constrained by its integral over solid angle viz:

$$\int_0^{4\pi} p_o(m_i, \alpha, \cos \chi) \frac{d\Omega}{4\pi} = 1$$

The average conservative phase function over the size distribution is given by the optical average:

$$p_{oi}(\cos \chi) = \int_0^\infty p_o(m_i, \alpha, \cos \chi) \hat{n}_i(r) \sigma^{sca}(m_i, \alpha) \frac{dr}{\sigma_i^{sca}(\lambda)}$$

$$= \int_0^\infty p_{oi}(m_i, \alpha, \cos \chi) n_i(r) \sigma^{sca}(m_i, \alpha) \frac{dr}{\kappa_i^{sca}(\lambda)}$$

where an integration over solid angle clearly yields:

$$\int_0^\infty p_{oi}(\cos \chi) \frac{d\Omega}{4\pi} = 1$$

The phase function definition which includes the effects of absorption is simply:

$$p(m_i, \alpha, \cos \chi) = \omega_o(m_i, \alpha) p_o(m_i, \alpha, \cos \chi)$$

where:

$$\omega_o(m_i, \alpha) = \frac{\sigma_i^{sca}(m_i, \alpha)}{\sigma(m_i, \alpha)}$$

is termed the single scattering albedo. The optically averaged representation of this phase function is:

$$p_i(\cos \chi) = \int_0^\infty p(m_i, \alpha, \cos \chi) \hat{n}_i(r) \sigma(m_i, \alpha) \frac{dr}{\sigma_i(\lambda)}$$

$$= \int_0^\infty p(m_i, \alpha, \cos \chi) n_i(r) \sigma(m_i, \alpha) \frac{dr}{\kappa_i(\lambda)}$$

or hence:

$$p_i(\cos \chi) = \omega_{oi}(\lambda) p_{oi}(\cos \chi)$$

where the PSD averaged single scattering albedo is given by:

$$\begin{aligned}\omega_{oi}(\lambda) &= \frac{\sigma_i^{sca}(\lambda)}{\sigma_i(\lambda)} \\ &= \frac{\kappa_i^{sca}(\lambda)}{\kappa_i(\lambda)}\end{aligned}$$

The Legendre polynomial representation of the Mie phase function is written:

$$p(m_i, \alpha, \cos \chi) = \sum_{\ell=0}^{\infty} \omega_{\ell}(m_i, \alpha) P_{\ell}(\cos \chi)$$

where $P_{\ell}(\cos \chi)$ are Legendre polynomials (Ambramowitz and Stegun, 1972). Integrating over the size distribution yields the optically averaged representation:

$$p_i(\cos \chi) = \sum_{\ell=0}^{\infty} \omega_{\ell i}(\lambda) P_{\ell}(\cos \chi)$$

where:

$$\begin{aligned}\omega_{\ell i}(\lambda) &= \int_0^{\infty} \omega_{\ell}(m_i, \alpha) \hat{n}_i(r) \alpha(m_i, \alpha) \frac{dr}{\sigma_i(\lambda)} \\ &= \int_0^{\infty} \omega_{\ell}(m_i, \alpha) n_i(r) \alpha(m_i, \alpha) \frac{dr}{\kappa_i(\lambda)}\end{aligned}$$

Aggregate Aerosol Model Parameterization

For aggregate collections of individual aerosol components one can define an aggregate normalized size distribution:

$$\begin{aligned}\hat{n}(r) &= \sum_i \gamma_i \hat{n}_i(r) \quad \text{where} \quad \sum_i \gamma_i = 1 \\ \gamma_i &= \frac{N_i}{N} \quad \text{and} \quad N = \sum_i N_i\end{aligned}$$

With this definition we clearly have:

$$\int_0^{\infty} \hat{n}(r) dr = 1$$

The actual number density is then simply:

$$\begin{aligned}n(r) &= \sum_i n_i(r) \\ &= N \sum_i \gamma_i \hat{n}_i(r)\end{aligned}$$

The volume of the PSD normalized to a single particle is:

$$\hat{v}_i = \int_0^{\infty} \frac{4\pi}{3} r^3 \hat{n}_i(r) dr$$

The fractional volume associated with all the particles of component i is:

$$c_i = V_i / V = N_i \hat{v}_i / V$$

The fractional volume and fractional number density are accordingly interrelated by the expressions given below:

$$c_i = \frac{\gamma_i \hat{v}_i}{\sum_i \gamma_i \hat{v}_i}$$

$$\gamma_i = \frac{c_i / \hat{v}_i}{\sum_i c_i / \hat{v}_i}$$

Volume extinction and scattering coefficients for the aggregate aerosol distribution are given by:

$$\kappa(\lambda) = N \sigma(\lambda)$$

$$\kappa^{sca}(\lambda) = N \sigma^{sca}(\lambda)$$

where:

$$\sigma(\lambda) = \sum_i \gamma_i \sigma_i(\lambda) \quad \text{and} \quad \sigma^{sca}(\lambda) = \sum_i \gamma_i \sigma_i^{sca}(\lambda)$$

The optically averaged conservative phase function takes on the form:

$$\begin{aligned} p_o(\cos \chi) &= \frac{\sum_i \sigma_i^{sca}(\lambda) p_{oi}(\cos \chi)}{\sigma^{sca}(\lambda)} \\ &= \frac{\sum_i \kappa_i^{sca}(\lambda) p_{oi}(\cos \chi)}{\kappa^{sca}(\lambda)} \end{aligned}$$

In a similar fashion as above the phase function is expressed as an optical mean weighted by the component extinction coefficients. This yields:

$$p(\cos \chi) = \omega_o(\lambda) p_o(\cos \chi)$$

where the aggregate single scattering albedo is given by:

$$\omega_o(\lambda) = \frac{\sigma^{sca}(\lambda)}{\sigma(\lambda)} = \frac{\kappa^{sca}(\lambda)}{\kappa(\lambda)}$$

Finally, the aggregate aerosol Lengdre formulation can be expressed as:

$$p(\cos \chi) = \sum_{l=0}^{\infty} \omega_l(\lambda) P_l(\cos \chi)$$

By integrating over solid angle and exploiting the orthogonality properties of the Lengdre polynomials one finds:

$$\omega_l(\lambda) = \frac{\sum_i \omega_{li}(\lambda) \alpha_i(\lambda) \gamma_i}{\sigma(\lambda)} = \frac{\sum_i \omega_{li} \kappa_i(\lambda)}{\kappa(\lambda)}$$

Log Normal Size Distributions

A common and convenient means of describing the particle size distribution is in terms of the log normal size distribution viz:

$$\frac{dN}{d \log r} = \frac{N}{\sqrt{2\pi} \log \sigma} e^{- (\log r - \log r_N)^2 / 2 \log^2 \sigma}$$

where the log is referenced to the base 10. The parameter r_N is commonly called the *geometric mean radius* while σ is the *geometric standard deviation*. As written this relation has the following mathematical properties:

$$\int_{-\infty}^{\infty} \frac{dN}{d \log r} d \log r = N$$

$$\int_{-\infty}^{\infty} \log r \frac{dN}{d \log r} \frac{d \log r}{N} = \log r_N$$

$$\int_{-\infty}^{\infty} (\log r - \log r_N)^2 \frac{dN}{d \log r} \frac{d \log r}{N} = \log^2 \sigma$$

The form of these expressions is clearly independent of the logarithmic base for the (defined) curve parameters $r_N = 10^{\log r_N}$ and $\sigma = 10^{\log \sigma}$. The volume (or mass) distribution is given by:

$$\frac{dV}{d \log r} = \frac{4}{3} \pi r^3 \frac{dN}{d \log r}$$

After some manipulation this can be written as:

$$\frac{dV}{d \log r} = \frac{4}{3} \pi r^3 \frac{N}{\sqrt{2\pi} \log \sigma} e^{- (\log r - \log r_N)^2 / 2 \log^2 \sigma}$$

where r_3 is an effective mean volume radius per particle in as much as the integration of the above expression yields:

$$\bar{v} = \frac{1}{N} \int_{-\infty}^{\infty} \frac{dV}{d \log r} d \log r = \frac{4}{3} \pi r_3^3$$

Because the volume distribution retains the log-normal form, r_V can be interpreted as a geometric mean radius (weighted by the volume distribution) viz:

$$\int_{-\infty}^{\infty} \log r \frac{dV}{d \log r} \frac{d \log r}{V} = \log r_V$$

As well it will be noted, from the form of the exponential term for $dV/d \log r$ above, that the log normal volume distribution retains the same standard deviation ($\log \sigma$) as the log normal distribution for the number density. The two volume based mean radii are related to the geometric mean radius r_N by:

$$\log r_3 = \log r_N + \frac{3}{2} \ln 10 \log^2 \sigma \quad \text{or} \quad \ln r_3 = \ln r_N + \frac{3}{2} \ln^2 \sigma$$

$$\log r_V = \log r_N + 3 \ln 10 \log^2 \sigma \quad \text{or} \quad \ln r_V = \ln r_N + 3 \ln^2 \sigma$$

These expressions were derived by explicitly deducing the log normal form for $dV/d \log r$ above and thence equating terms. It will be noted that the log and ln expressions are self consistent (i.e. derivable one from the other).

In a similar fashion one can obtain analogous surface expressions. The form of these expressions is identical to the volume expressions except that one replaces S for V , r_S for r_V , r_2 for r_3 , and $\pi r^2 : \pi r_2^2$ for $4/3 \pi r^3 : 4/3 \pi r_3^3$. The two radii parameters are given by:

$$\log r_S = \log r_N + 2 \ln 10 \log^2 \sigma \quad \text{or} \quad \ln r_S = \ln r_N + 2 \ln^2 \sigma$$

$$\log r_2 = \log r_N + \ln 10 \log^2 \sigma \quad \text{or} \quad \ln r_2 = \ln r_N + \ln^2 \sigma$$

In a good deal of the fundamental aerosol research the particle dimensions are reported in terms of diameter rather than radius. This implies some trivial changes in the above expressions which for the sake of completeness are noted here:

$$\frac{dN}{d \log D} = \frac{dN}{d \log r} = \frac{N}{\sqrt{2\pi} \log \sigma} e^{-(\log D - \log D_N)^2 / (2 \log^2 \sigma)}$$

where $\log \sigma$ is the same as above and where:

$$\log D_N = \int_{-\infty}^{\infty} \log D \frac{1}{N} \frac{dN}{d \log D} d \log D = \log 2 + \log r_N$$

Columnar Parameters

The total number of particles in a one cm^2 atmospheric column between the radii r and $r + dr$ per unit radius increment is termed the differential abundance. For a single aerosol component the differential abundance is related to the differential number density by:

$$\begin{aligned} a_i(r) &= \int_0^{\infty} n_i(r, h) dh \\ &= \hat{n}_i(r) \int_0^{\infty} N_i(h) dh \\ &= \hat{n}_i(r) A_i \end{aligned}$$

where A_i is the total abundance for all radii. Clearly:

$$\int_0^{\infty} a_i(r) dr = A_i$$

The extinction optical depth is expressed as:

$$\begin{aligned} \tau_i &= \int_0^{\infty} \kappa_i(h, \lambda) dh \\ &= A_i \sigma_i(\lambda) \end{aligned}$$

In a similar fashion one can write for the scattering optical depth (similar expression for the absorption optical depth):

$$\begin{aligned} \tau_i^{\text{scat}} &= \int_0^{\infty} \kappa_i^{\text{scat}}(h, \lambda) dh \\ &= A_i \sigma_i^{\text{scat}}(\lambda) \end{aligned}$$

For the aggregate aerosol the differential abundance is clearly:

$$\begin{aligned} a(r) &= \int_0^{\infty} n(r, h) dh \\ &= \int_0^{\infty} N(h) \hat{n}(r) dh \\ &= A \hat{n}(r) \quad \text{where} \quad A = \int_0^{\infty} N(h) dh \end{aligned}$$

is the total number abundance for the aggregate aerosol. The aggregate aerosol optical depths are written:

$$\begin{aligned}
 \tau &= \int_0^{\infty} \kappa(h, \lambda) dh \\
 &= A \sigma(\lambda) \\
 \tau^{sca} &= \int_0^{\infty} \kappa^{sca}(h, \lambda) dh \\
 &= A \sigma^{sca}(\lambda)
 \end{aligned}$$

Parameterization of Altitude Profiles

The number density altitude profile is given by:

$$h_i(z, r) = \frac{n_i(z, r)}{n_i(0, r)}$$

If the size distribution is independent of altitude one can write:

$$h_i(z, r) = h_i(z) = \frac{N_i(z)}{N_i(0)} = \frac{\kappa_i(z, \lambda)}{\kappa_i(0, \lambda)}$$

The equivalent column length referenced to the surface concentration is defined by:

$$H_i = \int_0^{\infty} h_i(z) dz = \frac{A_i}{N_i(0)}$$

where H_i is termed the scale height represents the height of an atmospheric column if all the particles of component i were compressed to the number density at the surface. If $h_i(z)$ varies exponentially as $\exp(-hk)$ then clearly k^{-1} is the scale height. The optical depth can be written:

$$\tau_i = N_i(0) H_i \sigma_i(\lambda)$$

and the aggregate optical depth as:

$$\tau = N(0) \sum_i \gamma_i(0) \sigma_i(\lambda) H_i$$

APPENDIX A.2: RELATIVE HUMIDITY MODELS

Particle Growth Model

As per Hanel (1976) one assumes that the total volume of a wet particle is the sum of dry particle volume and the volume of the pure water condensed on it viz:

$$V = V_o + V_w$$

If ρ_o, μ_o and ρ_w, μ_w are the densities and masses of the dry particle and the water respectively we may write:

$$\frac{V}{V_o} = 1 + \frac{\rho_o}{\rho_w} \frac{\mu_w}{\mu_o}$$

By employing the equivalent radii $r(0) = (3V_o/4\pi)^{1/3}$ and $r = (3V/4\pi)^{1/3}$ this expression can be transformed into an explicit equation for the wet radius:

$$r = r(0) \left[1 + \frac{\rho_o}{\rho_w} \frac{\mu_w}{\mu_o} \right]^{1/3}$$

The wet particle mass m_w is a strong function of the water activity a_w given by:

$$a_w = f \exp \left[- \frac{2\sigma v_w}{R_w T r(a_w)} \right]$$

where f is the relative humidity ($0 \leq f \leq 1$), σ is the surface tension on the wet particle surface, v_w the specific volume of pure water, T the absolute temperature in degrees Kelvin, and R_w the specific gas constant of pure water. An evaluation of the exponential term for room temperature conditions yields (Shettle and Fenn, 1979):

$$a_w = f \exp \left[- \frac{0.001056}{r(a_w)} \right]$$

According to Shettle and Fenn variations in curvature effect due to typical departures of atmospheric temperature from room temperature are less than 2%. Given the coupled expressions for a_w and r , input values for f and $r(0)$, and representative values of the water activity dependent ratio $\mu_w(a_w)/\mu_o$ and the density ratio ρ_o/ρ_w one can iteratively solve for the wet particle equivalent radius (r).

Variation of Refractive Index With Relative Humidity

As indicated by Shettle and Fenn (1979) the refractive index of the wet particle is simply the volume weighted mean of the dry and wet refractive indices:

$$\begin{aligned}
 m &= \frac{m_w V_w + m_b V_0}{V} \\
 &= m_w + (m_b - m_w) \frac{V_0}{V} \\
 &= m_w + (m_b - m_w) \left[\frac{r_0}{r} \right]^3
 \end{aligned}$$

where r is obtained from the iterative procedures described in the previous section.

Variation of Log Normal Parameters

Except for very small particle sizes ($r < .01 \mu\text{m}$) the variation of water activity with radius is quite weak (a_w is approximately given by the relative humidity f) and the particle growth ratio $r/r(0)$ is practically constant. If the governing size distribution is log normal and if no significant contributions to the size distribution arise from the very small particles then one may continue to describe the wet particle distribution by a log normal expression with an appropriate shift in r_N towards larger radii. This follows from the definition of r_N as given above in the discussion of the log normal parameterization, viz:

$$\begin{aligned}
 \log r_N(f) &= \int_{-\infty}^{\infty} \log r(f) \frac{dN}{d \log r} \frac{d \log r}{N} \\
 &= \int_{-\infty}^{\infty} \left[\log r(0) + \log \frac{r(f)}{r(0)} \right] \frac{dN}{d \log r} \frac{d \log r}{N} \\
 &= \log r_N(0) + \log \left[\frac{r(f)}{r(0)} \right]
 \end{aligned}$$

where $r(f)$ represents the particle radius at relative humidity f . Employing the above relation for the wet to dry particle radii ratio yields:

$$r_N(f) = r_N(0) \left[1 + \frac{\rho_o \mu_w}{\rho_w \mu_b} \right]^{1/3}$$

The simple proportionality of the geometric mean radius (r_N) when substituted into the defining equation for the geometric standard deviation (σ) yields:

$$\log^2 \sigma(f) = \log^2 \sigma(0)$$

Cumulative Particle Size Distribution Effects

The volume averaged refractive index can be written:

$$\begin{aligned} d \langle m \rangle &= \frac{m_w (dV - dV_0) + m_0 dV_0}{V} \\ &= m_w \frac{dV}{V} + \frac{(m_w - m_0) dV_0}{V} \end{aligned}$$

or hence by integrating over volume and employing the log normal descriptions of the dry and wet particle size distributions we obtain:

$$\langle m \rangle = m_w + (m_0 - m_w) \frac{r_3^3(0)}{r_3^3(a_w)}$$

where r_3 is the effective mean volume radius per particle as defined above in the discussion of the log normal function and its associated parameters. As noted above the calculations are considerably simplified since one is only required to find a functional form for $r_N(a_w)$ and $\alpha(a_w)$ as a function of relative humidity or a_w .

The definition of a functional form for $r_N(a_w)$ and $\alpha(a_w)$ necessitates the development of representative mean model for the mass ratio μ_w / μ_0 as a function of water activity and an evaluation of the density ratio ρ_0 / ρ_w (the dependent parameters of the $r / r(0)$ ratio above). Figures A.2.1 (a) and A.2.1 (b) show the variation of the mass ratio as a function of $(1 - a_w)$ for two different types of aerosols (urban Model 1 and rural Model 6 respectively) as measured by Hanel (1976).

An interesting phenomena observed in the analysis of Hanel's data was a type of hysteresis effect wherein the variation of the mass ratio versus water activity was different depending on whether the measurements were made in conditions of decreasing or increasing water activity. In practice this phenomenon manifests itself as an abrupt increase in particle size with increasing water activity (deliquescence point) followed by a more gradual increase as the log of $(1 - f)$ with increasing relative humidity (see Tang et al., 1981 for example). If however the relative humidity is decreased down to a point below the deliquescence point (79.5 % relative humidity for $(\text{NH}_4)_2\text{SO}_4$ particles) a state of supersaturation lingers such that a significant humid mass exists well below the deliquescence point.

In the light of the above remarks on the lack of dependence between water activity and particle radius (and as evidenced by the resemblance of the two different water activity curves) we arbitrarily selected the urban Model 1 curve tabulations of Hanel to represent the water activity dependence of the Leitch water soluble aerosol (c.f. Section 2.1.1) along with a dry density of 1.8 g/cm^3 . The latter value represents a density typical of sulfate particles (see for example Sloane, 1984).

In order to facilitate the incorporation of the water activity data into our particle growth model some simple empirical relations were deduced for the data of Figures A.1.2 (a). These relations served as well to produce mean values of mass ratio at those values of water activity characterized by an uncertainty error bar. In the case of the region below the deliquescence point this approach produced an effective average between the states of supersaturation and pre deliquescence.

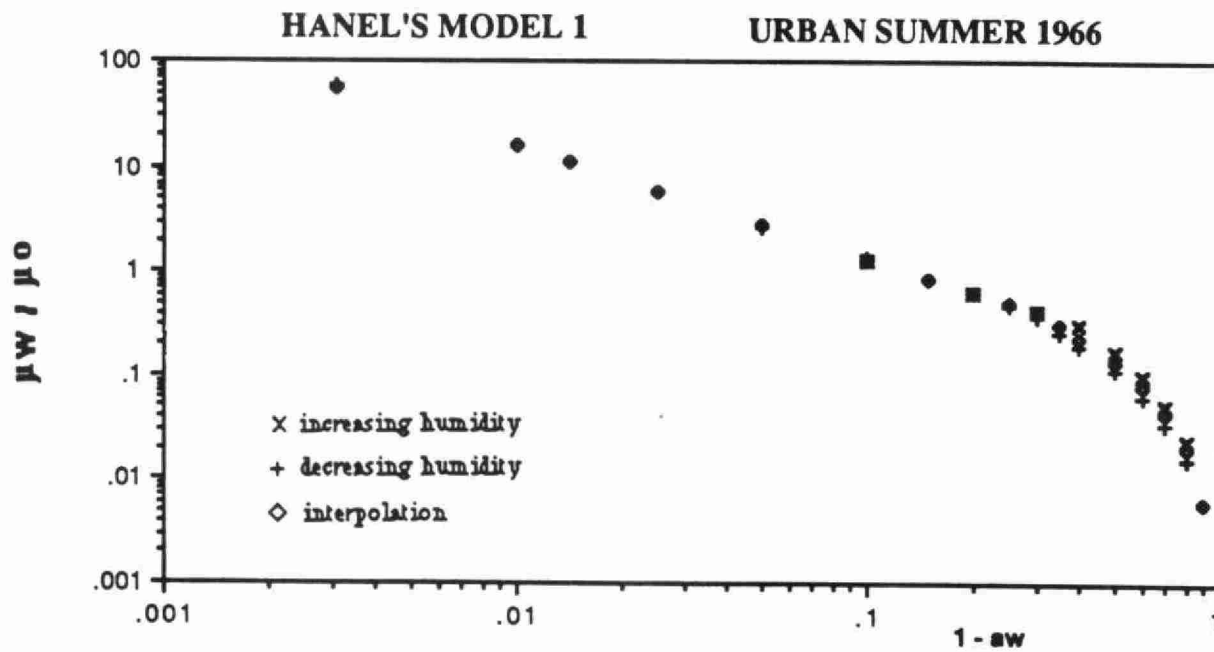


Fig. A.2.1 a)

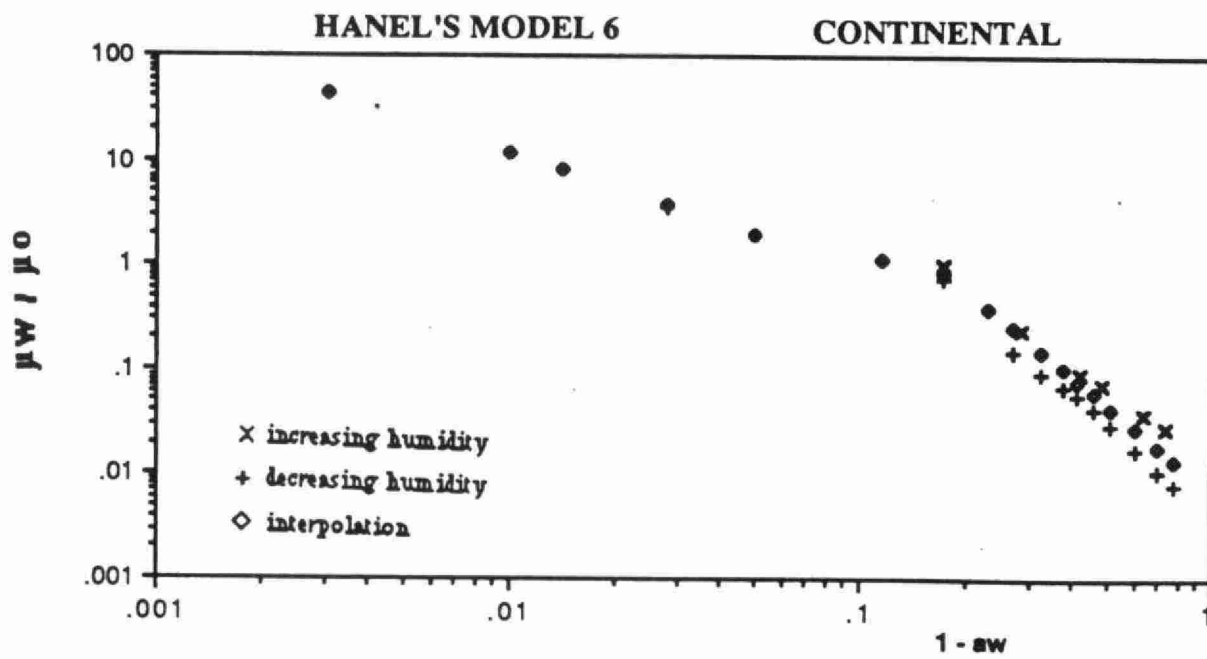


Fig. A.2.1 b)

These relations are given by;

$$\begin{aligned}\mu_w / \mu_o &= 0.0217a_w + 0.375a_w^2 + 0.08333a_w^3 & 0.00 < a_w < 0.30 \\ &= 0.00810 \exp(5.6091 a_w) & 0.30 < a_w < 0.70 \\ &= 0.1083 (1 - a_w)^{-1.0821} & 0.70 < a_w < 0.997\end{aligned}$$

Effective Relative Humidity Over Altitude

In the main body of the text we associate relative humidity with the ground level value commonly measured by meteorological stations. In this section an effective relative humidity over altitude is defined and shown not to be substantially different from the ground level value.

The relative humidity is defined as:

$$f = e_v(T) / e_s(T)$$

where e_v is the ambient vapour pressure and e_s is the saturation vapour pressure. The saturation vapour pressure is given by the empirical relation (AES, 1987):

$$e_s(T) = a \exp \left[\frac{b(T - 273)}{c + (T - 273)} \right]$$

where T is in degrees Kelvin and $e_s(T)$ is in milli barrs ($a = 6.1121$; for $T > 273$, $b = 17.368$, $c = 238.88$ while for $T < 273$, $b = 17.966$, $c = 247.15$). The ambient vapour pressure can be expressed in terms of the ideal gas law as:

$$e_v(T) = .01 R_v \rho_v T$$

where R_v is the gas constant normalized to the molecular weight of water [$.461 \text{ J} / (\text{Kg} \cdot ^\circ\text{K})$] and ρ_v is the water vapour density [g / m^3]. These parameters were computed for two standard midlatitude atmospheric models (summer and winter versions as per McClatchey et al., 1971) in order to demonstrate the variation of relative humidity with altitude and with season (Table A.2.1).

The pertinence of relative humidity for atmospheric scattering problems stems from its influence on aerosol particle growth. An effective relative humidity should be an appropriately weighted average over altitude which accounts for aerosol optical activity. Accordingly, we defined the weighted integral:

$$f_{\text{eff}} = \frac{\int_0^{\infty} f(h) \kappa^{\text{scat}}(h) dh}{\int_0^{\infty} \kappa^{\text{scat}}(h) dh}$$

Table A.2.1 Relative humidity variations with altitude for standard-

Altitude	Pressure	Temperature	Sat. vapour pressure	Water vapour density	Rel. humidity
[km]	[mbarr]	[deg. Kelvin]	[mbarr]	[g/m**3]	[%]
Midlatitude Summer atmosphere					
0	1013	294	24.87	14.0	76.3
1	902	290	19.38	9.3	64.2
2	802	285	14.03	5.9	55.3
3	710	279	9.35	3.3	45.4
4	628	273	6.11	1.9	39.1
5	556	267	3.91	1.0	31.5
6	487	261	2.44	.61	30.1
7	426	255	1.49	.37	29.2
8	372	248	.81	.21	29.6
9	324	242	.645	.12	20.8
10	281	235	.234	.064	29.6
Midlatitude Winter atmosphere					
0	1018	272	5.77	3.5	76.2
1	897	269	4.45	2.5	69.6
2	790	265	3.40	1.8	64.7
3	694	262	2.58	1.2	56.0
4	608	256	1.58	.66	49.2
5	531	250	.94	.38	46.4
6	463	244	.55	.21	43.3
7	402	238	.31	.085	30.4
8	347	232	.17	.035	22.5
9	299	226	.087	.016	19.1
10	257	220	.044	.0075	17.4

where κ^{scat} is the volume scattering coefficient for hygroscopic aerosols. For an exponentially decreasing aerosol number density of scale height H one can write:

$$f_{\text{eff}} = \frac{\int_0^{\infty} f(h) \exp[-h/H] dh}{\int_0^{\infty} \exp[-h/H] dh}$$

Applying this equation to the profiles of Table A.2.1 and assuming an aerosol scale height of 1 km yields $f_{\text{eff}}/f(0)$ ratios of .95 and 1.00 for the summer and winter atmospheres respectively. A somewhat extreme scale height of 3 km yields values of .85 and .93 respectively.

These computations clearly indicate that the effective relative humidity may without serious error be replaced by the relative humidity commonly measured at ground level. A slightly more precise approach would be to employ a mean ratio value (i.e slightly less than unity).

A.3: SOME USEFUL APPROXIMATIONS

The purpose of this section is to present some relevant approximations which help to simplify the physical interpretations presented in the main body of the text. These approximations were not used to create the tables and the figures in the main body but rather serve as a means of quantifying variations to the first order or better.

(a) Mass scattering efficiency for sulfates

Figure A.3.1 shows some calculations of the ratio of wet to dry geometric mean radius (computed from first principles without assuming a constant ratio $r(f)/r(0)$, for a geometric standard deviation $\sigma = 1.24$ and a density ratio of $\rho_o / \rho_w = 1.8$ g/cm³) as a function of relative humidity. These points can be fitted with a set of sectionally linear functions similar to those developed for the ratio of wet to dry mass in Appendix A.2. However for the level of approximation employed in this section a single monotonic relationship suffices. Accordingly an expression of the form:

$$r_N(f) = r_N(0) [1 - f]^{-1.18}$$

yields an accuracy of better than 6% relative to the points shown in Figure A.3.1 (relative humidities between 0 and 95%). This model is applicable within the range of validity ascribed to the simple log normal results deduced in Appendix A.2 (average particle size $\gg .01\mu\text{m}$).

Hansen and Travis (1974) defined an *effective radius* for scattering given by:

$$r_{\text{eff}} = \frac{\int_0^{\infty} r \pi r^2 n(r) dr}{\int_0^{\infty} \pi r^2 n(r) dr}$$

with an *effective variance* given by:

$$v_{\text{eff}} = \frac{1}{r_{\text{eff}}^2} \frac{\int_0^{\infty} (r - r_{\text{eff}})^2 \pi r^2 n(r) dr}{\int_0^{\infty} \pi r^2 n(r) dr}$$

In the case of a log normal distribution the effective variance reduces to a particularly simple and familiar form, viz:

$$\ln r_{\text{eff}} = \ln r_N + \frac{5}{2} \ln^2 \sigma \quad \text{or}$$

$$r_{\text{eff}} = r_N \exp\left(\frac{5}{2} \ln^2 \sigma\right)$$

In order to obtain a simple and rapid approximation to the computation of scattering coefficients one can substitute the expression for the effective radius into the *anomalous diffraction approximation* (Deirmendjian, 1969):

$$Q_{\text{sca}} = 2 \left(1 + \frac{2}{\rho^2}\right) - \frac{4}{\rho} \left(\sin \rho + \frac{\cos \rho}{\rho}\right)$$

$$\text{where } \rho = 2 \left(\frac{2\pi r}{\lambda}\right) (m_r - 1)$$

**SULFATE GEOMETRIC MEAN PARTICULE RADIUS
VS RELATIVE HUMIDITY (NATURAL LOG SCALE)**

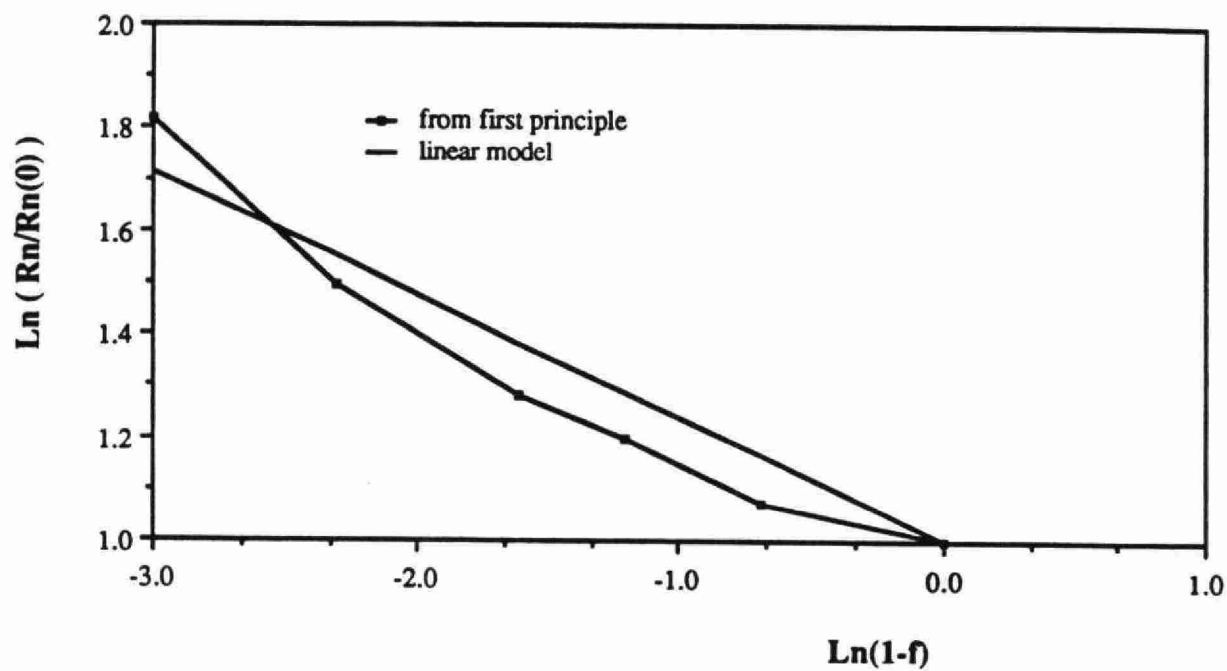


Fig. A.3.1

and where Q_{sca} (defined in Appendix A.1) is the unitless scattering efficiency. The range of validity for this approximation is nominally that the complex part of the refractive index is zero or negligible, the real part of the refractive (m_r) is close to unity and that the size parameter $\alpha = (2 \pi r / \lambda)$ is $\gg 1$. In practice it yields useful numbers beyond the nominal range of validity (in particular if a correction factor introduced by Deirmendjian (1969) is employed). For our purposes we employed the above expression without refinement. Table A.3.1 is a comparison of scattering efficiency calculations using the anomolous diffraction approximation and exact Mie calculations applied to log normal size distributions. In both cases the relative humidity effects were computed using the algorithms defined in Appendix A.2. The table shows that the approximation becomes considerably less reliable as the wavelength increases into the near IR spectral region.

The dry sulfate *mass scattering efficiency* is defined as (c.f. Section 2.2.3 of the main text):

$$\varepsilon(\lambda) = \frac{\Delta \kappa^{\text{sca}}(\lambda)}{\Delta \text{SO}_4^=}$$

For a change in atmospheric state characterized by a simple increase in the total number of aerosols (c.f. continental standard or urban standard models of Table 2.1.4.3) the mass scattering efficiency for a three component atmosphere (sulfates, soots and dust like particles) becomes:

$$\varepsilon(\lambda) = \frac{(\gamma_{\text{soot}}/\gamma_{\text{SO}_4^=}) \sigma_{\text{soot}}}{\mu_{\text{SO}_4^=}} + \frac{(\gamma_{\text{dust}}/\gamma_{\text{SO}_4^=}) \sigma_{\text{dust}}}{\mu_{\text{SO}_4^=}} + \varepsilon(\lambda)_{\text{SO}_4^=}$$

where the denominator of the first two terms is simply the mass of a single dry $\text{SO}_4^=$ particle and the γ 's represent number density fractions (c.f. Appendix A.1). The last term can be written explicitly as:

$$\varepsilon(\lambda)_{\text{SO}_4^=} = \frac{Q_{\text{SO}_4^=} \pi r_2^2}{\frac{4}{3} \pi r_3^3(0) \eta D}$$

where r_2 and r_3 are area and volume radii defined for a log normal distribution in Appendix A.2, η is the molecular weight fraction of sulfate to ammonium sulfate particles and D is the density of ammonium sulfate (1.8 g/cm^3). Employing the expressions for the log normal radii deduced in Appendix A.1, the relative humidity approximation defined above and the expression for effective radius one finds:

$$\varepsilon_{\text{SO}_4^=}(\lambda) \sim \frac{Q_{\text{SO}_4^=} (1-f)^{-36}}{\frac{4}{3} \eta D r_{\text{eff}}(0)}$$

For fine particles defined by $1.5 \leq \rho \leq 4.5$ the ratio Q/ρ is approximately constant ($\sim .8$ using the anomolous diffraction approximation). Accordingly the sulfate scattering efficiency term above varies approximately as $.8 \rho_{\text{eff}}(f)$ for small-particle size distributions. In this region then, we may characterize the scattering as being dominated by volume effects since the scattering cross section varies roughly as the cube of the radius. The mass scattering efficiency expression becomes:

$$\varepsilon(\lambda)_{\text{SO}_4^=} \sim \frac{2.4 (m_r - 1) (1-f)^{-54}}{\lambda \eta D}$$

Table A.3.1

Comparison of exact scattering efficiency computations with values obtained using the Anomalous Diffraction Approximation (log normal size distribution)

	Wavelength [microm.]	A								
		0.4			0.55			0.633		
		m	Q	Q'	m	Q	Q'	m	Q	Q'
Relative humidity (%) rN reff										
0 .12 .135		1.530	2.066	1.908	1.530	1.011	1.128	1.530	.6833	.906
50 .129 .145		1.495	2.086	1.905	1.492	1.047	1.125	1.495	.7183	.904
70 .144 .161		1.451	2.186	1.946	1.449	1.132	1.155	1.451	.7946	.928
80 .154 .173		1.430	2.246	2.005	1.427	1.202	1.196	1.430	.8548	.964
90 .180 .202		1.396	2.494	2.205	1.393	1.412	1.345	1.396	1.036	1.092
95 .245 .234		1.371	2.886	2.562	1.368	1.773	1.642	1.371	1.351	1.353

Notes

m = real part of the refractive index (m(water) = 1.339, 1.333, 1.332 for 0.4, 0.555, and 0.633 microm. respectively)

Q = exact scattering efficiencies computed by applying the first principle particle growth equations, arbitrarily exact Mie calculations, and and subsequently integrating $Q(2\pi r/\lambda)$ over the entire size distribution

Q' = scattering efficiency from the anomalous diffraction approximation

A = log normal (sulfate) size distribution

(rN(0) = .12 microm., sigma(0) = 1.24)

rN = geometric mean radius, reff = effective radius [microm.]

and hence is independent of particle sizing parameters. The other components of the total sulfate mass scattering efficiency (soot and dust) are sufficiently small at visible wavelengths that they do not significantly disturb this condition of approximate constancy.

Actual values of the mass scattering efficiency (computed using the anomalous diffraction approximation and the relative humidity algorithms of Appendix A.2) at a wavelength of 0.55 μm are graphed in Figure A.3.2 as a function of the dry effective radius. The dashed region for which approximate constancy of ϵ applies is indicated. The dry effective radius was allowed to vary by either changing the dry geometric mean radius ($.12 \leq r_N(0) \leq .24$) or the geometric mean standard deviation ($1.2 \leq \sigma \leq 2.6$) until the wet effective radius ($\rho_{\text{eff}}(f)$) exceeded the fine particle limits (indicated as dashed lines on the graph).

(b) Single scattering albedo and the mixing ratio of soot to sulfates

At a given altitude in the atmosphere the aerosol single scattering albedo is given by (c.f. Appendix A.1):

$$\begin{aligned} \omega_o &= \frac{\kappa^{\text{sca}}(\lambda)}{\kappa(\lambda)} \\ &= \frac{N_C \sigma_C^{\text{sca}} + N_{\text{SO}_4} \sigma_{\text{SO}_4}^{\text{sca}} + N_D \sigma_D^{\text{sca}}}{N_C \sigma_C + N_{\text{SO}_4} \sigma_{\text{SO}_4} + N_D \sigma_D} \end{aligned}$$

where the subscripts C, SO_4 and D refer respectively to carbonaceous soot, sulfate and dust like particles and the symbol "N" represents number density. If the contribution of the dust like particles is neglected along with absorptive component of the sulfates, the expression for ω_o reduces to:

$$\begin{aligned} \omega_o &= \frac{\omega_o^C(\lambda) x + 1}{x + 1}, \quad \text{where} \\ x &= \frac{N_C}{N_{\text{SO}_4}} \frac{\sigma_C(\lambda)}{\sigma_{\text{SO}_4}^{\text{sca}}(\lambda, f)} \end{aligned}$$

and where $\omega_o^C(\lambda)$ is the single scattering albedo for soot particles only. The relative humidity (f) dependence of the sulfate scattering cross section is shown explicitly. This latter parameter along with the ratio of soot to sulfate scattering efficiencies is easily computed using Mie scattering computations. Accordingly there exists an approximate one to one relationship between the aerosol single scattering albedo and the soot to sulfate number density mixing ratio.

This simplification can be exploited to extract the single scattering albedo given a value of the mixing ratio and relative humidity or conversely a value of the mixing ratio given an estimate of the single scattering albedo and the relative humidity. Figure A.3.3 is a graph of the aerosol single scattering albedo as a function of the mixing ratio parameter "x" computed for the urban standard and continental standard aerosol models (see Chapter 2 in the main body of the test) at two different relative humidities and a wavelength of 0.633 μm . The dashed curve is a plot of the simplified expression presented directly above. The difference between the two curves, which is not large, could be further improved by introducing empirical correction factors.

(c) Error rate approximations

The error rate calculations performed in the main body of the text can be, at least in a first order sense, vastly extended with respect to the variation of the input parameters. To this end we introduce the analytical/empirical function for apparent reflectance:

$$\rho^* = \rho T \exp[-k_1 \epsilon \text{SO}_4^-] + k_2 \rho \epsilon \text{SO}_4^- + (k_1 - k_2) \rho_c \epsilon \text{SO}_4^- + \rho_r$$

MASS SCATTERING EFFICIENCY VS EFFECTIVE (DRY) RADIUS

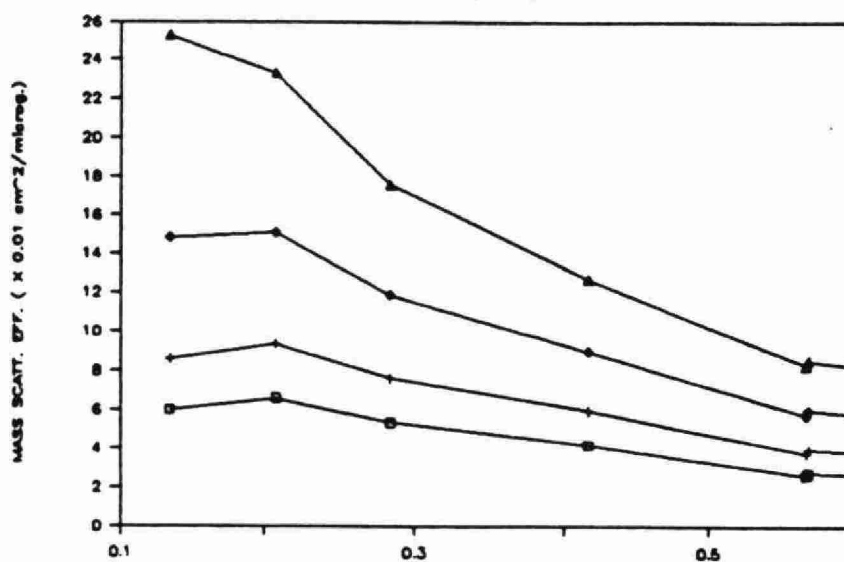


Fig A.3.2

EFFECTIVE (DRY) RADIUS (microns)

RELATIVE HUMIDITY : \square 0% $+$ 70% \diamond 90% \triangle 95%

ALBEDO VS SOOT MIXING RATIO WAVELENGTH = 0.550 MICRONS

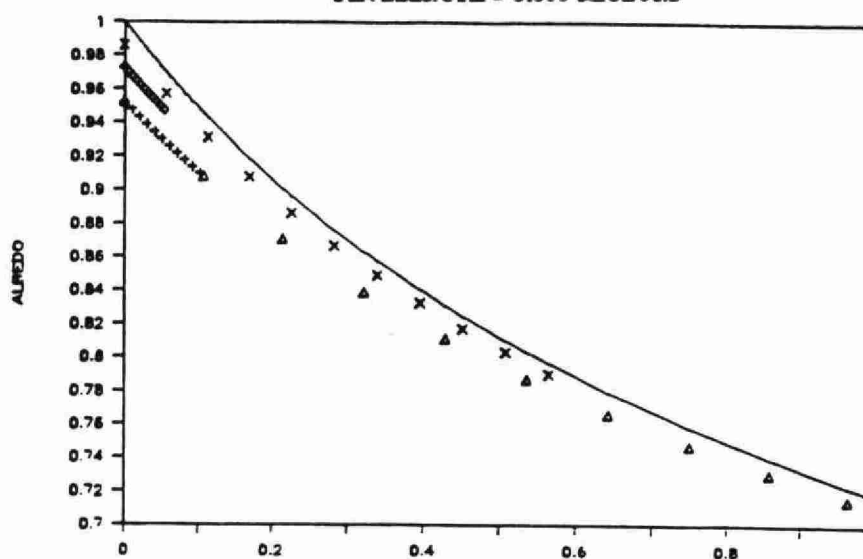


Fig A.3.3

SOOT MIXING RATIO $(X = \frac{M_s \sigma_s^{tot}}{M_{tot} \sigma_{tot}^{scat}})$

— Linear approximation

+ Continental 70%

 \triangle Urban 70% \diamond Continental 90% \times Urban 90%

where k_1 and k_2 are constants to be determined, ρ_c is the critical reflectance, ρ is the surface reflectance, ϵ is the aerosol mass scattering (per unit mass of sulfates), ρ_r is the background apparent reflectance in the absence of sulfates and T is a transmission function which accounts for the effects of attenuation due to molecules and aerosol attenuators other than sulfates. This simplistic model is constructed around the assumptions (i) that the apparent reflectance is linear with surface albedo (ii) that the apparent reflectance is linear with sulfate concentration in the presence of a non reflecting surface (iii) that the addition of a reflecting surface adds an exponential attenuation term plus a term linear with sulfate concentration and (iv) that a critical reflectance exists where all apparent reflectance lines intersect independent of the sulfate concentration (c.f. Section 3.4.2 of the main text). The latter assumption is relaxed somewhat in the model since a unique intersection point exists only for small sulfate concentrations. A further simplification (which is not an intrinsic limitation of the model above) was to assume that the critical reflectance was independent of the scattering efficiency or hence of the relative humidity. Finally, the expression includes the tacit assumption that changes in the apparent reflectance due to variations in the phase function are second order.

Given the above analytical equation it is a simple matter to derive the three basic partial derivatives (error rates) introduced in Chapter 4. For simplicity we drop the standard partial derivative subscripts unless their inclusion is essential to an understanding of a particular equation. The first error rate is obtained by straight differentiation, viz:

$$\frac{\delta SO_4^-}{\delta \rho^*} = \frac{1/\epsilon}{k_1 \rho_c + k_2 (\rho - \rho_c) - k_1 \rho_c T \exp(-k_1 \epsilon SO_4^-)}$$

This error rate shows most the principal properties of main text Figure 4.1.1 including the change of sign across the critical reflectance, and the reduction of the error slope with increasing optical activity (increasing ϵ). It does not respond to the abrupt non linear dependences on sulfate concentration which are responsible for some of the more extreme excursions seen in the same Figure. Table A.3.2 below summarizes some of the comparisons made.

Given the above expression and given that the denominator is not strongly dependent on ϵ one can express the dependence of this error rate in terms of a reference error rate according to the approximate relation:

$$\frac{\delta SO_4^-}{\delta \rho^*} = \frac{\epsilon_{ref}}{\epsilon} \left(\frac{\delta SO_4^-}{\delta \rho^*} \right)_{ref}$$

For the surface reflectance error rate one can write (constant ρ^*):

$$0 = \left(\frac{\delta \rho^*}{\delta SO_4^-} \right)_{\rho} \Delta SO_4^- + \left(\frac{\delta \rho^*}{\delta \rho} \right)_{SO_4^-} \Delta \rho$$

If the sulfate differential is due to a change in surface reflectance under conditions of constant apparent reflectance one can replace the differentials by their appropriate partial derivatives and after some rearrangement obtain:

$$\left(\frac{\delta SO_4^-}{\delta \rho} \right)_{\rho^*} = - \left(\frac{\delta SO_4^-}{\delta \rho^*} \right)_{\rho} \left(\frac{\delta \rho^*}{\delta \rho} \right)_{SO_4^-} \quad \text{where;}$$

$$\left(\frac{\delta \rho^*}{\delta \rho} \right)_{SO_4^-} = \epsilon SO_4^- k_2 + T \exp(-k_1 \epsilon SO_4^-)$$

Unless the sulfate concentration is very large the latter term is of the order of T . The surface reflectance error rate is

consequently strongly associated with the apparent reflectance error rate with a change in sign, viz:

$$\left(\frac{\delta SO_4}{\delta \rho}\right)_{\rho^*} \sim - \left(\frac{\delta SO_4}{\delta \rho^*}\right)_{\rho}$$

and one may effectively describe its behavior in reference to the apparent reflectance error rate. This approximate correspondance can be verified by comparing the main text error rate curves in Figures 4.1.1 and 4.1.3.

The sulfate mass scattering efficiency error rate reduces to the expression:

$$\frac{\delta SO_4}{\delta \epsilon} = - \frac{SO_4}{\epsilon}$$

This simple relation results because the analytical expression for ρ^* defined above is constant if the product ϵSO_4 is constant. The sign of this error rate is always negative because an increase in ϵ implies a greater optical thickness which must be offset by a decrease in sulfate concentration if the apparent reflectance is to remain constant.

If the change in ϵ is brought about by a change in relative humidity then the actual value of the error rate (absolute value) will be less than that indicated above. This is because an increase in relative humidity implies a decrease in phase function at large scattering angles typical of satellite remote sensing (see the main text Figure 2.2.2.3 for example). Accordingly an increase in ϵ due to an increase in relative humidity induces a decrease in the phase function and hence a reduced requirement for the offsetting sulfate reduction. Figure 4.1.2 in the text clearly illustrates this effect.

In the case where the change in ϵ is due to a change in relative humidity the mass scattering efficiency error rate is easily converted into a relative humidity error rate, viz:

$$\frac{\delta SO_4}{\delta f} = \frac{\delta \epsilon}{\delta f} \frac{\delta SO_4}{\delta \epsilon}$$

As noted above in the previous section, the mass scattering efficiency can be expressed approximately in terms of its dry value as:

$$\epsilon = \epsilon(0) (1 - f)^{-n} \quad \text{so that;}$$

$$\frac{\delta \epsilon}{\delta f} = \frac{n\epsilon}{1 - f} \quad \text{and hence;}$$

$$\frac{\delta SO_4}{\delta f} = - SO_4 \frac{n}{1 - f}$$

where f is in the fractional representation. The exponent " n " varies with particular (dry) size region and generally increases with decreasing (dry) particle size. It can be computed from numerical values of ϵ such as those presented in Figure A.3.1.

The linear increase of mass scattering efficiency error rate magnitude with equivalent sulfate concentration is a phenomenon which can be observed (except for the abrupt non linear changes) in the main text Figure 4.1.2. If a given atmospheric state differs from a reference state only in that ϵ is different at the same relative humidity, the mass scattering efficiency error rate can accordingly be related to the reference error rate by the expression:

$$\frac{\delta SO_4^-}{\delta \epsilon} = \frac{\epsilon_{\text{ref}}}{\epsilon} \left(\frac{\delta SO_4^-}{\delta \epsilon} \right)_{\text{ref}}$$

Table A.3.2 Apparent reflectance and apparent reflectance error rate ($\delta SO_4^- / \rho^*$) comparisons between 5S calculations and a simple analytical model (see text). Conditions are nadir geometry, solar zenith angle = 45° , $0.55 \mu\text{m}$ wavelength and the urban variant model. The selected model parameters were $\rho_c = .2$, $\rho_r = .036$, $k_1 = 2.88\text{E-}4$ and $k_2 = 0$ (the model was largely insensitive to the exact values of k_1 and k_2 if $k_1 - k_2$ was kept constant). The mass scattering efficiencies for 70%, 90% and 95% relative humidity were respectively 6.84, 13.0, and 23.4.

(a) Apparent reflectance

ρ	SO_4^- [$\mu\text{g}/\text{m}^3$]	f [%]	ρ^* (5S)	ρ^* (analytical approximation)
0.0	0	70	.036	.036
0.0	50	70	.0571	.0557
0.0	50	90	.0729	.0734
0.0	50	95	.0981	.103
0.5	0	70	.450	.451
0.5	50	70	.412	.431
0.5	50	90	.406	.417
0.5	50	95	.404	.399

(b) apparent reflectance error rate ($\mu\text{g}/\text{m}^3$ per percentage increment in ρ^*)

ρ	SO_4^-	f [%]	$\delta SO_4^- / \rho^*$ (5S)	$\delta SO_4^- / \rho^*$ (analytical approximation)
0.0	0	70	38	25.4
0.0	50	70	21	25.4
0.0	50	90	10	13.4
0.0	50	95	6	7.41
0.5	0	70	-5	-23.7
0.5	50	70	-29	-28.9
0.5	50	90	-37	-18.6
0.5	50	95	<-100	-15.5

References for Appendix A

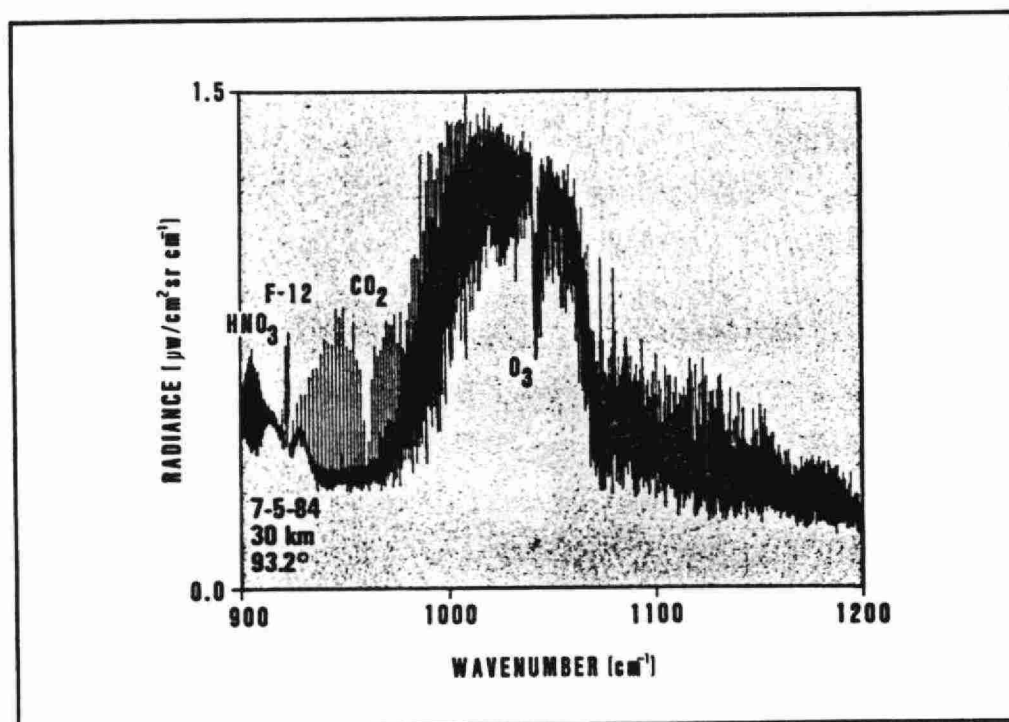
- Abramowitz, M., I. A. Stegun, (1972), Handbook of Mathematical Functions, Dover, New York.
- AES (Atmospheric Environment Service - Environment Canada), (1987), Fichier Climatologique # 014.
- Born, M., E. Wolf, (1965), Principles of Optics, Pergammon Press, New York.
- Deirmendjian, D., (1969), Electromagnetic Scattering on Spherical Polydispersions, American Elsevier, New York.
- Hanel, Gottfried, (1976), The Properties of Atmospheric Aerosol Particles as a function of the Relative Humidity at Thermodynamic Equilibrium with the Surrounding Moist Air, Adv. in Geophysics, **19**, pp. 74 - 183.
- Hansen, J. E., L. D. Travis, (1974), Light Scattering in Planetary Atmospheres, Space Science Reviews, **16**, pp. 527-610.
- McClatchey et al., (1971), Optical Properties of the Atmosphere, AFCRL - TR - 71 - 0279, Environ. Research paper no 354, L. G. Hanscom Field, Bedford, Mass, USA.
- Tang, I. N., Wong, W. T., H. R. Munkelwitz, (1981), The Relative Importance of Atmospheric Sulfates and Nitrates in Visibility Reduction, Atmospheric Environment, **15**, pp. 2463-2471.
- Wickramasinghe, N. C., (1973), Light Scattering Functions for Small Particles with Applications in Astronomy, Wiley, Toronto.

APPENDIX B

Comparison of Radiative Transfer Models Used to Determine Atmospheric Optical Parameters from Space

Modeling of the Atmosphere

 SPIE Volume 928



Laurence S. Rothman
Editor

7-8 April 1988
Orlando, Florida

Critical Reviews of Optical Science and Technology
Modeling of the Atmosphere

The papers appearing in this book comprise the proceedings of the meeting mentioned on the cover and title page. They reflect the authors' opinions and are published as presented and without change, in the interests of timely dissemination. Their inclusion in this publication does not necessarily constitute endorsement by the editors or by SPIE.

Please use the following format to cite material from this book:

Author(s), "Title of Paper," *Modeling of the Atmosphere*, Laurence S. Rothman, Editor, SPIE Vol. 928, page numbers (1988).

Library of Congress Catalog Card No. 88-61026
ISBN 0-89252-963-6

Copyright © 1988, The Society of Photo-Optical Instrumentation Engineers. Individual readers of this book and nonprofit libraries acting for them are freely permitted to make fair use of the material in it, such as to copy an article for use in teaching or research. Permission is granted to quote excerpts from articles in this book in scientific or technical works with acknowledgment of the source, including the author's name, the book name, SPIE volume number, page, and year. Reproduction of figures and tables is likewise permitted in other articles and books, provided that the same acknowledgment-of-the-source information is printed with them and notification given to SPIE. Reproduction or systematic or multiple reproduction of any material in this book (including abstracts) is prohibited except with the permission of SPIE and one of the authors. In the case of authors who are employees of the United States government, its contractors or grantees, SPIE recognizes the right of the United States government to retain a nonexclusive, royalty-free license to use the author's copyrighted article for United States government purposes. Address inquiries and notices to Director of Publications, SPIE, P.O. Box 10, Bellingham, WA 98227-0010 USA.

Published by

SPIE—The International Society for Optical Engineering
P.O. Box 10, Bellingham, Washington 98227-0010 USA
Telephone 206/676-3290 (Pacific Time) • Telex 46-7053

SPIE (The Society of Photo-Optical Instrumentation Engineers) is a nonprofit society dedicated to advancing engineering and scientific applications of optical, electro-optical, and optoelectronic instrumentation, systems, and technology.

Printed in the United States of America.

Cover illustration: Atmospheric radiance spectra in the $900\text{--}1200\text{ cm}^{-1}$ region obtained with SCRIBE, 0.06 cm^{-1} resolution cooled interferometer. See paper on "High resolution studies of atmospheric infrared emission and absorption spectra," by A. Goldman and D. G. Murcray on pp. 42-58.

Comparison of Radiative Transfer Models used to Determine Atmospheric Optical Parameters from Space

Alain ROYER, Norman T. O'NEILL, Anthony DAVIS * and Laurent HUBERT

CARTEL, Université de Sherbrooke, Sherbrooke, Québec, Canada J1K 2R1

* Department of Physics, McGill University, Montréal, Québec, Canada, H3A 2T8

ABSTRACT

An array of models and techniques exist for the calculation of the atmospheric backscattered radiance and ground reflected radiance received at satellite altitudes. In remote sensing applications, where one deals in mega-byte units of data, it is essential that these models be computationally fast while retaining a reasonable degree of accuracy. We have evaluated a number of such models (Lowtran 6, Turner, Discrete ordinates method, 5S) relative to an accurate multiple scattering, multi-layer (Dave) model in order to assess the performance of these models in an inversion scheme for aerosol optical depth.

The Turner and single scatter Lowtran 6 models generally produced large errors in apparent reflectance. Overall, the Turner model was not significantly better than the Lowtran 6 model except at near nadir geometries and non zero albedos. The 5S model which is orders of magnitude more rapid than the DOM model was significantly more accurate than the L6 and Turner models. The accuracy of the inversion procedures for the extraction of aerosol optical depth from satellite apparent reflectance was then analyzed for the two most precise models (DOM and 5S). For typical measurement conditions, the 5S inversion errors were found to be of the order of .1 in a turbid atmosphere case (aerosol optical depth approximately .5). The DOM produced the most impressive results in terms of comparisons with the Dave computations. It's time of execution, however, is a serious constraint with respect to satellite remote sensing applications.

INTRODUCTION

Arbitrarily exact numerical methods for the solution of the radiative transfer equation in planetary atmospheres have evolved in parallel with the processing power of digital computers (see for example Hansen and Travis)^{1,6}. In recent years there has been a natural and beneficial tendency to rationalize the cumbersome numerical overhead associated with generalized solutions by extracting the essential physical characteristics governing a particular problem in order to achieve solution accuracies commensurate with measurement precision. In terrestrial remote sensing applications where one deals in megabyte units of data the rationalization approach is a necessity born of a need to achieve practical data processing throughput rates. This problem is further complicated by the existence of spatial inhomogenities in the atmosphere which, short of a full scale 3 dimensional radiative transfer solution, require at least a mosaicing of individual solutions. Finally, if the intent is to invert remote sensing data for purposes of studying the atmosphere itself, the tractibility of the inversion methodology is clearly dependent on the speed and simplicity of the radiative transfer solution.

The objective of this paper is to evaluate a number of commonly used radiative transfer models in terms of relative precision and speed and to investigate the implication of these constraints on inversion algorithms for the extraction of aerosol optical parameters from passive remote sensing imagery. Aerosols are here defined to be particles whose dimension is the order of a wavelength and whose optical variation is largely confined to the troposphere. The wavelength region of interest extends from the near UV (.4 μm) to the near IR (1.6 μm).

The approximate radiative transfer models which simulate radiance signals received at satellite altitudes represent various levels of sophistication ranging from single scatter models to numerical single layer solutions of the radiative transfer equation. The strategy employed in this study was to analyze these models relative to a multilayer multiple scattering numerical solution (Dave)¹. Our goal was thus to clarify the uncertainty associated with

modeling contributions to the total error budget and hence facilitate tradeoff decisions of speed versus accuracy in model selection.

In the first section of the paper we present a review of past radiative transfer work in the context of remote sensing and inversion methodologies. The second section deals with the relevant radiative transfer concepts followed by a description and physical interpretation of the radiative transfer models which we selected for comparison. These models identified as L6 (Lowtran 6 single scattering model (Kneizis et al.)², the Turner model (Turner and Spencer)³, 5S ("Simulation of the Satellite Signal in the Solar Spectrum", Tanré et al.)⁴) and DOM (discrete ordinates method, Liou⁵, O'Neill⁶) are either readily available as computer codes or are well described in the literature. In the third section the models are compared with the baseline DAVE results in terms of apparent reflectance differences as a function of a variety of geometrical and environmental parameters. The subsequent section reviews the implication of these differences in terms of inversion procedures for optical depth. We conclude by presenting a strategy for the exploitation of the models investigated.

1. BACKGROUND

For remote sensing applications the driving force behind the development of radiative transfer models was a requirement for atmospheric corrections to remove what was considered to be a contaminating influence on the signal reflected from the terrestrial surface (see ref. Bariau et al.⁷ for a comprehensive survey of remote sensing inspired radiative transfer models). In as much as the estimation of atmospherically scattered signals (path radiance) is critical whether one speaks of atmospheric correction or inversion, the models developed in the former application have proven valuable in the latter. Note that, within the context of this present study, we are excluding from consideration those semi-empirical or ratio types of approaches which extract values of the path radiance from other radiometric measurements (see ref. Gordon et al.⁸ for example).

The first step towards a pragmatic radiative transfer algorithm was the development of the Turner model (Turner and Spencer)³. This model which was intended to be an improvement over single scattering models was appealing in its analytical simplicity and rapidity of execution. An advancement over this type of model was realized by Gordon⁸ and Tanré et al.⁹ who revived the concept first introduced by Sekara¹⁰ of effectively separating the molecular and non molecular radiance fields. Further improvements included a capability for modeling the effects of spatially inhomogeneous surface reflectance (Tanré et al.)¹¹, more realistic 2 layer modeling of vertical inhomogeneities (Deschamps et al.)¹² and a simple method to account for errors associated with the decoupling assumption of the Rayleigh and aerosol radiance fields (ibid).

The inversion of radiative transfer models to extract inherent optical parameters is a process susceptible to modeling errors and radiometric calibration errors. Modeling errors can be further classified into two types: numerical modeling errors which result from approximations applied to shortcut the computational work necessary to achieve an arbitrarily exact solution of the radiative transfer equation and physical modeling errors which result from limitations in the characterization of the optical parameters input to the radiative transfer equation. The first type is the subject of this paper.

The physical modeling errors are coupled to the amount of apriori knowledge and degree of physical reality incorporated into a given input parameter to the radiative transfer model. In the context of an inversion procedure the parameters to be inverted (which are normally input parameters to the radiative transfer equation) are forced to converge to values which reflect the reality of their individual constraints and the nominal values assigned to the other input parameters. Depending on the type of inversion which is being performed the physical modeling errors can include: phase function variations related to changes in size distribution (Martellacci et al.)¹³, variations in the real and complex parts of the refractive index (Fraser and Kaufman¹⁴; Hanel¹⁵), the neglect of polarization effects

(Hansen and Travis¹⁶; Kattawar et al.¹⁷), departures from Mie scattering phase functions (Schuerman)¹⁸, and the effects of atmospheric stratification (Liou)¹⁹ as well as horizontal inhomogeneity (Mishin)²⁰.

Other sources of physical modeling errors are related to the influence of thin cirrus clouds (Saunders and Kriebel²¹), the effects of spatial non homogenieties in surface reflectance (Tanré et al.¹¹; Mekler and Kaufman²²) and departures from the Lambertian assumption (Tanré et al.)²³. Gaseous absorption and the way in which it is incorporated in the modeling may also play a significant role. Real perturbations from nominal assumed values for absorption due to amongst others, water vapour, nitrogen dioxide, and ozone (visible spectral region) may, depending on the precision required and the wavelength range selected, bias the radiative transfer inversion algorithm.

Errors of radiometric calibration have increased in importance with the evolution of modeling and sensor technologies. The first generation of broad band sensors (GOES-VISSR, NOAA-AVHRR, and NUMBUS-7-CZCS) produced useful results which however suffered from the absence of post launch calibrations (Fraser et al.²⁴; Frouin et Gauthier²⁵; Gordon²⁶) and limited radiometric resolution (Griggs)²⁷.

The aerosol optical parameters which are most readily extracted by inversion techniques include the aerosol scattering optical depth used as an indicator of total columnar aerosol concentration, the single scattering albedo as a measure of absorption (Kaufman)²⁸ and optical depth spectral coefficients as indicators of the average atmospheric size distribution (Aranuvachapun)²⁹. The principal influence on radiance variation and hence the most easily determined optical parameter is the aerosol scattering optical depth. Inversion algorithms for the extraction of this parameter are further simplified by it's strong linearity versus radiance over large ranges. This relationship is well known in modeling studies and has been observed in empirical comparisons between satellite data and ground based extinction measurements (Griggs²⁷; Mekler et al.³⁰; Norton et al.)³¹.

2. THE RELEVANT RADIATIVE TRANSFER THEORY AND MODEL DESCRIPTION

2.1 Statement and Reduction of the problem

In this section a brief overview of radiative transfer theory is presented in order to facilitate and complement the discussions of the various models which were studied. More detailed and comprehensive reviews can be found in fundamental texts such as Chandrasekhar³², Lenoble³⁴ and Hansen and Travis¹⁶.

The radiation field in and around the earth's atmosphere is best described by the concept of radiance $I(\mathbf{r}, t; \Omega, \lambda)$; the amount of EM flux (energy/surface /time) propagating into direction Ω (unit vector) at wavelength λ per unit of solid angle per unit of wavelength, measured at position \mathbf{r} and time t . I obeys the following kinetic equation in a medium of constant refractive index:

$$\frac{1}{c} \frac{\partial I}{\partial t} + \Omega \cdot \nabla I = -\alpha(I-S) \quad (1)$$

where c is the speed of light, ∇ the gradient operator, and α the volume extinction coefficient (i.e. absorption plus scattering). The source function S is given by:

$$S(\mathbf{r}, t; \Omega, \lambda) = \frac{\omega_0}{4\pi} \oint p(\Omega, \Omega') I(\mathbf{r}, t; \Omega', \lambda) d\Omega' \quad (2)$$

where the integral symbol represents an integration in solid angle over all directions (4π steradians).

This describes coherent scattering processes (i.e. excluding redistribution in wavelength). The single-scattering albedo ω_0 is defined as the ratio of the scattering (σ) to extinction (α) coefficients. The phase function p depends on $\Omega \cdot \Omega' = \cos(\text{scattering angle})$. We adopt the usual normalization for p , viz:

$$\oint p(\Omega, \Omega') d\Omega' = 4\pi \quad (3)$$

To determine I completely, boundary conditions must be specified, these boundary conditions take the form of incoming radiance at all interfaces of the medium with its environment. In the case of planetary atmospheres, the boundary conditions are specified by an external source of (collimated) radiation from above and, often, a partially reflective surface below.

The general three-dimensional Radiative Transfer (RT) problem is extremely difficult to solve although progress is being made towards a general method (Stevens)³³. Nevertheless many solutions have been obtained in particular cases (one of which is mentioned further in connection with the 5S model). The time-dependent problem has been applied to lidar signal analysis.

In the rest of this study (and most RT research to date), stationarity and horizontal homogeneity are assumed. For geometry which is plane parallel the RT equation becomes:

$$\mu \frac{dI}{dz} = -\alpha(I - S) \quad (4)$$

where μ is the direction cosine relative to the vertical axis (Ω_z) and z is the vertical position coordinate. I and S are now functions of z , μ , ϕ (azimuthal angle) and λ (wavelength). The λ dependency enters through the optical parameters α , σ , ω_0 and p which may as well be functions of z . In this context, one can define the dimensionless space coordinate known as *optical depth*:

$$\tau = \int_z^\infty \alpha(z') dz' \quad (5)$$

Hence the standard RT integro-differential equation:
$$\frac{dI}{d\tau} = I - \frac{\omega_0}{4\pi} \oint p I d\Omega' \quad (6)$$

with boundary conditions $I(0; \mu, \phi) = E_s \delta(\mu + \mu_s) \delta(\phi)$, $\mu < 0$ $I(\tau^*; \mu, \phi) = \frac{\rho}{\pi} F_-(\tau^*)$, $\mu > 0$ (7)

where
$$F_\pm(\tau) = \int_0^{2\pi} \int_0^\pi I(\tau; \mu, \phi) \mu d\mu d\phi \quad (8)$$

designate up/downwelling irradiances. E_s is the extra-terrestrial irradiance incident at zenith angle $\theta_s = \cos^{-1} \mu_s$ in the plane $\phi = 0$, τ^* is the optical thickness of the atmosphere ($z: 0 \rightarrow \infty$) and ρ is the reflectance of a Lambertian surface located at $\tau = \tau^*$. For simplicity we have dropped the explicit dependence of I on λ .

Notice that (6) admits the integrating factor $\exp(-\tau/\mu)$. Accordingly the formal solution to the RT equation yields the (total) radiance:

$$I(\tau; \mu, \phi) = I(\tau^*; \mu, \phi) e^{-\frac{(\tau^* - \tau)}{\mu}} + \int_{\tau}^{\tau^*} S(t; \mu, \phi) e^{-\frac{(t - \tau)}{\mu}} \frac{dt}{\mu} \quad (9)$$

for upwelling radiation ($\mu > 0$). The first term represents (reflected) radiation emerging from the bottom of the atmosphere while the second term (path radiance) is the radiation resulting from atmospheric scatter.

2.2 Various approaches for solving the RT problem

The solution offered by equation (9) is deceptive in its simplicity since the real difficulty lies in evaluating the source function S . A number of approaches are reviewed in Lenoble^{3,4}. She distinguishes between "exact", "computational" and "approximate" methods. The exact solutions such as those which reduce to Chandrasekhar's X and Y functions provide analytical expressions for $I(\tau; \mu, \phi)$ in terms of the parameters μ_s , ρ , ω_0 , τ^* and ρ . The phase function is often expressed as the Legendre polynomial summation:

$$p(\cos\theta) = \sum_0^{\infty} \beta_l P_l(\cos\theta) \quad (10)$$

Rayleigh scattering by particles much smaller than the wavelength of incident radiation is described by two terms ($\beta_0 = 1$, $\beta_2 = .5$) while more anisotropic phase functions characteristic of atmospheric aerosols require a relatively large number of terms.

Computational methods are essentially numerical recipes that converge toward the exact solution if enough computer time is afforded. Our study includes two such methods: spherical harmonics (DAVE) and the DOM. Other examples are Monte-Carlo simulations, adding/doubling and successive orders of scattering (see Hansen and Travis¹⁶ for a review).

Following Irvine³⁵ the approximate methods can be further separated into two categories. The first type are those that model the phase function exactly but employ an approximate solution to the RT equation. The Turner model and the L6 (single scattering) model are classical examples of this category which typically involve an approximate expression being taken for the radiance integrand of the source function in equation (2). The second type are those models that utilize an approximate form for the phase function in order to derive an exact solution to the resulting radiative transfer problem. The Sobolev technique which is employed in one of our test models (5S) employs this approach by truncating the Legendre expansion of the phase function after two terms.

2.3 Application to Remote Sensing - Geometrical and Radiometric Conventions

RT theory is applied in satellite remote sensing to predict the path radiance and hence the total radiance above the atmosphere (i.e. $I^* = I(0; \mu, \phi)$ in equation (9)). Figure 2.1 is a schematic diagram which shows the pertinent parameters used to describe the geometry of an exo-atmospheric radiance measurement.

It is desirable to normalize the upwelling radiance in order to work with some dimensionless measure of the satellite signal. A natural choice is the apparent reflectance defined by:

$$\rho^* = \frac{\pi I^*}{\mu_s E_s} \quad (11)$$

For a given atmospheric state the satellite measured (total) apparent reflectance is a function of the wavelength, the boundary conditions parameters ρ , θ_s , and the viewing geometry angles ϕ and $\theta_v = \cos^{-1} \mu$. The values of wavelength adopted, in our comparisons, span the visible to near IR atmospheric window: $\lambda = \{.455, .555, .655, .8455, 1.61\}$. The range of values chosen for the boundary conditions parameters were $\rho = 0.0(0.2)0.8$ and $\theta_s = \{30^\circ, 45^\circ, 60^\circ, 70^\circ, 75^\circ\}$. The viewing geometry angles which represent the original independent

variables of RT theory were assigned the values $\theta_v = 0^\circ(10^\circ)70^\circ$ and $\phi = 0^\circ(30^\circ)180^\circ$. In all, 8400 points in parameter space were computed per atmospheric state and per model (see Table 3.1).

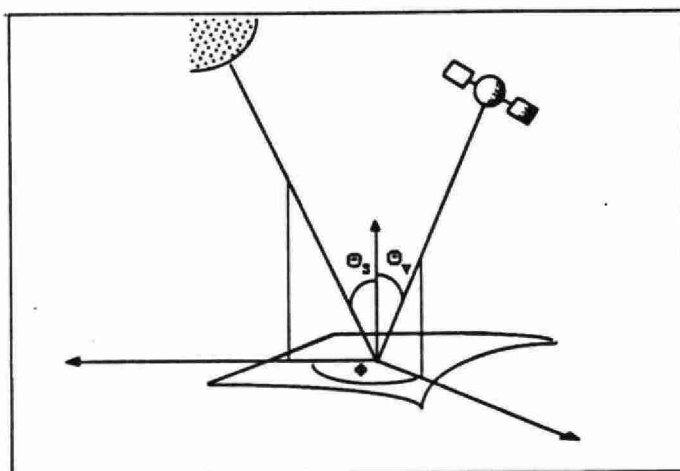


Figure 2.1 Schematic diagram of satellite measurement geometry ; θ_s is the sun's zenith angle, θ_v is the observer's zenith angle and ϕ is the observer's azimuth angle relative to the solar plane.

2.4 Description of radiative transfer models

In terrestrial remote sensing applications the total optical depth (τ^*) employed in a given model is composed of scattering contributions from Rayleigh or molecular particles (τ_R), absorbing and scattering contributions from aerosols (τ_A), and absorption contributions from particular molecular constituents ($\Sigma\tau_{gas}$). The models employed in the comparative study were either multi-layer (Dave and L6) or single layer (Turner, DOM, and 5S). The single layer models ignore vertical variations in the phase function and assume a unique representation which is a weighted mean of the Rayleigh and aerosol phase functions where the weights are proportional to the total Rayleigh optical depth and the aerosol (scattering) optical depth respectively (see Turner for example). The multi-layer models admit vertical variations in the phase function which is taken as a Rayleigh/aerosol mean weighted by the volume scattering coefficients characterizing each layer. The justification for employing the single layer approach is that, at least at the boundaries of the atmosphere, the radiance contributions arriving from all points along the line of sight are effectively represented by an atmospherically averaged phase function. Aerosol and Rayleigh optical depths which are the critical optical parameters in determining atmospheric scattering contributions must however be identical for all models.

Dave Model

Dave¹ describes an extensive data base of atmospheric radiance calculations produced using the spherical harmonics approximation. We shall briefly review the main ideas, some of which are used in the development of the other models discussed below. First of all, I is decomposed into its "direct" and "diffuse" components. The solution for the diffuse component is obtained by summing the separate contributions of a radiation field resulting from only a collimated (solar) source only (input conditions defined by (7) with $\rho = 0$) and a radiation field whose only source of illumination is an underlying Lambertian surface of reflectance ρ (boundary conditions (7) with $E_s = 0$). The source function for the collimated source is given by:

$$S(\tau; \Omega) = \frac{\pi_0}{4\pi} \left[\oint p(\Omega, \Omega') I(\tau; \Omega') d\Omega' + p(\Omega, \Omega_s) E_s e^{-\frac{\tau}{\mu_s}} \right] \quad (12)$$

which accounts for primary scattering of sunlight as an internal source. Invoking the linearity of (6), the two solutions are combined to yield I anywhere in the atmosphere from $\tau = 0$ to $\tau = \tau^*$.

The method of solution begins with a (truncated) Fourier series in ϕ of both the radiance and phase function $p(\mu, \phi; \mu', \phi')$. Each coefficient of the radiance Fourier series is then solved for independently by expanding the corresponding phase function coefficients into an associated Legendre polynomial series in μ and μ' . The derived RT expression for each radiance Fourier coefficient is then integrated over μ to yield radiance coefficient moments. The result is a system of simultaneous 1st-order ordinary differential equations in terms of the radiance coefficient moments.

The moments are then used to derive the source function for substitution into an azimuth independent version of equation (9). Finally, having solved for all the azimuth coefficients the Fourier series is computed to yield the radiance at a given value of ϕ . This is done for all levels in an atmosphere which may be subdivided into any number of layers to account for optical stratification in the vertical direction.

Models to be tested

The four models which were compared with the DAVE model are described below. Table 2.1 summarizes the salient features of each.

Table 2.1: Model features

MODELS	MULTIPLE SCATTERING	MULTI-LAYERED	GASEOUS ABSORPTION	RELATIVE EXECUTION TIME
DAVE	yes	yes	yes	very slow
DOM	yes	no	no +	slow
TURNER	approximately *	no	no +	fast
L6	no	yes	yes	moderate **
SS	approximately *	no	yes	fast

* Applies to a model that combines two-flow and single scattering ideas.

+ These models can be corrected by an ad hoc multiplicative term.

** Due principally to spherical relative geometry computations.

(i) DOM

This model was proposed originally by Chandrasekhar³², applied by Liou⁵ and refined by Stamnes³⁶. Like the spherical harmonics approximation discussed above the method employs a (truncated) Fourier expansion of I in ϕ . One proceeds in an identical fashion as above but stops short of the integration of each azimuth independent RT equation over μ . Rather the source function component of the azimuth independent RT equation is replaced by a Gaussian quadrature approximation to eventually yield an algebraic eigenvalue problem.

The number of Gaussian pivot points used in the quadrature is generally referred to as the number of streams and defines the precision of a given DOM application. The solution of the eigenvalue problem (which exploits certain matrix symmetries noted by Stamnes³⁶) yields a general solution to which the boundary value conditions (7) are applied. The resulting linear system of simultaneous equations yields values of the radiance azimuth coefficients at

discrete (Gaussian) values of μ . These discrete coefficients are then substituted into the source function and a second quadrature performed to yield the source function at any desired value of μ (Stamnes)³⁶. One then proceeds as outlined above to evaluate the azimuth coefficients and Fourier series.

Although the DOM can be formulated as a multi-layer model (Liou)¹⁹ the version used in this study was single layered. The number of streams employed in the computations was 32 (see Section 3). The effect of gaseous absorption was folded in by multiplying ρ^* by $\exp[-(\frac{1}{\mu_s} + \frac{1}{\mu}) \Sigma \tau_{gas}]$.

(ii) Turner

This model, formulated by Turner and Spencer³, yields a closed-form expression for I^* . The authors derive a simple analytical expression for the source function S by substituting in an angularly primitive expression for the integrand radiance I in equation (2). The first term of this expression is the sum of a double delta-function aligned with the solar and anti-solar directions of the solar beam and weighted by $F_{\pm}(\tau)$ respectively (equation 8). The second term is an isotropic expression which attempts to account for the source function contributions of surface-reflected irradiance. The relevance of this intermediate radiance expression is that its integral over solid angle yields fairly reliable two flow estimations of the downwelling and upwelling irradiances at every level in the atmosphere.

The Turner model was originally developed for conservative scattering ($\omega_0=1$). Although the code could be easily extended to accommodate non conservative scattering, we chose to retain the model in its original form. Gaseous absorption is included following the same recipe employed for the DOM.

(iii) L6

This is the 6th version of a series of codes produced by the AFGL (Kneizis et al.)². The primary purpose of this model is to compute atmospheric transmittance $\exp[-\int_A^B \alpha(s)ds]$ between two arbitrary points A and B. This is done for a variety of atmospheric components including ozone, N₂, HNO₃ and water vapour at moderate spectral resolution (20 cm⁻¹), from the thermal IR (350 cm⁻¹ = 28.6 μ m) to the near UV (40000 cm⁻¹ = .25 μ m). At IR wavelengths the model utilizes an assumption of local thermodynamic equilibrium to compute the contribution of thermal emission.

For our purposes the most relevant feature of L6 is its incorporation of a single scatter code to permit calculations of exo-atmospheric radiance (or hence apparent reflectance). The single scatter contribution is obtained by substituting the second term of equation (12) into equation (9).

The L6 code as utilized for our calculations accounted for only the reflected component of direct solar radiation. Accordingly the contribution of downwelling diffuse radiation to the reflected term of equation (9) plus the contribution of reflected and then scattered radiation to the second term of (9) is ignored. As well the code was modified to correct for a factor of 2 differences between the L6 surface reflected radiance and the radiance expected from a Lambertian (constant reflectance) surface. This discrepancy was also noted by Richter³⁷.

Other features of L6 include its incorporation of spherical refractive geometry and the treatment of vertical stratification in terms of a multi-layer atmosphere. For the range of geometries employed in this study, the exclusion or inclusion of spherical refractive geometry does not play a critical role in the evaluation of the single-scatter dominated radiance computed with L6. The multi-layer aspect complicates comparisons made with L6. In order to impose user-defined α and p values above the boundary-layer (0-2 km), it was necessary to modify the driver program. As well, care was required to ensure that the optical depths utilized in our comparisons were compatible with the L6 optical parameters.

iv) 5S

This model (Tanré et al.)⁴ departs from the previous approaches since the authors literally build, piece-by-piece, an analytical expression for the total apparent reflectance:

$$\rho^*(\rho, \theta_s; \theta_v, \phi) = \rho_{atm}(\theta_s; \theta_v, \phi) + \rho \frac{T(\theta_s)T(\theta_v)}{1 - \rho a} \quad (13)$$

The parameters of this expression are:

- Intrinsic atmospheric reflectance (ρ_{atm}): This term is the sum of separately derived formulae for Rayleigh and aerosol apparent reflectances. The aerosol contribution is obtained using a Sobolev approximation combined with a single scatter model. Aside from geometrical dependencies the form derived is an explicit function of the aerosol parameters τ_A , the phase function p , and the asymmetry factor ($g = \langle \cos \chi \rangle = \beta_1 / 3$, χ = scattering angle).
- Total atmospheric transmittance ($T(\theta)$): This factor is the sum of a direct transmission term plus a diffuse radiation transmission term. The latter which is obtained from a delta-Eddington approximation is an explicit function of τ^* and g .
- Spherical albedo (a) is a function of τ^* alone and is obtained using a semi-empirical expression based on single-scattering and Monte-Carlo simulations.

Like DOM and Turner, 5S is a single-layer model, gaseous absorption is also treated in an independent fashion by the application of a transmission factor to equation (14). The 5S code includes its own routine for computing gaseous transmittance. One noteworthy extension of 5S, discussed elsewhere (Davis and Royer)^{3,8}, is the accommodation of a simple but effective model for simulating inhomogeneous ground conditions.

3. COMPARISON OF MODELS

The four models were compared with the Dave model over a variety of input geometrical parameters and four different atmospheres (Table 3.1). These atmospheres range from a pure molecular or Rayleigh atmosphere (identified as aerosol type 1) to a fairly turbid atmosphere with a total (absorption plus scattering) aerosol optical depth at .5 μm of about 0.5 (aerosol type 4). The aerosol type 4 atmosphere is characterized by weak aerosol and molecular absorption and a Deirmendjian^{3,9} Haze L (continental) size distribution. The aerosol type 3 atmosphere is identical to aerosol type 4 except that its aerosol abundance is only one fifth of the type 4 value. Aerosol type 5 is characterized by an optical thickness which is less than that employed in aerosol type 3 and a Deirmendjian Haze M (maritime) size distribution. The phase functions utilized in the study were computed for each aerosol type and each of the 5 input wavelengths using either Mie scattering functions (Royer et al.)^{4,10} or Legendre coefficients (O'Neill)⁶.

L6 and 5S are delivered with a selection of standard molecular and aerosol atmospheres. To establish a significant comparison basis, all models were run for identical atmospheres. This necessitated the development of a common input data base of optical parameters (Table 3.1) which had to be adapted to fit the input requirements of each model. Moreover, 5S, and to some extent, L6 feature a variety of user-friendly interpolation and integration schemes as well as techniques for calculating geometry, aerosol mixtures, ground surface reflectances from standard reflectance datasets and conversions from visibility to aerosol optical thickness. These features were bypassed or eliminated or adapted for our study.

Data bases of total apparent reflectance (ρ^*) were computed and subtracted from the DAVE data base to yield an ensemble of difference files for each of the four models as a function of four different aerosol types. Representative plots of these differences are displayed in Figures 3.1 to 3.5 respectively as a function of the geometrical parameters

TYPE OF ATMOSPHERE

Mid latitude summer: water vapour content: 2.96 g.cm⁻²;
 ozone content: .308 atm. cm.

Vertical profile: 16 levels for pressure, temperature, ozone and water vapor from 0 to 60 km.

TYPE OF AEROSOL

#		Refractive index	Size distribution (modified gamma)	Total Aerosol # density (10 ⁶ /cm ³)
3	Thin Haze L	1.5 - 1.0.01	$\alpha = 2, b = 15.1186, \gamma = 0.5$	19.815
4	Thick Haze L	1.5 - 1.0.01	$\alpha = 2, b = 15.1186, \gamma = 0.5$	99.075
5	Haze M	1.5 - 1.0.01	$\alpha = 1, b = 8.9443, \gamma = 0.5$	4.673

Vertical profile: same 16 levels for aerosols # density

RELATED PARAMETERS

Wavelength (um):	.455	.555	.655	.8455	1.61
Aerosol Single Scattering Albedo					
Aerosol Types					
3,4	.89712	.91264	.92311	.93498	.94505
5	.83485	.85626	.87314	.89568	.93448
Aerosol Asymmetry Factors					
3,4	.71701	.71273	.71014	.70487	.65885
5	.75206	.73794	.72847	.71785	.70093
Aerosol Scattering Optical Depths					
3	.08938	.09110	.09040	.08456	.04867
4	.44689	.45544	.45198	.42281	.24335
5	.04086	.04301	.04460	.04628	.04212
Aerosol Absorption Optical Depths					
3	.01025	.00872	.00753	.00588	.00283
4	.05123	.04359	.03764	.02941	.01417
5	.00813	.00722	.00648	.00539	.00305
Rayleigh Scattering Optical Depths					
1 (Rayleigh) 3,4,5	.21320	.09448	.04823	.01730	.00129
Ozone Optical Depths					
1,,3,4,5	.00157	.02772	.01848	.00000	.00000
Water Vapour Optical Depths					
1,3,4,5	.00000	.00000	.00000	.00529	.00000
Carbon Dioxide Optical Depths					
1,3,4,5	.00000	.00000	.00000	.00000	.01499
Total Optical Depths					
1	.21477	.12220	.06671	.02259	.01628
3	.31440	.22201	.16463	.11303	.06778
4	.71299	.62132	.55631	.47479	.27382
5	.26378	.17242	.11779	.07426	.06144

INPUT PARAMETER RANGES FOR RADIATIVE TRANSFER CALCULATIONS

Viewing angle	0, 10, 20, 30, 40, 50, 60, 70	(figure 3.1)
Azimuth angle	0, 30, 60, 90, 120, 150, 180	(figure 3.2)
Solar zenith angle	30, 45, 60, 70, 75	(figure 3.3)
Wavelength	.4550, .5550, .6550, .8455, 1.61	(figure 3.4)
Ground albedo	0, .2, .4, .6, .8	(figure 3.5)

Table 3.1 Summary of the optico-physical atmospheric parameters and input parameters used for the radiative transfer comparisons. All angles are in degrees.

(θ_v , ϕ and θ_s), the wavelength and the surface reflectance. We describe below the general behavior of the reflectance differences for each model.

With certain exceptions the errors tended to increase with decreasing wavelength or effectively increasing total optical depth (Figure 3.4), increasing slant range of the observer's line of sight or solar beam (Figures 3.1, 3.3) and increasing aerosol optical depth (i.e. as a function of model type). Except for the L6 model (and the Turner model to a less severe extent) the errors were reasonably independent of surface albedo (Figure 3.5). The errors in the figures and the rms errors reported below can be interpreted in a relative sense by noting that the apparent reflectance in a zero ground reflectance atmosphere is of the order of .1 for short wavelengths (.5 μ m; see Figure 4.1a for example) and .05 for near IR wavelengths (.85 μ m). The perspective which is most pertinent to the present study is how the $\Delta\rho^*$ errors translate into errors in aerosol optical depth obtained by inversion (Section 4 below).

1. L6 model - Not unexpectedly, the single scattering computations of the L6 model produced large apparent reflectance errors relative to the Dave model. Of note in the zero albedo figures, where backscattering is important and the optical line of sight is large relative to nadir ($\phi=0$ in the zero albedo case of Figure 3.1a for example) is the predominance of single scattering over multiple scattering. This effect persists for aerosol type 3 and aerosol type 5 until the optical depth is sufficiently large (aerosol type 4) that multiple scattering masks the low order scattering influence. The large negative errors observed for the non zero albedo cases (e.g. $\sim -.25$ in the aerosol 4 case of Figure 3.1a) are related to the fact that the single scatter model accounts only for the directly reflected term of the total apparent radiance and as well underestimates the direct term by ignoring the downwelling diffuse irradiance at ground level.

2. Turner Model - Our computations showed that the Turner model was not substantially better than the single scatter model except in near nadir configurations and conditions of non-zero surface albedo. Apparent reflectance errors were largest in the neighbourhood of the region corresponding to solar beam backscatter (Figures 3.1a and 3.2 : $\phi=0$, aerosol type 4). This effect which is particularly evident in the more turbid atmospheres (i.e. the atmospheres characterized by more anisotropic phase functions) is an unfortunate artifact of the delta function representation taken for the source function radiance (see Section 2 above). Rms averages performed on the figures presented in this section indicated that for the Rayleigh case $\Delta\rho^* \leq .03$ at $\lambda = .555 \mu\text{m}$ and $\leq .006$ at $\lambda = .8455 \mu\text{m}$. For aerosol type 4 the analogous parameters were respectively $\Delta\rho^* \leq .09$ and $.08$.

3. 5S Model - This model produced the most satisfactory results given the simplicity of its formulation. The greatest errors occurred at large values of the observer's or solar beam slant range and at large optical depth. This level of disparity is not unknown to the authors of 5S and can be improved upon by means of a relatively simple modification to the code which accounts for the coupling of the Rayleigh and aerosol radiance fields (Deschamps et al.)¹². Rms errors of apparent reflectance in the Rayleigh atmosphere case amounted to $\Delta\rho^* \leq .003$ at both .555 and .8455 μm wavelengths. For aerosol type 4 the maximum errors were respectively .02 and .03 for the .555 and .8455 μm wavelengths. For near nadir configurations these errors decreased by about one order of magnitude.

4. DOM Model - Although not a computationally simple model in the sense of 5S or Turner, the DOM model is significantly faster than the DAVE code given that computations are performed for a single layer only. It was thus of some interest to investigate the level of error obtained for an arbitrarily accurate single layer model relative to the multilayer DAVE model.

To test the convergence of the DOM model computations for the standard number of streams employed (32), comparisons were made with the Dave calculations at 16, 24, and 48 streams. Above 24 streams no significant improvement was noted in the relative precision. For the majority of nadir cases tested (with varying solar zenith angle and albedo in the aerosol type 4 atmosphere) the small reflectance errors in going from 32 to 48 streams changed by less than 50%. This suggests that these errors are primarily due to multi-layer versus single layer differences between the Dave and DOM models.

For the Rayleigh atmosphere the difference between DOM and DAVE results was $\leq .0002$. We note however that the neglect of polarization in both models can lead to extreme errors $\leq 23\%$ relative to a complete solution in

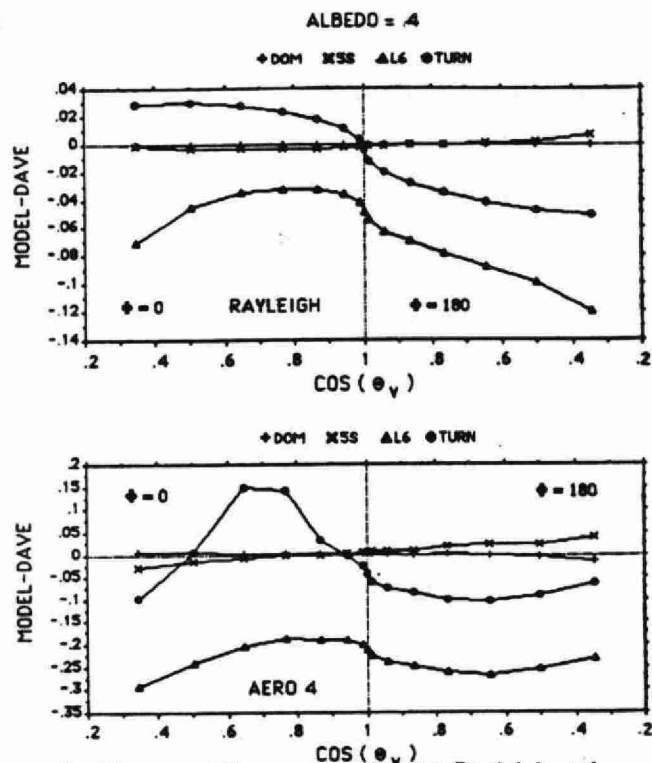
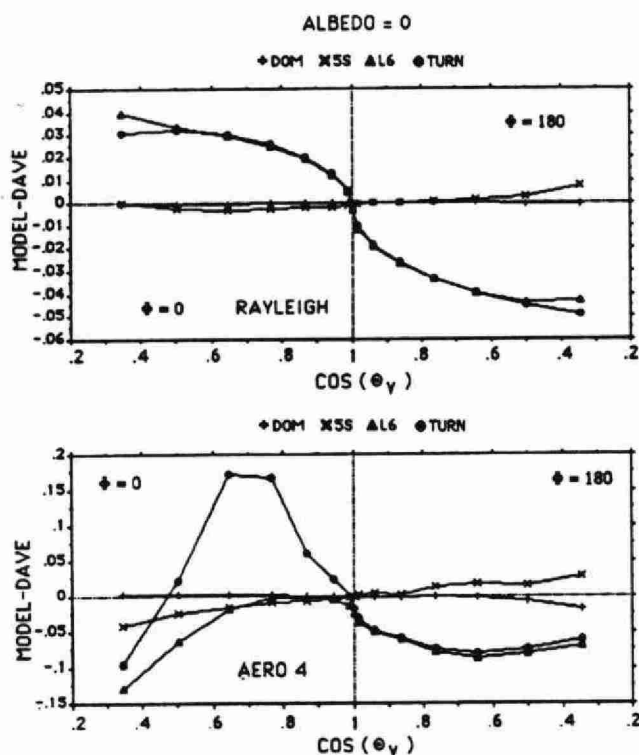


Figure 3.1a Apparent total reflectance differences (relative to the Dave model) computed for the Rayleigh and aerosol type 4 (AERO 4) atmospheres as a function of the cosine of the observer's zenith angle for a wavelength of $.555 \mu\text{m}$ and a solar zenith angle of 45 degrees. $\Phi = 0$ represents a radiance ray in the solar plane travelling towards the sun (backscatter direction) while $\Phi = 180$ is in the solar plane traveling in the anti-solar (forward scattering) direction. Each curve represents the results for a single test model (DOM, SS, L6 or Turner).

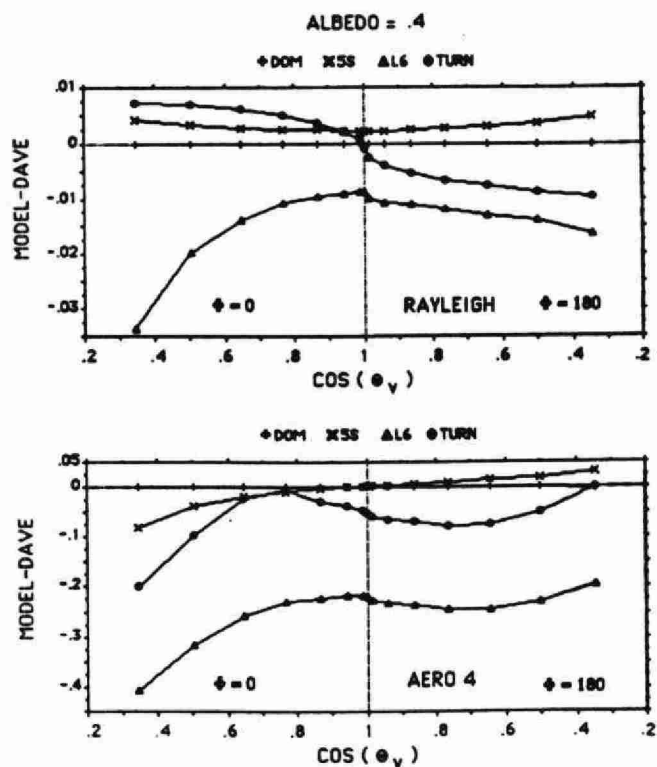
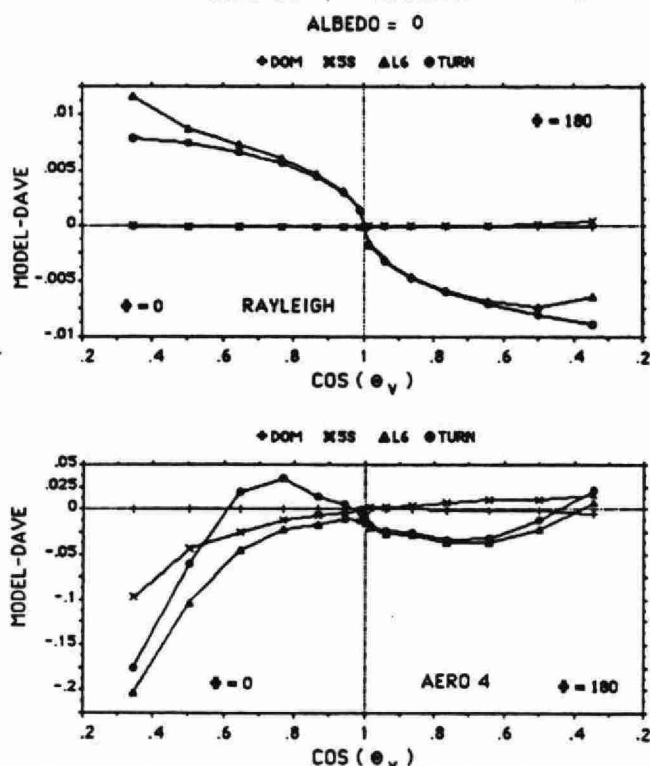


Figure 3.1b Identical key as described for Figure 3.1a except the wavelength is $.8455 \mu\text{m}$

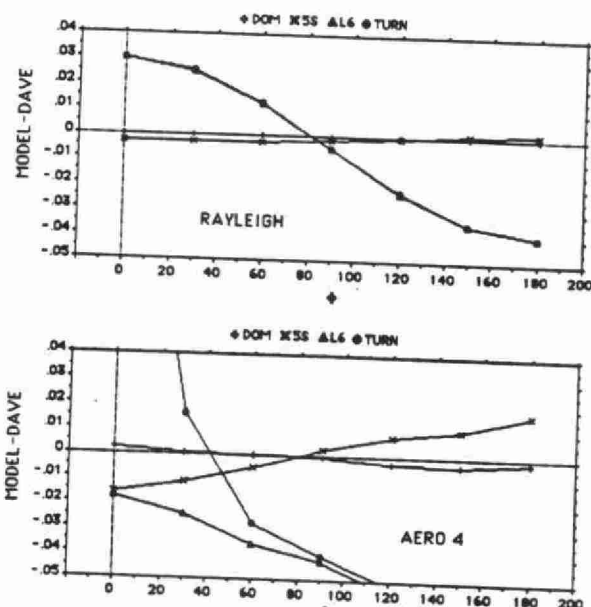


Figure 3.2 Apparent total reflectance differences (relative to the Dave model) computed for the Rayleigh and aerosol type 4 (AERO 4) atmospheres as a function of the observer's azimuth angle for a wavelength of $.555 \mu\text{m}$. The observer's zenith angle is 50 degrees, the solar zenith angle 45 degrees, and the surface albedo zero.

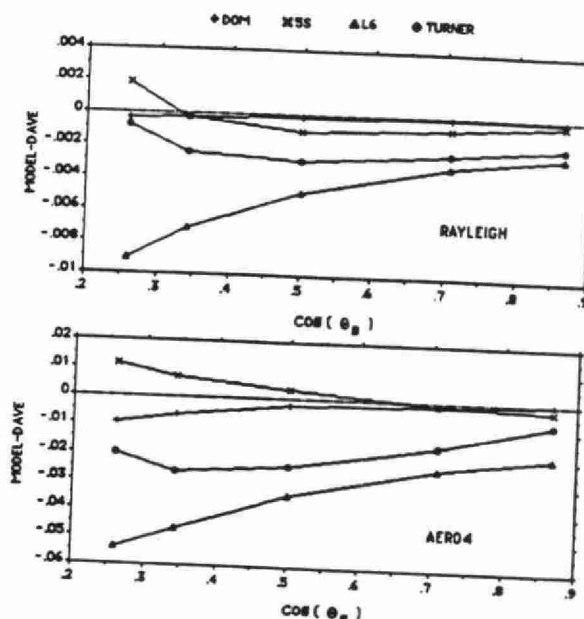


Figure 3.3 Apparent total reflectance differences (relative to the Dave model) computed for the Rayleigh and aerosol type 4 (AERO 4) atmospheres as a function of the cosine of the solar zenith angle for a wavelength of $.555 \mu\text{m}$. The geometry was nadir viewing and the surface albedo was taken to be zero.

terms of Stokes vectors for a Rayleigh atmosphere (Kattawar et al.)¹⁷. For aerosol type 4 the error maximum computed for the figures in this section were .005 and .002 for $\lambda = .555$ and $.8455 \mu\text{m}$ respectively. The effects of polarization in this latter case are considerably less critical (ibid).

4. INVERSION ANALYSIS

Our principal interests in evaluating the accuracy of the models was to determine their relative performance in an inversion algorithm for the extraction of aerosol optical depth. The inversion methodology employed was to simply derive aerosol optical depths from curves versus total apparent reflectance (i.e. the actual reflectance derived from satellite data). In practice, this approach requires apriori information on ground reflectance. The estimation of this parameter represents a source of error beyond the scope of this paper.

Figure 4.1 shows some representative runs of all 4 models over a range of aerosol optical depths for selected geometric and optical parameters. In changing from zero to non zero albedo (0.4) one can note a reverse in slope due to the same phenomenon observed by Kaufman²⁸. Accordingly there exists a singularity intermediate to the two albedos where the apparent reflectance is independent of the aerosol optical depth. Thus, at this critical reflectance point, an inversion scheme for extracting optical depth from total apparent reflectance will not converge. This singularity is however optimal for extracting the single scattering albedo.

Given the results of the previous section and frequent non-convergence problems which occurred for the Turner and L6 models we chose to concentrate our analysis of aerosol optical depth inversion errors on the 5S and DOM models. The speed of the 5S model permitted the production of a data base of optical depth inversion errors relative to the DAVE model for the complete set of input parameters shown in Table 3.1. These results were compared with inversion errors deduced from a number of selected DOM runs.

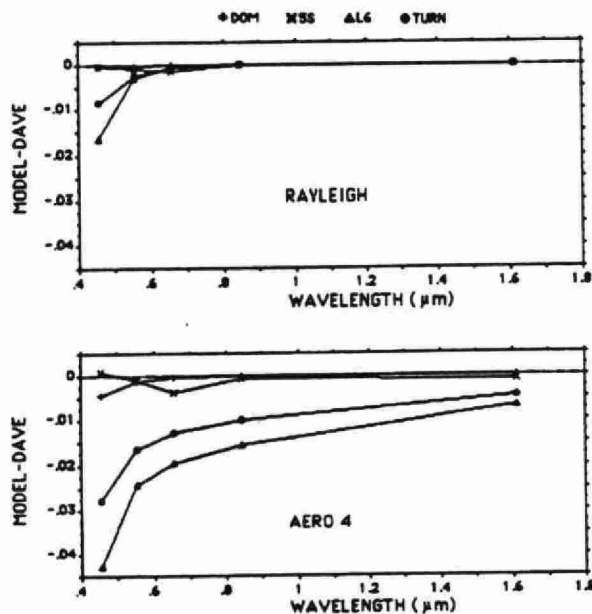


Figure 3.4 Apparent total reflectance differences (relative to the Dave model) computed for the Rayleigh and aerosol type 4 (AERO 4) atmospheres as a function of wavelength for a 45 degree solar zenith angle. The geometry was nadir viewing and the surface albedo was taken to be zero.

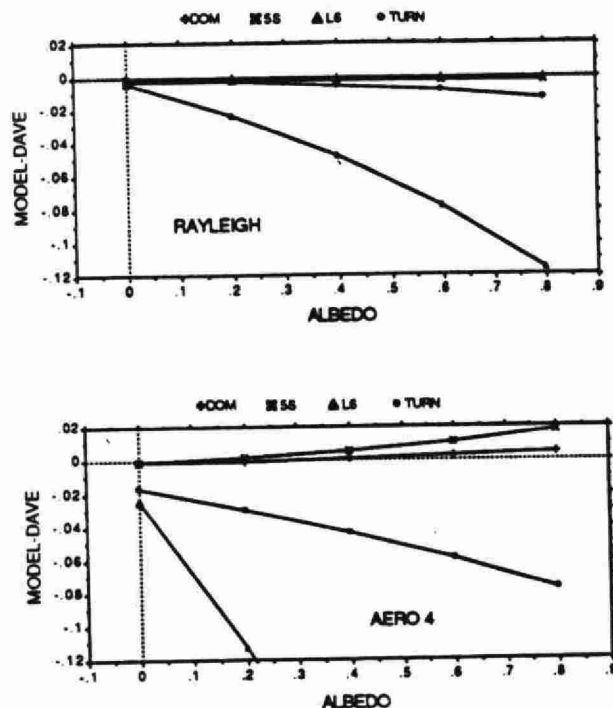


Figure 3.5 Apparent total reflectance differences (relative to the Dave model) computed for the Rayleigh and aerosol type 4 (AERO 4) atmospheres as a function of surface albedo for a 45 degree solar zenith angle. The geometry was nadir viewing and the wavelength .555 μm .

Figure 4.2 shows a representative set of the computed inversion errors for the 5S model as a function of various input parameters. The variation versus wavelength tends to decrease with increasing wavelength although this was not always a constant feature with the 5S inversions. The small peak at .655 μm reflects an equivalent (absorbing) molecular optical depth disparity of about .1 between the DAVE and 5S codes. This disparity which was maximal at .655 μm effectively demonstrates the level of error which can result from differences in molecular absorbing models if the gaseous contribution is interpreted as an aerosol optical depth variation. Note however that the disparities between 5S and DAVE absorption models are fairly extreme; the corresponding differences between 5S and L6 are considerably less.

Variations in the correlation of inversion error magnitudes ($\Delta\tau_A$) with the apparent reflectance errors ($\Delta\rho^*$) of Section 3 were most strongly influenced by the behavior of the slope $d\tau_A/d\rho^*$ in the neighbourhood of the Kaufman critical reflectance (ρ_c). The error magnitudes seen on the plot versus albedo show an expected rapid rise on both sides of the critical surface albedo defined by Kaufman. Values of $d\tau_A/d\rho^*$ at surface reflectance values removed from the critical reflectances were typically of the order of 10 or larger. From simple geometric considerations (c.f. Figure 2 of ref. Kaufman)²⁸ an increase in surface albedo to a value ρ results in an increase of error by a factor of approximately $[-\rho_c/(\rho - \rho_c)]$.

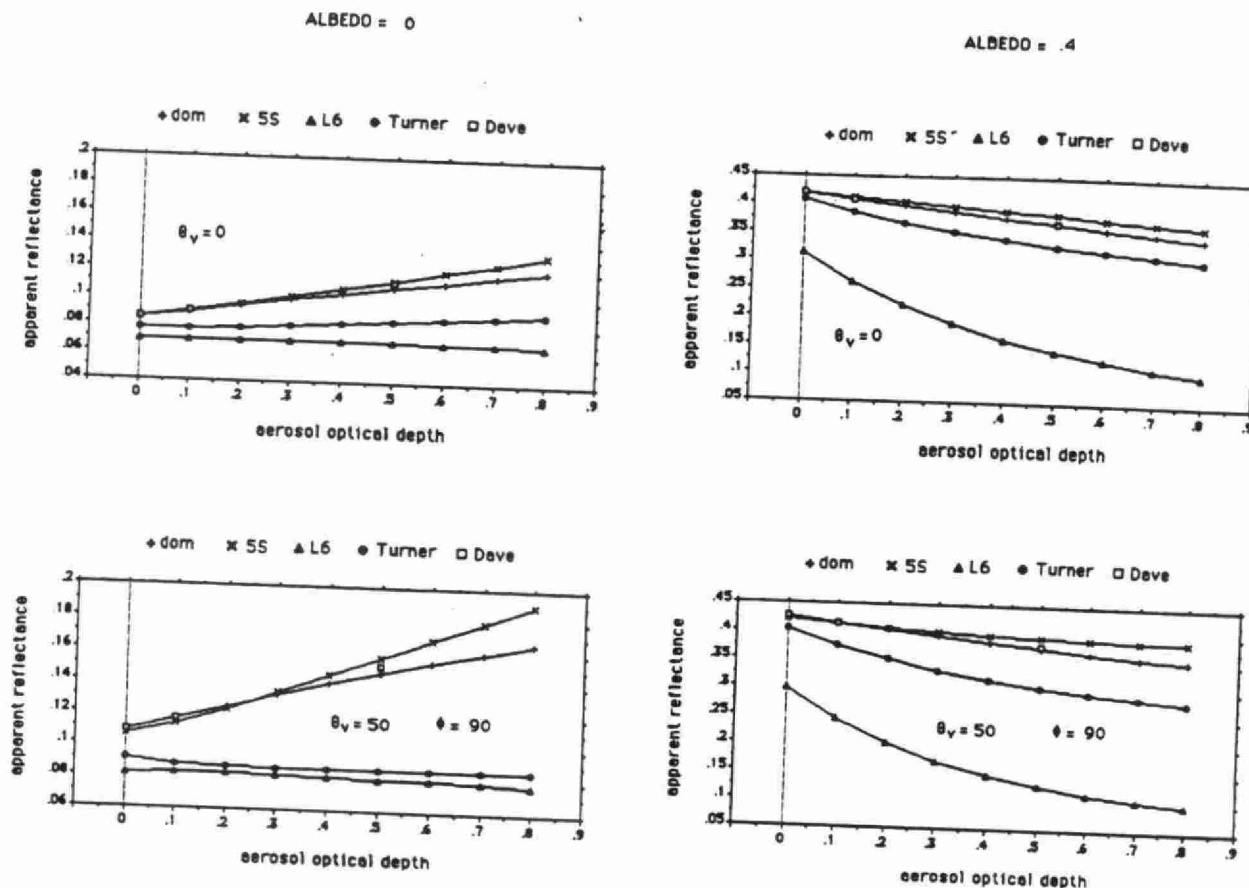


Figure 4.1 (a) Apparent total reflectances for all 4 test models as a function of the aerosol optical depth (absorption plus scattering). The surface albedo was zero, the solar zenith angle 45 degrees, and the wavelength .455 μm .

(b) Same parameters as (a) for a surface albedo of 0.4.

For aerosol type 4, a surface albedo of zero, a solar zenith angle of 45 degrees and a nadir viewing geometry the inversion error is generally less than .06 for all wavelengths (Figure 4.2 versus wavelength). As the zenith view angle increases the inversion error can increase to values as large as .26 at 50° and .4 at 70° (.455 μm). The DOM errors were, because of effects related to the slope dr/dr^* , on occasion just as large as the 5S results. However relative behavior in the errors computed for the limited range of input parameters selected (nadir viewing and 45 degrees solar zenith angle) were fairly well represented by the dr^* errors noted above. For off nadir angles it is expected that the DOM inversion errors, relative to the 5S errors, will be smaller by a factor in rough proportion to the ratio of dr^* errors found in Section 3.

5. SUMMARY AND CONCLUSIONS

We have compared four common radiative transfer codes to determine their accuracy relative to an exact solution of the radiative transfer equation in a multilayer aerosol-molecular atmosphere. The computed disparities were then evaluated in terms of their impact on an inversion procedure for extracting optical depth from exoatmospheric measures of total apparent reflectance.

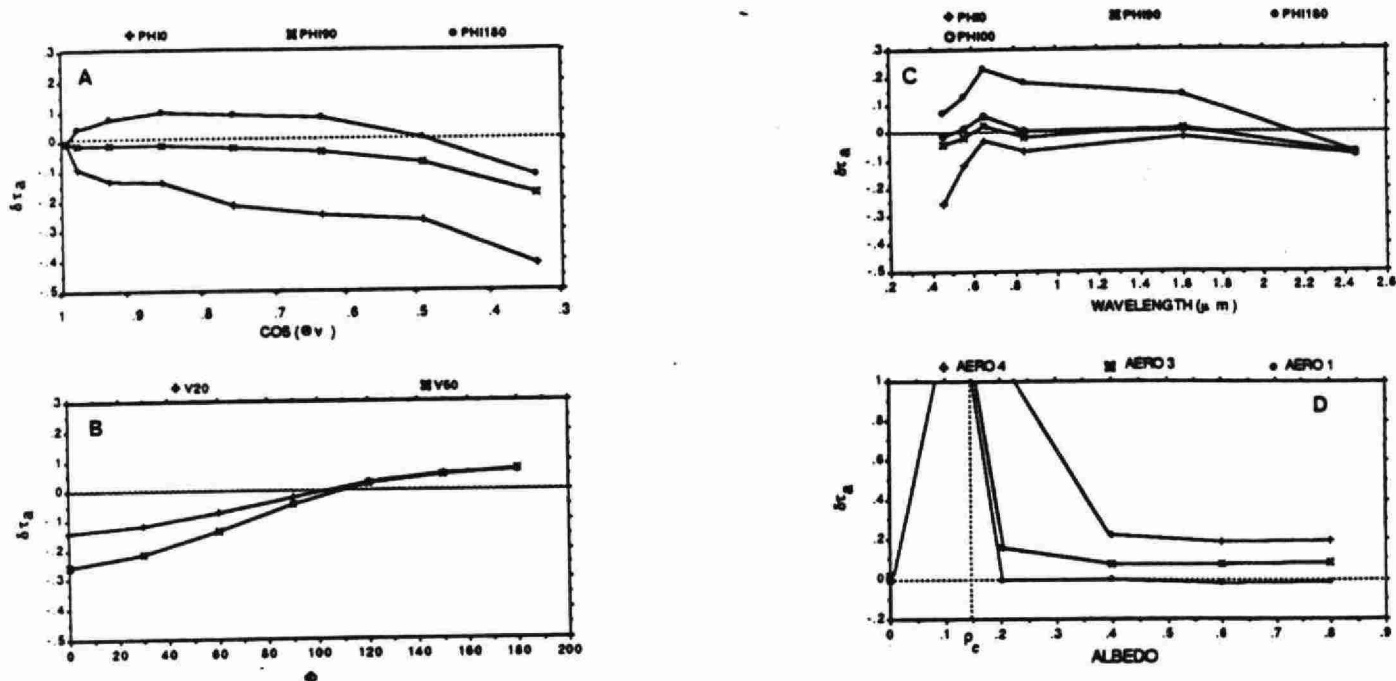


Figure 4.2 (A): Computed aerosol optical depth error of the 5S model relative to the Dave computations for the aerosol type 4 atmosphere (corresponding to $\tau_a = .5$) as a function of the cosine of the observers zenith angle. The wavelength is $.455 \mu m$, the solar zenith angle 45 degrees and the surface albedo zero. The values of the observers azimuth angle are noted above the figure.

(B): Same as for (A) but for varying azimuth angle (observer's zenith angle noted above the figure).

(C): Aerosol optical depth error as a function of wavelength for a nadir viewing geometry. The solar zenith angle is 45 degrees and the surface albedo zero.

(D): Varying surface albedo for the three aerosol types. The wavelength is $.455 \mu m$ and the geometry is nadir viewing. ρ_c defines the critical ground reflectance (see text).

The Turner and single scatter (Lowtran 6) models generally produced large errors in apparent reflectance which led to unacceptably large inversion errors. Overall the Turner model was not significantly better than Lowtran 6 model except at near nadir geometries and non zero albedos. This weakness of the Turner model implies that hybrid versions which renormalize the Turner model to more accurate nadir results do not significantly improve the model away from the point of normalization.

Although the DOM produced the most impressive results in terms of comparison with the Dave model and inversion errors its time of execution (in particular for phase functions which are more anisotropic than those employed in this study) is a serious constraint. However the incorporation of this model in an interpolation algorithm which requires only a limited number of solutions per image (Teillet et al.)⁴¹ is a compromise approach which makes numerical solutions more competitive with analytical models such as 5S. Furthermore the single layer feature of the model we employed represents a significant savings in execution time relative to multi-layer models. The excellent agreement which was obtained relative to the Dave model bears further investigation in terms of developing a bias correction algorithm which can be used to adjust single layer computations to multi-layer results as a function of aerosol altitude profile parameters.

The 5S model which is orders of magnitude more rapid than the DOM model (depending on the number of streams used in the latter) was significantly more accurate than the Lowtran 6 and Turner models. Apparent reflectance errors were systematically smaller in the near nadir direction and were on the whole about an order of magnitude larger than the DOM apparent reflectance errors. The inversion errors relative to the Dave computations were frequently in excess of .1 in optical thickness for the most turbid aerosol-type 4 atmosphere ($\tau_A = 0.5$ at $.555 \mu\text{m}$). These results would be significantly improved if the Rayleigh/aerosol coupling modifications outlined by Deschamps et al.¹² were incorporated in the 5S model.

The computed inversion errors depend on an a priori knowledge of optical parameters, the most critical of which, is the ground surface reflectance. In addition the quantity selected for inversion (total apparent reflectance) is, at least in the neighbourhood of the critical (Kaufman) reflectance, inferior to an inversion on the path radiance contribution (whose slope is always positive in typical atmospheric conditions). The optimal inversion procedure is in fact some combination of a path radiance based scheme below the critical reflectance and a surface reflection based approach above the critical reflectance. Further investigation in terms of information content as a function of surface reflection is needed in this respect.

6. ACKNOWLEDGEMENTS

This project was supported in part by NSERC, Canada (Grants No. A8643 and A1765) and by the Ontario Ministry of the Environment (Project No. 349 G). We would like to thank S. Lovejoy, P. Gabriel and R. Davies for helpful discussions.

7. REFERENCES

1. DAVE, J.V. (1978). Extensive Datasets of the Diffuse Radiation in Realistic Atmospheric Models with Aerosols and Common Absorbing Gases, *Solar Energy*, 21, 361-369.
2. KNEIZIS, F.X. et al. (1983). Atmospheric Transmittance/Radiance: Computer code LOWTRAN 6. *Air Force Geop. Lab.*, AFGL-TR-83-0187.
3. TURNER, R.E., M.M. SPENCER (1972). Atmospheric Model for the Correction of Spacecraft Data, *Proc. of the 8th Int. Symp. on Rem. Sens. of Enviro.*, Ann Arbor, 895-934.
4. TANRÉ, D. et al. (1985). Simulation of the Satellite Signal in the Solar Spectrum (5S). *Proc. of the 3rd Int. Col. on Spectral Signatures of Objects in Rem. Sens.*, Les Arcs, France, ESA SP-247, 315-319.
5. LIOU, K.N. (1973). A numerical experiment on Chandrasekhar's Discrete Ordinate Method for Radiative Transfer: application to cloudy and hazy atmospheres, *J. of Atmos. Scie.*, 30, 1303-1325.
6. O'NEILL, N.T. (1982). A radiative Transfer Experiment in an urban atmosphere, Ph.D., *Center for Res. in Experimental Space Science*, York University, Toronto, Ontario, 207 p.
7. BARIOU, R., D. LECAMUS, F. LE HENAFF (1986). Dossiers de télédétection: Corrections atmosphériques, Centrale régional de télédétection, *Université de Rennes 2*, Haute Bretagne, 116 p.
8. GORDON, H.R. (1978). Removal of Atmospheric Effects from Satellite Imaging of the Oceans, *Applied Optics*, 17, 1631-1635.
9. TANRÉ, D., HERMAN, M., DESCHAMPS, P.Y., A. DE LEFFE (1979). Atmospheric Modeling for Space Measurements of Ground Reflectances, Including Bidirectional Properties, *Applied Optics*, 18, 3587-3594.
10. SEKERA, Z. (1956). Recent Developments in the study of the Polarization of Sky Light, *Advances in Geophysics*, 13, 43-104.
11. TANRÉ, D., M. HERMAN, P.Y. DESCHAMPS (1981). Influence of the Background Contribution Upon Space Measurements of Ground Reflectance, *Applied Optics*, 20, 3676-3684.
12. DESCHAMPS, P.Y., HERMAN, M., D. TANRÉ (1983). Modeling of the Atmospheric Effects and its Application to the Remote Sensing of Ocean Colour, *Applied Optics*, 22, 3751-3758.
13. MARTELLACCI, C., G. FIOCCO, G.P. GOBBI (1986). Effects of Atmospheric Aerosol Size Distributions on the Retrieval of Surface Spectral Radiance from Satellite, *Proc. ISLSCP Conference*, Rome, Italy, EAS SP-248, 371-377.
14. FRASER, R.S., Y.J. KAUFMAN (1985). The Relative Importance of Aerosol Scattering and Absorption in Remote Sensing, *IEEE Trans. on Geos. and Rem. Sens.*, FGE-23, 625-633.

15. HANEL, G. (1981). An attempt to interpret the humidity dependencies of the aerosol extinction and scattering coefficients, *Atmo. Envi.*, 15, 403-406.
16. HANSEN, J.E., L.D. TRAVIS, (1974). Light Scattering in Planetary Atmospheres, *Space Science Reviews*, 16, 527-610.
17. KATTAWAR, Q.W., G.N. PLASS, S.J. HITZFELDER (1976). Multiple Scattered Radiation Emerging from Rayleigh and Continental Haze Layers. 1: Radiance, polarization and neutral points, *Applied Optics*, 15, 632-647.
18. SCHUERMAN, D.W. (ed), (1979). Light Scattering by Irregularly Shaped Particles, *Plenum Press*, New York.
19. LIOU, K.N. (1975). Applications of the Discrete-Ordinate Method for Radiative Transfer to Inhomogeneous Aerosol Atmospheres, *J. of Geophys. Res.*, 80, 3434-3440.
20. MISHIN, I.V. (1985). Estimation of Radiation-Induced Distortions of the Earth's Optical Image in a Horizontally Inhomogeneous Atmosphere, *Soviet J. of Rem. Sens.*, 4, 458-463.
21. SAUNDERS, R.W. and K.T. KRIEBEL (1988). An improved method for detecting clear sky and cloudy radiances from AVHRR data. *Int. J. Rem. Sens.*, 9, 123-150.
22. MEKLER, Y., KAUFMAN, Y.J. (1982). Contrast reduction by the atmosphere and the retrieval of the nonuniform surface reflectance, *Applied Optics*, 21, 310-316.
23. TANRÉ, D., HERMAN, M., DESCHAMPS, P.Y. (1983). Influence of the atmosphere on space measurements of directional properties, *Applied Optics*, 22, 733-741.
24. FRASER, R.S., KAUFMAN, Y.J. and R.L. MAHONEY (1984). Satellite measurements of aerosol mass and transport, *Atmo. Environ.*, 18, 2577-2584.
25. FROUIN, R., C. GAUTHIER (1987). Calibration of NOAA-7, AVHRR, GOES-5, and GOES-6 VISSR/VAS solar channels, *Rem. Sens. of Environ.*, 22, 73-101.
26. GORDON, H.R. (1987). Calibration Requirements and methodology for remote sensors viewing the ocean in the visible. *Rem. Sens. of Environ.*, 22, 103-126.
27. GRIGGS, M. (1987). Satellite measurements of tropospheric aerosols, *NASA CR-3459, NASI-15898*, 58 p.
28. KAUFMAN, Y.J. (1987). Satellite Sensing of aerosol absorption. *J. Geophys. Res.*, 92, 4307-4317.
29. ARANUVACHAPUN, S. (1986). The atmospheric optical depth spectrum determined from CZCS radiance. *Int. J. Rem. Sens.*, 7, 105-118.
30. MEKLER, Y., QUENZEL, H., OHRING, L. and I. MAURUS (1977). Relative atmospheric aerosol content from ERTS observations, *J. Geophys. Res.*, 82, 967-970.
31. NORTON, C.C., MOSHER, F.R., HINTON, B., MARTIN, D.W., SANTEK, D. and W. KUHLOW (1980). A model for calculating desert aerosol turbidity over the oceans from Geostationary satellite data, *J. Appl. Meteor.*, 19, 633-646.
32. CHANDRASEKHAR, S. (1960) Radiative Transfer, *Dover Publications*.
33. STEVENS G.L. (1987) Radiative Transfer in Spatially Inhomogeneous, Two-dimensional, Anisotropically Scattering Media, *J. Quant. Spectrad. Tran.*, 36, pp 51-67.
34. LENOBLE J. (Ed.), (1974) Standard Procedures to Compute Radiative Transfer in a Scattering Atmosphere (part I), *IAMAP, NCAR*, Boulder, Col.
35. IRVINE, W.M. (1965). Multiple Scattering by Large Particles, *Astrophysical J.*, 142, 1563-1575.
36. STAMNES, K., R.A. Swanson (1981) A New Look at the Discrete Ordinate Method for Radiative Transfer Calculations in Anisotropically Scattering Atmospheres, *Journal of Atmospheric Science*, 38, 387-399.
37. RICHTER R. (1985) Some Aspects of Atmospheric Radiance Model Lowtran 6, *Int. J. Remote. Sensing.*, 6, No.11, pp1773-1777.
38. DAVIS A. and ROYER A., (1987) Effet de la Diffusion Atmosphérique sur l'Apparence d'une Cible de Petites Dimensions, *11 th Can. Symp. Rem. Sens.*, Waterloo, Ont.
39. DEIRMENDJIAN, D. (1969) Electromagnetic Scattering on Spherical Polydispersions, *Elsiever*.
40. ROYER, A., BERNIER, R., ADLER, V. and D. PILON (1985). Calcul de la diffusion de la lumière par les aérosols: description des programmes MIELOR et résultats obtenus. *Bull. de recherche no 80, Université de Sherbrooke, Sherbrooke, Québec*, 63 p.
41. TEILLET, P. M., O'NEILL, N. T., KALINAUSKAS, A., STURGEON, D., G. FEDOSEJEVS (1987). A Dynamic Regression Algorithm for Incorporating Atmospheric Models into Image Correction Procedures, *Proc. of IGARSS'87*.

APPENDIX C

Particle Growth Model Considerations

Appendix C: Particle Size Considerations

A drop growth program was obtained from Richard Leitch of the Cloud Physics branch Atmospheric Environment Service. It is designed to calculate the scattering phase function of an internally/externally mixed polydispersion of aerosol particles comprising of up to 3 different types of particles. It was suggested by Leitch to conduct a comparison of this model with the externally mixed mie model of Royer, described in the main text and referred to here as the CARTEL model.

Changes made to AES program

- Modes changed so that size distributions can be overlapping.
- Modified gamma size distribution added (for mode 1).
- Size ranges increased for comparison with CARTEL.
- Cosmetic changes to use 3 element vectors instead of 3 variables for modes.

Summary of program

The following is a brief pseudo-code description of the drop growth scatting program.

Start

Read in the parameters

- Thickness of layer
- Wavelength
- updraft acceleration (0) †
- number of time steps (large)
- Last time

- Starting temperature and pressure (STP used)
- Do dry and wet particle calculation ? (yes)
- Type of particle (chose up to 3 of the following)
 $NaCl, (NH_4)_2SO_4, NH_4HSO_4, H_2SO_4, NaNO_3, H_2O, Ca(NO_3)_2$
- soluble mass fraction
- Density of insoluble part
- Index of refraction of insoluble part
- Time increment
- Bin sizes for particle size ranges 0.01-0.09, 0.1-0.9, 1.0-39.9, 40-99, 100-200
- Total number of aerosols each type
- Effective radius of aerosol each type
- Effective variance of radius each type
- Ratio of primary peak to secondary peak for bimodal distribution or if modified gamma size distribution used gamma.
- Lower boundary of distribution (one for each mode)
- Upper boundary of distribution (one for each mode)
- Size distribution type : gamma, bimodal, log-normal, power-law, modified gamma
- Updraft velocity(0) †
- Thermal accomodation coefficient (set to 1) †
- Base condensation coefficient (set to 1) †
- Starting relative humidity
- Number of carbon groups in the fatty acid surfactant (19) †

- Reference radius, (turns on/off surfactant effect) †
- Molar fraction of sites not occupied by organic material during initial growth (set to 0.99) †

†These parameters were not relevant to this study, values chosen to have no effect on calculations.

Define particles

Constants are stored for each type of particle (constants changed to agree with CARTEL input parameters see tables 2.1.1.1 and 2.1.3.1).

Generate size distribution

Use input size distribution, start, stop radii and effective radius and variance to generate size distribution.

Beginning of calculation loop

If dry particles skip growth loop first time through and goto phase function.

Beginning of growth loop

Grow particles based on relative humidity, and salt concentration. Two methods based on salt concentration (low-high) used. References given in code are Mason, 1971 and Pruppacher and Klett, 1978.

Calculate phase function

Mie calculations (see for example Wickramasinghe, 1973).

Printout results

Print size distribution, phase function and scattering parameters.

Return to beginning of calculation loop until time > end time.

End of program

Comments and discussion

The AES model uses effective mean radius and effective variance. The standard deviation and the geometric radius given by the CARTEL model are related to these quantities in the following manner.

In Appendix A.1 the log normal size distribution is given as :

$$\frac{dN}{d \log r} = \frac{N}{\sqrt{2\pi} \log \sigma} e^{-\frac{(\log r - \log r_n)^2}{2 \log^2 \sigma}} \quad (1)$$

The same equation is expressed by Hansen and Travis (1974) as:

$$N(r) = \frac{1}{\sqrt{2\pi} \sigma_g r} e^{-\frac{(\ln r - \ln r_g)^2}{2 \sigma_g^2}} \quad (2)$$

where the total number of particles has been normalized to 1.

Observing that:

$$dN = n(r) dr \quad (3)$$

$$d \log r = \frac{\log r}{r} dr \quad (4)$$

and

$$\log r = \log e \ln r \quad (5)$$

we can compare the two equation and deduce that

$$\sigma_g = \ln \sigma \quad (6)$$

$$r_n = r_g \quad (7)$$

The effective radius is defined by Hansen and Travis (1974) as

$$r_e = \frac{\int_0^\infty r^3 n(r) dr}{\int_0^\infty r^2 n(r) dr} \quad (8)$$

This can be expressed as:

$$r_e = 3 \frac{\int_0^\infty 4/3 \pi r^3 n(r) dr}{\int_0^\infty 4 \pi r^2 n(r) dr} \quad (9)$$

$$= 3 \frac{\hat{V}}{\hat{S}} \quad (10)$$

$$= \frac{r_3^3}{r_2^2} \quad (11)$$

This gives us the expression:

$$\ln r_e = 3 \ln r_s - 2 \ln r_2 \quad (12)$$

$$= 3 \ln r_n + 9/2 \ln^2 \sigma - 2 \ln r_n - 2 \ln^2 \sigma \quad (13)$$

$$= \ln r_n + 5/2 \ln^2 \sigma \quad (14)$$

$$= \ln r_g + 5/2 \sigma^2 \quad (15)$$

Hansen and Travis (1974) give a relationship between the effective radius r_e , effective variance v_e and geometric radius r_g :

$$r_g = \frac{r_e}{(1 + v_e)^{5/2}} \quad (16)$$

Taking the log of both sides we obtain :

$$\ln r_g = \ln r_e - 5/2 \ln(1 + v_e) \quad (17)$$

$$\ln r_e = \ln r_g + 5/2 \ln(1 + v_e) \quad (18)$$

comparing with equation 15 we must have :

$$\sigma^2 = \ln(1 + v_e) = \ln^2 \sigma \quad (19)$$

To summarize the geometric radius r_g and the standard deviation σ are related to the effective radius r_e and the effective variance v_e as follows :

$$v_e = e^{\ln^2 \sigma} - 1 \quad (20)$$

$$r_e = r_g (1 + v_e)^{5/2} \quad (21)$$

These relationships were used to convert the input values of table 2.1.1.1 for use in the AES program.

It was difficult to determine what the exact comparison should be for the internally mixed and externally mixed aerosol models. While the externally mixed models have a volume ratio the AES programme needs a mass fraction (soluble to total). A calculation was performed to determine the mass fractions from the volume fraction given in table 2.1.3.1.

$$M_F = \frac{V_s d_s}{V_s d_s + V_{insol} d_{insol}} \quad (22)$$

where

$$M_F = \text{mass fraction, soluble to total} \quad (23)$$

$$V_s = \text{volume of soluble aerosol} \quad (24)$$

$$d_s = \text{density of soluble aerosol} \quad (25)$$

$$V_{insol} = \text{volume of insoluble aerosol} \quad (26)$$

$$d_{insol} = \text{density of insoluble aerosol} \quad (27)$$

Using 2.00 gm/cc as the density of soot and 1.80 gm/cc as the density of the soluble aerosol the mass fractions for the continental and urban internal mixtures were calculated and are shown in table C.1

Continental						
R. H. (%)	0	50	70	80	90	95
V_F	0.29/0.1	0.33072/0.0098	0.3533/0.0091	0.4495/0.0078	0.5715/0.006	0.6466/0.005
M_F	0.963	0.966	0.972	0.981	0.988	0.992
Urban						
V_F	0.61/0.22	0.6811/0.1771	0.7760/0.1264	0.8155/0.1041	0.8821/0.0665	0.9320/0.0384
M_F	0.714	0.776	0.847	0.876	0.923	0.956

Table C.1: Mass Fractions

Program validation

A comparison was made using the AES program with Deirmendjian Haze L, Haze H, Haze M models (Deirmendjian, 1969) and SRA + water soluble model (Masuda and Takashima, 1988). These phase functions and values for the scattering coefficients were reproduced accurately.

The AES program must go through several time loops to grow the aerosols. The number of time steps needed was studied so as not to run the program beyond the time needed for convergence to a solution. Table C.2 shows the variation of the value for the phase function at 0 degrees as a function of time for a water soluble aerosol at 95 % relative humidity at 550 nm. Setting the last time step to be 0.04 sec was felt to be adequate

for this study.

Time step (s)	Phase function (0 deg.)	% change
0.00	8.13689	
0.01	10.03803	18.9
0.02	10.41801	3.6
0.03	10.50699	0.8
0.04	10.53174	0.2

Table C.2 : Time for convergence

Figure C.1 shows the variation of the phase function with relative humidity for $(NH_4)_2SO_4$ at 550nm.

As part of the validation procedure the single particle phase functions were calculated and compared with the CARTEL model results (table C.3). This comparison showed the differences in the particle growth procedures in the two programs. Below the deliquescence point of $(NH_4)_2SO_4$, 79% the results are very close, less than 2 % difference. Above the deliquescence point where the particles will grow the results are quite different due to the change in the particle size distribution caused by droplet growth.

Relative Humidity %	AES Program	CARTEL Model
95	15.3770	10.61567
90	10.5317	7.95237
80	6.9779	6.37056
70	5.7313	5.81405
50	4.9148	5.00754
0	4.5576	4.57088

Table C.3: Phase function at 0 degrees

A more relevant comparison might be at for angles in the backscattered direction. Table C.4 shows a comparison for the phase function at a

scattering angle of 136 degrees.

Relative Humidity %	AES Program	CARTEL Model
95	0.06774	0.07681
90	0.07170	0.08429
80	0.08546	0.09536
70	0.10633	0.10503
50	0.13755	0.13276
0	0.15814	0.15889

Table C.4: Phase function at 136 degrees

Once again the differences are greater for relative humidities greater than 80%, here the % difference is between 10-15 % . The scattering cross section is an important parameter and is compared in table C.5. There are significant differences for relative humidities > 80 %.

Relative Humidity %	AES Program	CARTEL Model
95	5.5483E-9	2.7542E-9
90	2.4019E-9	1.5306E-9
80	9.6486E-10	9.7266E-10
70	6.8763E-10	8.0620E-10
50	5.5293E-10	5.9871E-10
0	5.0436E-10	5.0170E-10

Table C.5: Scattering cross section cm^2

The single scattering albedo was also compared and proved to be less

sensitive to the differences in growth model (table C.6).

Relative Humidity %	AES Program	CARTEL Model
95	0.9987	0.9932
90	0.9965	0.9880
80	0.9884	0.9813
70	0.9775	0.9777
50	0.9666	0.9703
0	0.9603	0.9649

Table C.6: Single scattering albedo

Particle growth rate was evaluated by using the change in size distribution maximum as a function of relative humidity (Table C.7). Except for the smooth transition around the deliquescence point the results are the same as those found by Tang et al 1981 for a similar study.

Relative Humidity %	Size dist. r_N maximum 10^{-6} m	r/r_0
95	0.251	2.22
90	0.197	1.74
80	0.152	1.35
70	0.133	1.17
50	0.119	1.05
0	0.113	1.00

Table C.7: Size distribution number density maximum radius

Discussion

The initial reason for this study was to compare the effects of treating the aerosols as an internal or external mixture. The results suggest that the different growth models may be more significant for this particular aerosol model than internal/external treatments. Figure C.2 is variation with relative humidity for continental model at 550nm using table 2.1.1.1 Leaitch model and figure C.3 is urban model. The dust component has not been included since the AES model did not produce the same results for a dust aerosol alone. The differences in the growth model may confuse a direct comparison of phase functions. Figure C.4 is the size distribution as a function of relative humidity. Table C.8 contains the values for the

forward and backscattering directions. The volume scattering cross section is tabulated in table C.9.

Relative Humidity	Phase Function 136 degrees		Phase Function 0 degrees	
	Cont.	Urban	Cont.	Urban
95	0.06729	0.0661	15.07792	14.77224
90	0.06995	0.06578	10.45494	9.99415
80	0.08281	0.09815	6.89182	6.41811
70	0.10933	0.14186	5.63640	5.27573
50	0.14705	0.17993	4.83736	4.58726
0	0.16958	0.18893	4.49158	4.35756

Table C.8 Internally Mixed Results (No dust)

Relative Humidity	AES model (no dust)		CARTEL model	
	Cont.	Urban	Cont.	Urban
95	5.4182E-9	5.1946E-9	2.7423E-9	2.16817E-9
90	2.3751E-9	2.2028E-9	1.5608E-9	1.26902E-9
80	9.540E-10	8.742E-10	1.0219E-9	8.5897E-10
70	6.684E-10	6.234E-10	8.612E-10	7.3665E-10
50	5.442E-10	4.914E-10	6.608E-10	5.8417E-10
0	4.954E-10	4.465E-10	5.672E-10	5.1289E-10

Table C.9 Scattering cross section cm^2

References

- Deirmendjian, D., 1969. *Electromagnetic Scattering on Spherical Polydispersions*. American Elsevier Pub. Co, Inc., New York, 290pp.
- Hansen, J. E. and L. D. Travis, 1974. Light scattering in planetary atmospheres. *Space Sci. Rev.*, 16:527-610.
- Mason, B. J., 1971. *The Physics of Clouds*. Clarendon Press, Oxford, 671pp.
- Masuda, K. and T. Takashima, 1988. Dependence of the radiation just above and below the ocean surface on atmospheric and oceanic parameters. *Applied Optics.*, 27:4891-4898.
- Pruppacher, H. R. and J. D. Klett, 1978. *Microphysics of Clouds and Precipitation*. D. Reidel Pub. Co., Boston, 714 pp.
- Tang, I., W. Wong and H. Munkelwitz, 1981. The relative importance

of atmospheric sulfates and nitrates in visibility reduction. *Atmospheric Environment*, 15:2463-2471.

Wickramasinghe, N. C., 1973. *Light Scattering Functions for Small Particles, with Applications in Astronomy*. Wiley, New York, 506pp.

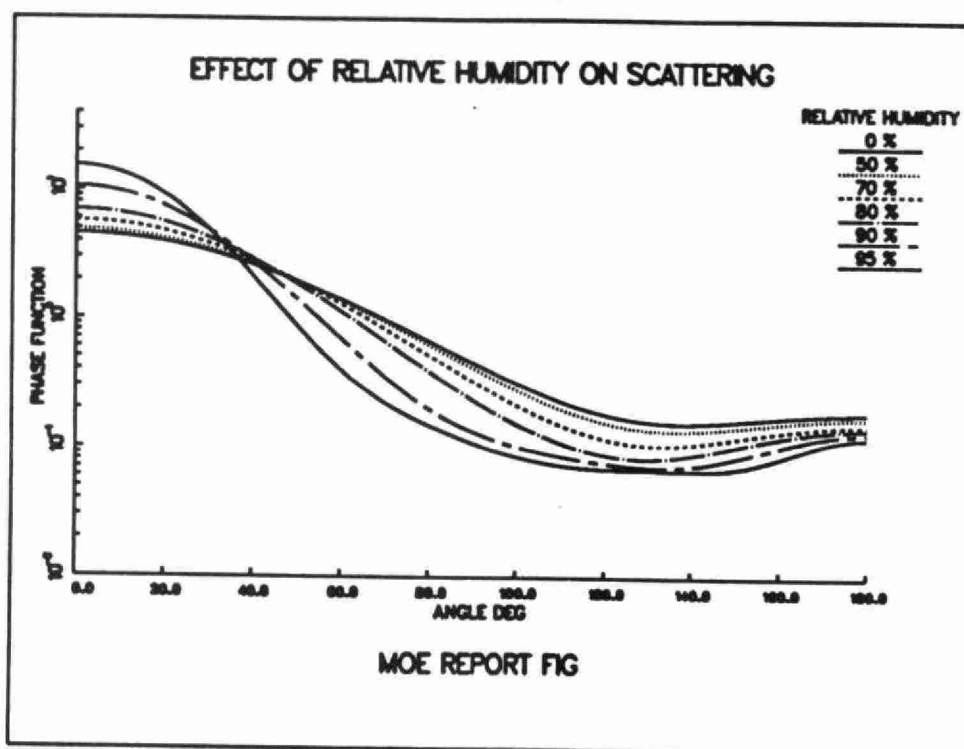


Figure C.1 Water soluble, 550 nm.

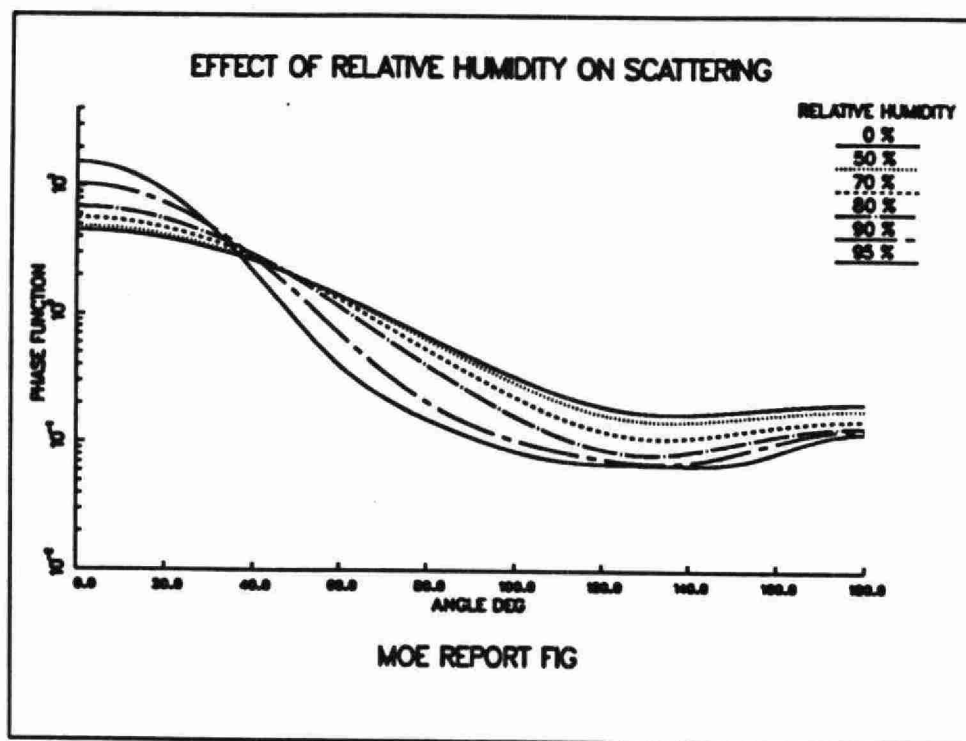


Figure C.2 Internal Mixture, continental, 550 nm.

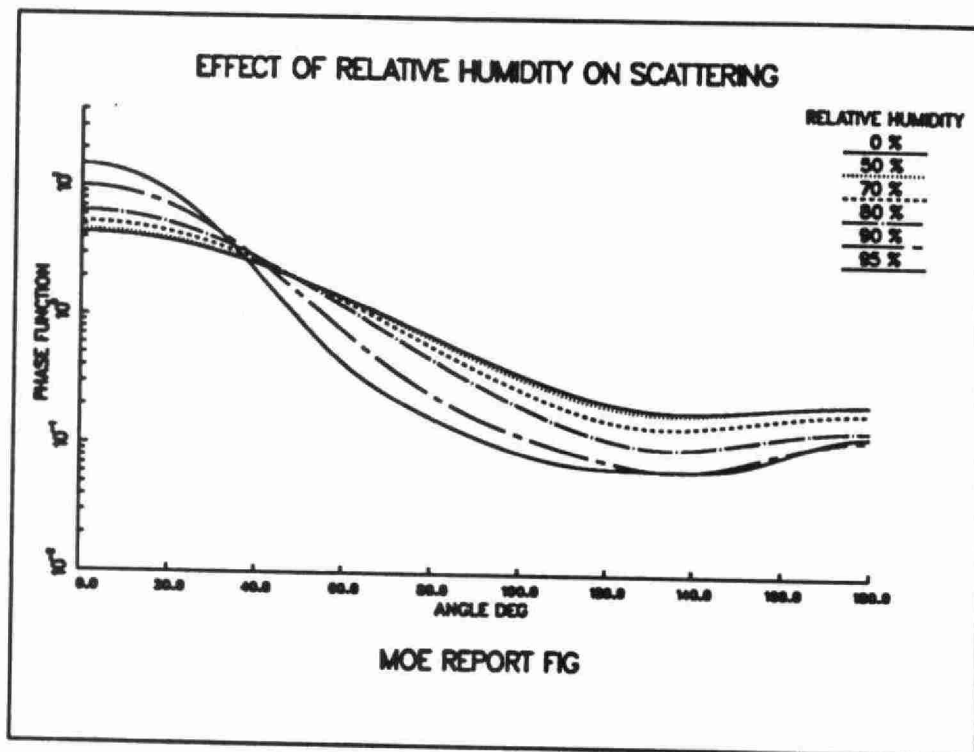


Figure C.3 Internal mixture, urban, 550nm.

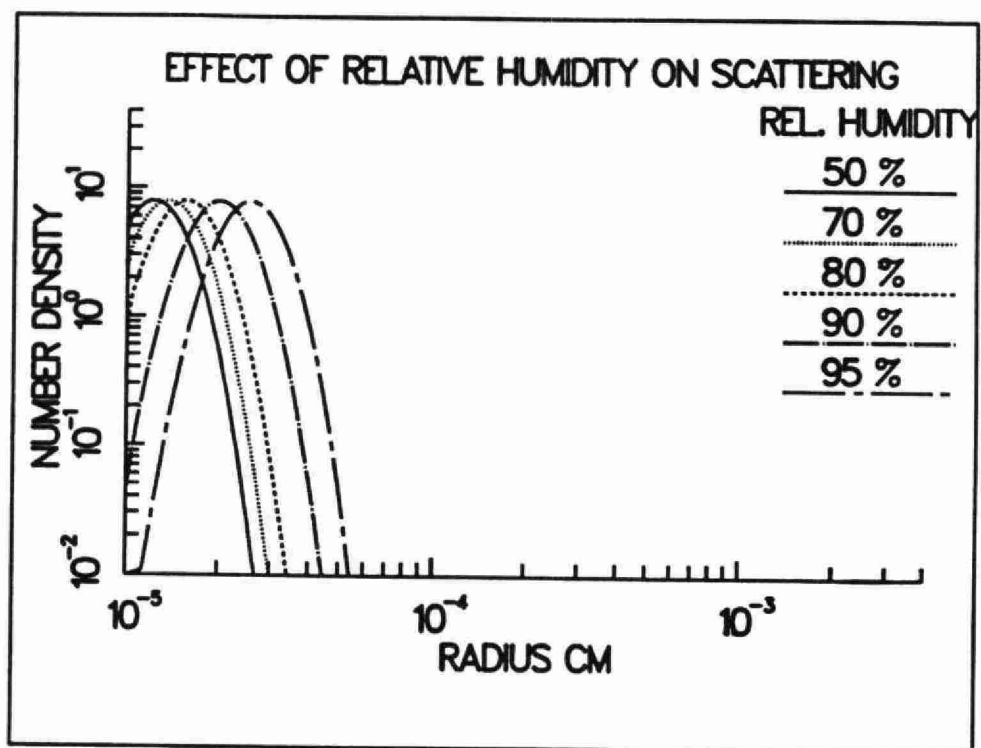


Figure C.4 Particle growth.



(7234)

TD/890/C75/MOE

TD/890/C75/MOE
O'Neill, N.T.
Critical evaluation
of atmospheric abhb
c.2 a aa